Thermal conductivity of mixed oxide fuel (MOX) : effect of temperature, elementary chemical composition, microstructure and burn-up in reactor

Plamen Bonev

UNIVERSITÉ DE LORRAINE

École doctorale 608: SIMPPE

Thermal conductivity of mixed oxide fuel (MOX) : effect of temperature, elementary chemical composition, microstructure and burn-up in reactor.

THÈSE

présentée et soutenue publiquement le 20 décembre 2023

pour l'obtention du

Doctorat de l'Université de Lorraine

(mention Energie et Mécanique)

par

Plamen Bonev

Composition du jury

Président :	Jean-Luc Battaglia	Professeur des universités, Université de Bordeaux
Rapporteurs :	Marat Khafizov	Professeur associé, Ohio State University
	Philippe Le Masson	Professeur des universités, Université Bretagne-Sud
Examinateurs :	Andrea Quaini	Ingénieur de recherche, CEA Saclay
	Dragos Staicu	Ingénieur de recherche, JRC-Karlsruhe
	Fabien Bruneval	Directeur de recherche (HDR), CEA Saclay
	Benjamin Rémy	Directeur de la thèse, Université de Lorraine
Invités :	Nathalie Chauvin	Encadrante de la thèse, CEA Cadarache
	Jacques Lechelle	Directeur de recherche (HDR), CEA Cadarache

Laboratoire d'Energétique et de Mécanique Théorique et Appliquée (LEMTA) — UMR 7563
Centre national de la recherche scientifique (CNRS), Université de Lorraine

Remerciements

Ce travail n'aurait jamais été possible sans l'aide et le soutien de plusieurs personnes, que j'aimerais particulièrement remercier, dans ce texte.

Tout d'abord, j'aimerais remercier mes encadrants de thèse, Nathalie Chauvin et Benjamin Rémy.
Nathalie, merci pour tout le savoir que tu m'as apporté tout au long de ces trois années de thèse, en particulier sur le combustible nucléaire. Ces connaissances me seront précieuses durant toute ma carrière. Merci également pour tous tes conseils pour arriver à garder le sang-froid durant les moments stressants de la thèse. Merci pour ta disponibilité, car tu t'es toujours rendue disponible pour moi (même en congés). Et à ne pas oublier la mission à JRC que je n'aurais jamais pu effectuer sans ton aide.
Benjamin, merci pour ta confiance en moi et tes mots toujours bienveillants. Tu t'es toujours montré compréhensif. Merci également pour les connaissances que tu m'as transmis, concernant les méthodes inverses et en particulier les méthodes Bayésiennes. Nous n'avons pas pu passer autant de temps que voulu en face à face, au vue de la distance entre Nancy et Cadarache, mais j'ai beaucoup apprécié le peu de temps que l'on a passé ensemble au LEMTA.

Je tiens à exprimer mes vifs remerciements à Marat Khafizov et à Philippe Le Masson d'avoir accepté de rapporter ma thèse. Les échanges que nous avons eus pendant la soutenance ont été très enrichissants. Je remercie également les autres membres du jury : Fabien Bruneval, Dragos Staicu, Jean-Luc Battaglia et Andrea Quaini d'avoir examiné mon travail. Globalement, j'aimerais remercier tous les membres du jury de s'être déplacés jusqu'au CEA Cadarache pour participer à ma soutenance de thèse en présentiel.

J'aimerais également remercier Jacques Lechelle pour ses conseils et sa disponibilité. Merci, Jacques, pour tes mots encourageants concernant mon travail et pour ton aide, en particulier, concernant les calculs thermodynamiques sur le paramètre d'ordre à courte distance. Merci également d'avoir participé à mon jury de thèse en tant que membre invité.

Mes remerciements vont également à Johann Bouchet et Michel Freyss, qui m'ont aidé à comprendre les phénomènes se produisant à l'échelle de l'atome.

J'aimerais exprimer ma gratitude à Jérôme Lamontagne, Mireille Bauer et Carole Valot pour avoir suivi mon travail durant ces trois années et pour m'avoir donné la possibilité d'effectuer mes travaux de thèse au CEA Cadarache dans les meilleures conditions.

Je voudrais également remercier le chef du laboratoire LEVA, Arnaud Monnier d'avoir été là dans les moments les plus délicats de la thèse. Merci, Arnaud, pour ta disponibilité et pour tes précieux conseils durant la rédaction de la thèse.

Je souhaite également dire « Merci » à quelques collègues du LEVA qui ont également marqué mon chemin durant ces trois années- Fabien, Tommaso, Isabelle et Denis. Merci pour vos conseils toujours aussi bienveillants.

A mes amis- Adrien, Julie, Robin de la « Team LEVA », j'adresse mes profonds remerciements. Nos soirées et sorties à la plage, avec la pastèque sur la tête, resteront pour toujours dans

ma mémoire. Merci également à Daria, Vincent, Guilherme, Giulia (Giu Giu), Veronica (Ve), Luca (le Maître de la pizza), Quentin et Ambre (les loulous), Anaelle, Sébastien, Paul, Nicolas, Matteo (les deux), Matthieu, Théo, Baptiste, Jules pour tous les moments passés ensemble, à rigoler de tout et de rien.
A mes amis-collègues, Etienne et Jean-Mathieu merci pour vos conseils amicaux et bienveillants.

Et finalement, un « MERCI » très spécial et de tout mon cœur va à deux personnes, deux docteurs, qui m'ont particulièrement marqué: Hakima Bouizem (La Lionne) et Ali Moussaoui. Je remercie la vie de m'avoir offert la chance de vous croiser.

Et pour finir, je tiens à dire le plus grand des « MERCI » à ma famille qui n'a jamais cessé de croire en moi et à m'offrir chaleur et amour inconditionnel.

Abstract

Mixed oxide fuel (MOX) is the nuclear fuel, used in fourth generation reactors, also called fast neutron reactors (FNR). Those reactors operate at very high temperatures (between 1500 and 2500 K). Thermal conductivity is therefore an essential material property to reactor safety. In fast reactor operating conditions, MOX is not only subject to high temperatures, but also to local changes in chemical composition and microstructure, which can have great impact on thermal conductivity. The effect of plutonium content is of particular interest for FNR applications, not only due to its local changes during irradiation, but also because fast reactors can be used to recycle plutonium, in a large range of plutonium atomic content (*i. e.* from 15 to 45 at. %) depending on the core design and the fuel cycle objective. Thermal conductivity models should therefore be predictive in a wide range of plutonium contents.

Most modeling approaches are semi-empirical in their temperature-dependency description of thermal conductivity, and are purely empirical in terms of plutonium and oxygen content-dependency. Those approaches are therefore limited by the number of available experimental data, especially concerning high temperatures (above 2000 K) and high plutonium contents (above 30 at %). The extrapolation of those models beyond their experimental range of validity can therefore lead to high modeling uncertainties.

To address this problem, in this work, we propose to build a model, based on physical foundations. This model is based on a theoretical assessment of the contribution to thermal conductivity of each of the three (quasi)particles responsible for heat transport in oxide fuels: phonons, polarons and photons. The effect of temperature, plutonium and oxygen content on thermal conductivity is therefore clearly identified. Plutonium-oxygen content correlated effects were in particular observed, which do not appear in empirical approaches.
This work also allowed to improve the understanding of irradiation-induced effects on thermal conductivity in FNR irradiation conditions.

The model, proposed in this work was compared to the most up-to-date experimental data on thermal conductivity of MOX fuels, counting a total of 6619 experimental points, originated from different institutions: CEA, European projects, IAEA, OECD. Experimental data confirmed the effect of plutonium content, predicted in this work and in particular provided an experimental evidence for the plutonium-oxygen content correlated effects.
The model was implemented into the CEA fuel performance code *GERMINAL*, from the simulation software platform *PLEAIDES*, to simulate the fuel behavior during the INTA-2 irradiation experiment. The predicted fuel temperature was compared to thermocouple measurements and showed good consistency, highlighting the adequate use of our model in fuel performance codes.

Résumé

Le combustible à oxyde mixte (MOX) est le combustible nucléaire utilisé dans les réacteurs de quatrième génération, également appelés réacteurs à neutrons rapides (RNR). Ces réacteurs fonctionnent à des températures très élevées (entre 1500 et 2500 K). La conductivité thermique est donc une propriété essentielle pour la sécurité des réacteurs. Dans les conditions de fonctionnement des RNRs, le MOX est non seulement soumis à des températures élevées, mais aussi à des modifications locales de la composition élémentaire chimique et de la microstructure, qui peuvent avoir un impact important sur la conductivité thermique. L'effet de la teneur en plutonium est particulièrement intéressant pour les applications en RNR, non seulement en raison de ses changements locaux pendant l'irradiation, mais aussi parce que les réacteurs à neutrons rapides peuvent être utilisés pour recycler le plutonium, dans une large gamme de teneur atomique en plutonium (de 15 à 45 at. %) en fonction de la conception du cœur et de l'objectif du cycle du combustible. Les modèles de conductivité thermique devraient donc être prédictifs dans une large gamme de teneurs en plutonium.

La plupart des approches de modélisation sont semi-empiriques dans leur description de la conductivité thermique en fonction de la température, et sont purement empiriques en termes de dépendance à la teneur en plutonium et en oxygène. Ces approches sont donc limitées par le nombre de données expérimentales disponibles, en particulier pour les températures élevées (supérieures à 2000 K) et les teneurs élevées en plutonium (supérieures à 30 at.%). L'extrapolation de ces modèles au-delà de leur domaine de validité expérimentale peut donc conduire à des incertitudes de modélisation élevées.

Pour répondre à ce problème, nous proposons dans ce travail un modèle construit sur des fondements physiques. Ce modèle est basé sur une évaluation théorique de la contribution à la conductivité thermique de chacune des trois (quasi)particules responsables du transport de chaleur dans les combustibles oxydes : les phonons, les polarons et les photons. Les effets de la température, de la teneur en plutonium et en oxygène sur la conductivité thermique sont donc clairement identifiés. Des effets corrélés entre la teneur en plutonium et en oxygène ont notamment été observés, ce qui n'apparaît pas dans les approches empiriques.
Ce travail a également permis d'améliorer la compréhension des effets induits par l'irradiation en RNR sur la conductivité thermique.

Le modèle proposé dans ce travail a été comparé aux données expérimentales les plus récentes sur la conductivité thermique des combustibles MOX, comptant un total de 6619 points expérimentaux, provenant de différentes institutions : CEA, projets européens, AIEA, OCDE. Les données expérimentales ont confirmé l'effet de la teneur en plutonium, prédit dans ce travail, et ont en particulier fourni une preuve expérimentale des effets corrélés de la teneur en plutonium et en oxygène.
Le modèle a été implémenté dans le code de performance *GERMINAL*, de la plateforme logicielle *PLEAIDES*, afin de simuler le comportement du combustible pendant l'expérience d'irradiation INTA-2. La température de combustible calculée a été comparée aux mesures de thermocouple et a montré une bonne cohérence, soulignant l'utilisation adéquate de ce modèle dans les codes de performance.

Contents

General introduction

The key material property, driving heat transfer in solids, is thermal conductivity. Precise knowledge of this property is essential when studying nuclear fuels, especially oxide fuels. In nominal operating conditions, the temperatures, attained by an oxide fuel are situated in the range $T \in [298 - 2500]$ K, depending on the reactor type (fast or thermal reactor). Oxide fuels, such as UO_2 or **M**ixed **Ox**ide fuels $(U,Pu)O_2$, also called MOX have a relatively high melting temperature (*i. e.* around $T_m = 2850$ K) [1]. Thermal conductivity should be known with high precision in order to evaluate the margin to melt of the fuel, which is a crucial parameter in fuel safety evaluations.
Thermal conductivity of nuclear fuels depends on multiple parameters. One of those parameters is temperature. Indeed, fuel temperature depends on thermal conductivity, which in turn depends on temperature.
During irradiation in a fast reactor, MOX fuel undergoes significant changes in its elementary chemical composition. These changes are driven by the creation of fission products (FP) and the migration of plutonium and oxygen, radially over the fuel pellet. The elementary chemical composition of MOX fuel is therefore crucial in thermal conductivity modeling.
Other parameters, related to the fuel's microstructure can also undergo changes, due to irradiation and also need to be taken into account. Those parameters mainly concern porosity and grain size.

Reported work on thermal conductivity modeling of MOX fuels is mostly based on semi-empirical approaches, which do not include a sufficient number of physical parameters to be able to model the effect of the above-mentioned parameters in a physical manner [2–4]. Those models are based on a fit of thermal conductivity experimental data. Consequently, those models are not predictive beyond their experimental range.
In this work, to avoid problems, related to extrapolating a semi-empirical model beyond its domain of validity, we propose to introduce physical parameters in thermal conductivity modeling. Introducing more physics therefore increases the extrapolation ability of the model to ranges, which are not covered by semi-empirical approaches. This is in particular true for the effect of plutonium content, which is generally not taken into account, due to the use of highly scattered experimental data in a very limited range $y \in [0.1 - 0.3]$ [3–6]. This is also true for the effect of temperature above 2200 K, which in most work is modeled, using very few experimental data points [2]. In this work, we account for a correlated plutonium-oxygen

content effect, which is not considered in semi-empirical approaches, due to high data scattering, especially at temperatures above 2200 K. The model, developed in this work is compared to the most exhaustive up-to-date experimental data on thermal conductivity of MOX fuel, counting a total of 6619 experimental points. The model is also implemented into the fuel performance code *GERMINAL V3* [7] of the fuel simulation software platform *PLEIADES* [8], in order to simulate the effect of this thermal conductivity model on the fuel's local temperature.

This thesis is a part of the CINNA (**C**ombustibles **IN**novants pour les réacteurs refroidis au sodium-**NA**) project, from the CEA R4G (Réacteurs de Quatrième Génération) program.

Introduction générale

La conductivité thermique est la principale propriété des matériaux qui détermine le transfert de chaleur dans les solides. La connaissance précise de cette propriété est essentielle pour l'étude des combustibles nucléaires et en particulier des combustibles oxydes. En fonctionnement nominal, les températures atteintes par un combustible oxyde se situent dans l'intervalle $T \in [298 - 2500]$ K, en fonction du type de réacteur (rapide ou thermique). Les combustibles oxydes, tels que UO_2 ou les combustibles mixtes $(U,Pu)O_2$, également appelés MOX, ont une température de fusion relativement élevée (*i. e.* autour de $T_m = 2850$) [1]. La conductivité thermique doit être connue avec une grande précision afin d'évaluer la marge à la fusion du combustible, qui est un paramètre crucial dans les évaluations de sûreté.
La conductivité thermique des combustibles nucléaires dépend de plusieurs paramètres. L'un de ces paramètres est la température. En effet, la température du combustible dépend de la conductivité thermique, qui dépend elle-même de la température.
Lors de l'irradiation dans un réacteur rapide, le combustible MOX subit des modifications importantes de sa composition chimique élémentaire. Ces changements sont pilotés par la création de produits de fission (PF) et la migration du plutonium et de l'oxygène, radialement sur la pastille de combustible. La composition chimique élémentaire du combustible MOX est donc un élément crucial dans la modélisation de la conductivité thermique.
D'autres paramètres, liés à la microstructure du combustible, peuvent également subir des modifications sous l'effet de l'irradiation et doivent être pris en compte. Ces paramètres concernent principalement la porosité et la taille des grains.

Les travaux publiés dans la littérature sur la modélisation de la conductivité thermique des combustibles MOX sont principalement basés sur des approches semi-empiriques, qui n'incluent pas un nombre suffisant de paramètres physiques pour pouvoir modéliser l'effet des paramètres susmentionnés de manière physique [2–4]. Ces modèles sont basés sur un ajustement des données expérimentales de conductivité thermique. Par conséquent, ces modèles ne sont pas prédictifs au-delà de leur plage expérimentale.

Dans ce travail, pour éviter les problèmes liés à l'extrapolation d'un modèle semi-empirique au-delà de son domaine de validité, nous proposons d'introduire des paramètres physiques dans la modélisation de la conductivité thermique. L'introduction de paramètres physiques augmente donc la capacité d'extrapolation du modèle dans des domaines qui ne sont pas couverts

par les approches semi-empiriques. Ceci est particulièrement vrai pour l'effet de la teneur en plutonium, qui n'est généralement pas pris en compte, en raison de l'utilisation de données expérimentales très dispersées dans une gamme très limitée $y \in [0.1 - 0.3]$ [3–6]. Il en va de même pour l'effet de la température au-dessus de 2200 K, qui, dans la plupart des travaux, est modélisé à l'aide de très peu de données expérimentales. Dans ce travail, nous tenons compte d'un effet corrélé de la teneur en plutonium et en oxygène, qui n'est pas pris en compte dans les approches semi-empiriques, en raison de la forte dispersion des données, en particulier à des températures supérieures à 2200 K.

Le modèle développé dans ce travail est comparé aux données expérimentales les plus récentes sur la conductivité thermique des combustibles MOX, comptant un total de 6619 points expérimentaux. Le modèle est également implémenté dans le code de performance du combustible *GERMINAL V3* [7] de la plateforme logicielle de simulation du combustible *PLEIADES* [8], afin de simuler l'effet de ce modèle de conductivité thermique sur la température locale du combustible.

Cette thèse s'inscrit dans le cadre du projet CINNA (**C**ombustibles **IN**novants pour les réacteurs refroidis au sodium-**NA**) du programme R4G (Réacteurs de Quatrième Génération).

Chapter 1

Context and motivations

Contents

Summary

In this chapter, we will start by setting the nuclear context of this thesis, by introducing the fourth generation reactors and their advantage, compared to second or third generation reactors. We will then refine the context of this thesis, by introducing the main phenomena, which affect the fuel thermal behavior in the reactor and in particular thermal conductivity. We will continue with exposing the state of the art on thermal conductivity modeling. This state of the art will be done in separate sections, covering all of the parameters of interest in thermal conductivity modeling for Fast Neutron Reactor (FNR) MOX fuels. We will then finish by exposing the motivations of this work and in particular the novelties, compared to reported work on this subject. The plan of the manuscript will then be presented.

Résumé

Dans ce chapitre, nous commencerons par définir le contexte nucléaire de cette thèse, en présentant les réacteurs de quatrième génération et leurs avantages par rapport aux réacteurs de deuxième ou troisième génération. Nous affinerons ensuite le contexte de cette thèse en présentant les principaux phénomènes qui affectent le comportement thermique du combustible dans le réacteur et en particulier la conductivité thermique. Nous continuerons en exposant l'état de l'art sur la modélisation de la conductivité thermique. Cet état de l'art sera présenté dans des sections séparées, couvrant tous les paramètres d'intérêt dans la modélisation de la conductivité thermique pour les combustibles FNR MOX. Nous terminerons en exposant les motivations de ce travail et en particulier les nouveautés, par rapport aux travaux publiés dans la littérature sur ce sujet. Le plan du manuscrit sera ensuite présenté.

1.1 Nuclear context: fourth generation reactors

This thesis fits into the framework of research into fourth-generation nuclear reactors (GEN IV). Most of those reactors are Fast Neutron Reactors (FNR), due to the use of a fast neutron spectrum (*i. e.* neutron's kinetic energy > 0.1 MeV), compared to second or third generation reactors, which use a thermal neutron spectrum (*i. e.* neutron's kinetic energy ≈ 0.025 eV) [9, 10].

Fourth generation reactors have multiple advantage, compared to third or second generation reactors. One of them is their capacity to use a greater amount of natural uranium. The latter is composed of 99.3 % of non-fissile U^{238} and of only 0.7 % of fissile U^{235} [11]. During the nuclear chain reaction, non-fissile U^{238} can capture a neutron, and transform into fissile Pu^{239}. In thermal reactors, the slow nature of the neutrons does not allow this capture to occur as efficiently as in fast reactors, therefore limiting thermal reactors to use only fissile U^{235}. Given the low proportions of fissile U^{235} in natural uranium, the fuel needs to be enriched to around 3 % of U^{235} in order to be used in thermal reactors. The fast spectrum of fast reactors however allows to produce Pu^{239} out of the non-fissile U^{238}, therefore increasing the capacity of those reactors to use more of the natural uranium. For the same mass of natural uranium, fast reactors can therefore produce 50 to 100 times more electricity than thermal reactors [12].
Another advantage of fast reactors is their capacity of burning off some of the waste, contained in spent fuel: minor actinides. Thermal reactors cannot do this efficiently [13]. The interest in burning minor actinides lies in the fact that the volume, toxicity and lifespan of the longest-living radioactive waste are considerably reduced.
A final advantage of those reactors, that bears mentioning in this work and which will partially set the scientific context of this thesis, is plutonium management. A 1000 MWe Light Water Reactor (LWR) (*i. e.* third generation reactor) gives rise to about 25 tons of spent fuel a year, containing up to 290 kilograms of plutonium [14]. The latter is then reprocessed and used to produce Mixed Oxide fuel (MOX) $(U,Pu)O_2$. The use of MOX fuel therefore contributes to closing the fuel cycle. However, unlike fast reactors, thermal reactors are limited to use only small amounts of plutonium (*i. e.* below 15 % of plutonium). Fast reactors can use high amounts of plutonium in MOX fuel (*i. e.* above 30 % of plutonium), highlighting their greater recycling capacity, compared to thermal reactors. Given the use of high-plutonium MOX fuels in fast reactors, it is necessary to know the properties of MOX fuels in terms of heat transport and mechanical behavior over a wide range of plutonium contents. Plutonium content will be one of the main subjects of interest in this thesis.

In addition to plutonium content, other parameters should also be considered to guarantee reactor safety, related to the use of MOX fuels in fast reactors. Those parameters are related to fuel temperature, microstructure and chemical composition during irradiation. To have a global view of the phenomena, occurring during irradiation, we will introduce the MOX microstructure and chemical composition, at the fabrication of the fuel and during irradiation.

1.2 Microstructure and chemical composition of MOX fuel

1.2.1 After fabrication

To fabricate MOX fuel, for FNR applications, the process used in France is called COCA (**CO**broyage **CA**darache) [15]. This process uses UO_2 and PuO_2 powders, which are co-milled in proportions corresponding to the final target plutonium content. The MOX microstructure, obtained with this process, is homogeneous in terms of pore and plutonium content distribution. The obtained fuel density corresponds to 95 % of the theoretical one.
MOX fuel crystallizes in the fluorite system. Due to the atmosphere during sintering, the fabrication process leads to a hypostoichiometric MOX (*i. e.* the oxygen/metal ratio is lower than 2). The chemical formula of MOX is the following:

$$U_{1-y}Pu_yO_{2-x}$$

where x represents the deviation from stoichiometry and y the atomic plutonium content $= \frac{[Pu]}{[U]+[Pu]}$.

1.2.2 During irradiation

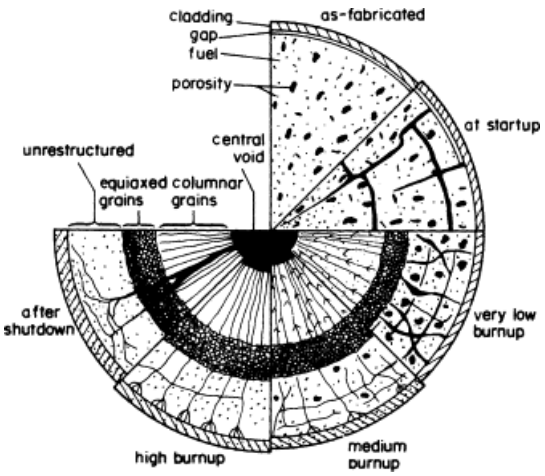

Figure 1.1: Illustrative scheme of the microstructure changes at different burn-up rates (from [16])

When irradiated, the fuel goes through microstructure and chemical composition changes, from the very first seconds of irradiation. We will focus on those, occurring in FNR conditions. At a sufficiently high linear power, the fuel goes through a radial temperature gradient, which can attain 1500 K over 2.5 mm of pellet radius. This temperature gradient is the reason for most microstructure and chemical composition changes (see Figure 1.1).

1.2.2.1 *Microstructure changes*

The literature term to speak about microstructure changes during irradiation, is "fuel restructuring" [11, 17]. The latter is mainly driven by pore migration. This phenomenon is explained by a vapor transport mechanism in which fuel at the surface of the hot side of a pore vaporizes, then condenses on the cool side of the pore [11, 17]. Pore migration leads to the formation of a central void, called central "hole" [18–21] (see Figures 1.1 and 1.2). The fuel is radially divided

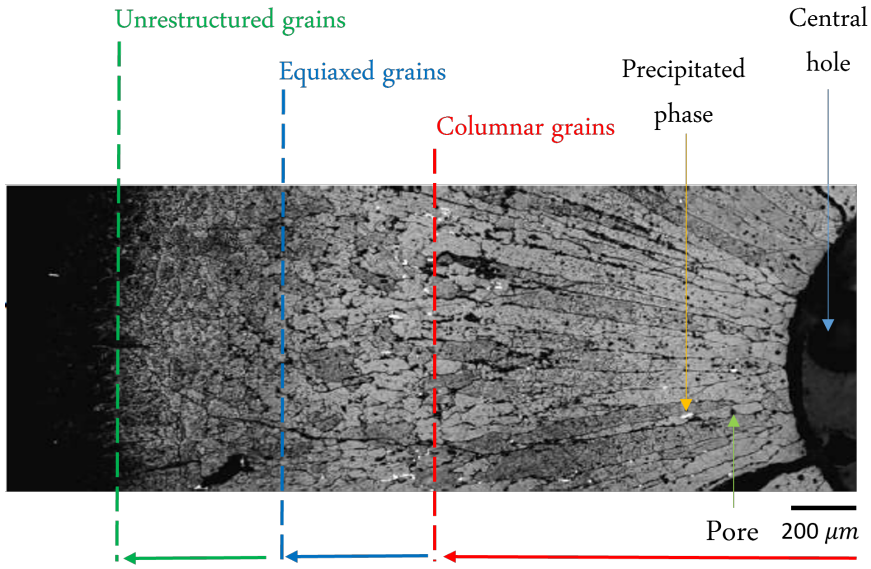

Figure 1.2: Ceramography after chemical etching of the NESTOR-3 FNR MOX fuel (at 1400 mm from the bottom of the pin) [22]

in three regions, which differ by their grain size [23]. We therefore observe columnar grains, close to the central hole, then equiaxed grains at mid-radius and finally close to the pellet external region, grains with a similar size to those after fabrication, called unrestructured region (see Figures 1.1 and 1.2). The grain size, obtained after fabrication depends on the fabrication process, but on average it is situated between 3 and a few tens of microns. The columnar grains can reach the size of 1 mm. Figure 1.2 shows a ceramography after chemical etching, on a MOX fuel, irradiated in the Phenix fast reactor: the NESTOR-3 fuel [24, 25].
Irradiation can also induce important micro and macro mechanical cracking of the fuel, which can have severe impact on heat transport.

1.2.2.2 *Elementary chemical composition changes*

In addition to microstructure changes, the chemical composition is also modified during irradiation. Indeed, nuclear fission produces the so-called fission products (FPs). Those can either dissolve into the fuel matrix or form precipitated phases [26, 27]. Irrespective of their form, fission products have consequent impact on heat transport. In addition to the creation of FPs, important chemical composition changes occur in terms of plutonium and oxygen content, due to high thermal gradient in FNR conditions [21, 28]. This gradient induces the migration of plutonium and oxygen radially over the fuel pellet. The literature term for plutonium or oxygen migration is "redistribution". Plutonium redistributes towards the center of the pellet, whereas

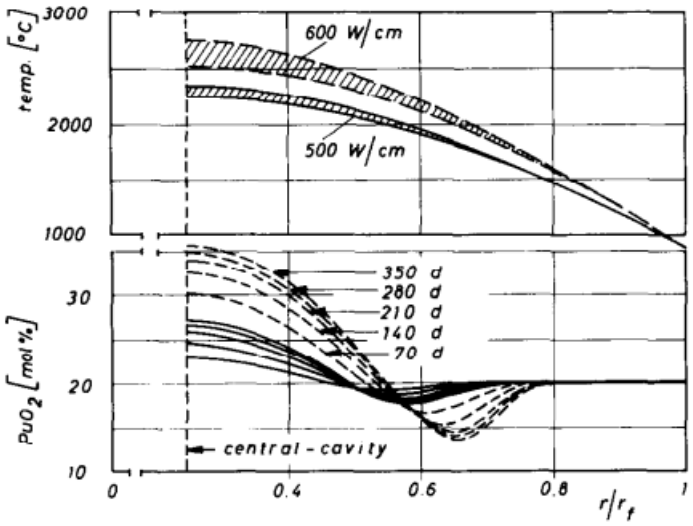

Figure 1.3: Radial redistribution of plutonium at different irradiation instances (in days), according to [29]

oxygen to the external part of the pellet [29]. Plutonium can reach up to 30 % of redistribution. That is, close to the pellet's periphery, the plutonium content is the same as after MOX fabrication, whereas close to the central hole, the plutonium content is 30 % greater (see Figure 1.3).
Since oxygen also exhibits radial redistribution, the oxygen/metal ratio can take values in the range $[1.91 - 2]$ (see Figure 1.4).

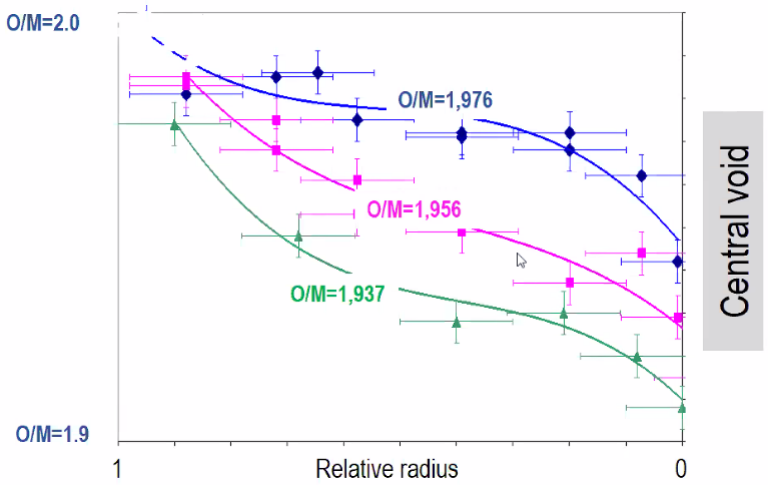

Figure 1.4: Radial redistribution of oxygen, due to high temperature gradient in FNR irradiations [30].

1.2.3 Simulation of the fuel behavior under irradiation

To simulate the above-mentioned phenomena and their consequence on the thermo-mechanical behavior of the fuel, CEA uses the *PLEIADES* platform (**P**late-forme **L**ogicielle pour les **E**lements **I**rradiés dans les **A**ssemblages, **D**emonstration, en **E**xpériminetation, ou en **S**ervice)

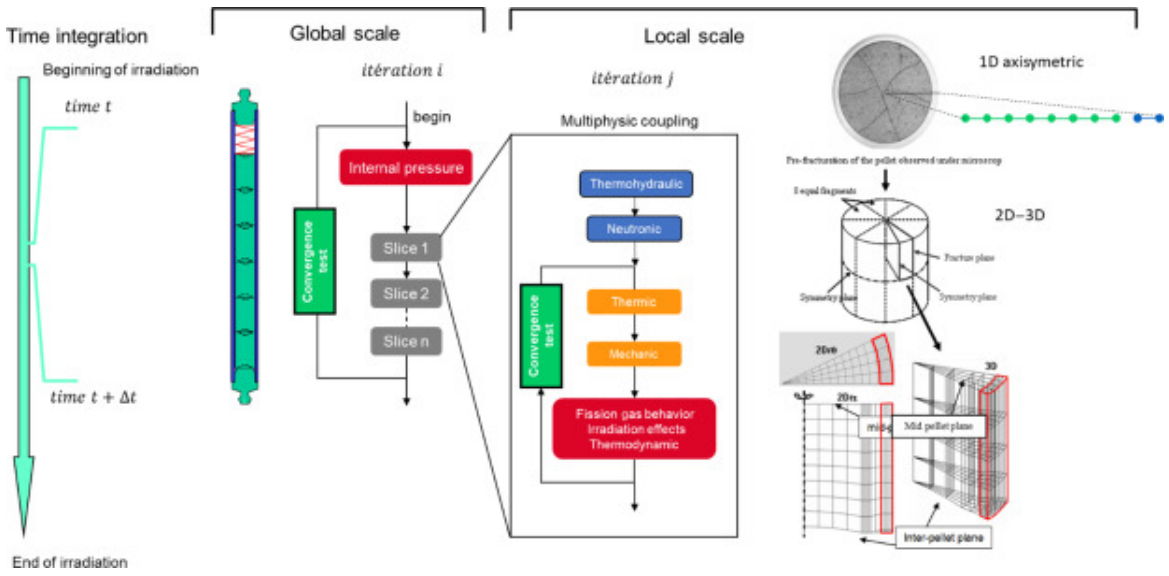

Figure 1.5: PLEIADES generic computational scheme (from [8])

[8]. *PLEIADES* is a software platform that brings together behavioral models, material laws and fuel performance codes for the various nuclear power systems. The fuel performance codes of this platform are *ALCYONE* [31] and *GERMINAL* [7] for Pressurized Water Reactors (PWR) and FNR fuel rod types respectively [8]. For more information about the different algorithms, and models used in the *PLEIADES* software, the reader may refer to [8].

To provide accurate results, fuel performance codes require physical models. One of the most crucial models for fuel safety evaluations is the model for thermal conductivity. The latter contributes, together with other properties, to explain the local fuel temperature and thus the fuel melting margin. To provide the most accurate estimate of the fuel melting margin, the thermal conductivity model must be based on physical foundations. Most models for thermal conductivity, reported in the literature are based on empirical approaches, which strongly depend on the available experimental data [2, 3, 32]. In the following sections, we will present those approaches.

1.3 State of the art on thermal conductivity modeling of MOX

A non-exhaustive review of the reported thermal conductivity models will be presented here. Further details on the models will be given in the associated chapters.

1.3.1 Temperature variation of thermal conductivity

The temperature dependency of most thermal conductivity models for fresh MOX fuel (*i. e.* unirradiated), used in fuel performance codes, are based on the two following equations [3–5]:

$$\lambda_{m,0}(\boldsymbol{T}) = \frac{1}{A + B\boldsymbol{T}} + \frac{C}{\boldsymbol{T}^n} \exp\left(-\frac{E}{k\boldsymbol{T}}\right) \tag{1.1}$$

or

$$\lambda_{m,0}(\boldsymbol{T}) = \frac{1}{A + B\boldsymbol{T}} + D\boldsymbol{T}^3 \tag{1.2}$$

where $\lambda_{m,0}$ is the thermal conductivity of the unirradiated (U,Pu)O_2 fuel matrix, and A, B, C, D, E, n are physical parameters, the meaning of which will become more clear in the following sections. Equations 1.1 and 1.2 differ in terms of their Arrhenius $\frac{1}{T^n}\exp\left(-\frac{E}{k\boldsymbol{T}}\right)$ or cubic $\boldsymbol{T}^3$ increase with temperature.

No reason for choosing either of those two temperature variations has been clearly identified in the literature. Indeed, most authors use thermal conductivity experimental data to fit the constants of the model, by the least-squares method [3–6, 33]. Therefore, the temperature dependency is most certainly compensated by the constants (*i. e.* D in Equation 1.2 and C, n and E in Equation 1.1). In addition, the physical meaning of the fitted constants has never been clearly explained, therefore making it difficult to say which temperature variation is physically correct. Another difficulty in modeling the temperature variation of thermal conductivity above 2000 K is the missing experimental data. Indeed, most authors use very few measurement points to fit their high-temperature thermal conductivity term. For example, Philipponneau [2] only used 4 (λ_i, T_i) points, above 2200 K, to fit the D constant in DT^3. The use of so few measurements leads to large modeling uncertainties at temperatures, that are easily achieved in fast reactors. Indeed, in nominal FNR conditions, the temperature close to the pellet center can achieve 2500 K, which is close to the melting temperature of MOX fuel (i. e. $\approx$ 2850 K [1]). Therefore, improving the accuracy of thermal conductivity at these temperatures should be the primary concern for reactor safety.

1.3.2 Effect of plutonium content on thermal conductivity

The discrepancies between various models concerning the temperature dependence of thermal conductivity are not the only subject of concern. Indeed, plutonium content, which is a parameter of crucial importance in FNR applications, is often not taken into account in thermal conductivity modeling. One of the few authors, who studied the effect of plutonium content on thermal conductivity is Bonnerot [5]. However, in Bonnerot's study, the experimental data, used to fit a thermal conductivity model only covered MOX fuels with plutonium contents lower than 30 at. %. We recall that in FNR MOX fuel, plutonium redistribution can yield concentrations attaining 60 at. % close to center of the fuel pellet. This would be the case for a MOX fuel with 45 at. % of plutonium at its fabrication. Therefore, thermal conductivity models for FNR applications should be predictive at least until 60 at. % of plutonium. Higher concentrations than 60 at. % should also be covered since fast reactors can be used as plutonium burners, depending on the countries' plutonium management policies.

Figure 1.6 shows the temperature variation of thermal conductivity of MOX, predicted by several models. We observe that the model of Bonnerot yields surprisingly lower values, when evaluated beyond its domain of validity (*i. e.* for $y = \frac{[\mathrm{Pu}]}{[\mathrm{U}] + [\mathrm{Pu}]}$ >0.3). In particular for $y = 0.8$, Bonnerot yields an almost zero thermal conductivity at $T = 3000$ K. This does does not seem physical given that at $T > 2850$, MOX fuel attains its melting point and therefore

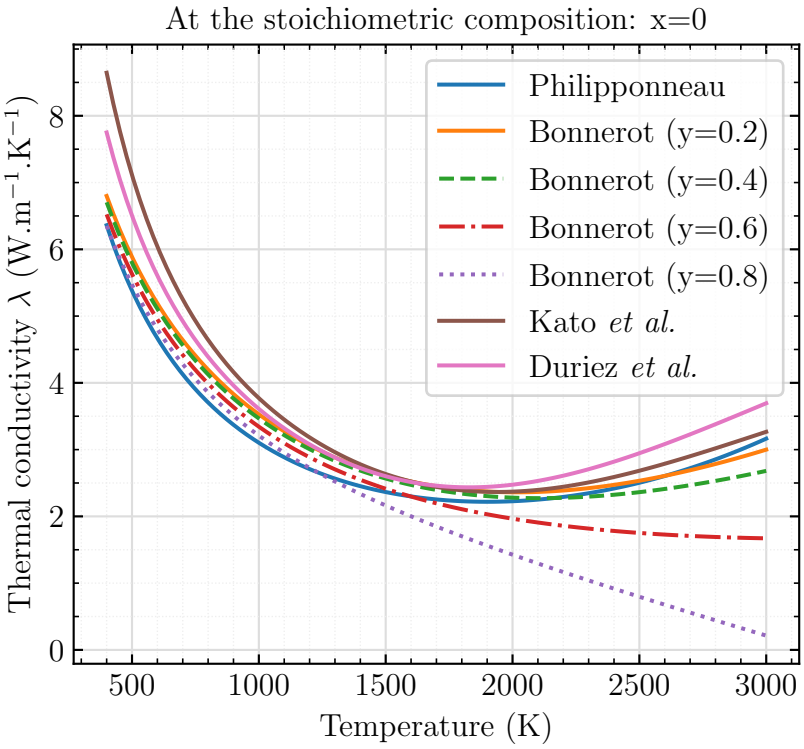

Figure 1.6: Temperature variation of thermal conductivity of MOX fuel, predicted by several models: Philipponneau [2], Bonnerot [5] (for multiple plutonium contents), Duriez *et al.* [4], Kato *et al.* [3]

thermal conductivity is expected to be much higher. Magni *et al.* [33] also included a plutonium content dependency in their model. However, they predict a very slight plutonium effect: of the order of 10^{-6} % of thermal conductivity decrease from $y = 0.05$ to $y = 0.45$, which is negligible to the plutonium content dependency, predicted by Bonnerot. A more exhaustive study of the effect of plutonium, reported in different work will be presented in Chapter 4.

1.3.3 Effect of fission products on thermal conductivity

As mentioned previously, **F**ission **P**roducts (FPs), can either dissolve into the fuel matrix or create precipitated phases. The main soluble FPs (*i. e.* which dissolve into the fuel matrix) are Y, Zr and rare earths (*i. e.* La, Ce, Pr, Nd, Pr, Sm, Eu, Gd) [11]. The precipitated phases are metallic: **F**ive **M**etal **P**recipitates (FMP), composed of Mo, Ru, Tc, Rh, Pd and oxide **G**rey **P**hase (GP) - $(BaZr)O_3$ [11, 26, 27, 34, 35].

Most thermal conductivity models, taking into account the effects of fission products are based on PWR UO_2 **SIM**ulated **F**uel (SIMFuel) experimental data [32, 36, 37]. SIMFuels are fresh fuels, doped with stable fission products (FPs), the concentration of which can be controlled during fabrication [38]. Performing thermal property measurements on SIMFuels therefore provides understanding of the separate effect of FPs, without considering other irradiation-induced effects: gas bubbles, micro-cracks, lenticular pores [39].
However, using PWR UO_2 SIMFuel data to model the effect of FPs on FNR MOX fuel may

lead to high uncertainties. Indeed, the nuclear fission of Plutonium 239, contained in FNR MOX fuel, yields two times more metallic fission products (*i. e.* Mo, Ru, Rh, Pd, Tc) than the fission of Uranium 235 in PWR UO_2 fuel [35, 40] (see Table 1.1). The FMP phase is therefore more abundant in MOX than in UO_2 fuels.

Chemical group	**Elemental yield**		
	^{235} U	^{239} Pu	15 % ^{239} Pu + 85% ^{238}U
Zr+Nb	29.8	20.4	21.9
Y+rare earths*	53.4	47.1	49.3
Ba+Sr	14.9	9.60	10.9
Mo	24.0	20.3	20.6
Ru+Tc+Rh+Pd	26.3	51.6	45.6
Cs+Rb	22.6	18.9	20.9
I+Te	1.20	7.00	
Xe+Kr	25.1	24.8	

Table 1.1: Reconstruction of the table, given in [35, 40]. The elemental yields correspond to the number of fission products per 100 atoms of fissioned ^{235} U, ^{239} Pu or 15 % ^{239} Pu + 85% ^{238}U.
* Lanthanum, cerium, praseodymium. neodymium, promethium, samarium, europium, and gadolinium.

This leads to the conclusion that the chemical composition of UO_2 PWR SIMFuels and MOX FNR SIMFuels is different. Using a thermal conductivity model, based on UO_2 PWR SIMFuels, to represent the effect of FPs on FNR MOX fuel therefore does not seem appropriate.

Two different SIMFuel-based approaches exist in the literature [2, 32, 36, 37]. The first approach, used by Philipponneau [2] consists of adding a burn-up β dependent term in the phonon contribution to thermal conductivity of fresh fuel:

$$\lambda_{irr} = \frac{1}{(A_0 + 0.44\beta) + B_0 \cdot T} \tag{1.3}$$

where the irr and 0 subscripts refer to irradiated and fresh fuel. The A_0 and B_0 are phonon constants, the physical meaning of which will be detailed in Chapter 3. The burn-up β can be understood as the number of fissions per initial metal atom. One of the most widely used units to describe the burn-up in reactor is % FIMA (**F**ission per **I**nitial **M**etal **A**tom). 13 % FIMA of burn-up therefore means that over 100 of initial heavy atoms, 13 have gone through a nuclear fission.
To develop Equation 1.3, Philipponneau used experimental data on FNR MOX SIMFuels [39] The β-dependent term is supposed to account for the effect of all types of FPs: dissolved and precipitated.

Another approach, based on the work of Lucuta *et al.* [32, 36, 37] consists of separating the effect of dissolved and precipitated FPs in two terms. To develop the term, accounting

for dissolved FPs, Lucuta *et al.* [32, 36, 37] used experimental data on UO_2 PWR SIMFuels, instead of FNR MOX SIMFuels.
In addition to the effect of FPs, Lucuta *et al.* [32, 36, 37] added a third term, related to the radiation damage: atom displacement from the initial lattice position, due to the collision of the fissile isotope with a neutron. Thermal conductivity of irradiated fuel, according the approach of Lucuta *et al.*, can be expressed as follows:

$$\lambda_{irr} = \lambda_0 \cdot F_{prec,FP}(q) \cdot F_{diss,FP}(\beta) \cdot F_{rad}(T) \tag{1.4}$$

where $F_{\text{prec, FP}}(q)$ is the factor, accounting for precipitated FPs with volume fraction q, $F_{\text{diss, FP}}(\beta)$- for dissolved FPs and $F_{rad}(T)$ for radiation damage.

This approach presents certain application difficulties, as it requires information on microstructure (*i. e.* precipitated phases of volume fraction q), burn-up β and temperature T. This information is not systematically provided. To estimate the volume fraction of precipitated phases, Lucuta *et al.* [32, 36, 37] used a well-known equation linking the total amount of precipitated phases q and the burn-up β: $q = 0.0038 \times \beta$ [41]. This equation is however strictly empirical and is based on PWR UO_2 data.

The validity of the approach of Lucuta *et al.* was approved for UO_2 fuels, irradiated in PWR conditions [32] and is used in the *ALCYONE* fuel performance code of the *PLEIADES* platform [8, 31]. Until 2020, there was no evidence of the Lucuta model's ability to describe experimental thermal conductivity data on MOX fuels, irradiated in FNR irradiation conditions. In 2020, in the framework of the ESNII+ project [25], pioneering experimental data on FNR MOX fuel, irradiated at high burn-up rates (*i. e.* 13 and 8 % FIMA) was published [25]. Lucuta's equation was proven to be inconsistent with the measurements on FNR MOX fuels, irradiated at high burn-up rates [25]. Before 2020, the only available experimental data of thermal conductivity of FNR MOX fuel was that of Yamamoto *et al.* [42]. However, the thermal conductivity measurements were performed on pellets irradiated at low burn-up rates (<3.5 % FIMA). Therefore, no significant effect of irradiation was observed in comparison to the thermal conductivity of fresh fuels and no recommendation for the effect of irradiation in FNR conditions was provided.

It should be emphasized that the physics of irradiated fuels, especially in FNR conditions is complex and that phenomena, such as "JOG" (**J**oint **O**xyde-**G**aine) (see Figure 1.7) or "ROG" (**R**éaction **O**xyde-**G**aine in French or FCCI (**F**uel **C**ladding **C**hemical **I**nteraction) in English) formation can also affect thermal conductivity. Similarly to plutonium and oxygen, fission products can migrate radially, by atomic diffusion [11, 22, 35].

For example, Cs diffuses towards the pellet periphery, creating another phase, called the "JOG" (see Figure 1.7) with the following chemical formula: Cs_2MoO_4 [44–46]. Elements from the cladding can also migrate towards the fuel, creating a phase called ROG in French, or FCCI in English [43, 46].

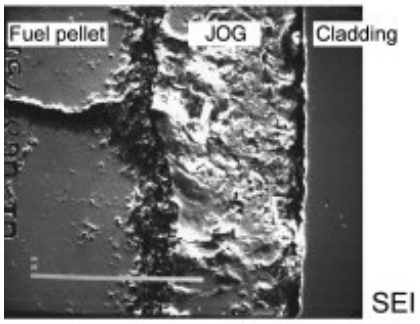

Figure 1.7: X-ray image analysis of JOG formation on the G357 pin (MOX fuel with 30 % of Pu), irradiated in the JOYO reactor at 12.7 % FIMA [43].

The effect of JOG and ROG on thermal conductivity of MOX fuel is not included in modeling due to the complex nature of those phenomena.

1.3.4 Effect of other irradiation-induced phenomena

In addition to the creation of fission products, other irradiation-induced phenomena can also have an impact on thermal conductivity. Those phenomena include lattice point defects, such as oxygen vacancies and interstitials, or extended defects: dislocations and dislocation loops [47].
Most reported work on the effect of point or extended irradiation-induced defects are based on Molecular Dynamics (MD) calculations on UO_2 systems [48–51].
To our knowledge, for MOX fuel, no such calculations were reported in the literature. It was outside the scope of this work to model the effect of oxygen interstitials or extended lattice defects.

1.3.5 Effect of porosity on thermal conductivity

Thermal conductivity modeling should also account for porosity. Indeed, as already mentioned, due to porosity migration during irradiation in FNR conditions, MOX fuel becomes strongly heterogeneous in terms of porosity shape, form and spatial distribution [11]. Multiple literature reviews on the effect of porosity on thermal conductivity of nuclear fuels have been reported in the literature [52–66]. Some of those studies are based on analytical approaches [52, 54, 67] and others on **F**inite **E**lement **M**ethod (FEM) or **F**ast **F**ourier **T**ransform (FFT) calculations [68–71]. An exhaustive state of the art on those reviews is available in Annex A. In fuel performance codes (*e. g.* *GERMINAL* and *ALCYONE*), porosity is taken into account using analytical expressions. Indeed, including FEM or FFT calculations in fuel performance codes would strongly increase computation time. Choosing the analytical expression, which suits the particular needs of *GERMINAL* or *ALCYONE* is therefore crucial to correctly predict the effect of porosity on thermal conductivity, during irradiation.

Using a predictive analytical model for the effect of porosity on thermal conductivity is

not only crucial to correctly simulate the fuel behavior in reactor, but also to accurately "measure" the thermal conductivity of the (U,Pu)O_2 fuel matrix. Indeed, thermal conductivity measurements provide information about the effective thermal conductivity of the material (*i. e.* including grain boundaries and porosity). Therefore, to extract the thermal conductivity of the fuel matrix from measurements, a correction for the effect of porosity and grain boundaries, should be applied. To our knowledge, no analytical model for the effect of grain boundaries was reported in the literature, and most empirical models intrinsically account for grain boundaries.

To correct for pores of volume fraction p, different analytical models can be used. For example, Duriez *et al.* [4] and Philipponneau [2] used a porosity correction of the type: $\frac{\lambda_p}{\lambda_m} = \frac{1-p}{1+2p}$, where λ_p and λ_m refer to the **p**orous material (*i. e.* the measured thermal conductivity) and the fuel **m**atrix, respectively. Kato *et al.* [3] used instead $\frac{\lambda_p}{\lambda_m} = \frac{1-p}{1+0.5p}$. Other work [33] are based on: $\frac{\lambda_p}{\lambda_m} = (1-p)^{2.5}$.
The main similarities between all those models reside in the following assumptions:

1. Thermal conductivity of the pores is negligible to that of the fuel matrix
2. Pores do not interact with each other (*i. e.* diluted pores)

Some porosity correction models were shown to be suitable for spherical pores, others for lenticular ones [52, 54, 60]. For example, most authors use the general expression:

$$\frac{\lambda_p}{\lambda_m} = \frac{1-p}{1+\beta p} \tag{1.5}$$

where β is adapted for the particular shape of the pores: $\beta = 0.5$ for spherical pores or $\beta = 2$ for flatter pores (*i. e.* lenticular).
If the pore shape, volume fraction and distribution is known for each measured MOX fuel, thermal conductivity measurements can be corrected for porosity, by applying the most adapted analytical model. However, in most work, authors do not specify the MOX microstructure and the choice of a particular porosity correction model seems random. An accurate choice of the analytical expression, suitable for the particular microstructure of the measured MOX fuel is crucial. An inadequate use of a porosity correction model can lead to an inaccurate estimate of thermal conductivity of the fuel matrix and therefore of the effect of chemical composition.

The above-mentioned models should be used with precaution, not only due to their strong assumptions on the shape, volume fraction and distribution of the pores, but also because they are based on strong assumptions on the thermal conductivity of the pore. If the assumption on pore shape (*i. e.* spherical) holds for fabrication pores and intragranular gas bubbles, the assumption on the thermal conductivity of the pore (*i. e.* negligible to that of the fuel matrix) may no longer hold for pores with greater size or for pores, containing different types of gas (in particular He, Xe or Kr) [60, 61].
It should also be mentioned that nano-scale fission gas bubbles can also form [72]. To account for nano-scale gas bubbles, other models are used. Some of those are presented in references [73, 74]. In this work, we cover only micro-scale gas bubbles and fabrication pores.

1.3.6 Effect of grain size and boundaries on thermal conductivity

To our knowledge, literature data about the effect of grain size and boundaries in nuclear ceramics is limited. Millet *et al.* [75–77] calculated the effect of grain size and boundaries on thermal conductivity of UO_2 fuel, using phase-field simulation techniques. According to their work, thermal conductivity decreases with grain size. Indeed, grain boundaries play the role of thermal barriers through their so-called Kapitza resistance. The latter occurs through phonons scattering due to the atomically disordered interfacial region. However, to our knowledge, no reliable experimental proof about the effect of grains on nuclear ceramics has been reported in the literature. For this reason, the effect of grain size was not covered in this doctoral research.

1.4 Motivations of this work

The modeling approach of most published work on thermal conductivity of MOX fuels consists of (1): providing a simple general temperature variation of the matrix' thermal conductivity and (2): fitting the unknown model parameters, using available experimental data on the effective thermal conductivity. The two main disadvantages of this approach are (1): the number of available experimental data and (2): the temperature, plutonium and oxygen content ranges, covered by the experimental data. In other words, those models are only predictive in a specific range of temperature, plutonium and oxygen content. This was highlighted in Bonnerot's model for the effect of plutonium content, which yields a zero thermal conductivity at $T = 3000$ K, when evaluated beyond its domain of validity. In addition, most authors who investigated the effect of plutonium content on thermal conductivity, based their study on PWR MOX fuels, in which plutonium content does not exceed $y = 0.3$ [2–5, 78–82]. Therefore, such empirical correlations for the effect of plutonium content may induce high modeling uncertainties, when applied to FNR MOX fuels, given the plutonium redistribution, occurring in fast reactor irradiation conditions. It follows the same for the effect of fission products on thermal conductivity of FNR MOX fuel. The use of PWR UO_2 experimental data to model the FNR MOX fuels may not be appropriate.

In addition, the thermal conductivity dependency on temperature, plutonium and oxygen content could be biased by an inappropriate use of a porosity correction model to deduce thermal conductivity of the fuel matrix from the effective (*i. e.* measured) one.

To sum up, the motivations of this work arise from:

1. missing physical foundation of the temperature variation of thermal conductivity, especially at high temperatures.
2. the use of experimental data, which most of the time does not cover FNR MOX fuels.
3. missing understanding of the effect of FPs on MOX fuels, irradiated in FNR conditions.
4. the frequently accepted hypothesis, that pores have zero thermal conductivity, in most porosity correction models.

This thesis proposes a model, based on physical foundations. We namely take into account:

1. the effect of plutonium content ($\mathbf{y} \in [0.05 - 0.95]$)
2. deviation from stoichiometry ($x \in [0.00 - 0.10]$)
3. temperature ($T \in [385 - 2850]$)
4. porosity volume fraction ($p \in [0.00 - 0.10]$)
5. concentration of fission products, under both dissolved or precipitated form
6. atom displacement during irradiation

1.5 Plan of the manuscript

The manuscript is divided into four main chapters (excluding this context chapter):

1. In the first chapter, we will study the effect of both microstructure and FPs on thermal conductivity. We will be concerned with the effect of porosity on thermal conductivity, which will allow us to choose an appropriate porosity correction model to deduce matrix thermal conductivity from effective thermal conductivity measurements. In the same chapter, we will study the effect of FPs on FNR MOX fuel. We will propose a new model, based on pioneering experimental data on FNR MOX fuels, irradiated at high burn-up rates.
2. The next chapter looks at the physical basis of the thermal conductivity of the MOX fuel matrix, taking into account the contributions of phonons, polarons and photons.
3. In Chapter 4, we will use the most up-to-data experimental data set, composed of 6619 experimental points, to estimate some model parameters by inverse methods and validate the proposed model.
4. Finally, the proposed model will be implemented into the *GERMINAL (V3)* fuel performance code from the software platform *PLEIADES*, to simulate the fuel temperature, during the INTA-2 experiment in the JOYO fast neutron reactor in Japan. The calculated fuel temperature will be compared to the in-pile (*i. e.* in the reactor) measured temperature.

Chapter 2

Modeling of the effective thermal conductivity of $(U,Pu)O_2$ fuel: taking into account microstructure and irradiation-induced effects

Contents

Summary

In this chapter, we model the effect of porosity and fission products on thermal conductivity. The chapter is therefore divided into two sections.

Firstly, we will study the effect of porosity (fabrication pores, gas bubbles and cracks). To do so, we will use an analytical method, which allows us to consider the effect of pore size, shape and the type of gas, contained in the pores. Most models for the porosity effect on thermal conductivity are based on the assumption that pores are spherical, diluted into the fuel matrix and have zero thermal conductivity. In this chapter, we will verify if those assumptions hold for the particular case of MOX fuel, by considering its porosity network, after both fabrication and irradiation. This section therefore starts by presenting the different types of pores, occurring in fabricated and irradiated MOX fuel. Then the analytical approach, used in this work to verify the above-mentioned assumptions, will be presented. We will finish by presenting the results and conclude.

Secondly, we will study the effect of the microstructure, resulting from the accumulation of fission products on the thermal conductivity of FNR MOX fuel. Most published work on irradiated fuel concern Pressurized Water Reactor (PWR) MOX fuel. Furthermore, irradiation-induced effects on thermal conductivity are generally modeled, using experimental data on PWR SIMulated Fuels (SIMFuels). In this work, a novel approach for estimating the thermal conductivity of irradiated MOX fuel, under FNR irradiation conditions, will be presented. This approach is based on pioneering experimental data on FNR MOX fuel, irradiated at high burn-up rates (8 and 13 % FIMA) and *GERMINAL (V2)-Thermo-Calc (V4.1)/TAF-ID (V11)* calculations. In this work, new parameters are introduced in modeling, which do not appear in reported research on the subject.

Résumé

Dans ce chapitre, nous modéliserons l'effet de la microstructure (à savoir la porosité) et de l'irradiation sur la conductivité thermique. Le chapitre est donc divisé en deux sections.

Tout d'abord, nous étudierons l'effet de la porosité. Pour ce faire, nous utiliserons une méthode analytique qui permet de prendre en compte l'effet de la taille et de la forme des pores ainsi que le type de gaz qu'ils contiennent. La plupart des modèles relatifs à l'effet de la porosité sur la conductivité thermique reposent sur l'hypothèse que les pores sont sphériques, dilués dans la matrice du combustible et que leur conductivité thermique est nulle. Dans ce chapitre, nous vérifierons si ces hypothèses sont valables pour le cas particulier du combustible MOX, en considérant son réseau de porosité, après fabrication et irradiation. Cette section commence donc par présenter les différents types de pores présents dans le combustible MOX fabriqué et irradié. Nous présenterons ensuite l'approche analytique utilisée dans ce travail pour vérifier les hypothèses mentionnées ci-dessus. Enfin, nous présenterons les résultats et conclurons.

Deuxièmement, nous étudierons les effets induits par l'irradiation sur la conductivité thermique du combustible MOX FNR. La plupart des travaux publiés sur le combustible irradié concernent le combustible MOX, utilisé dans les Réacteurs à Eau Pressurisée (REP). En outre, les effets induits par l'irradiation sur la conductivité thermique sont généralement modélisés à l'aide de données expérimentales sur des combustibles, dites Combustibles SIMulés (SIMFuels). Dans ce travail, une nouvelle approche pour l'estimation de la conductivité thermique du combustible MOX irradié, dans les conditions d'irradiation des Réacteurs à Neutrons Rapides, sera présentée. Cette approche est basée sur des données expérimentales pionnières sur le combustible FNR MOX, irradié à des taux de combustion élevés (8 et 13 % FIMA) et sur des calculs *GERMINAL (V2)-Thermo-Calc (V4.1)/TAF-ID (V11)*. Dans ce travail, de nouveaux paramètres sont introduits dans la modélisation, qui n'apparaissent pas dans les recherches rapportées sur le sujet.

2.1 Type of pores in MOX fuels

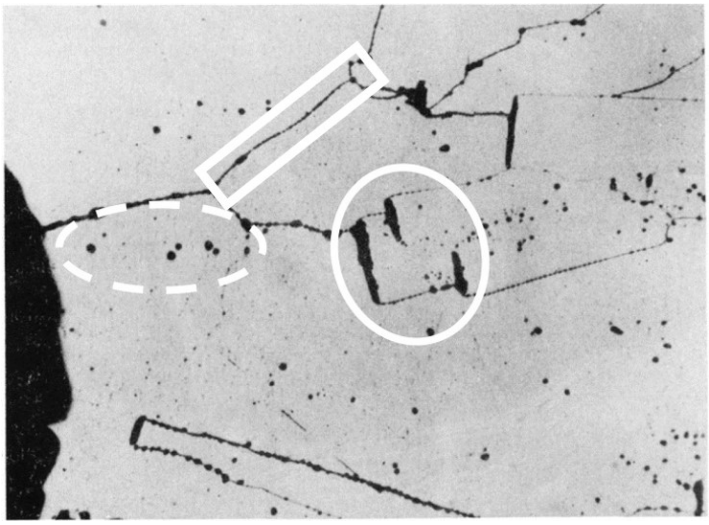

Figure 2.1: Photomicrograph of an oxide fuel with two types of pores: spherical (dashed circle) and lenticular (solid circle), migrating towards the central void (on the extreme left part of the image). The solid rectangular represents a micro-crack. [34, 83]

We distinguish three types of pores in MOX fuel, caused by either the fabrication process or by irradiation conditions [11] (see Figure 2.1):

- spherical pores, resulting from fabrication process.
- micro-scale gas bubbles, resulting from the creation of gaseous fission products, during irradiation, which can take either a spherical or a lenticular form.
- lenticular pores, due to pores migration during irradiation.

Micro and macro cracking, due to local mechanical stress can also occur.

The size of the first type of pores depends on the fabrication process. For instance, in Europe, the fabrication process of the FNR MOX fuel (*i. e.* COCA) yields pores of an average diameter of 1 µm. On the other side, the Japanese fabrication process is slightly different and yields pores of an average diameter of 10 µm. At the **B**eginning **O**f **L**ife (BOL) of the fuel, those pores are filled with helium at a pressure of 1 bar. During irradiation, they are progressively filled with gaseous fission products (mainly with xenon and krypton) with respective average molar fractions of $x_{Xe} = 0.85$ and $x_{Kr} = 0.15$.

The size of the second type of pores is highly dependent on where these pores are located relative to the grain boundaries (GB). For instance, those pores, also called "gas bubbles" can be inter or intragranular and can measure from a few tens of nanometers to 50 µm. Those bubbles are filled with gaseous fission products and unlike pores from fabrication, their pressure can go up to 20 MPa (see Table 2.1) [11, 34, 35, 84]. Intragranular gas bubbles are mainly spherical, whereas the intergranular can also be lenticular (see Figure 2.2).

	As fabricated	Minimum value	Maximum value
Grain size	1-30 µm	0.5 µm	1mm
Pores diameter from fabrication	1 µm	1 µm	10 µm
Pores diameter from irradiation	-	1 µm	50 µm
Pressure in the gas bubbles	1 bar	1 bar	20 MPa
MOX Density	95 % th.d	20 % th.d	100 % th.d

Table 2.1: Microstructure characteristics of FNR MOX fuel, in terms of pore and grain size, and pressure in the gas bubbles

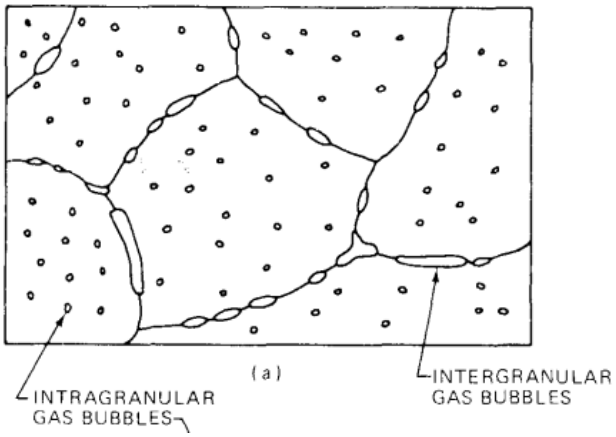

Figure 2.2: Illustrative scheme of inter and intragranular gas bubbles in nuclear fuel [35]

Lenticular pores occur from the migration process of the fabrication pores towards the central hole (see Figure 2.1)
Figure 2.3 dresses a global picture of the microstructure of irradiated FNR MOX fuel at high burn-up rates (*i. e.* 8 % FIMA).

2.2 Modeling of the effect of porosity on thermal conductivity

In this modeling, we consider:

1. radiation through the pore
2. conduction by the type of gas, contained in the pore
3. pores of spherical shape, which are representative of the fabrication pores and of some gas bubbles

Indeed, conduction by gas in the pores and radiation through the pores may yield a non-negligible pore thermal conductivity.
In most published work, one uses the simplified version of Maxwell-Eucken [85, 86], recalled here:

$$\frac{\lambda_p}{\lambda_m} = \frac{1-p}{1+0.5\cdot p}$$

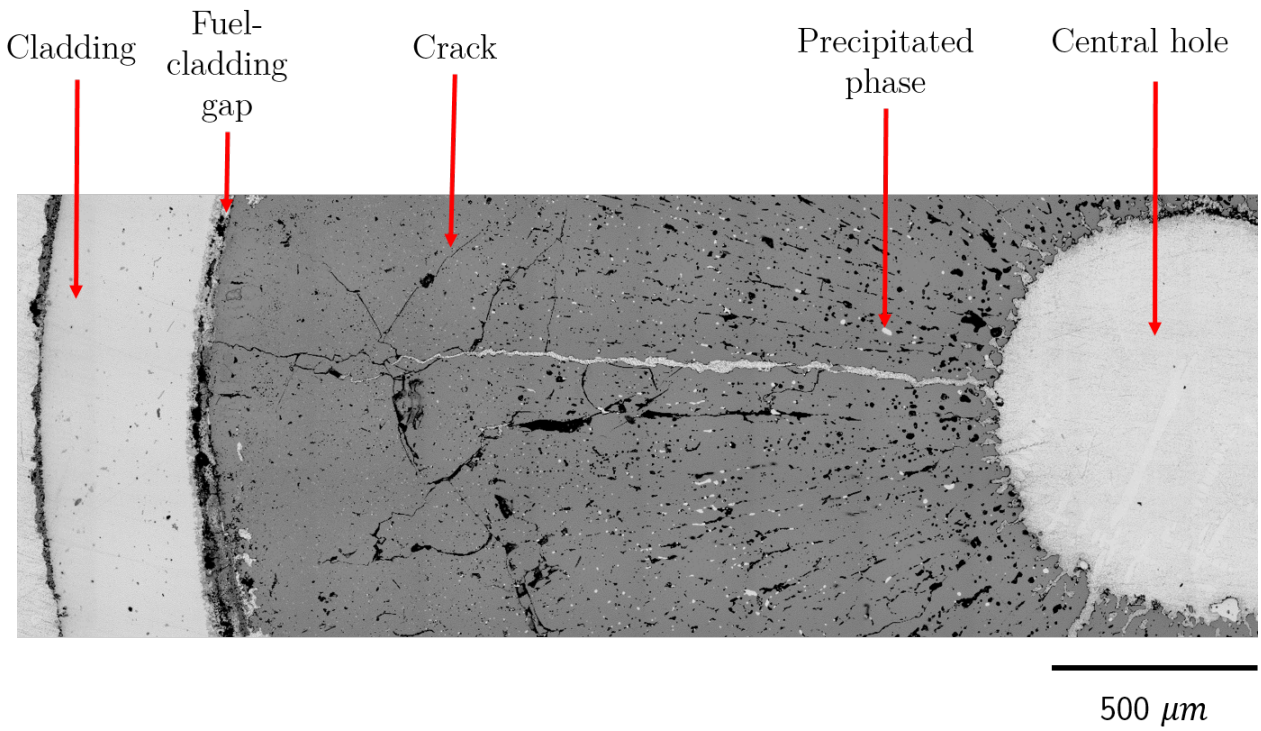

Figure 2.3: Ceramography of the NESTOR-3 FNR MOX sample, from 1400 mm of the bottom of the fissile column, irradiated at 8 % FIMA. [22]

based on the assumption that thermal conductivity of the pores is negligible to that of the fuel matrix $\lambda_{pores} \ll \lambda_m$.
In this work, we use the Fricke's equation for spherical pores, which takes the following form (see Annex B):

$$\frac{\lambda_p}{\lambda_m} = \frac{1-p}{1+\beta \times p} = \frac{1-p}{1 - \dfrac{p(1-\Lambda)+4\Lambda-1}{2p(\Lambda-1)+2+\Lambda} \times p} \tag{2.1}$$

where Λ is the ratio between the thermal conductivity of the pores λ_{pores} and that of the fuel matrix λ_m:

$$\Lambda = \frac{\lambda_{pores}}{\lambda_m} \tag{2.2}$$

Thermal conductivity of the pores λ_{pores} is composed of two terms: conduction (by gas) and radiation. We therefore write: $\lambda_{pores} = \lambda^r_{pores} + \lambda^c_{pores}$, where the r and c superscripts refer to radiation and conduction respectively.

2.2.1 Radiation through the pore

The radiative term mainly depends on pore's radius R, fuel's emissivity ϵ and temperature:

$$\boxed{\lambda^r_{pores} = 4T^3 \epsilon R \sigma} \tag{2.3}$$

For further information about the theoretical background behind this equation, the reader may refer to [61].
Emissivity is needed to compute the radiative contribution. To date, no experimental data on MOX fuel have been reported in the literature. Nevertheless, as a first approximation, we can use UO_2 data on total hemispherical emissivity. Fink [87] proposed an empirical value of $\epsilon = 0.85 \pm 0.05$. Other empirical estimations are temperature-dependent [88]:

$$\epsilon = 0.78557 + 1.5263.10^{-5}T \tag{2.4}$$

We compared both approaches: considering a constant and a temperature dependent emissivity. As shown in Figure 2.4, using a constant or temperature-dependent emissivity does not impact

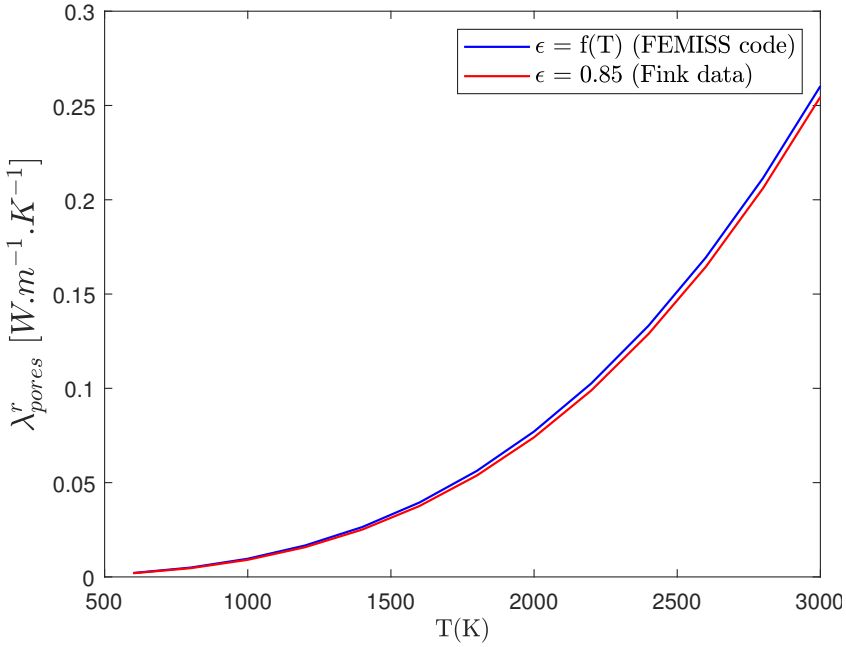

Figure 2.4: Variation with temperature of thermal conductivity due to radiation across the pores, using a temperature-dependent emissivity model (FEMISS code) and a constant value (Fink [87])

the radiative contribution by more than 1 %. In the following sections, λ^r_{pores} will be computed using the constant value, given by Fink.

2.2.2 Conduction by the gas, contained in the pore

Here we consider a gas mixture. From the work of Lindsay and Bromley [89], the thermal conductivity of a gas mixture is expressed as:

$$\boxed{\lambda^c_{pores} = \lambda_{mix,g} = \sum_{i=1}^{n} \frac{\lambda_{i,g}}{1 + \sum_{i \neq j}^{n} \Psi_{i,j} \frac{x_j}{x_i}}} \tag{2.5}$$

Where:

n : number of constituents of the gas mixture
$\lambda_{mix,g}$: thermal conductivity of the gas mixture ($\mathrm{W\,m^{-1}\,K^{-1}}$)
$\lambda_{i,g}$: thermal conductivity of each gas i ($\mathrm{W\,m^{-1}\,K^{-1}}$)
$\Psi_{i,j}$: term, function of the molecular weight of each gas M_i and its thermal conductivity $\lambda_{i,g}$, given by Brokaw [90]:

$$\Psi_{i,j} = \Phi_{i,j}\left\{1 + 2.41\frac{(1-\frac{M_i}{M_j})(0.142-\frac{M_i}{M_j})}{\left(1+\frac{M_i}{M_j}\right)^2}\right\} \tag{2.6}$$

$$\Phi_{i,j} = \frac{\left\{1+\left(\frac{\lambda_{i,g}}{\lambda_{j,g}}\right)^{1/2}\left(\frac{M_i}{M_j}\right)^{1/4}\right\}^2}{2\sqrt{2}\left(1+\frac{M_i}{M_j}\right)^{1/2}} \tag{2.7}$$

Two ways of assessing the thermal conductivity of each gas $\lambda_{i,g}$ can be used: considering both pressure and temperature, or only temperature. In this work, both approaches were studied. The effect of pressure was found negligible and therefore we chose the approach, where only temperature is considered. This approach empirically describes the thermal conductivity of a gas as follows [91, 92]:

$$\lambda_{i,g}(T) = a_{i,g}T^{b_{i,g}} \tag{2.8}$$

Table 2.2 resumes the coefficients $a_{i,g}$ and $b_{i,g}$ for Helium, Krypton and Xenon, reported in different work. In this work, the URGAP code values were used [93], as they are deemed the

	Code							
	BISON [92]		**ROCHE [private]**		**URGAP [93]**		**FRAP [94]**	
Gas type	$a_{i,g}$	$b_{i,g}$	$a_{i,g}$	$b_{i,g}$	$a_{i,g}$	$b_{i,g}$	$a_{i,g}$	$b_{i,g}$
Xenon	$4.351.\ 10^{-5}$	0.8616	$5.14.\ 10^{-5}$	0.83	$4.6556.\ 10^{-5}$	0.84256	$9.825.\ 10^{-5}$	0.7334
Krypton	$8.247.\ 10^{-5}$	0.8363	$8.11.\ 10^{-5}$	0.83	$9.8938.\ 10^{-5}$	0.80079	$19.66.\ 10^{-5}$	0.7006
Helium	$263.9.\ 10^{-5}$	0.7085	$284.\ 10^{-5}$	0.7	$176.32.\ 10^{-5}$	0.77227	$253.1.\ 10^{-5}$	0.7146

Table 2.2: Empirical coefficients to compute the thermal conductivity of each gas $\lambda_{i,g}$, using Equation 2.8, according to the values, used in several codes.

most accurate, given the use of an exhaustive set of experimental data to calibrate them.

2.2.3 Comparison of both contributions

We compared both terms: the radiative (Equation 2.3) and the conductive (Equation 2.5), for two cases:

1. the gas mixture is composed of 100 % He, representative of the gas in the **B**eginning **O**f **L**ife (BOL) of the fuel.
2. the gas mixture is composed of 8.75 % Helium, 84.75 % Xenon and 6.5 % Krypton, representative of the gas at the **E**nd **O**f **L**ife (EOL) of the fuel.

Beginning Of Life (BOL)

Pores of size, higher than 1 µm are not observed in fresh MOX fuel (*i. e.* at BOL). Despite this fact, we evaluated the radiative term in the range $R \in [1 - 50]$ µm for sensitivity purposes. As shown in Figure 2.5, the conductive term outweighs the radiative one even for relatively high pore sizes (*i. e.* 50 µm). Therefore, the effective thermal conductivity of the pore is driven by the conduction by Helium, which attains 0.84 $\mathrm{W\,m^{-1}\,K^{-1}}$ at $T = 3000$ K.

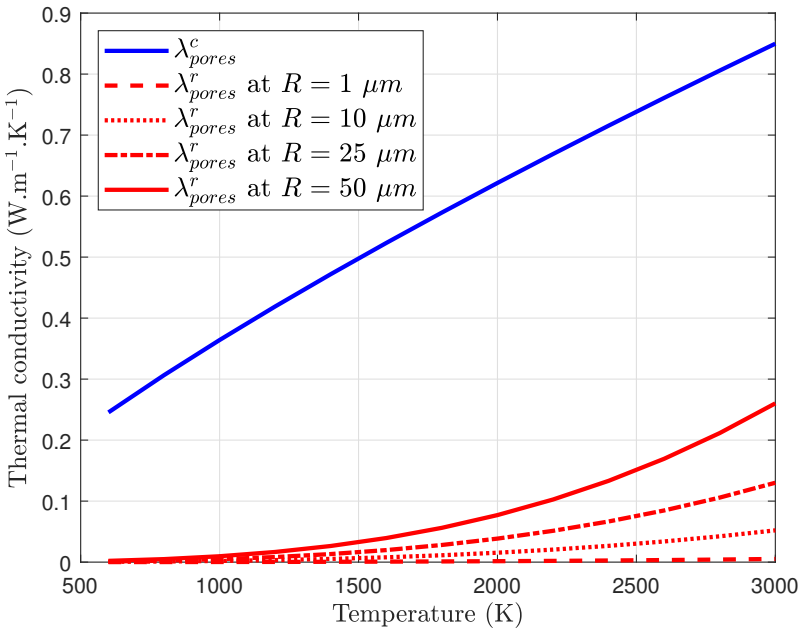

Figure 2.5: Comparison of λ^c_{pores} and λ^r_{pores} for 4 different pore radii. The gas composition is 100 % Helium (*i. e.* BOL composition).

End of Life (EOL)

As shown in Figure 2.6, thermal conductivity due to gas conduction is now divided by a factor of 40 at $T = 3000$ K, since Xe and Kr have a negligible thermal conductivity, compared to He. The radiation term is therefore almost of the same order of magnitude as the conductive term at $T = 3000$ K, at $R = 50$ µm. However, even if radiation through the pores is taken into account, the total effective thermal conductivity of the pore is negligible compared with that obtained at the BOL. In this scenario, the assumption of negligible pore thermal conductivity is therefore legitimate.

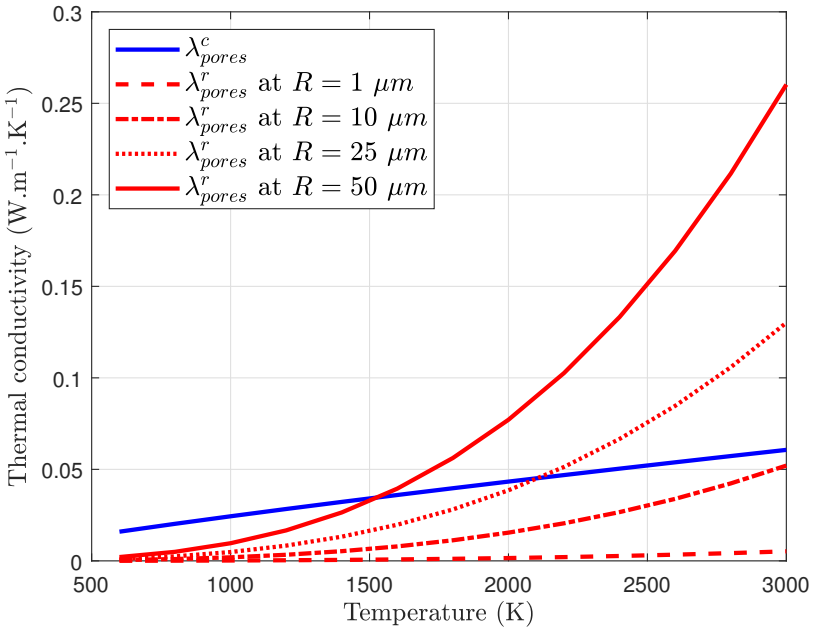

Figure 2.6: Comparison of λ^c_{pores} and λ^r_{pores} for 4 different pore radii. The gas composition is 8.75 % Helium, 84.75 % Xenon and 6.5 % Krypton (*i. e.* EOL composition)

2.2.4 Comparison with other analytical approaches

We compared Fricke's method, which takes the thermal conductivity of the pores into account, with two other commonly used analytical approaches, both based on the assumption that pores have a negligible thermal conductivity, compared to that of the fuel matrix. These approaches both take the expression :

$$\frac{\lambda_p}{\lambda_m} = \frac{1-p}{1+\beta p} \tag{2.9}$$

where $\beta = 0.5$ for spherical pores or $\beta = 2$ for flatter pores (*i. e.* lenticular). The thermal conductivity model of Philipponneau [2] for the fuel matrix λ_m was used for the calculations. As shown in Figure 2.7, for low porosity volume fractions (*i. e.* here at $p = 0.05$), thermal conductivity at EOL agrees to quite a good extend with the Maxwell-Eucken formulation. Indeed, at the EOL, the pore's effective thermal conductivity is almost zero, due to the highly non-conductive Xe and Kr. Despite the increasing importance of the radiative contribution with temperature, radiation contributes only 20 % of the pore's effective thermal conductivity.

The Maxwell-Eucken formulation agrees with our calculations at the BOL (*i. e.* pores filled with helium), highlighting the validity of applying the Maxwell-Eucken formulation even when the thermal conductivity of the pore is not zero.

The formulation for flatter pores, $\beta = 2$, in turns, does not agree with neither the BOL nor the EOL calculations. Indeed, in this work, we considered spherical pores, given the shape of the fabricated pores and some of the gas bubbles. The comparison of this study with $\beta = 2$ for lenticular pores therefore shows that the shape factor has a non-negligible effect on thermal con-

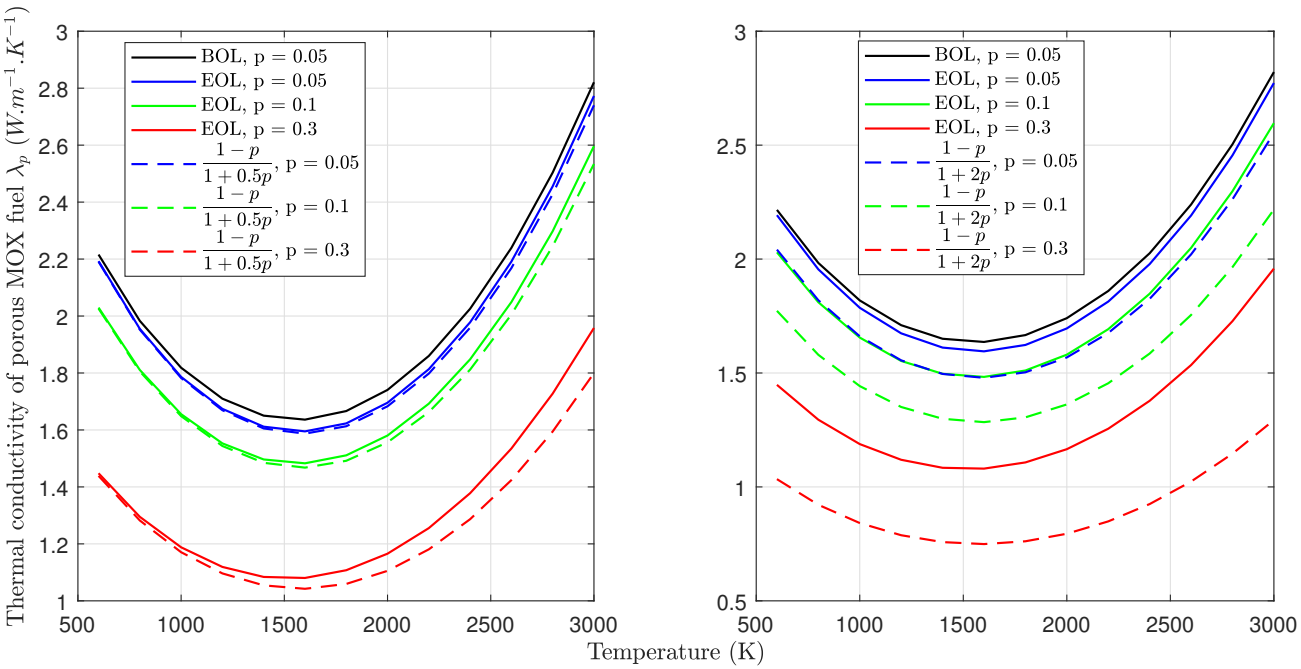

Figure 2.7: Temperature variation of thermal conductivity of porous MOX, calculated with the Fricke method at BOL (gas: Helium, pore size: $R = 1$ µm) and EOL (gas: mixture of 8.75 % Helium, 84.75 % Xenon and 6.5 % Krypton, pore size: $R = 50$ µm). The comparison with Equation 2.9 for $\beta = 0.5$ (spherical pores) and $\beta = 2$ (lenticular pores) was also shown.

ductivity predictions. In particular, choosing a form factor of $\beta = 2$ for lenticular pores results in a lower thermal conductivity than the Fricke and Maxwell-Eucken factors for spherical pores.

In addition to the effect of gas content, pore radius and form factor, the volume fraction of porosity can also induce discrepancies between the results obtained with the different models. In particular, for higher porosity (here $p = 0.30$), Fricke's method no longer agrees with either model. This is due to the assumption of an interaction-free porosity network, which is no longer true when porosity exceeds a certain value. In general, for $p > 0.10$, percolation begins to form, leading to open porosity [54–56]. As a result, most analytical methods are no longer valid for porosity fractions above $p = 0.10$.

2.2.5 Conclusion

In this study, we assessed the thermal conductivity of the pore and saw that when the gas, contained in the pore is composed of:

1. 100 % He, thermal conductivity of the pore is driven by gas conduction, yielding the non-negligible value of around 0.84 $\mathrm{W\,m^{-1}\,K^{-1}}$ at $T = 3000$ K.
2. 8.75 % Helium, 84.75 % Xenon and 6.5 % Krypton, thermal conductivity of the pore is mostly driven by the radiation across the pore, yielding an almost zero thermal conductivity.

We have compared Fricke's analytical approach with other approaches, based on the assump-

tion of non-conducting pores. Fricke's method agrees with the Maxwell-Eucken expression for spherical pores ($\beta = 0.5$), in the two scenarios studied here: BOL and EOL. This observation highlighted the valid use of the Maxwell-Eucken formulation even when the thermal conductivity of the pore is not zero (*i. e.* when the pore is filled with He). We also compared the results of the Fricke method with another analytical approach, which takes lenticular pores into account (*i. e.* $\beta = 2$ in the equation 2.9). This comparison revealed that the choice of a particular form factor can lead to significant discrepancies. In particular, the choice of $\beta = 2$ underestimates thermal conductivity compared to Maxwell-Eucken and Fricke for spherical pores.

2.3 Modeling of irradiation-induced fission products and porosity on thermal conductivity.

In this section, we will model the effect of irradiation-induced fission products and porosity on the thermal conductivity of MOX fuels, irradiated in FNR irradiation conditions. The FNR MOX fuel, studied in this work was irradiated in the framework of the NESTOR-3 irradiation in the Phenix reactor [22, 25].

2.3.1 Methodology

In this work, we will use the modeling approach of Lucuta *et al.* [32, 36, 37], introduced in the previous chapter. Thermal conductivity of irradiated fuel, with this approach takes the following form:

$$\frac{\lambda_{irr}}{\lambda_0} = F_{prec,FP}(p,q) \cdot F_{diss,FP}(\beta) \cdot F_{rad}(T) \tag{2.10}$$

where:

$$F_{prec,FP}(p,q) = \frac{2(1-p+2q)}{p+2(1-q)} \tag{2.11}$$

$$F_{diss,FP}(\beta) = \left(\frac{1.09}{\beta^{3.265}} + \frac{0.0643}{\sqrt{\beta}}\sqrt{T}\right) \arctan\left(\frac{1}{\frac{1.09}{\beta^{3.265}} + \frac{0.0643}{\sqrt{\beta}}\sqrt{T}}\right) \tag{2.12}$$

$$F_{rad}(T) = 1 - \frac{0.2}{1+\exp\left(\frac{T-900}{80}\right)} \tag{2.13}$$

where p it the volume fraction of pores, q the volume fraction of precipitated phases and β the burn-up, expressed in % FIMA. The irr and 0 subscripts refer to irradiated and fresh fuel, respectively.
To apply this model, information on fuel temperature, burn-up, and microstructure, is required. To obtain this information, we performed two types of calculations.

First, a thermomechanical calculation was performed, using the fuel performance code *GERMINAL V2* [7] (from the *PLEIADES* fuel simulation platform [8]).
The input data for this calculation were the irradiation conditions of the NESTOR-3 fuel. *GERMINAL V2* allowed us to determine the composition and microstructure of the irradiated

fuel.
The latter were then used as input parameters for a thermochemical calculation, performed by the thermodynamic software *Thermo-Calc V4.1.* and the *TAF-ID V11* database [44] (see Figure 2.8). We therefore obtained information about the crystal phases and their respective volume fractions, needed to assess $F_{\text{prec, FP}}$.

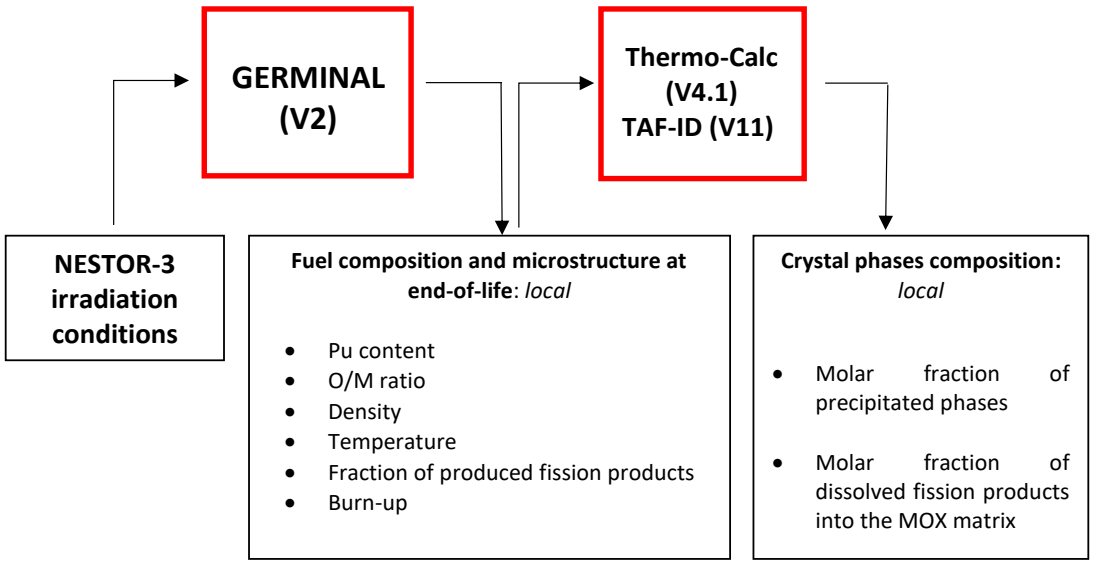

Figure 2.8: Scheme of the input/output parameters of the GERMINAL – Thermo-Calc calculation

2.3.2 Presentation of the NESTOR-3 fuel and experimental data

NESTOR-3 fuel was subject to (1): thermal property measurements, using the **LA**ser **F**lash (LAF) technique [25] (thermal diffusivity and heat capacity, allowing to calculate thermal conductivity) and (2): **P**ost-**I**rradiation **E**xaminations (PIE) [22].

2.3.2.1 Thermal property measurements

Thermal diffusivity and heat capacity measurements were performed on two samples, taken from two axial positions on the fissile column: **M**aximum **F**lux **P**lane (MFP) and **T**op of the **F**issile **C**olumn (TFC) axial region. The estimated burn-ups for those regions are 8 and 13 % FIMA respectively. Measurements were performed at three radial positions for each axial region: close to the central hole, at mid-radius and close to the fuel periphery (see Figure 2.9).

2.3.2.2 Post-irradiation examinations

Several destructive **P**ost-**I**rradiation **E**xaminations (PIE) were performed to characterize the NESTOR-3 fuel in the MFP region. These include **S**canning **E**lectron **Microscopy** (SEM), **S**econdary-**I**on **M**ass **S**pectrometry (SIMS), and **E**lectron **P**robe **M**icroAnalysis (EPMA) (see Figure 2.10).

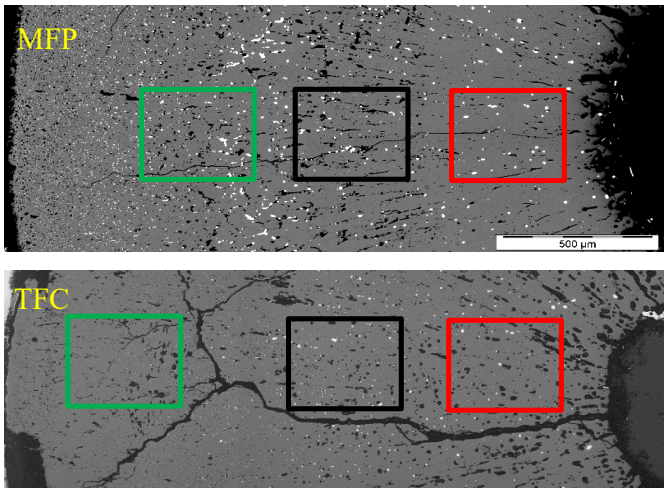

Figure 2.9: Ceramography at both the MFP and TFC regions of the NESTOR-3 MOX fuel [22]. Location of the samples for thermal properties measurements with respect to the fuel external radius R: $r = 0.54R$ (red), $r = 0.65R$ (black), $r = 0.78R$ (green) in the MFP region and $r = 0.52R$ (red), $r = 0.67R$ (black), $r = 0.81R$ (green) in the TFC region.

2.3.3 Results obtained by the GERMINAL (V2) - Thermo-Calc (V4.1), TAF-ID (V11) calculation

The thermal conductivity model, used in this simulation was that of Philipponneau [2]. The joint oxyde-gaine model (JOG) [46] has been described elsewhere [8].
Table 2.3 shows the results for the volume fraction of precipitates and the molar fraction of dissolved FPs, obtained with the GERMINAL-Thermo-Calc calculation. The latter were compared to the experimental study of Parrish *et al.* [27, 34] on the phases' composition of FNR MOX fuels irradiated at 3.4, 13.7 and 21.3 % FIMA.

Irradiation	Pu (mol. %)	Axial position(*) (x/L)	Radial position(**) (r/R)	Burn-up (% FIMA)	Porosity (vol. %)	FMP (vol. %)	GP (vol. %)	Dissolved FPs (mol. %)
NESTOR-3 [22]	22	0.83	0.52	7.91	4.49^a	0.43^a	2.28^a	1.59^a
			0.67	7.99	5.15^a	0.41^a	2.09^a	1.63^a
			0.81	8.02	5.26^a	0.35^a	2.00^a	1.43^a
		0.66	0.54	12.21	$2.99^a/3.90^b$	0.64^a	4.24^a	$2.32^a/2.30^b$
			0.65	12.32	$5.26^a/3.90^b$	0.72^a	4.12^a	$2.08^a/2.46^b$
			0.78	13.17	$5.26^a/3.90^b$	1.49^a	3.55^a	$2.50^a/3.31^b$
Parrish *et al.* [27]	26	0.90	0.30		-	1.01^b	0.00^b	-
			0.60	3.40	-	0.87^b	0.00^b	-
			0.80		-	0.00^b	0.00^b	-
	29	0.75	0.20		-	2.77^b	5.86^b	-
			0.55	13.70	-	1.53^b	3.38^b	-
			0.90		-	1.81^b	0.00^b	-
	29	0.97	0.25		-	0.60^b	8.71^b	-
			0.50	21.30	-	2.48^b	0.76^b	-
			0.75		-	1.89^b	0.25^b	-

Table 2.3: Comparison of the available experimental data on FNR MOX fuels with the results obtained by the Thermo-Calc calculations.
a: Measured, *b:* Calculated,
(*): Position x on the fissile column (of length L), from which the sample was taken.
(**): Position r on the fuel pellet (of radius R), where the measurements were performed.

We also compared the calculated results with the experimental characterizations on the sample from the MFP axial region.
Figure 2.10 shows X-ray maps of the metallic FMP (Ru, Mo, Pd, Rh, Tc) and oxide GP $BaZrO_3$ precipitated phases in the MFP region.

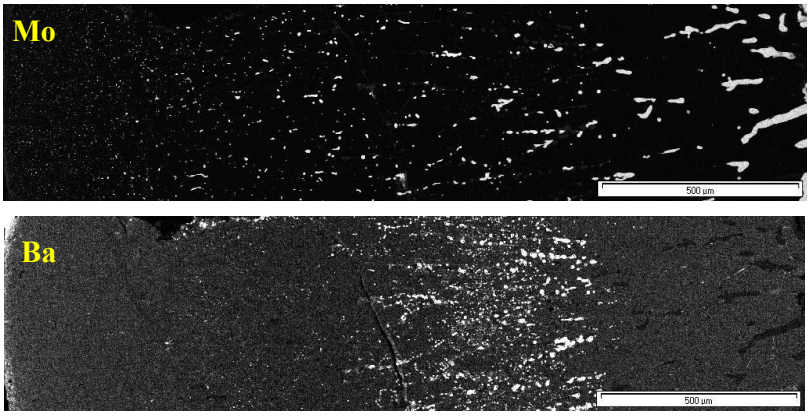

Figure 2.10: X-ray maps of both the precipitated metallic (FMP) and oxide (GP) phases in the MFP region.

The size of the metallic precipitates is observed to be larger near the central hole and smaller at the periphery of the pellet. The oxide precipitates are observed mainly in the middle of the pellet radius (here from 0.48 R to 0.64 R). Their surface fraction seems to be higher than that of the metallic precipitates. This experimental observation confirms our Thermo-Calc results, which show higher volume fractions of oxide precipitates than metallic precipitates, at all three radial positions.
However, the Thermo-Calc results show some discrepancies with the radial X-ray maps of the oxide phase, especially at 0.54 R and 0.78 R. In these regions, the X-ray maps do not show the existence of the oxide phase, which contradicts the Thermo-Calc results, which indicate oxide phase volume fractions of 4.25 % and 3.55 % respectively. The radial distribution of the oxide phase, as calculated by Thermo-Calc, is also compared to that of the B (ACO-3) fuel sample, reported by Parrish *et al.* [27, 34]. In this sample, the volume fraction of the oxide phase increases radially when approaching the centre of the pellet, attaining a maximum value of 5.86 % (see Table 2.3). This trend is consistent with our Thermo-Calc results but not with the X-ray maps, which instead show a maximum value at mid-radius rather than at the centre of the pellet. No experimental data is available in the TFC region to assess the calculated volume fractions of the precipitated phases.
Regarding the radial distribution of the metallic phase, the X-ray maps in the MFP region are in agreement with Parrish *et al.* [27, 34], as they show that the metallic phase is mainly present at the centre of the pellet. However, our calculated values are 2-3 times lower than the experimentally determined values for the B (ACO-3) fuel irradiated at a burn-up comparable to that of the NESTOR-3 fuel in the MFP region. This observation highlights the possible underestimation of the computed values of the volume fraction of metallic precipitates in the MFP region.
Regarding the concentration of dissolved FPs, the comparison between the calculated values

and the EPMA results is shown in Figure 2.11. The thermodynamic estimations are consistent

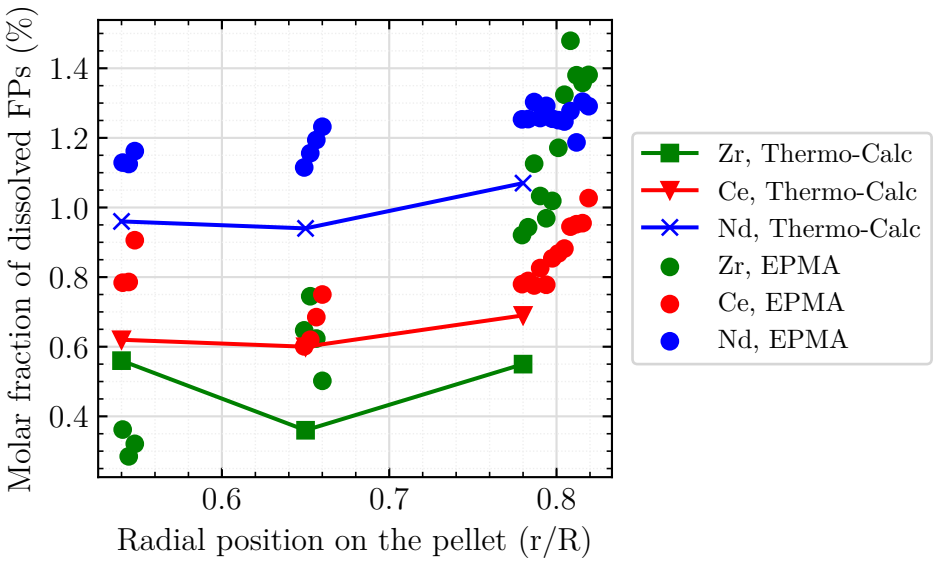

Figure 2.11: Comparison of the calculated molar fraction of dissolved FPs with the EPMA examinations in the MFP region.

with the EPMA examinations, except for those related to zirconium. The EPMA yields the total amount of Zr in the fuel, and therefore accounts for both dissolved and precipitated Zr in the $BaZrO_3$ phase. However, the Thermo-Calc calculations shown in Figure 2.11 only account for dissolved Zr. Therefore, the observed discrepancies seem reasonable.

2.3.4 Application of the original Lucuta model

The application of the Lucuta model, using the input parameters, calculated in this work (see Table 2.3) is compared to the experimental data on the NESTOR-3 fuel in Figure 2.12. The thermal conductivity of the fresh samples λ_0 was calculated from thermal diffusivity (d), heat capacity (C_p) and hydrostatic density (ρ) measurements, using the formula $\lambda = \rho C_p d$. The details related to those measurements have been described elsewhere [25]. The same approach as for λ_0 was used to determine λ_{irr}. However, no hydrostatic density measurements were performed in the TFC region. Therefore, a hypothesis on the density is made to calculate the thermal conductivity in this region. This assumption is discussed in more detail in the following sections.

As shown in Figure 2.12, the original Lucuta model fails to reproduce the experimental data. In the following sections, we will propose a modification of this model.

2.3.5 Modification of the original Lucuta model

2.3.5.1 Effect of fission products, forming precipitated phases

The model proposed by Lucuta *et al.* for the effect of precipitated phases takes into account both porosity and precipitated phases. To isolate the effect of porosity or precipitated phases,

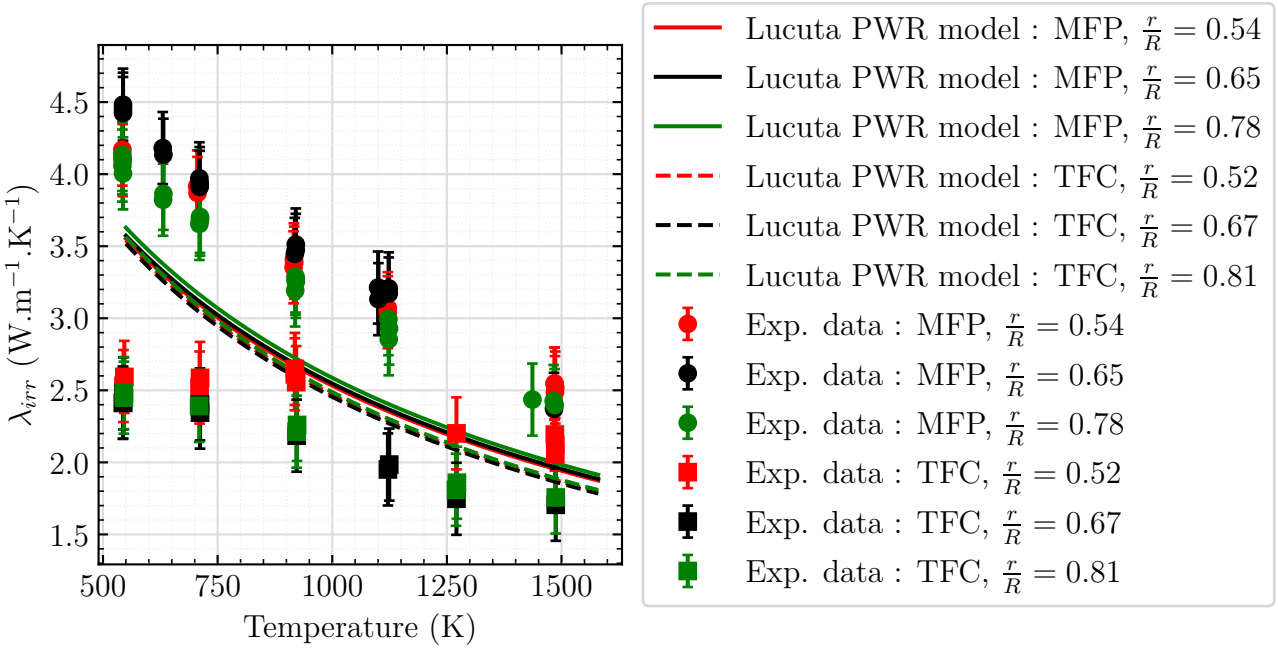

Figure 2.12: Temperature variation of thermal conductivity, as predicted by the original Lucuta model [32] and as measured at the MFP and TFC axial regions [25].

either the volume fraction of precipitates or the porosity must be set to zero. The origin of this equation is Maxwell-Eucken's formula for n dispersed phases in a matrix, where λ_i is the thermal conductivity of the i-th dispersed phase [95]:

$$\frac{\lambda_p}{\lambda_m} = \frac{1 + 2\sum_{i=1}^{n} v_i \frac{1-\frac{\lambda_m}{\lambda_i}}{1+2\frac{\lambda_m}{\lambda_i}}}{1 - \sum_{i=1}^{n} v_i \frac{1-\frac{\lambda_m}{\lambda_i}}{1+2\frac{\lambda_m}{\lambda_i}}} \tag{2.14}$$

The equation, used by Lucuta *et al.* to account for both porosity and precipitated phases at the same time (see Equation 2.11) can be deduced from Equation 2.14 in three steps:

1. Setting $v_1 = q$ (in Equation 2.14) for the total volume fraction of precipitates with thermal conductivity $\lambda_1 = \lambda_{prec}$.
2. Setting $v_2 = p$ (in Equation 2.14) for the total volume fraction of precipitates with thermal conductivity $\lambda_2 = \lambda_p$.
3. Making the following assumption: $\lambda_{prec} \gg \lambda_m$ and $\lambda_p \ll \lambda_m$

Lucuta *et al.* however consider the metallic and oxide precipitates in a single term, taking as input parameters the total fraction of the precipitates (q) and their "mean" thermal conductivity λ_{prec}. Nevertheless, Figure 2.13 shows that the thermal conductivity of the oxide phase is lower than that of the matrix. Using this equation is thus equivalent to approximating all the phases as being metallic (*i. e.* $\lambda_{prec} \gg \lambda_m$). Therefore, the equation, used by Lucuta *et al.* to account for both porosity and precipitated phases (see Equation 2.11) overestimates the precipitated phases' effect on thermal conductivity.

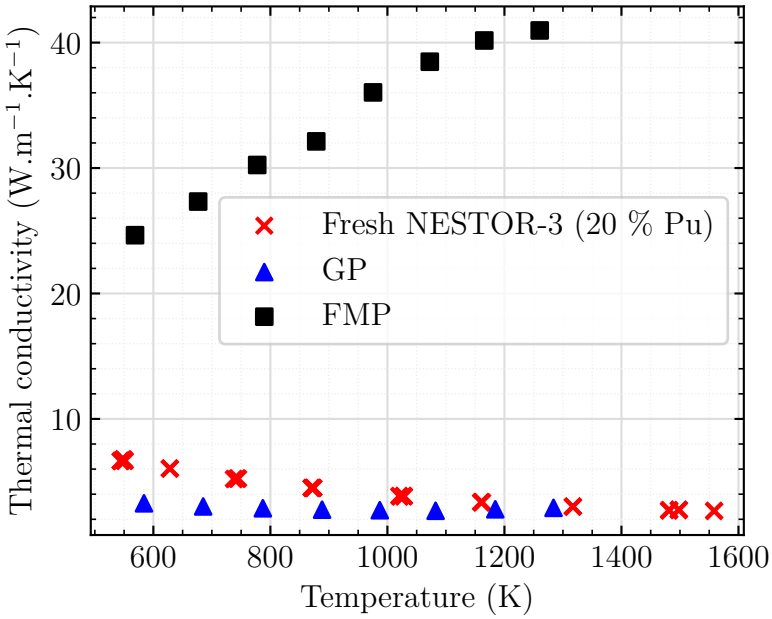

Figure 2.13: Temperature variation of thermal conductivity, as measured for the oxide phase (GP) [96], the metallic phase (FMP) [97] and the fresh (*i. e.* unirradiated) NESTOR-3 fuel (20 at. % Pu) [25]

In this work, we propose to use Maxwell-Eucken's formula for two dispersed phases with volume fractions v_{ox}, v_{met} and respective thermal conductivity λ_{ox}, λ_{met}, without making any simplifying assumptions.
Information about v_{ox}, v_{met} is provided by the GERMINAL-Thermo-Calc calculation, whereas λ_{ox}, λ_{met} were deduced from an experimental fit of the measurements in [96] and [97] respectively, giving:

$$\lambda_{ox} = \lambda_{GP} = \frac{1}{8.523 \cdot 10^{-2} + 3.936 \cdot 10^{-4} \times T} + 6.037 \cdot 10^{-10} T^3 \tag{2.15}$$

$$\lambda_{met} = \lambda_{FMP} = 2.589 \cdot 10^{-2} \cdot T + 9.951 \tag{2.16}$$

2.3.5.2 Effect of fission products, dissolved in the fuel matrix

In this work, we propose to introduce the Nd-content as the parameter, driving the effect of dissolved FPs on thermal conductivity. Two key reasons have been identified for choosing Nd over other dissolved rare earths (Pr, Sm, Eu, Gd or Y), or over the non-negligible amount of dissolved Zr.
Firstly, EPMA [22] and GERMINAL-Thermo-Calc results (see Table 2.4 and Figure 2.11) show that Nd is the predominant FP in the fuel matrix, followed by Zr and Ce in almost equal proportions.
Secondly, Fukushima *et al.* [98–102] showed that Nd and other rare-earths have a similar effect on thermal conductivity. Kurosaki *et al.* [103] showed that the effect of dissolved Zr and Nd on the degradation of thermal conductivity in (U,Ce)O_2 is similar for

temperatures below 1100 K. Regarding the effect of Ce, to our knowledge, no experimental data

Axial region	**TFC**			**MFP**		
Radial region	0.52 R	0.67 R	0.81 R	0.54 R	0.65 R	0.78 R
Element	**Molar fraction (%)**					
Nd	0.68	0.69	0.70	0.96	0.94	1.07
Ce	0.44	0.44	0.45	0.62	0.61	0.69
Zr	0.34	0.36	0.15	0.56	0.36	0.55
Gd	0.13	0.13	0.13	0.18	0.16	0.18
Total	1.59	1.63	1.43	2.32	2.08	2.50

Table 2.4: Molar fraction of dissolved FPs, calculated by GERMINAL-Thermo-Calc.

on MOX fuels with dissolved Ce have been reported in the literature. However, in their work, Kurosaki *et al.* [103] mention that $(U,Ce)O_2$ and $(U,Pu)O_2$ have a similar chemical and/or thermodynamic behavior [104]. Given the small effect of plutonium content in $(U,Pu)O_2$ fuels at low temperatures (*i. e.* T<1500 K)[2, 105], we assume that small amounts (here 0.66 mol %) of dissolved Ce would have a negligible effect on the degradation of thermal conductivity, compared to Nd.

To model the effect of dissolved Nd into the fuel matrix, we used experimental data from the work of Fukushima *et al.* [99, 100] on MOX fuels with 1.5, 3, 6 and 10 mol % dissolved Nd. The thermal conductivity degradation of the irradiated fuel matrix λ_m with respect to that of the fresh fuel matrix λ_0 was calculated using experimental data on fresh NESTOR-3 fuel with 20 at. % Pu [25]. The following equation was therefore provided:

$$\lambda_m\left(c_{Nd}\right) = \frac{1}{A\left(c_{Nd}\right) + B\left(c_{Nd}\right)T} = \frac{1}{A_0 + f_1(c_{Nd}) + (B_0 + f_2(c_{Nd}))\cdot T} \tag{2.17}$$

where:

$$\begin{aligned} f_1(c_{Nd}) =& 3.731\times10^{-2}\times c_{Nd} - 2.842\times10^{-3}\times c_{Nd}^2 + 18.891\times10^{-5}\times c_{Nd}^3 \\ f_2(c_{Nd}) =& \ 45.021\times10^{-7}\times c_{Nd} - 81.163\times10^{-8}\times c_{Nd}^2 \end{aligned} \tag{2.18}$$

where c_{Nd} is expressed in mol. %.
In this work, $A_0 = 2.178\times10^{-2}$ m K W^{-1} and $B_0 = 23.171\times10^{-5}$ m W^{-1}, which corresponds to the fresh NESTOR-3 fresh fuel.
The functional form of Equation 2.17 represents the contribution of phonons to the thermal conductivity of dielectric solids [105]. Several authors have shown that this equation successfully describes experimental data on actinide oxide fuels at temperatures below 1500 K [2, 3, 99, 105]. The factor, describing the effect of dissolved FPs on thermal conductivity, can therefore be written as follows:

$$F_{diss,FP}\left(c_{Nd}\right) = \frac{\lambda_m\left(c_{Nd}\right)}{\lambda_0} \tag{2.19}$$

The c_{Nd} parameter should be considered as the "equivalent" molar concentration of dissolved Nd, as it takes into account dissolved Nd, Ce, Zr and Gd (*i. e.* all FPs with a molar concen-

tration greater than 0.1 %).
Figure 2.14 compares our work (Equation 2.17) with that of Lucuta *et al.* (Equation 2.12) on the thermal conductivity of the fuel matrix. The experimental data of Fukushima *et al.* and that on the fresh NESTOR-3 fuel are also shown.
At $\beta = 12.5$ % FIMA, the original Lucuta model is in agreement with experimental data on MOX fuels with 6 mol. % dissolved Nd. However, in this work, the measured and calculated fractions of dissolved FPs are lower than 3.31 mol. % (see Table 2.3).
The burn-up dependent model of Lucuta *et al.*, therefore, appears to overestimate the thermal conductivity decrease.

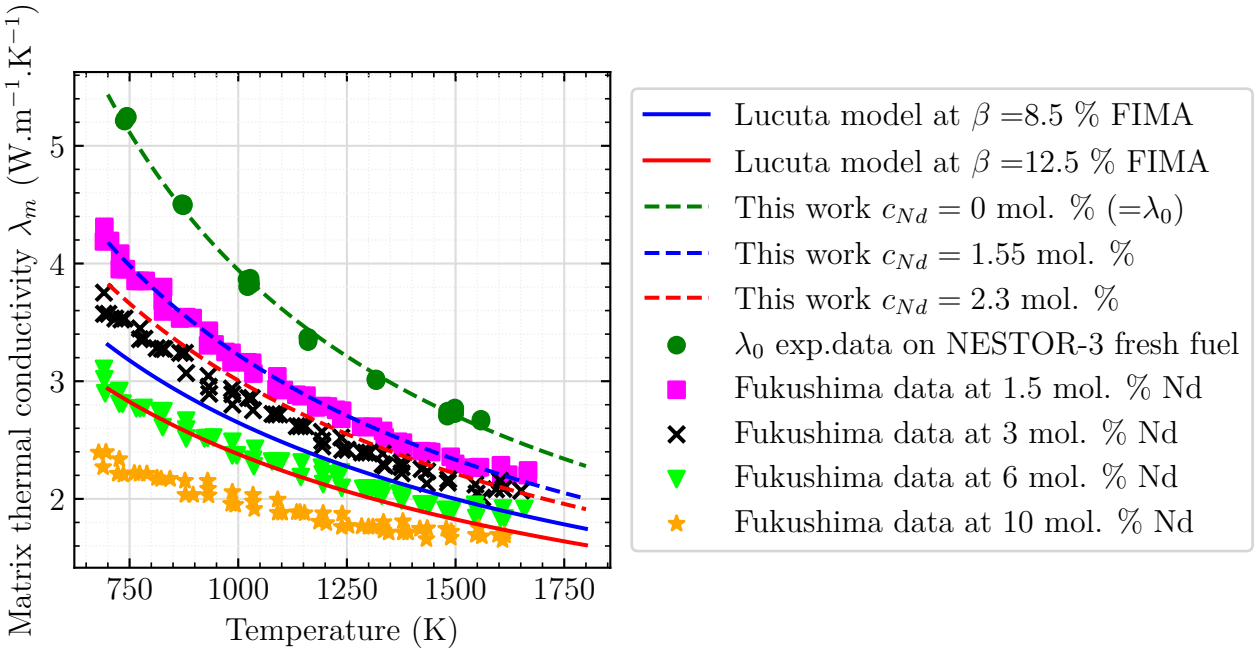

Figure 2.14: Variation with temperature of the fuel matrix' thermal conductivity, as predicted by this work (Equation 2.17), by the original Lucuta model (Equation 2.12) and as measured by Fukushima *et al.* [99]. Measurements on fresh NESTOR-3 fuel were also shown [25]

2.3.5.3 Effect of porosity

The effect of porosity was studied on the previous section. In this section, instead of using the Maxwell-Eucken correction, we chose to use the rather temperature-dependent model of Brandt and Neuer [59]:

$$F_{pores}(p,T) = 1 - \alpha(T)p \tag{2.20}$$

where $\alpha(T) = 2.6 - 0.5 \times 10^{-3}(T - 273)$. This factor was derived from experimental data on UO_2 fuels covering porosity volume fractions up to $p = 0.30$. This factor not only covers porosity fractions, which could not be considered by the classical analytical approaches, which are based on diluted pores (*i. e.* implying $p < 0.10$), but also empirically accounts for the temperature variation of thermal conductivity, due to radiation and gas conduction. Indeed, in irradiated fuel, porosity can exceed $p = 0.10$ and therefore most of the analytical approaches, covered in the previous section (see Section 2.2) are no longer valid. The use of the Brandt and

Neuer model therefore gathers the extrapolation capacity of the model to porosity fractions until $p = 0.30$ and the empirical consideration of the pore thermal conductivity through its temperature dependency. We recall that porosity correction, used in the original model of Lucuta *et al.* is that of Maxwell-Eucken, which does not present the above-mentioned advantage of the Brand and Neuer model.

In Philipponneau's work [2], another corrective factor was used, which considers the pore shape, instead of the effective thermal conductivity of the pore. The dependence of the pore shape is represented in the σ term in $\frac{1-p}{1+(\sigma-1)\times p}$. This factor has also been discussed in [32]. To account for flatter pore shapes, Philipponneau [2] considered a form factor of $\sigma = 3$.

Brandt and Neuer's factor [59] is compared with the Philipponneau [2] and Lucuta [32] models in Figure 2.15.

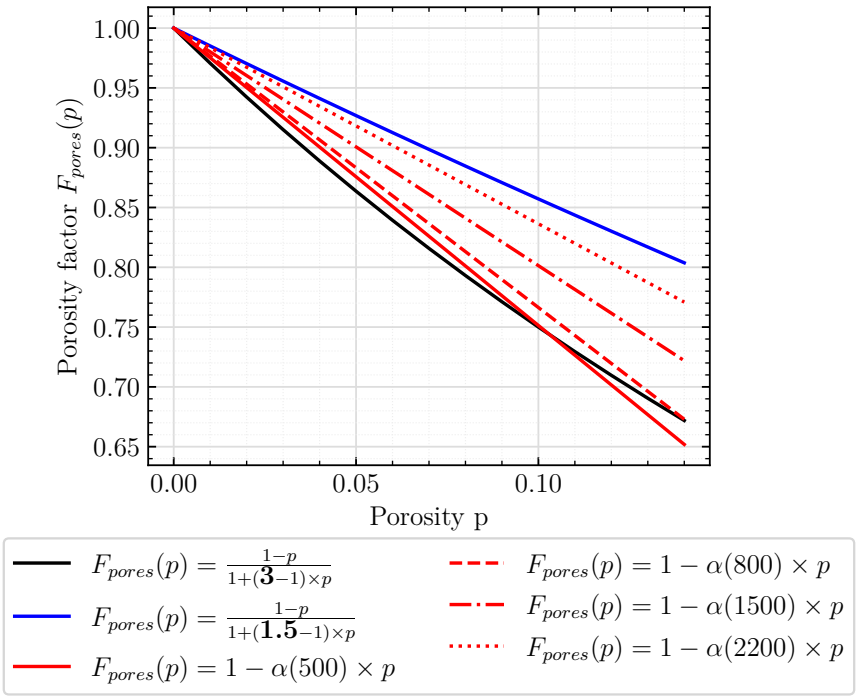

Figure 2.15: Comparison between the porosity factor, used in this work for multiple temperatures (red lines) and the models used in the work of Philipponneau [2] (black solid line) and Lucuta *et al.* [32, 36, 37] (blue solid line).

At 500 K, good agreement is observed between Brandt and Neuer and the model used in Philipponneau's work for flatter pore shapes (*i. e.* $\sigma = 3$). Brandt and Neuer's model can therefore be used to represent the effect of flatter pores on thermal conductivity, although no form factor is included in Equation 2.20.
The choice of a form factor of $\sigma = 1.5$ (*i. e.* as taken in the work of Lucuta *et al.* [32]) yields values 14 % higher than Philipponneau and Brandt and Neuer at $T = 500$ K and $p = 0.10$. The use of a model, limiting the pore shape to a spherical shape therefore leads to an underestimation of the effect of porosity on thermal conductivity at low temperatures.

Considering only the pore shape, without taking into account the effect of temperature (*i. e.* the effective thermal conductivity of the pore) could however lead to an overestimation of the effect of porosity on thermal conductivity. For instance, at $T = 2200$ K and $p = 0.10$, Philipponneau's model overestimates the effect of porosity by 10.3 %, compared to Brandt and Neuer's model.
The latter is therefore used in this work to account for both pore shapes, which could deviate from the spherical shapes, and temperature.

2.3.6 Integrated model: summary

The functional form of the thermal conductivity of MOX fuels, irradiated in FNR conditions, is the following:

$$\lambda_{irr}(T, p, v_i, \lambda_i, c_{Nd}) = \lambda_0(T) \cdot F_{pores}(p, T) \cdot F_{prec,FP}(v_i, \lambda_i) \cdot F_{diss,FP}(c_{Nd}, T) \cdot F_{rad}(T) \quad (2.21)$$

where:

$$\lambda_0(T) = \frac{1}{A_0 + B_0 T} \text{ ,if T} < 1500 \text{ K}$$

$$F_{pores}(p, T) = 1 - \left(2.6 - 0.5 \times 10^{-3}(T - 273)\right) p$$

$$F_{prec,FP}(v_i, \lambda_i) = \frac{1 + 2\sum_{i=1}^{n} v_i \dfrac{1 - \dfrac{\lambda_m}{\lambda_i}}{1 + 2\dfrac{\lambda_m}{\lambda_i}}}{1 - \sum_{i=1}^{n} v_i \dfrac{1 - \dfrac{\lambda_m}{\lambda_i}}{1 + 2\dfrac{\lambda_m}{\lambda_i}}}$$

$$\lambda_i = \begin{cases} \dfrac{1}{8.523 \cdot 10^{-2} + 3.936 \cdot 10^{-4} \times T} + 6.037 \cdot 10^{-10} T^3 & \text{if } i = \text{GP : oxide phase} \\ 2.589 \cdot 10^{-2} \cdot T + 9.951 & \text{if } i = \text{FMP: metallic phase} \end{cases}$$

$$F_{diss,FP}\left(c_{Nd}, T\right) = \frac{\lambda_m\left(c_{Nd}, T\right)}{\lambda_0(T)}$$

$$\lambda_m\left(c_{Nd}, T\right) = \frac{1}{A\left(c_{Nd}\right) + B\left(c_{Nd}\right) T} = \frac{1}{A_0 + f_1(c_{Nd}) + (B_0 + f_2(c_{Nd})) \cdot T}$$

$$f_1(c_{Nd}) = 3.731 \times 10^{-2} \cdot c_{Nd} - 2.842 \times 10^{-3} \cdot c_{Nd}^2 + 18.891 \times 10^{-5} \cdot c_{Nd}^3$$

$$f_2(c_{Nd}) = 45.021 \times 10^{-7} \cdot c_{Nd} - 81.163 \times 10^{-8} \cdot c_{Nd}^2$$

$$F_{rad}(T) = 1 - \frac{0.2}{1 + \exp\left(\dfrac{T - 900}{80}\right)}$$

where:

λ_{irr} : effective thermal conductivity of the irradiated fuel ($\mathrm{W\,m^{-1}\,K^{-1}}$)
λ_m : thermal conductivity of the irradiated fuel matrix ($\mathrm{W\,m^{-1}\,K^{-1}}$)
λ_0 : thermal conductivity of the fresh fuel matrix ($\mathrm{W\,m^{-1}\,K^{-1}}$)
λ_i : thermal conductivity of the i-th precipitated phase ($\mathrm{W\,m^{-1}\,K^{-1}}$)
A_0 and B_0 : phonon constants ($\mathrm{m\,K\,W^{-1}}$ and $\mathrm{m\,W^{-1}}$ respectively), see Equation 2.17
T : temperature (K)
p : volume fraction of pores ($0 < p < 1$), see Table 2.3
v_i : volume fraction of precipitated phases ($0 < v_i < 1$), see Table 2.3
c_{Nd} : equivalent molar concentration of Nd (mol. %), see Table 2.4

2.3.7 Validation of the modified model

Table 2.5 summarizes the input parameters, used for the validation of the model to the experimental data.

NESTOR-3	MFP (12.5 % FIMA)	TFC (8.5 % FIMA)
Volume fraction of pores	$p = 0.039$ (measure)	$p = 0.100$ (hypothesis)
Matrix thermal conductivity	$\lambda_m(c_{Nd} = \overline{c_{diss,FP}} = 2.30$ mol.%)	$\lambda_m(c_{Nd} = \overline{c_{diss,FP}} = 1.55$ mol.%)
Volume fraction of FMP	Parrish *et al.* exp. value [27, 34].	Thermo-Calc (this work)
Volume fraction of GP	Parrish *et al.* exp. value. [27, 34]	Thermo-Calc (this work)
Radiation damage	Annealed during measurements	Annealed during measurements

Table 2.5: Synthesis of the model input parameters, used for the validation of the model to experimental data

We made the assumption of a porosity volume fraction of $p = 0.10$ at the TFC axial region, due to missing hydrostatic density measurements. This value seems reasonable, given the greater amount of gas retention in the TFC region, compared to the MFP region (measured $p = 0.039$).
Table 2.6 shows that, in the TFC region, the amounts of Xe and Kr released are respectively 3.4 and 16.7 times higher than in the MFP region.

Sample	Xe (mol/g of fuel)	Kr (mol/g of fuel)
MFP (12.5% FIMA)	0.46×10^{-5}	0.38×10^{-6}
TFC (8.5% FIMA)	1.56×10^{-5}	6.35×10^{-6}

Table 2.6: Total quantity of fission gas, measured during the complete vaporization of the samples (Knudsen cell) [25].

Figure 2.16 shows the comparison between our model and the experimental data.

The model is able to describe the notable differences in thermal conductivity at the TFC and the MFP axial regions (4.5 (MFP) $\gg$ 2.5 (TFC) $\mathrm{W\,m^{-1}\,K^{-1}}$), namely due to the notable

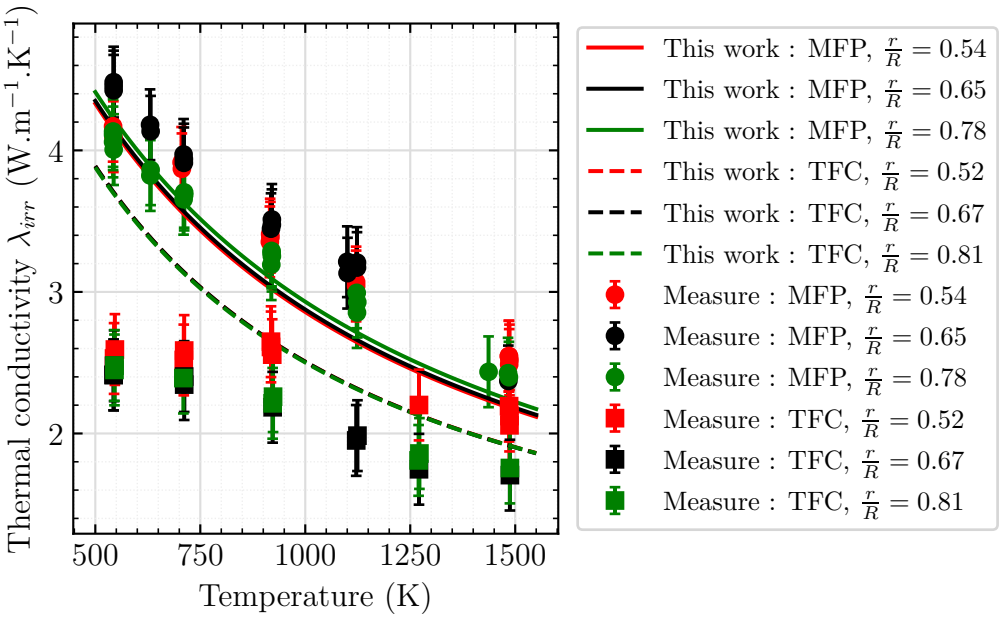

Figure 2.16: Thermal conductivity variation with temperature of irradiated NESTOR-3 FNR MOX fuel, as measured [25] and predicted in this work [24].

differences in porosity fraction, assumed in this work (*i. e.* $p = 0.039$ at the MFP, versus $p = 0.100$ at the TFC). The other model parameters (*i. e.* volume fraction of precipitates and molar fraction of dissolved FPs) could not explain those differences.
Indeed, the concentration of dissolved FPs is higher at the MFP region (see Table 2.4). If the differences in thermal conductivity were explained by dissolved FPs, we would observe a lower thermal conductivity at the MFP, which is not the case here.
The volume fraction of precipitates is higher in the axial region of the MFP, but not high enough to cause such large differences in thermal conductivity, even if our assumption was based on the volume fraction of precipitates, rather than on porosity.

The model correctly describes the experimental measurements at the MFP axial region in the whole temperature region.
At the TFC region, the model is consistent with measurements above 800 K, but underestimates the measurements by around 56 % below 750 K.
Several factors could be responsible for these discrepancies.

2.3.8 Discussion

2.3.8.1 Thermal conductivity of the irradiated fuel matrix

A possible explanation could be an underestimation of the thermal conductivity degradation of the fuel matrix.
Additional measurements on MOX SIMFuels with burn-up rates up to 13.5 % FIMA are required. This data can be used to quantify the effect of dissolved Nd, La, Ce, Pr and Zr on thermal conductivity over a wide range of burn-up rates.

2.3.8.2 JOG formation

JOG formation also bears mentioning when discussing discrepancies.
JOG is mainly composed of Cs_2MoO_4 [44–46]. Neither the EPMA experimental data, nor the calculations showed any significant amount of Cs or Mo in the fuel matrix. The latter is therefore not influenced by JOG. The model parameter, which can be impacted by JOG is the volume fraction of the FMP phase, since the latter contains Mo. Nevertheless, thermal conductivity is very slightly affected by metallic precipitates (see Table 2.7). Therefore, the

Effect	**Relative increase/decrease (in %) of λ_{irr} as opposed to λ_0 at T=500 K**			
	Lucuta original model		*This work*	
	MFP at $r = 0.54R$	TFC at $r = 0.52R$	MFP at $r = 0.54R$	TFC at $r = 0.52R$
Dissolved FPs	−51.8	−45.1	−35.7	−28.7
Precipitated FPs	+12.6	+8.3	+2.9	+0.1
Porosity	−5.7	−14.3	−9.7	−24.8

Table 2.7: The effect of FPs (dissolved and precipitated) and pores on the increase/decrease of thermal conductivity of irradiated fuel λ_{irr}, respective to fresh fuel λ_0. The different effects are calculated for both the initial model of Lucuta *et al.* [32, 36, 37] and the model developed in this work in both the MFP and TFC axial regions at $r = 0.54R$ and $r = 0.52R$ respectively

uncertainties related to JOG formation should not influence the thermal conductivity model's predictions.

2.3.8.3 Fuel temperature

Fuel temperature can be another source of uncertainty. The former is a GERMINAL output and has a direct impact on the Thermo-Calc calculations, since the latter are temperature-dependent. For this reason, we evaluated the effect of temperature on the Thermo-Calc results, and especially on the results for the elementary chemical composition of the fuel matrix (see Figure 2.17).

As shown in Figure 2.17, the amounts of Nd, Ce and La in the fuel matrix do not show any significant variation with temperature. Zr is the only temperature-dependent element. However, Zr is less present in the fuel matrix than Nd or Ce. Therefore, despite the temperature variations of Zr content, the total amount of FPs in the range T $\in$ [1000 – 1500] K increases by only 17 %. This increase is only 5 % for temperatures above 1500 K.
With those considerations, if one assumes an uncertainty of 200 K in fuel temperature, the corresponding relative uncertainty in the total fraction of dissolved FPs $\frac{\Delta c_{diss,FP}}{c_{diss,FP}}$ would be of only 12 % below 1500 K and 1.8 % above 1500 K. In our model, the total fraction of dissolved FPs is represented by the c_{Nd} parameter. Therefore, such errors on this parameter would induce only 0.1 % and $0.3 \cdot 10^{-2}$ % of uncertainty in thermal conductivity model predictions (at the MFP and $r = 0.65R$).

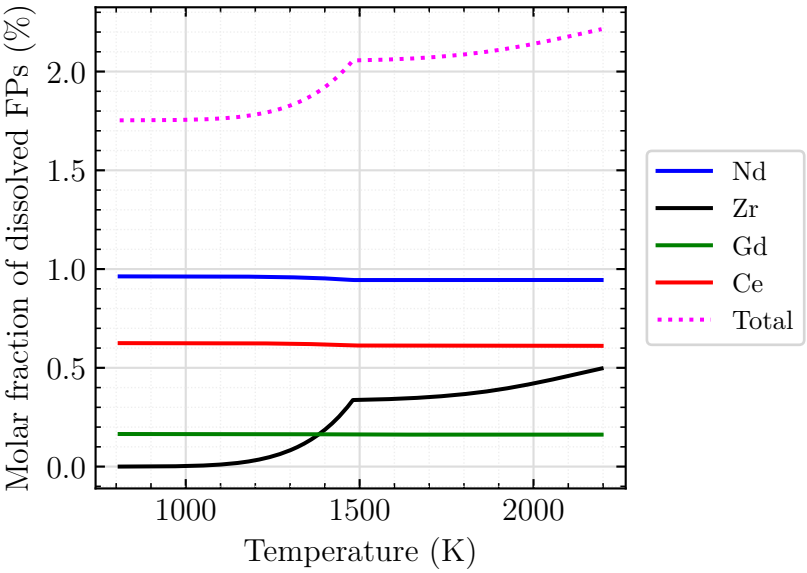

Figure 2.17: Effect of temperature on Thermo-Calc results for the elementary chemical composition of the irradiated NESTOR-3 fuel's (U,Pu,FPs)O_2 matrix. The calculation corresponds to the MFP region at $r = 0.65R$.

2.3.8.4 Radiation damage

As already mentioned in the previous chapter, radiation damage translates atom's displacement from its initial lattice position, due to the collision of the fissile isotope with a neutron. According to Lucuta *et al.*, when a certain temperature is exceeded (*i. e.* $\approx$ 1100 K), radiation damage is recovered.

For this reason, in order to avoid uncertainties, related to radiation damage, thermal diffusivity measurements are performed at cooling, once the fuel has gone through a first "recoil" heating cycle. Therefore, if the model of Lucuta *et al.* was accurate, measurements would not show any sign of radiation damage. However, as shown in Figure 2.16, measurements at the TFC axial region show a particular temperature profile below 700 K, which is characteristic of the temperature-variation of thermal conductivity, when radiation damage is still present in the fuel.

This observation led to the conclusion that the radiation damage model, proposed in the work of Lucuta *et al.* may not be valid in the case of the NESTOR-3 fuel.

Further research is needed into the effect of radiation damage on thermal conductivity.

2.3.8.5 Actinide migration

As previously mentioned, other factors, such as actinide migration, could influence the GERMINAL-Thermo-Calc outputs. However, due to the complex nature of those phenomena, a quantification of the uncertainty related to those factors could not be provided.

2.3.8.6 *Dissolved fission gas atoms*

Dissolved fission gas atoms can influence the thermal conductivity of the matrix, as mentioned in Reference [32].
However, the EPMA results showed very low amounts of dissolved fission gas atoms (< 0.07 mol. %) [22]. Although no EPMA was available in the TFC region, the GERMINAL-Thermo-Calc calculation did not show the presence of fission gas atoms. In this work, we only consider the most present dissolved FPs (*i. e.* with concentrations above 0.1 mol. %). Therefore, no parameters related to the dissolved fission gas atoms could be included in modeling.
The higher amounts of Xe and Kr, released during the Knudsen Cell experiment [25] in the TFC region have been discussed in terms of gas bubbles. The latter may justify the assumed higher fractional porosity of $p = 0.1$ in the TFC region.

2.3.8.7 *Plutonium redistribution*

Plutonium redistribution also bears mentioning. EPMA results in the MFP region showed a plutonium redistribution of about $\pm$ 15 % compared to fresh NESTOR-3 fuel (*i. e.* 20 mol. %). Nevertheless, many authors [2, 5, 105–107] have shown that the effect of plutonium on thermal conductivity is negligible, within the plutonium content ranges studied here (*i. e.* 20 $\pm$ 3 mol. %) and more importantly within the temperature range of interest (*i. e.* T $<$ 1500 K). Therefore, in this chapter, the effect of plutonium content on thermal conductivity was omitted.

2.3.8.8 *Comparison with the Philipponneau model*

While Lucuta *et al.*'s model is considered a PWR model, since it is based on PWR UO_2 SIMFuel data, Philipponneau [2] has proposed another model for FNR MOX, based on data for FNR MOX SIMFuels [39], with simulated burn-up rates of 10 % FIMA.
The approach in the work of Philipponneau is different from Lucuta *et al.*, in two ways:

1. Philipponneau used FNR MOX SIMFuels with only one simulated burn-up rate (10 % FIMA), versus Lucuta *et al.* who used PWR UO_2 SIMFuels with four simulated burn-up rates ($\beta \in [1.5 - 8]$ % FIMA).
2. The burn-up dependency in the model of Philipponneau is linear: $A_{irr} = A_0 + 0.44\beta$, whereas Lucuta *et al.* proposed a rather complex function of the burn-up, involving the $\arctan(\beta, T)$ function (see Equation 2.12).

Figure 2.18 shows a comparison between our model, those of Lucuta *et al.* [32, 36, 37] and Philipponneau [2], together with the experimental data on the NESTOR-3 fuel. In the MFP region, Philipponneau's model yields slightly lower values than our model and the experimental data. In the TFC region, both the Philipponneau model and our model overestimate the thermal conductivity, for temperatures below 1000 K.

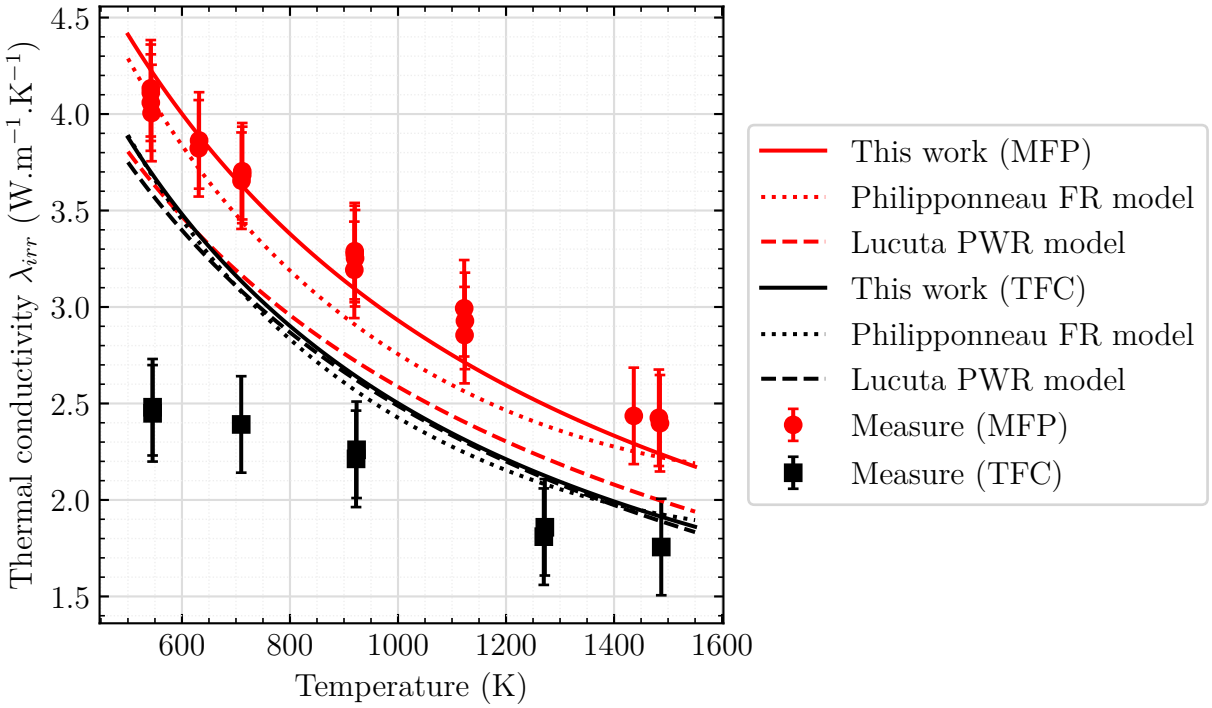

Figure 2.18: Comparison of the thermal conductivity model, developed in this work (solid lines) with experimental data (NESTOR-3) and other models (Lucuta *et al.* [32, 36, 37] in dashed lines and Philipponneau [2] in dotted lines). Philipponneau's model is plotted for a stoichiometric fuel (*i. e.* at a deviation from the stoichiometry of zero).

2.4 Conclusion and perspectives

Thermal conductivity modeling of fuels for Fast Neutron Reactors (FNR) is difficult due to the high temperatures involved, resulting in significant differences in microstructure and composition compared with fuels for thermal (or Pressurized Water Reactors (PWRs)).
In this work, a new model was developed. It was based on the equation proposed in the work of Lucuta *et al.* [32, 36, 37].
The model requires knowledge of the volume fraction of the precipitated metal and oxide phases, the burn-up rate and the porosity. This information was obtained by a GERMINAL-Thermo-Calc calculation. The calculations were compared with experimental characterizations of the NESTOR-3 fuel, as well as with published experimental results for other FNR MOX fuels [27, 34]. Discrepancies were observed between the calculated volume fractions of the metallic and oxide phases and the experimental estimates. On the other hand, the calculated concentration of dissolved FPs in the matrix in the axial region of the MFP was compared with EPMA examinations and gave satisfactory results.

In this work, we showed that the original Lucuta model failed to reproduce the thermal conductivity experimental data for the specific case of the NESTOR-3 FNR MOX fuel.
We therefore proposed a new model, following three essential modifications:

1. Replacing the Maxwell-Eucken's simplified expression, accounting for the total amount

of precipitate phases, assuming that their thermal conductivity is negligible to the fuel matrix, by a **proper use of the general Maxwell-Eucken equation, accounting for the thermal conductivity of each phase separately and for its volume fraction** (*i. e.* Equation 2.14)
2. Replacing the burn-up, as the driving parameter of the thermal conductivity of the irradiated fuel matrix, by the **concentration of dissolved FPs in the matrix** (*i. e.* Equation 2.17).
3. Replacing the Maxwell-Eucken's simplified expression for spherical and non conductive pores by a **temperature-dependent porosity factor, valid for porosity volume fractions up to** $p = 0.30$ (*i. e.* Equation 2.20).

The physical description of the original Lucuta *et al.*'s model was therefore improved, due to:

1. The introduction of physical parameters, intrinsic to the chemical composition of the fuel matrix: the fraction of dissolved FPs.
2. The use of less simplifying assumptions, namely concerning pore shape and temperature-variation of the porosity correction, as well as the thermal conductivity of the precipitated phases.

The model gives satisfactory results, when compared with experimental data, especially above 700 K. In particular, the model successfully reproduces the differences in thermal conductivity between the MFP and the TFC axial regions. In this work, we have shown that these differences are due to porosity.

Currently, only two sets of measurements on FNR MOX fuel irradiated at high burn-up rates (here 8.5 and 12.5 % FIMA) are available in the literature [25] and were used in this work.
In the framework of the ongoing ESFR-SMART [108] and PUMMA [109] projects, **new experimental measurements on irradiated MOX fuels under FNR conditions** (PAVIX [110], CAPRIX [111], and TRABANT [112]) will be provided to validate the model presented in this work and/or to increase its accuracy, by adding supplementary model parameters.

2.5 Conclusion et perspectives du chapitre

La modélisation de la conductivité thermique des combustibles pour les réacteurs à neutrons rapides (RNR) est difficile en raison des températures élevées, entraînant ainsi des différences significatives dans la microstructure et la composition, par rapport aux combustibles pour les réacteurs thermiques (ou à eau préssurisée (REP)).
Dans ce travail, un nouveau modèle a été développé. Ce dernier est basé sur l'équation, proposée dans les travaux de Lucuta *et al.* [32, 36, 37].
Le modèle nécessite la connaissance de la fraction volumique des phases précipitées métalliques et oxydes, du taux de combustion et de la porosité. Ces informations ont été obtenues par un calcul GERMINAL-Thermo-Calc. Les calculs ont été comparés aux caractérisations expérimentales du combustible NESTOR-3 ainsi qu'aux résultats expérimentaux publiés

pour d'autres combustibles RNR MOX [27, 34]. Certains écarts ont été observés entre les fractions volumiques calculées des phases métalliques et oxydées et les estimations expérimentales. D'autre part, la concentration calculée de PF dissous dans la matrice dans la région axiale du MFP a été comparée aux examens EPMA et a donné des résultats satisfaisants.

Dans ce travail, nous avons montré que le modèle Lucuta initial ne parvenait pas à reproduire les données expérimentales de conductivité thermique pour le cas spécifique du combustible MOX RNR de NESTOR-3.
Nous avons donc proposé un nouveau modèle, en procédant à trois modifications:

1. Remplacement de l'expression simplifiée de Maxwell-Eucken, qui tient compte de la quantité totale de phases précipitées, en supposant que leur conductivité thermique est négligeable par rapport à la matrice du combustible, par une **utilisation correcte de l'équation générale de Maxwell-Eucken, qui tient compte de la conductivité thermique de chaque phase séparément** (*i. e.* Equation 2.14)
2. Remplacement du taux de combustion, en tant que paramètre, régissant la conductivité thermique de la matrice irradiée, par la **concentration des PFs dissous dans la matrice** (*i. e.* Equation 2.17).
3. Remplacement de l'expression simplifiée de Maxwell-Eucken pour les pores sphériques et non conducteurs par un **facteur de porosité dépendant de la température, valable pour des porosités jusqu'à 30** vol. % (*i. e.* Équation 2.20).

La description physique du modèle initial de Lucuta *et al.* a donc été améliorée, grâce à :

1. l'introduction de paramètres physiques, intrinsèques à la composition chimique de la matrice du combustible : la fraction des PFs dissous.
2. l'utilisation d'hypothèses moins simplificatrices, notamment en ce qui concerne la forme des pores, la variation en température du facteur correctif de porosité, ainsi que la conductivité thermique des phases précipitées.

Le modèle proposé donne des résultats satisfaisants, vis-à-vis des données expérimentales, surtout à des températures supérieures à 700 K. En particulier, ce modèle reproduit avec succès les différences de conductivité thermique entre le **P**lan de **F**lux **M**aximal (PFM) et le **H**aut de **C**olonne **F**issile (HCF). Dans ce travail, nous avons montré que ces différences sont dues à la porosité.

Actuellement, uniquement deux jeux de mesure sur des combustibles MOX RNR irradiés à des taux de combustion élevés (ici 8.5 et 12.5 % FIMA) sont disponibles dans la littérature [25] et ont été utilisés dans ce travail. Dans le cadre des projets ESFR-SMART [108] et PUMMA [109], **de nouvelles mesures expérimentales sur des combustibles MOX irradiés dans les conditions des RNR** (PAVIX [110], CAPRIX [111], et TRABANT [112]) seront fournies pour valider le modèle présenté dans ce travail.

Chapter 3

Thermal conductivity modeling of the $(U,Pu)O_2$ matrix: taking into account chemical composition and temperature

Contents

Summary

In the previous chapter, we modeled the effect of pores and irradiation. The properties of interest were λ_p and λ_{irr}. To calculate the relative effect of pores and irradiation, with respect to the fresh fuel matrix λ_0, we used the model of Philipponneau [2]. However, as already mentioned in Chapter 1, the model of Philipponneau is empirical in terms of temperature, plutonium and oxygen content dependency. In this chapter, we propose to model the thermal conductivity of the fresh MOX fuel matrix λ_0, using a theoretical modeling of each of the three (quasi)particles, responsible for heat transport in oxide solids: phonons, polarons and photons.

This chapter is divided into three main sections, focused on each of the three contributions. The total thermal conductivity is then computed in a separate section. This chapter will reveal some pioneering results, related to the correlated plutonium-oxygen content effect, which is not taken into account in other reported thermal conductivity models. Sensitivity analysis on both model parameters and elementary chemical composition, led to the proposition of supplementary experimental data, which can be used in the future to validate the model. This data is of essential interest for reducing model uncertainties and is presented in a separate section. We will finish this chapter by providing a conclusion and some perspectives.

Résumé

Dans le chapitre précédent, nous avons modélisé l'effet des pores et de l'irradiation. Les propriétés d'intérêt étaient donc λ_p et λ_{irr}. Pour calculer l'effet relatif des pores et de l'irradiation, par rapport à la matrice de combustible frais λ_0, nous avons utilisé le modèle de Philipponneau [2]. Cependant, comme nous l'avons déjà mentionné au Chapitre 1, le modèle de Philipponneau est empirique en termes de dépendance à la température, au plutonium et à la teneur en oxygène. Dans ce chapitre, nous proposons de modéliser la conductivité thermique de la matrice du combustible MOX frais λ_0, en utilisant une modélisation théorique de chacune des trois (quasi)particules responsables du transport de la chaleur dans les solides oxides: les phonons, les polarons et les photons.

Ce chapitre est donc divisé en trois sections principales, axées sur chacune des trois contributions. La conductivité thermique totale est ensuite calculée dans une section séparée. Ce chapitre présentera quelques résultats novateurs, liés à l'effet corrélé de la teneur en plutonium et en oxygène, qui n'est pas pris en compte dans les modèles publiés dans la littérature. L'analyse de sensibilité aux paramètres du modèle et à la composition chimique élémentaire a permis de proposer des données expérimentales supplémentaires, qui pourront être utilisées à l'avenir pour valider le modèle. Ces données sont d'un intérêt essentiel pour réduire les incertitudes du modèle et sont présentées dans une section séparée. Nous terminerons ce chapitre par une conclusion et quelques perspectives.

3.1 Introduction

Thermal conductivity of the fuel matrix originates from different (quasi)particles' contributions. In this work, we consider three type of (quasi)particles: phonons, electrons (or even polarons) and photons. We can therefore write:

$$\lambda = \lambda^{ph} + \lambda^{el} + \lambda^{rad} \tag{3.1}$$

where the ph, el and rad superscripts refer to the phonons, electrons and photons (radiative contribution) respectively. In the following sections, each elementary contribution will be described and modeled.

3.2 Phonon contribution to thermal conductivity

3.2.1 Introduction to heat transfer by phonons

Phonons are (quasi)particles, originated from atom vibrations in solids [63]. If we consider the solid as a 3D arrangement of atoms, held together by springs (*i. e.* inter-atomic forces), the phonons can be seen as a set of waves, created by atoms' vibrations, propagating through the crystal.

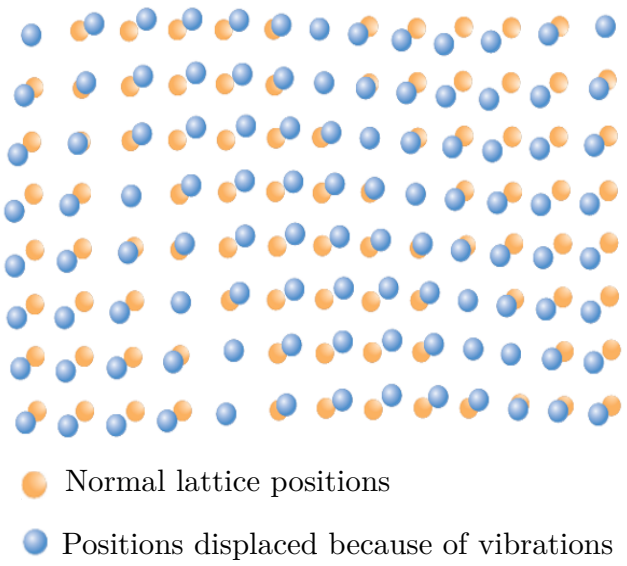

Figure 3.1: Illustration of a phonon propagating through the crystal

The propagation frequencies ω of the waves depend on the wave-vector k. This dependency is called the dispersion relation of the wave (*i. e.* $\omega(k) = f(k)$). In a 1D chain of 2 atoms with masses M_1 and M_2, two cases are possible: atoms vibrating in phase with each other (acoustic branches), and atoms vibrating out of phase with each other (optic branches). The optic branches have lower group velocity than the acoustic ones. For this reason, the optic

branches' contribution to heat transfer is negligible to that of the acoustic ones. [113].

Phonons do not behave like harmonic oscillators. In other words, they interact with each other, leading to a finite thermal conductivity. If phonons were harmonic oscillators, thermal conductivity would be infinite, because phonons would not interact. Two types of phonon-phonon interactions exist:

1. Normal, called N-processes
2. Umklapp, called U-processes

N-processes **conserve momentum**: when two phonons collide with each other, a third phonon is created, traveling in the same direction to the colliding phonons. U-processes however **do not conserve momentum**: when colliding with each other, the phonons create a third one, traveling in the opposite direction. The U-processes thus decrease thermal conductivity. A part from phonon-phonon interactions, phonon-impurity interactions can also lead to decrease thermal conductivity. Those impurities can be foreign atoms (FPs or other) dissolved into the matrix, oxygen vacancies, dislocations, grain size or grain boundaries. In this work, a particular attention will be paid to the effect of oxygen vacancies and foreign atoms (*i. e.* plutonium in UO_2 and uranium in PuO_2).
The effect of dislocations, grain size or boundaries will not be covered in this work. For further information about the effect of dislocation loops on thermal conductivity, the reader may refer to the work of Khafisov *et al.* [114]. The effect of grain size has been shown to be negligible for temperatures, higher than the Debye temperature θ_D for LiF systems [115]. The Debye temperature translates as the temperature, at which all phonon modes are excited. In this work, we focus on thermal conductivity modeling above θ_D and therefore grain size is not considered. Table 3.1 more generally illustrates the temperature dependencies of different types of impurities on the phonon contribution to thermal conductivity. [63].
In the next section, we make a literature review of the existing models for the phonon contribution to thermal conductivity.

Type of scattering	**Temperature dependency of λ^{ph}**
Low temperature regime ($T < \theta_D$)	
Intrinsic conductivity (*i. e.* U-processes)	$(\frac{T}{\theta_D})^3 e^{\left(\frac{\theta_D}{bT}\right)}$
Point defects	T^1
Dislocations	T^2
Grain size	T^3
External boundaries	T^3
High temperature regime ($T > \theta_D$)	
Phonon-phonon interactions	T^{-1}
Phonon-impurity interactions	T^0

Table 3.1: Table summarizing the temperature dependencies of all types of scattering mechanisms (*i. e.* intrinsic phonon-phonon interactions (U-processes) and extrinsic (all types of impurities)) from [116]

3.2.2 Modeling: state of the art

3.2.2.1 Semi-empirical approaches

As shown in Table 3.1, for temperatures higher than θ_D, the intrinsic conductivity (phonon-phonon) varies as T^{-1}, whereas the extrinsic (phonon-impurity) with T^0. The associated resistivity ($R = \lambda^{-1}$) thus varies as T^0 and T^1, respectively. In most published work, we denote $T^0 = A$ and $T^1 = BT$, leading to:

$$R^{ph} = R^{ph}_{ex} + R^{ph}_{in} = A + BT \tag{3.2}$$

where the *ex* and *in* subscripts stand for extrinsic and intrinsic. Thermal conductivity can thus be written as:

$$\lambda^{ph} = \frac{1}{R^{ph}} = \frac{1}{A + BT} \quad \text{if} \quad T > \theta_D \tag{3.3}$$

The most common approach to evaluate the A and B terms in Equation 3.3 is to estimate them by inverse methods, using thermal conductivity experimental data. Multiple estimates of A and B for MOX fuel were reported [3–6, 33, 117]. Table 3.2 summarizes some of the reported A and B coefficients for MOX fuel, with their respective deviation from stoichiometry x and plutonium content y dependencies.

Author (year)	**A** ($\mathrm{m\,K\,W^{-1}}$)	**B** ($\mathrm{m\,W^{-1}}$) $\cdot 10^{-4}$
Gibby (1969) [117]	$1.50 \cdot 10^{-2} + 3.55 \cdot x$	3.12
Washington *et al.* (1973) [118]	$3.70 \cdot 10^{-2} + 3.33 \cdot x$	2.37
Bonnerot (1986) [5]	$5.91 \cdot 10^{-2} + 4.17 \cdot x$	$2.25 + 0.547 \cdot y$
Philipponneau (1992) [2]	$-0.1055 + 1.52\sqrt{x + 0.00931}$	$2.885.10^{-4}$
Duriez *et al.* (2000) [4]	$3.24 \cdot 10^{-2} + 2.64 \cdot x$	$2.65 - 6.62 \cdot x$
Inoue (2000) [107]	$6.06 \cdot 10^{-2} + 27.54 \cdot 10^{-2}\sqrt{x}$	2.01
Kato *et al.* (2012) [3]	$1.59 \cdot 10^{-2} + 2.71 \cdot x$	$2.49 - 2.62 \cdot x$
Magni *et al.* (2020) [33]	$1.93 \cdot 10^{-2} + 1.06 \cdot 10^{-6} \cdot x + 2.63 \cdot 10^{-8} \cdot y$	$2.39 + 1.37 \cdot 10^{-9} \cdot y$

Table 3.2: Empirical A and B coefficients in $\frac{1}{A+BT}$, reported for MOX fuels, by several authors.

Other approaches, based on more fundamental theories can also be used to assess the phonon contribution to thermal conductivity.

3.2.2.2 Relaxation-Time approximation

One of those approaches is based on the "*relaxation-time approximation*" [119]. In this theory, the phonon distribution is restored to the equilibrium distribution at a rate proportional to the departure from equilibrium [120]. Thermal conductivity due to phonons thus takes the following form:

$$\lambda^{ph} = \frac{k}{2\pi^2 v_s}\left(\frac{kT}{\hbar}\right)^3 \int_0^{\theta_D/T} \frac{s^4 e^s}{\tau_C^{-1}\left(e^s - 1\right)^2} ds \tag{3.4}$$

where s is dimensionless $s = \hbar\omega/kT$, v_s is the sound velocity ($\mathrm{m\,s^{-1}}$), ω the phonon frequency ($\mathrm{s^{-1}}$), k the Boltzmann constant ($\mathrm{J\,K^{-1}}$), $\hbar$ the Reduced Planck constant $= \frac{h}{2\pi}$ ($\mathrm{J\,s}$), θ_D the

Debye temperature (K) and τ_C the total phonon-scattering relaxation time (s). If the phonon-scattering processes are considered independent of one another, the total scattering time τ_C is the sum of all individual processes: $\tau_C^{-1} = \sum_i \tau_i^{-1}$. Those individual processes can involve phonon-phonon scattering, or phonon-impurity scattering (*i. e.* point defects, dislocations, grain boundaries *etc.*) and are functions of both temperature and phonon frequency ω. However, *the relaxation-time approximation* does not consider phonon-phonon contributions, other than the U-processes. To consider both normal (N-processes) and Umklapp (U-processes), one can use the Callaway model.

3.2.2.3 Callaway model

As mentioned previously, the N-processes does not give raise to thermal resistivity as they conserve momentum [119, 120]. However, they can restore momentum and energy among phonons that undergo resistive processes (U-processes or phonon-impurity scattering). Callaway [121] thus adds a second term to the *relaxation-time approximation* to represent the effect of N-processes:

$$\lambda^{ph} = \frac{1}{3} C T^3 \left(\int_0^{\theta_D/T} \frac{x^4 e^x}{\tau_C^{-1} \left(e^x - 1\right)^2} dx + \frac{\left[\int_0^{\theta_D/T} \frac{\tau_C x^4 e^x}{\tau_N (e^x-1)^2} dx\right]^2}{\int_0^{\theta_D/T} \frac{\tau_C x^4 e^x}{\tau_N \tau_R (e^x-1)^2} dx} \right) \tag{3.5}$$

where τ_N and τ_R are the scattering time of the normal (N-processes) and resistive (U-processes or phonon-impurity) processes respectively. The total scattering time is thus $\tau_C^{-1} = \tau_N^{-1} + \tau_R^{-1}$. Although this model takes into account normal and resistive processes, it is not systematically applied for MOX fuel [122–124]. According to Klemens [123], if the scattering time of the phonon-impurity processes is lower than that for U-processes, the normal (N) processes' effect on thermal resistivity can be neglected. Gibby [122] assumes this condition for MOX fuel and thus neglects the N-processes.

3.2.2.4 Approach, used in this work

Applying either of the theoretical models mentioned above, requires not only knowledge of the phonons' spectra, but also of the different scattering processes' rates τ_i and their temperature and frequency dependencies. To our knowledge, no such data have yet been reported in the literature for (U,Pu)O_2.

In this work, Equation 3.3 will be used to estimate thermal conductivity due to phonons. The A and B terms in $\frac{1}{A+BT}$ will be calculated, using theoretical equations, based on the Ambegaokar and Abeles' approach (A term) [124] and the Julian approach (BT term) [125].

The advantage of using this approach is twofold:

1. Neither Ambegaokar's equation for A, nor Julian's for BT involves complex mathematical problems. The thermal conductivity **computation time is therefore low**.
2. Both **plutonium and oxygen content** are taken into account in the model.

This approach enables us to evaluate the effect of the chemical composition of MOX fuel on thermal conductivity, while keeping calculation time low. As mentioned in the introduction,

GERMINAL (V3) calculations will performed in Chapter 5, using the model, proposed in this work. Given the complexity of a fuel performance code, it is essential to keep computation time low.

3.2.3 Modeling of extrinsic thermal resistivity

As mentioned previously, here we use Ambegaokar and Abeles' approach [124] to model extrinsic thermal resistivity. This approach is based on Klemens' expression [123] for the phonon relaxation time τ due to a particular impurity i:

$$\tau_i(w) = \frac{4\pi\overline{v_p}^3}{\overline{V_a}\Gamma_i\omega^4} \tag{3.6}$$

where $\overline{v_p}$ is the mean phonon velocity ($\mathrm{m\,s^{-1}}$), $\overline{V_a}$ the atomic volume ($\mathrm{m^3}$), ω the phonon frequency (s^{-1}) and Γ_i the scattering cross section due to the i-th defect, expressed as follows:

$$\Gamma_i = f_i\left\{\left(\frac{M_i - \overline{M_{sub}}}{\overline{M_{sub}}}\right)^2 + 2\left[\left(\frac{G_i - \overline{G_{sub}}}{\overline{G_{sub}}}\right) - 6.4\gamma_\infty\left(\frac{r_i^{host} - \overline{r_{sub}}}{\overline{r_{sub}}}\right)\right]^2\right\} \tag{3.7}$$

where:

- f_i : atomic fraction of the i-th point defect (-)
- M_i : atomic mass of the i-th point defect ($\mathrm{kg\,mol^{-1}}$)
- r_i^{host} : atomic radius of the i-th point defect in the host lattice (m)
- G_i : average stiffness constant of the nearest neighbor bonds of defect atoms to the host lattice atoms (Pa)
- $\overline{G_{sub}}$: average stiffness constant of the host sub-lattice (Pa)
- $\overline{M_{sub}}$: mean atomic mass of the host sub-lattice ($\mathrm{kg\,mol^{-1}}$)
- $\overline{r_{sub}}$: mean ionic radii of the host sub-lattice (m)
- γ_∞ : high-temperature limit of the acoustic phonon mode Gruneisen parameter (-)

Therefore, according to Klemens [123], phonon-impurity scattering is due to a difference in (1): **mass**, between the impurity and the host lattice (*i. e.* the $M_i - \overline{M_{sub}}$ term), (2): **bonding strength** (*i. e.* the $G_i - \overline{G_{sub}}$ term) and (3): **size** (*i. e.* the $r_i^{host} - \overline{r_{sub}}$ term).
Based on Klemens' approach, Ambegaokar derives an equation for the phonon-impurity contribution (extrinsic) to thermal resistivity:

$$A = C\Gamma \tag{3.8}$$

where:

$$C = \frac{\pi^2 a^3 \theta_D}{12(3-x)\overline{v_p}^2 h} \tag{3.9}$$

x is the deviation from stoichiometry (in $U_{1-y}Pu_yO_{2-x}$), $\overline{v_p}$ is the mean phonon velocity ($\mathrm{m\,s^{-1}}$), h is the Planck constant (J s), a is the lattice parameter (m) and Γ the scattering cross section of both sub-lattices (*i. e.* the cation sub-lattice containing (U,Pu) and the oxygen sub-lattice). In the following sections, each of the input parameters (*i. e.* Debye temperature θ_D, mean

phonon velocity $\overline{v_p}$ and scattering cross section Γ and lattice parameter a) will be calculated for MOX fuel.

3.2.3.1 Debye temperature

In Debye's model, this physical parameter is related to the maximum phonon frequency, denoted ω_D by $\theta_D = \frac{\hbar\omega_D}{k}$ with k being the Boltzmann constant and $\hbar$ the reduced Planck constant (*i. e.* $\hbar = \frac{h}{2\pi}$). To calculate θ_D, knowledge on the phonon spectra (*i. e.* the dispersion relations $\omega(k)$) of the MOX material is required. Because of the complex dispersion relations of solids with more than one atom per unit cell (in MOX fuel this number is equal to 12), the derivation of θ_D by ω_D is difficult. Instead, the thermodynamic definition of the Debye temperature can be used [63]:

$$\theta_D = \left(\frac{h}{k}\right)\left(\frac{3n}{4\pi a^3}\right)^{1/3} V_s \tag{3.10}$$

where:

- θ_D : Debye temperature (K)
- n : number of atoms per unit cell, $n = 4 \times (3 - x)$, x being the deviation from stoichiometry
- a : lattice parameter (m)
- V_s : averaged sound velocity, integrated over several crystal directions ($\mathrm{m\,s^{-1}}$)
- k : Boltzmann constant ($\mathrm{J\,K^{-1}}$)
- h : Planck constant (J s)

To compute θ_D, the lattice parameter a and sound velocity V_s from *Hirooka et al.* [126] and *Kato et al.* [127] were used. For further information on those parameters, the reader can refer to Annexes C.1 and C.3. θ_D decreases with increasing deviation from stoichiometry x, and increases with increasing plutonium content (see Figure 3.2). The increasing tendency of θ_D with increasing plutonium content is consistent with experimental data, obtained by X-ray [128–130] and neutron [131] diffraction techniques on UO_2 and PuO_2. The latter show lower Debye temperature for UO_2 (*i. e.* $\in$ [377-383] K) [128, 131] than for PuO_2 (*i. e.* $\in$ [415-429] K) [129, 130].

3.2.3.2 Mean phonon velocity

The mean phonon velocity $\overline{v_p}$ can also be calculated with its thermodynamic expression:

$$\overline{v_p} = \left(\frac{2\pi k\theta_D}{h}\right)\left(\frac{\overline{V}}{6\pi^2}\right)^{1/3} \tag{3.11}$$

where $\overline{V}$ is the mean atomic volume per molecule of $U_{1-y}Pu_yO_{2-x}$ (m^3) (*i. e.* $\bar{V} = \frac{a^3}{4}$ where a is the lattice parameter).

The mean phonon velocity is proportional to θ_D, thus showing the same variations with x, y, and T as θ_D. The mean phonon velocity is in the range [4451 - 4622] $\mathrm{m\,s^{-1}}$ for

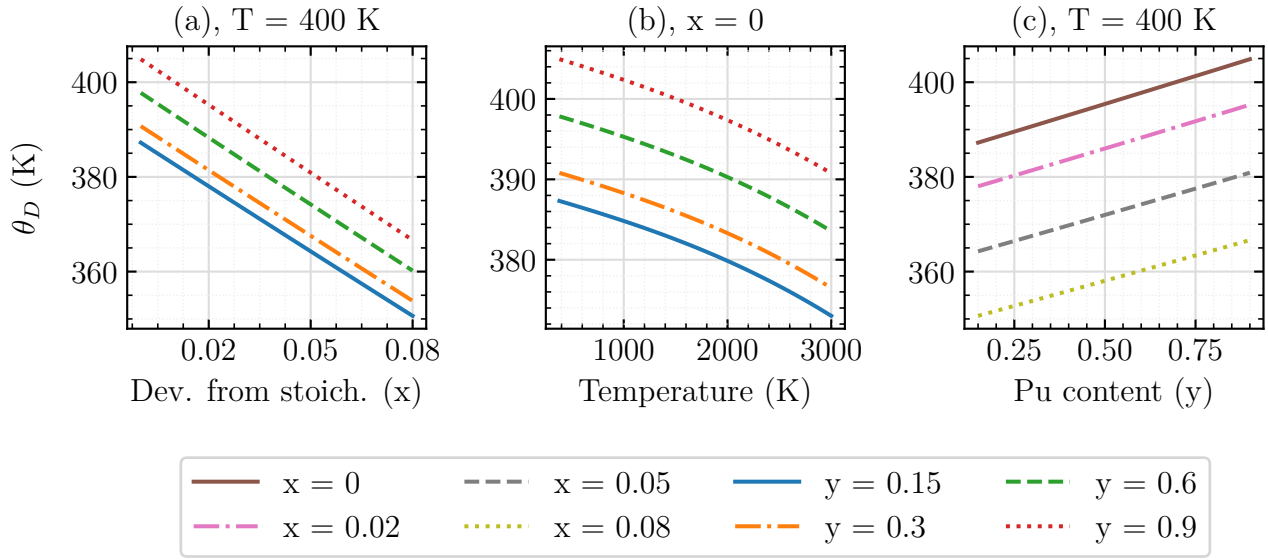

Figure 3.2: Predicted variation (in this work) of the Debye temperature with the deviation from stoichiometry x for different plutonium contents y, as calculated by equation 3.10

$y = [0.05 - 0.95]$ respectively. The increasing tendency of $\overline{v_p}$ with plutonium content is consistent with the reported values for UO_2 ($\overline{v_p} \in [4000 - 4300]$ m s^{-1}) [117, 132] and PuO_2 ($v_p = 4700$ m s^{-1}) [98]. Njifon [113] has showed similar increasing tendency of $\overline{v_p}$ with plutonium content. To perform electronic structure calculations, Njifon used Hubbard corrected density functional theory (DFT+U) and empirical potentials (EP) coupled with the Boltzmann transport equation (BTE). His DFT+U/BTE calculation gave a mean phonon velocity of about twice smaller than that calculated by equation 3.11.

3.2.3.3 Gruneisen parameter

To calculate the scattering cross-section Γ in Equation 3.8, knowledge on the high-temperature Gruneisen parameter γ_∞ is needed (see Equation 3.7). In this section, we assess γ_∞.
Gruneisen parameter measures how phonon frequencies change with volume. The former can be defined, relative to a particular phonon mode γ_i or as the average γ of all modes. In this work, knowledge of the average γ is required. The latter can be calculated either using γ_i, as follows:

$$\gamma = \frac{\sum_{i=1}^{3N} \gamma_i C_i}{\sum_{i=1}^{3N} C_i} \tag{3.12}$$

where γ_i is given by:

$$\gamma_i = -\frac{V}{\omega_i}\frac{d\omega_i}{dV} \tag{3.13}$$

with C_i being the contribution of each phonon mode to heat capacity C_v or, using the so-called thermodynamic definition:

$$\boxed{\gamma = \frac{\alpha V_m K_T}{C_v}} \tag{3.14}$$

where:

α : volumetric thermal expansion coefficient (K^{-1}) (see Equation C.4 in Annex C.2)
K_T : isothermal bulk modulus (Pa) (see Equation C.9 in Annex C.4)
V_m : molar volume $= \frac{a^3 N_a}{4}$ ($m^3\,mol^{-1}$), for a, see Equation C.8 in Annex C.3
C_v : molar heat capacity at constant volume ($J\,mol^{-1}\,K^{-1}$) (see Equation C.10 in Annex C.5)

Each of the material properties, needed to compute γ, is temperature-dependent. As mentioned previously, the high-temperature limit of γ is required. This limit corresponds to γ, evaluated at the Debye temperature θ_D [120]. We thus calculate $\gamma_\infty = \gamma(\theta_D)$ from Equation 3.14. Gruneisen parameter decreases with temperature (see Figure 3.3 b). Debye temperature is also

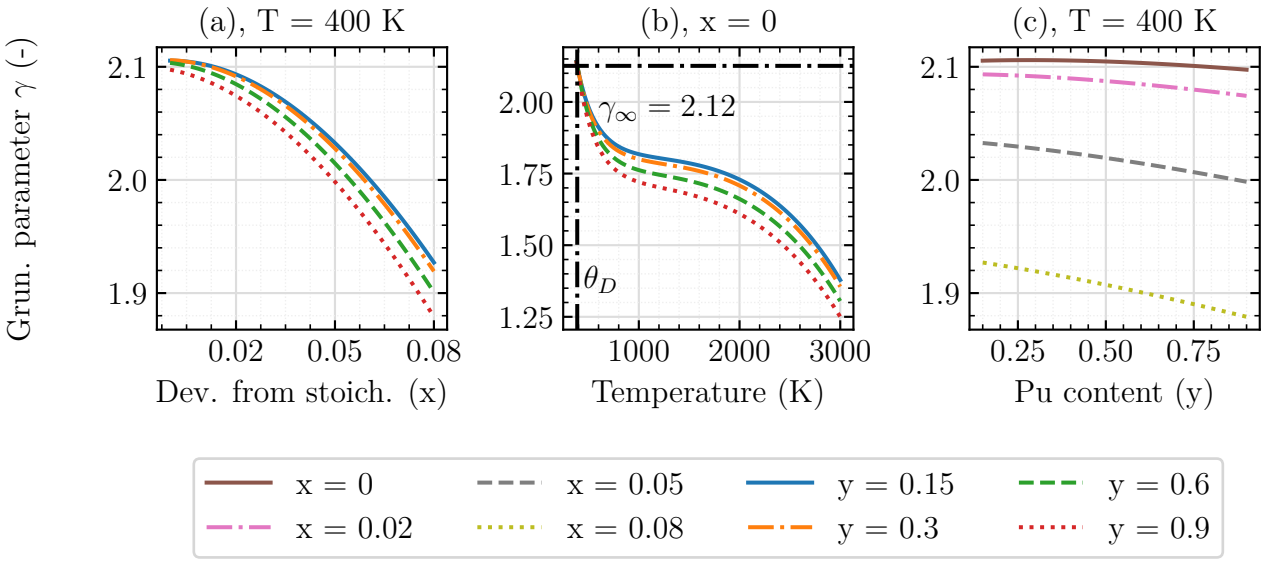

Figure 3.3: Predicted variation (in this work) of the Gruneisen parameter γ with (a): deviation from stoichiometry x, (b): temperature T, and (c): plutonium content y. The high-temperature Gruneisen parameter $\gamma_\infty = \gamma(\theta_D)$ is shown, together with the corresponding Debye temperature θ_D evaluated at $x = 0, y = 0.2, T = 400$ K. θ_D is also temperature-dependent (see Figure 3.2), thus inducing a temperature-dependency of γ_∞. For illustrative purposes, the value of γ_∞, showed in (b) corresponds to $\gamma_\infty = \gamma(\theta_D(x = 0, y = 0.2, T = 400))$

temperature-dependent (see Figure 3.2 b), thus inducing additional temperature dependency in γ_∞ (see Figure 3.4). The latter is a slowly increasing function of temperature.

Method	**Pu content (y)**					
	0 (UO_2)	**0.05**	**0.25**	**0.5**	**0.95**	**1 (PuO_2)**
DFT+U/BTE	1.88 [113]	-	2.23 [113]	2.10 [113]	-	2.11 [113]
EP/BTE	1.28 [113]	-	1.28 [113]	1.28 [113]	-	1.28 [113]
Exp. data	1.7 - 1.9 [131]	-	-	-	-	1.9 [129], 2.6 [130]
This work (Eq. 3.14 at 400 K)	2.13	2.13	2.12	2.11	2.08	2.08

Table 3.3: Comparison of γ, calculated in this work by Equation 3.14 at x = 0, T = 400 K, and literature data for UO_2 [131], PuO_2 [129, 130] and MOX [113]

As shown in Figure 3.3 a, Gruneisen parameter decreases with both deviation from stoichiometry x and plutonium content y. The relative decrease with y is lower than with x.
To our knowledge, the effect of x on γ has not been reported in the literature. However, Njifon *et al.* [113] studied the effect of plutonium content by DFT+U/BTE and EP/BTE techniques. They reported lower Gruneisen parameter at $y = 0.5$ than at $y = 0.25$ (see Table 3.3), which is consistent with the decreasing tendency with y, predicted by Equation 3.14. On the other hand, Njifon *et al.* predicted a higher γ for UO_2 than for PuO_2. This tendency highlights the non-linear variation of the Gruneisen parameter with plutonium content.
Our results for γ are consistent with literature data not only in terms of relative variation with y, but also in terms of absolute values. That is, $\gamma = 2.23$ at $y = 0.25$ in Njifon *et al.* [113] and $\gamma = 2.12$ at $y = 0.2$ in this work.
This observation highlights the adequate use of Equation 3.14 to estimate Gruneisen parameter, out of material properties (*i. e.* C_v, α, K_T, a).

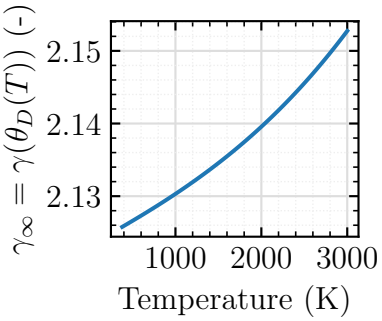

Figure 3.4: Predicted variation (in this work) of the high-temperature Gruneisen parameter $\gamma_\infty = \gamma(\theta_D(T))$ with temperature, calculated from Equation 3.14 at x = 0, y = 0.2 and at $T = \theta_D(T)$

3.2.3.4 Scattering cross-section

The scattering cross-section for MOX fuel takes the following form (see Annex D for more details on this equation):

$$\Gamma = 3\left(\frac{(1-y)M_U + yM_{Pu}}{(1-y)M_U + yM_{Pu} + (2-x)M_O}\right)^2 (\Gamma_{U^{4+}} + \Gamma_{Pu^{4+}} + \Gamma_{Pu^{3+}}) + \frac{3}{2}\left(\frac{(2-x)M_O}{(1-y)M_U + yM_{Pu} + (2-x)M_O}\right)^2 \Gamma_{O_v} \tag{3.15}$$

where M_O, M_{Pu} and M_U are the respective atomic masses of O, Pu and U atoms (see Table 3.4) and $\Gamma_{U^{4+}}, \Gamma_{Pu^{4+}}, \Gamma_{Pu^{3+}}$ and Γ_{O_v} the contributions of U^{4+}, Pu^{4+}, Pu^{3+} and O_v (v standing for vacancy) to phonon scattering. To calculate those contributions, a modified version of Equation 3.7 was used. For more information about the modified equation, see Annex D. This equation

takes the following form:

$$\Gamma_i = f_i \left\{ \left(\frac{M_i - \overline{M_{sub}}}{\overline{M_{sub}}} \right)^2 + \epsilon \left(\frac{r_i - \overline{r_{sub}}}{\overline{r_{sub}}} \right)^2 \right\} \tag{3.16}$$

The scattering cross section of the i-th defect thus involves two terms, characterizing the mass $(M_i - \overline{M_{sub}})$ and ionic radius difference $(r_i - \overline{r_{sub}})$ effect respectively, denoted Γ_i^M and Γ_i^R:

$$\Gamma_i = \Gamma_i^M + \Gamma_i^R = f_i \left\{ \left(\frac{M_i - \overline{M_{sub}}}{\overline{M_{sub}}} \right)^2 \right\} + f_i \left\{ \epsilon \left(\frac{r_i - \overline{r_{sub}}}{\overline{r_{sub}}} \right)^2 \right\} \tag{3.17}$$

where ε is given by:

$$\varepsilon = \frac{2}{9} \left(6.4 \times \gamma_\infty \left(\frac{1+\nu}{1-\nu} \right) \right)^2 \tag{3.18}$$

with ν being the Poisson ratio.

Ion	**Fractional occupancy** f_i	$\boldsymbol{r_i}$ $(\cdot\mathbf{10^{-9}})$ (m)	$\boldsymbol{M_i}$ (kg mol^{-1})	$\overline{\boldsymbol{r_{sub}}}$ (m)	$\overline{\boldsymbol{M_{sub}}}$ (kg mol^{-1})
U^{4+}	$1-y$	0.1001	0.238	$\overline{r_{U,Pu}}$	$\overline{M_{U,Pu}}$
Pu^{4+}	$y-2x$	0.0960	0.244	$\overline{r_{U,Pu}}$	$\overline{M_{U,Pu}}$
O^{2-}	$(2-x)/2$	0.1368	0.016	$\overline{r_O}$	$\overline{M_O}$
Pu^{3+}	$2x$	0.1100	0.244	$\overline{r_{U,Pu}}$	$\overline{M_{U,Pu}}$
O_v	$x/2$	0.1367	0	$\overline{r_O}$	$\overline{M_O}$

Table 3.4: Parameters for the calculation of Γ_i, using Equation 3.16

The presence of ϵ in Γ_i^R amplifies the radius term, with respect to the mass difference term. The scattering strength of a particular i defect will thus be driven by its radius difference with respect to the host sub-lattice.

$\Gamma_{Pu^{3+}}, \Gamma_{Pu^{4+}}$, $\Gamma_{U^{4+}}$ and Γ_{O_v} can be computed, using Equation 3.16, together with the associated parameters in Table 3.4 and the following expressions for the mean radius of each sub-lattice $\overline{r_{U,Pu}}$ and $\overline{r_O}$ and their atomic masses $\overline{M_{U,Pu}}$ and $\overline{M_O}$:

$$\overline{M_{U,Pu}} = (1-y)M_U + yM_{Pu} \tag{3.19}$$

$$\overline{M_O} = \frac{2-x}{2} M_O \tag{3.20}$$

$$\overline{r_{U,Pu}} = (1-y)r_{U^{4+}} + 2x \cdot r_{Pu^{3+}} + (y-2x)r_{Pu^{4+}} \tag{3.21}$$

$$\overline{r_O} = \frac{2-x}{2} r_{O^{2-}} + \frac{x}{2} r_{O_v} \tag{3.22}$$

It should be mentioned, that the cationic states of the Pu and U atoms, considered in this work

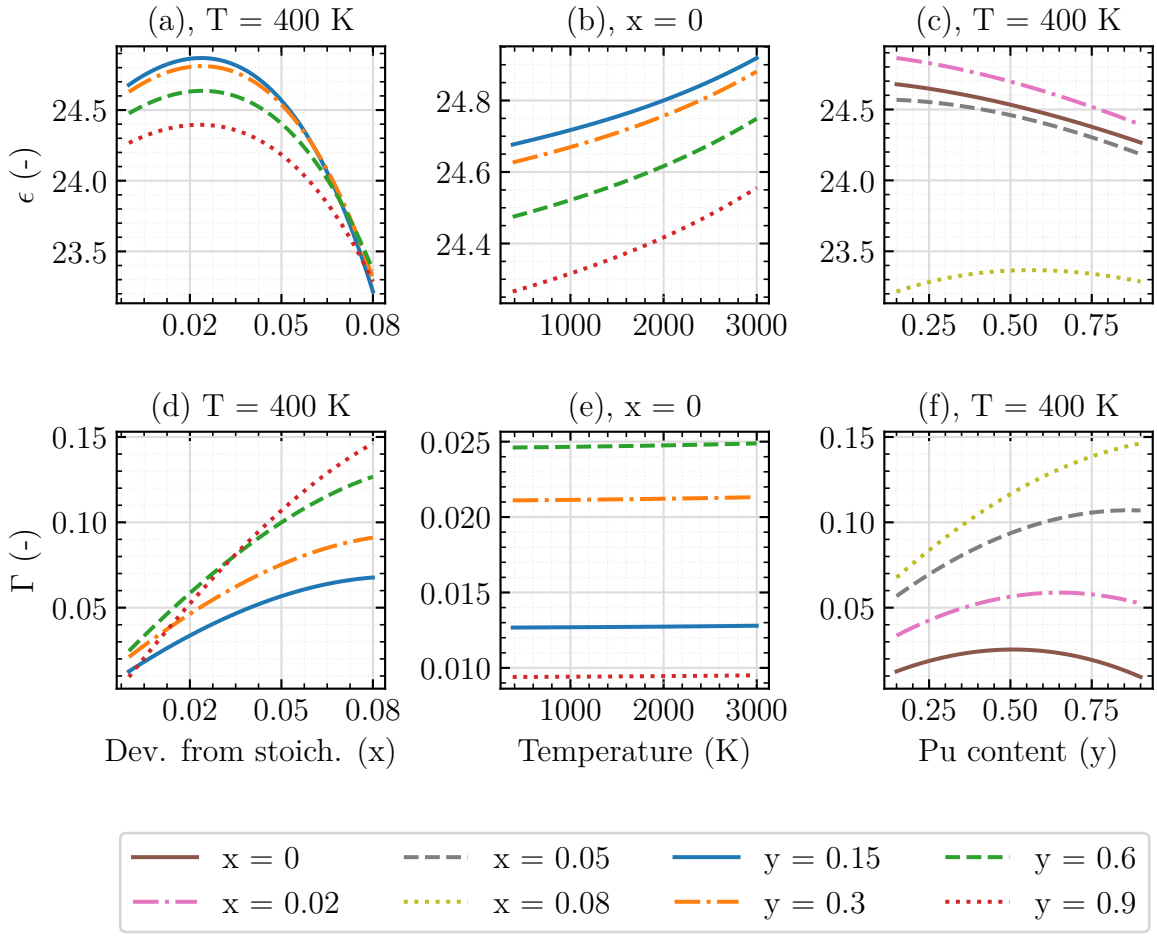

Figure 3.5: Predicted variation (in this work) variation of ϵ and Γ with deviation from stoichiometry (a, d), temperature (b, e) and plutonium content (c, f), for different plutonium contents (a,b,d,e) and deviations from stoichiometry (c,f).

are respectively Pu^{4+}, Pu^{3+} and U^{4+}. Indeed, to preserve the electroneutrality of the crystal, in case of missing oxygen atoms (*i. e.* oxygen vacancies), most reported work on the cationic states of the actinide atoms in MOX, consider that plutonium changes its state from Pu^{4+} to Pu^{3+} [133–136]. U^{3+} is most of the time not considered. This is why the concentration of Pu^{3+} cations is proportional to the deviation from stoichiometry x (see Table 3.4). Therefore, in order for the oxygen vacancies to be compensated by the Pu atoms, there should be enough Pu^{4+} cations. That is, **the following condition should be met**: $\boldsymbol{x < y/2}$, where y is the plutonium content (*i. e.* $y = [Pu^{4+}] + [Pu^{3+}]$).

Figure 3.5 shows the variation of both Γ and ϵ with deviation from stoichiometry, temperature and plutonium content. The parameter ε is more often considered as empirical (fitted to experimental data) because of many assumptions to derive its expression (*i. e.* $\frac{K_i}{K} \approx 1$ and $\frac{G_i - \overline{G_{sub}}}{\overline{G_{sub}}} \approx 0$). Duriez *et al.* [4] fitted this parameter to thermal conductivity experimental data, obtaining $\varepsilon = 25.85$. This value is consistent with the range $[23 - 25]$ (see Figure 3.5) obtained in this work. This highlights the adequate use of Equation 3.18 to calculate ϵ.

The scattering cross section Γ varies with both x and y. Its temperature dependency is slight. More commentary on those variations will be done in the next section, where we compute the extrinsic thermal resistivity.

3.2.3.5 Computation of extrinsic thermal resistivity

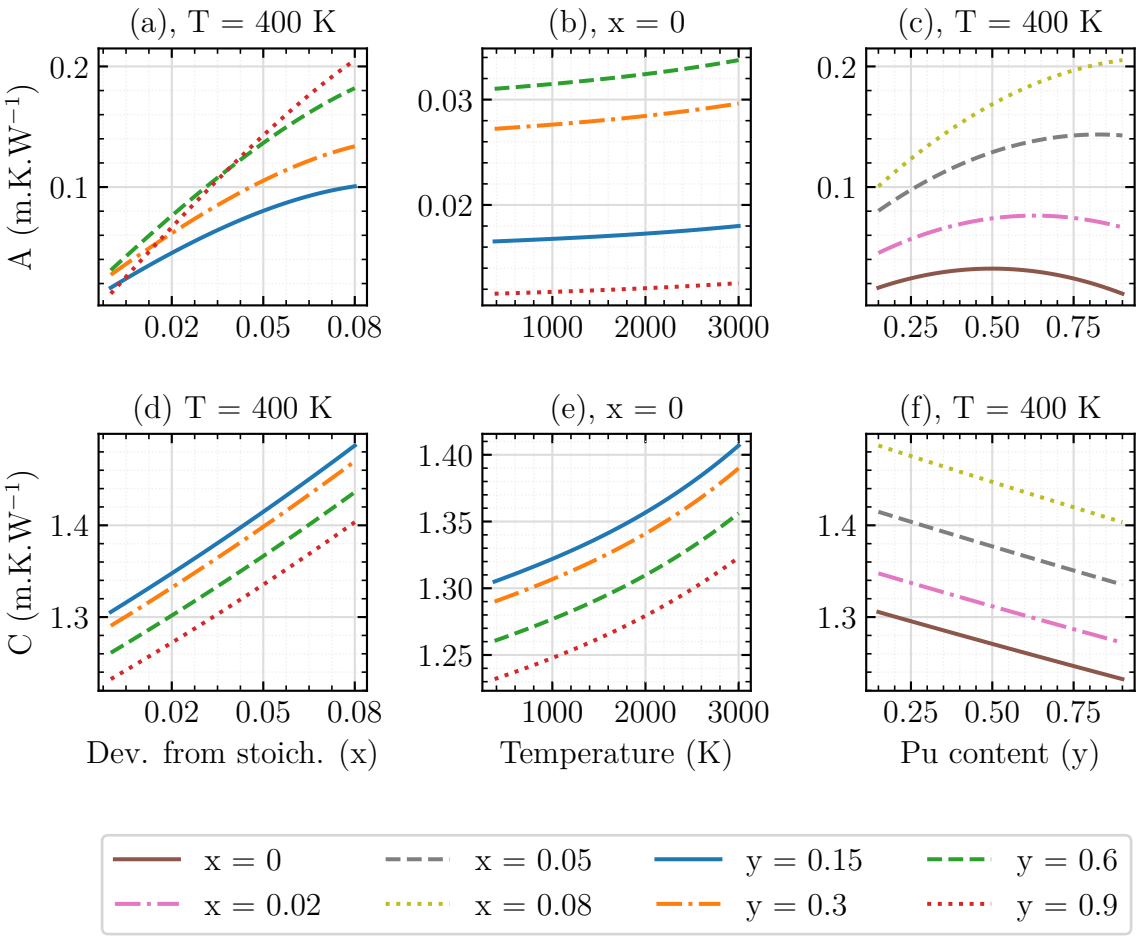

Figure 3.6: Predicted variation (in this work) of extrinsic thermal resistivity A and the C parameter in $A = C\Gamma$, with deviation from stoichiometry (a, d), temperature (b, e) and plutonium content (c, f), for different plutonium contents (a,b,d,e) and deviations from stoichiometry (c,f).

Using Equations 3.15 and 3.16 to calculate Γ, Equation 3.10 for θ_D and 3.11 for $\overline{v_p}$, the computation of extrinsic thermal resistivity is performed using Equation 3.8, recalled here:

$$A = C\Gamma = \frac{\pi^2 a^3 \theta_D}{12(3-x)\overline{v_p}^2 h}\Gamma$$

As shown in Figure 3.6 (a), A varies with deviation from stoichiometry and plutonium content. Those dependencies seem to be driven by the scattering cross section Γ, which exhibits the same variations with x and y (see Figure 3.5). Therefore, Γ seems to be **driving parameter, determining the effect of stoichiometry and plutonium content on**

thermal resistivity. Even though other parameters (*i. e.* θ_D, $\overline{v_p}$ and a) are also x and y dependent, they do not seem to impact the variations of A with x and y.

3.2.3.6 Oxygen content dependency

Oxygen deficiency contributes to increase thermal resistivity.

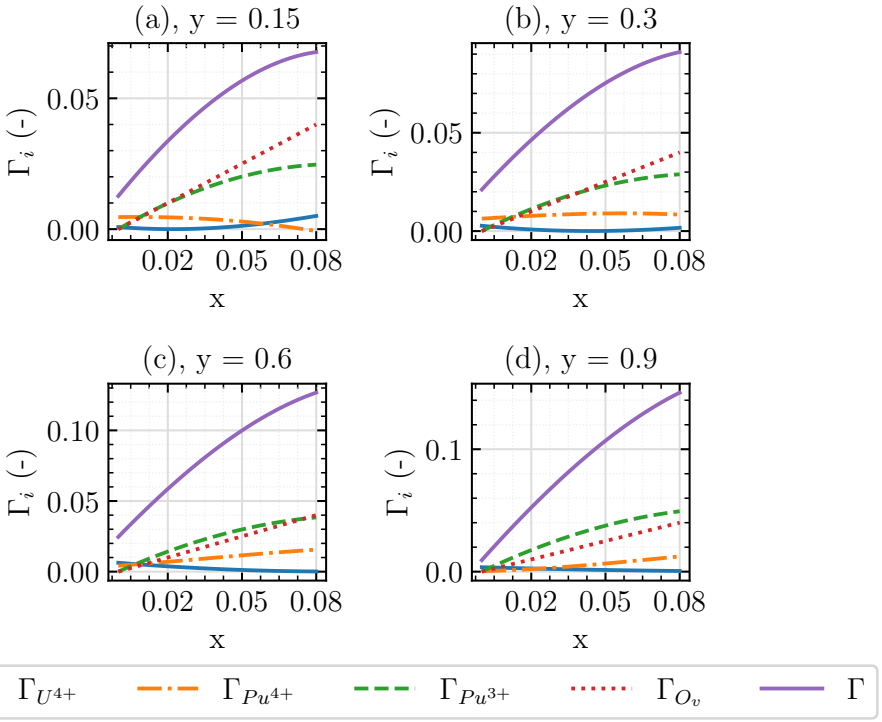

Figure 3.7: Predicted variation (in this work) with deviation from stoichiometry x of the individual contributions Γ_i to the total scattering cross section Γ, evaluated at four different plutonium contents.

As shown in Figure 3.7, the contribution from oxygen vacancies Γ_{O_v} increases with x (as expected). However, the increase of thermal resistivity with x is not only due to oxygen vacancies, but also due to Pu^{3+} cations, the fractional occupancy of which is equal to $f_{Pu^{3+}} = 2x$. The oxygen content effect on thermal resistivity is thus not only driven by the scattering strength of the oxygen vacancy itself (*i. e.* Γ_{O_v}), but also by the presence of Pu^{3+} cations. The latter contribute to increase thermal resistivity with oxygen deficiency more than the oxygen vacancies themselves, if plutonium content is high enough (*i. e.* $y > 0.5$). That is, $\Gamma_{Pu^{3+}}(x) > \Gamma_{O_v}(x)$.
Indeed, $\Gamma_{Pu^{3+}}$ increases with plutonium content. This is due to the radius difference of the Pu^{3+} cations, with respect to the (U, Pu) sub-lattice $\frac{r_{Pu^{3+}} - \overline{r_{sub}}}{\overline{r_{sub}}}$, which increases from 10 % at $y = 0.15$ to 14 % at $y = 0.90$.
Plutonium content thus amplifies the effect of stoichiometry.

3.2.3.7 *Plutonium content dependency*

At $x = 0$, plutonium content does not seem to impact thermal resistivity (see Figure 3.6). As

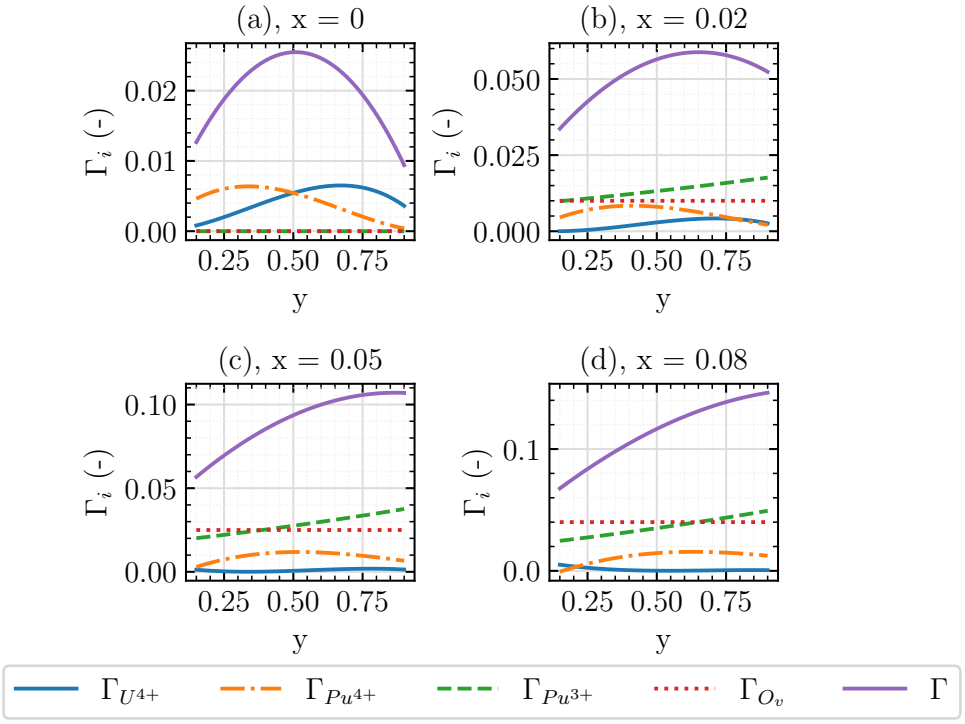

Figure 3.8: Predicted variation (in this work) with plutonium content of the individual contributions Γ_i to total scattering cross section Γ, evaluated at four different deviations from stoichiometry x.

shown in Figure 3.8, at $x = 0$, the scattering cross section Γ is mostly due to either $\Gamma_{Pu^{4+}}$ or $\Gamma_{U^{4+}}$.
That is, the plutonium content effect on thermal resistivity is due to the substituting Pu^{4+} cations (into UO_2) and U^{4+} cations (into PuO_2). Pu^{4+} and U^{4+} are however weak scattering centers, due to the low ionic radius difference between Pu^{4+} or U^{4+} and the (U, Pu) sub-lattice: only $\frac{r_{Pu^{4+}} - \overline{r_{sub}}}{\overline{r_{sub}}} = 3\%$ and $\frac{r_{U^{4+}} - \overline{r_{sub}}}{\overline{r_{sub}}} = 0.6\%$ at $y = 0.15$.
Adding foreign Pu atoms into UO_2 thus will only slightly affect thermal resistivity at $x = 0$. The maximum of thermal resistivity A (*i. e.* minimum of thermal conductivity) is obtained for $y = 0.5$.

Increasing x increases the number of Pu^{3+} cations (*i. e.* $f_{Pu^{3+}} = 2x$). As shown in Figure 3.8, the plutonium content dependency at high deviations from stoichiometry (*i. e.* $x > 0.04$) is rather driven by $\Gamma_{Pu^{3+}}$ than by $\Gamma_{Pu^{4+}}$ or $\Gamma_{U^{4+}}$. That is, the plutonium content effect on thermal resistivity when $x > 0.04$, is not explained by the scattering strength of the Pu^{4+} cations, but rather by that of Pu^{3+}, created due to deviation from stoichiometry.
Contrary to the variation of $\Gamma_{Pu^{4+}}$ with y at $x = 0$, attaining a maximum at $y = 0.5$, the $\Gamma_{Pu^{3+}}(y)$ variation is rather monotone with y.
Deviation from stoichiometry thus modifies the effect of plutonium content on thermal resistivity.

3.2.4 Modeling of intrinsic thermal resistivity

To model the effect of U-processes on thermal resistivity, and thus compute the BT term in $1/(A+BT)$, we use Slack's model [120]:

$$\boxed{BT = \frac{\gamma_\infty^2 n_a^{2/3}}{B^* \overline{M} \theta_D^3 \overline{V_a}^{1/3}} \cdot T} \tag{3.23}$$

where:

- BT : intrinsic thermal resistivity ($\mathrm{m\,K\,W^{-1}}$)
- γ_∞ : high-temperature Gruneisen parameter (see Equation 3.14)
- θ_D : Debye temperature (see Equation 3.10) (K)
- $\overline{M}$: mean atomic mass of the compound (here, in $\mathrm{g\,mol^{-1}}$): $\frac{(1-y)M_U + yM_{Pu} + (2-x)M_O}{3}$
- $\overline{V_a}$: mean atomic volume (here, in $\mathrm{Å}^3$): $\frac{(a \cdot 10^{10})^3}{4(3-x)}$, for a see Equation C.8 in Annex C.3
- n_a : number of atoms per unit cell : $4(3-x)$

where: B^* was first considered as a constant in Leibfried and Schlomann's work [137]: $B^* = 5.72 \times 10^{-6}$. Julian [125] reported an error in their value and proposed another value for B^*:

$$B^* = \frac{2.43.10^{-6}}{1 - \frac{0.514}{\gamma_\infty} + \frac{0.228}{\gamma_\infty^2}} \tag{3.24}$$

Slack [138] used $\gamma_\infty = 2$ in this expression and proposed: $B^* = 3.04 \times 10^{-6}$. Equation 3.23 is based on the generalized expression, firstly derived by Leibfried and Schlomann [137] and later developed by Julian [125]:

$$BT = \frac{\gamma_\infty^2}{B^* \overline{M} \theta_{D,ac}^3 \overline{V_a}^{1/3}} \cdot T \tag{3.25}$$

where $\theta_{D,ac}$ is the Debye temperature of acoustic phonon modes.

This expression, as pointed out by Slack, only holds for systems with 1 atom per unit cell: $n_a = 1$. To extend its validity to systems with more than one atom, Slack added a $n_a^{1/3}$ term and modified Julian's equation, which becomes.

$$BT = \frac{\gamma_\infty^2}{B^* \overline{M} \theta_{D,ac}^3 \overline{V_a}^{1/3} n_a^{1/3}} \cdot T \tag{3.26}$$

Slack pointed out another difficulty in the use of Equation 3.25 - computing $\theta_{D,ac}$.
To compute a property, relative to a specific phonon mode (here the acoustic), knowledge on the phonons spectra (*i. e.* dispersion relations) is required. The latter can be obtained either experimentally by inelastic phonons scattering techniques [131] or by calculations on the atomic scale by ab-initio (DFT) or EP (empirical potentials) techniques (Molecular Dynamics) [113]. For MOX fuel, no experimental data is available on the dispersion relations of phonons. The latter have been calculated by simulations on the atomic scale (DFT + U/BTE and EP/BTE techniques) in Njifon *et al.*'s work [113]. However, as no experimental data has been provided

do confirm the calculated results, Njifon *et al.*'s results were not used to calculate $\theta_{D,ac}$.
Slack [120] mentioned the difficulty in calculating the Debye temperature of the acoustic modes from phonon dispersion relations, and instead derived a simple relation between θ_D (the mean Debye temperature of all phonon modes: see Equation 3.10) and $\theta_{D,ac}$, based on Anderson's work [139]:

$$\theta_{D,ac} = \frac{\theta_D}{n_a^{1/3}} \tag{3.27}$$

where n_a is the number of atoms per unit cell.
Inserting Equation 3.27 into 3.26, one obtains Slack's model - Equation 3.23.

Computation of intrinsic thermal resistivity

Using Equation 3.10 for θ_D, C.8 for a (see Annex C.3), 3.14 for γ (to compute $\gamma_\infty = \gamma(T = \theta_D)$), one can compute intrinsic thermal resistivity BT, using Equation 3.23.

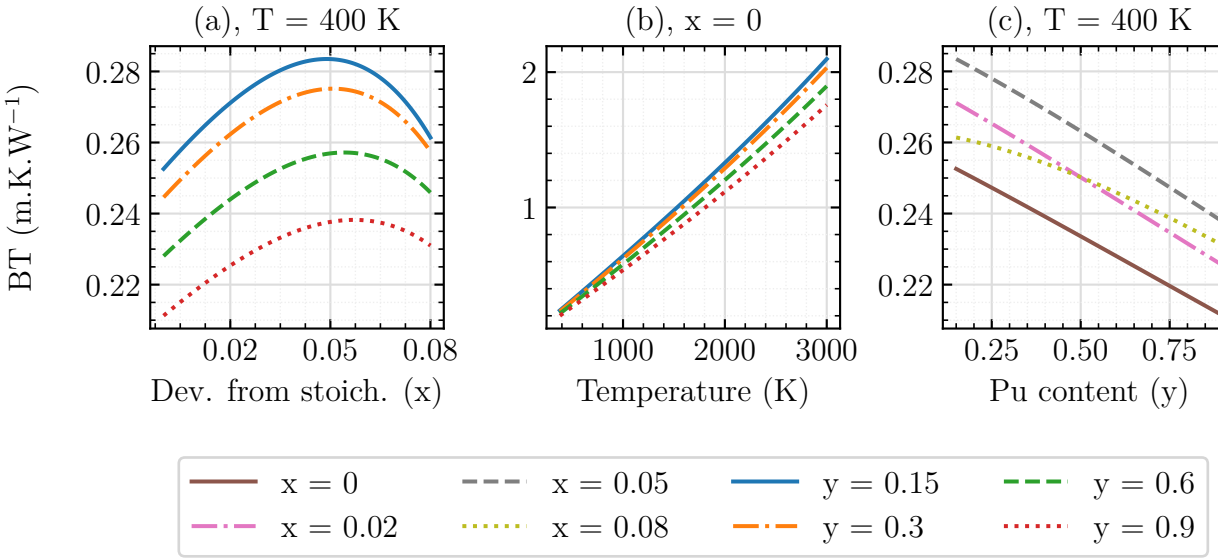

Figure 3.9: Predicted variation (in this work) of intrinsic thermal resistivity BT with (a): deviation from stoichiometry, (b): temperature and (c): plutonium content.

As shown in Figure 3.9, the effect of x and y on intrinsic thermal resistivity BT is negligible to that of temperature. In the expression of the intrinsic thermal resistivity BT, there is no parameter, which explicitly characterizes the effect of x and y, unlike the A term, which explicitly describes those effects by the scattering cross section Γ.

3.2.5 Computation of the phonon contribution to thermal conductivity

In the previous sections, both A and BT terms were computed separately and their x and y dependency were studied. To observe which term is responsible for most of the x and y dependency of the total thermal resistivity $A + BT$, we compared A and BT.

3.2.5.1 *Relative importance of A and BT on total thermal resistivity*

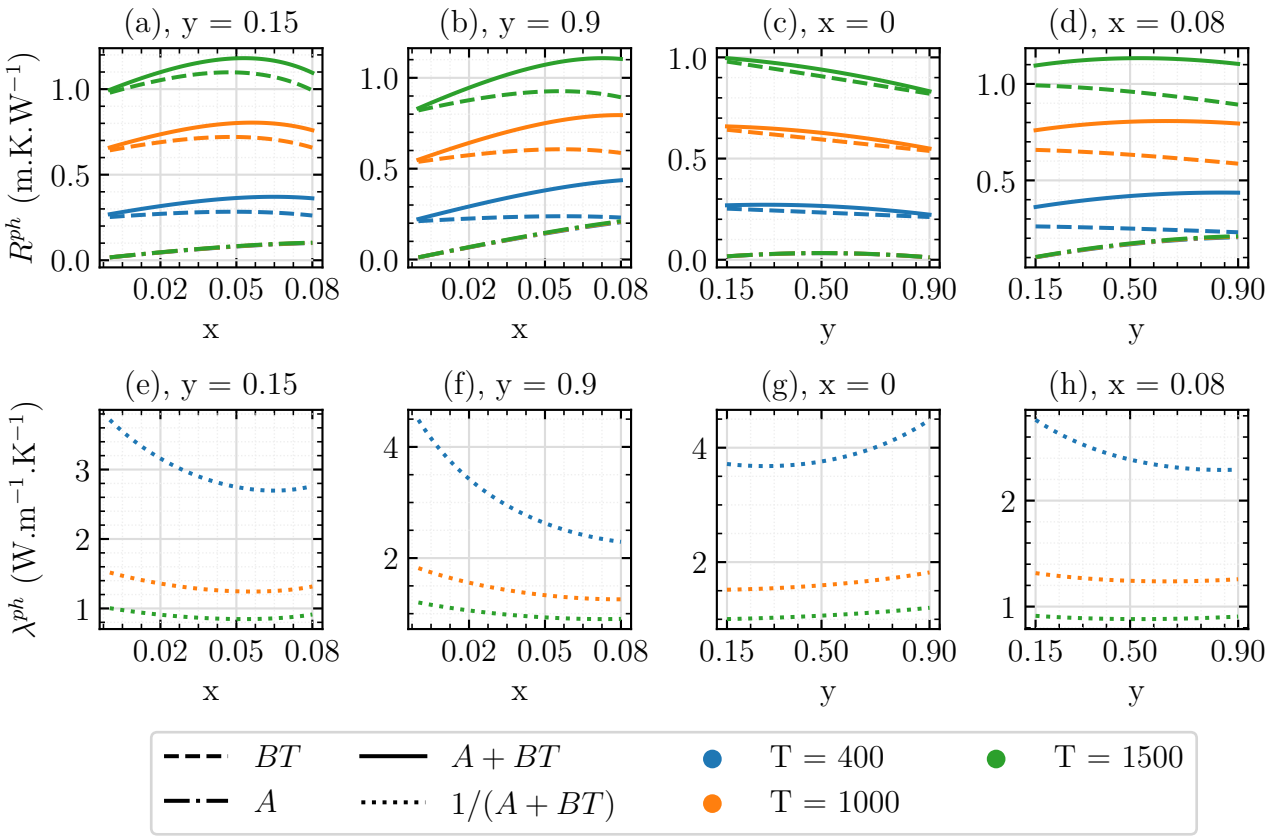

Figure 3.10: Predicted variations (in this work) of both thermal resistivity R^{ph} and conductivity λ^{ph} with deviation from stoichiometry x (a, b, e, f) and plutonium content y (c, d, g, h).

As shown in Figure 3.10, the intrinsic thermal resistivity BT **prevails over the extrinsic thermal resistivity** A for all x, y and T ranges studied here.
That is, the effect of phonon-phonon interactions on thermal resistivity is greater than that of phonon-impurity ones, whatever the amount of impurity in the system (*i. e.* regardless of x and y) and temperature.
This observation confirms some literature studies on thermal conductivity of solids [120, 125, 138], in which the phonon-impurity A term was neglected and only phonon-phonon term BT was considered. Slack *et al.* [120] for example validated thermal conductivity experimental data of more than 60 solids by considering only the BT term.
The A term's variations with x and y are however more important than those of BT. As shown in Figure 3.10 (b) and (d), even though $BT > A$, the variations of the total thermal resistivity $A + BT$ with x and y mostly follow those of the A term. Neglecting the latter could thus lead to an underestimation of the effect of oxygen and plutonium content.

Now that we have compared intrinsic and extrinsic thermal resistivity, we will compare the relative effects of plutonium and oxygen content on total thermal resistivity.

3.2.5.2 *Sensitivity analysis on the chemical composition*

To visualize the relative importance of the chemical composition of MOX on thermal conductivity, we will perform a "OAT" (one-at-a-time) sensitivity analysis [140, 141]. The latter consists of observing the effect of one particular model parameter, denoted β_i, on the model output, while all other model parameters are fixed to nominal values. The tool, used to perform this type of analysis is called the sensitivity coefficient, denoted X_i:

$$X_i = \frac{\partial f(\boldsymbol{\beta})}{\partial \beta_i} \tag{3.28}$$

where $f(\boldsymbol{\beta})$ is the model, $\boldsymbol{\beta}$ the parameters vector $\boldsymbol{\beta} =< \beta_1, ..., \beta_n >^{\mathrm{T}}$ and β_i the particular parameter, the sensitivity coefficient of which is calculated. Most of the time, the model parameters are not expressed in the same units. To compare their sensitivity coefficients, one thus uses the reduced sensitivity coefficients:

$$X_i^* = \beta_i \frac{\partial f(\boldsymbol{\beta})}{\partial \beta_i} = \frac{\partial f(\boldsymbol{\beta})}{\frac{\partial \beta_i}{\beta_i}} \tag{3.29}$$

which measure the difference in model output ∂f, due to a relative difference in the model parameter : $\frac{\partial \beta_i}{\beta_i}$.
The reduced sensitivity coefficients of λ^{ph}, with respect to x and y are compared in Figure 3.11.

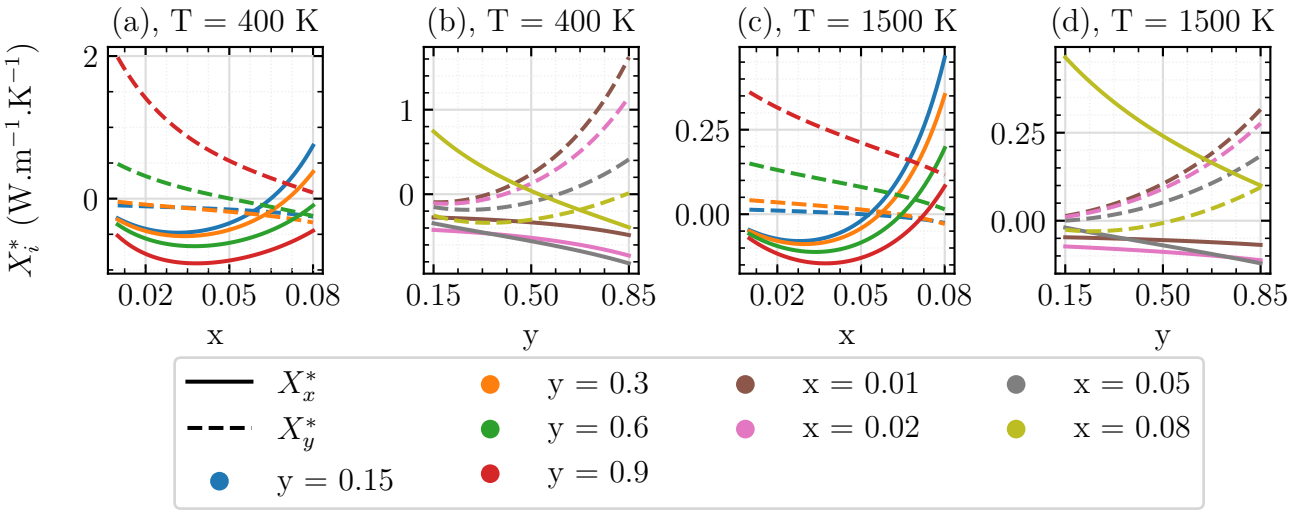

Figure 3.11: Variation of the reduced sensitivity coefficients X_i^* of x (solid lines) and y (dashed lines) with stoichiometry (a, c) and with plutonium content (b, d).

The following observations can be made:

1. The effect of plutonium gets amplified with the increase in plutonium content.
2. The effect of stoichiometry get amplified with the increase in deviation from stoichiometry.
3. The effect of plutonium content is higher than that of deviation from stoichiometry, when plutonium content is high. That is, at $y = 0.9$, $|X^*_{\lambda^{ph}}(y)| \gg |X^*_{\lambda^{ph}}(x)|$.

4. The effect of oxygen content is higher than that of plutonium, when plutonium content is relatively low (*i. e.* here $y < 0.3$). That is, at $y < 0.3$, $|X^*_{\lambda^{ph}}(x)| \gg |X^*_{\lambda^{ph}}(y)|$.

3.2.5.3 Sensitivity analysis on the model parameters

Sensitivity analysis was also performed on the model parameters. Such analysis is of crucial importance, when the model involves parameters, **deduced from measured properties**. For example, in this work, to calculate Debye temperature from Equation 3.10, we use empirical correlations (*i. e.* deduced from experimental data) for the lattice parameter a and the sound velocity in the medium V_s. Indeed, measurements can contain uncertainties, of various types, depending on multiple factors: experimental data set, chemical composition and microstructure changes during measurements *etc.* Performing sensitivity analysis on the model parameters allows to detect the model driving parameters- those, which induce the highest variations in model predictions. Those parameters need to be determined with the highest precision to reduce model uncertainties.

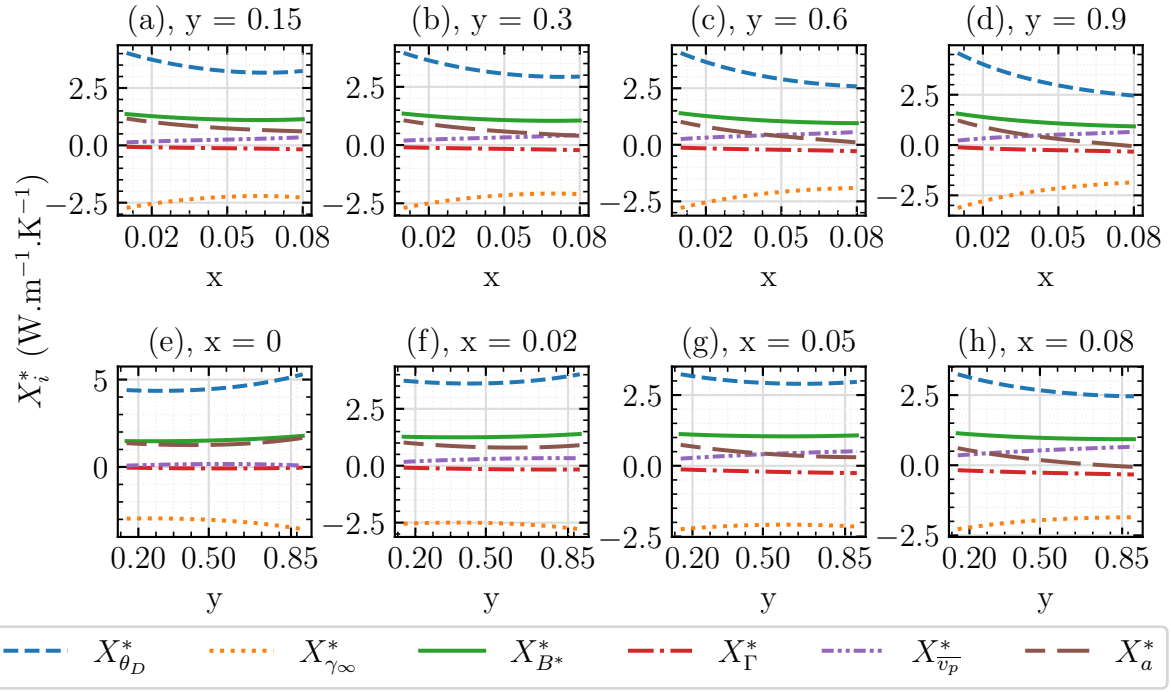

Figure 3.12: Variation of the reduced sensitivity coefficients X^*_i of the phonon model parameters with stoichiometry (a, b, c, d) and plutonium content (e, f, g, h) at $T = 1000$ K

As shown in Figure 3.12, **the driving model parameters are $\boldsymbol{\theta_D}$** and $\boldsymbol{\gamma_\infty}$, regardless of the chemical composition.
The Debye temperature θ_D was deduced from lattice parameter a (see Annex C.3), and sound velocity in the medium V_s (see Annex C.1).
The Gruneisen parameter γ_∞ was deduced from lattice parameter a, bulk modulus K_T (see Annex C.4), thermal expansion α (see Annex C.2) and heat capacity C_v (see Annex C.5).

To deduce which measured property (a, K_T, V_l, V_t, C_v or α) induce the highest variations (and thus uncertainties) in θ_D and γ_∞, we calculated the reduced sensitivity coefficients of those properties on θ_D and γ.
As shown in Figure 3.13, the property, which has **the lowest impact on θ_D is the longitudinal component of the sound velocity** V_l (see Equation C.2 in Annex C.1). The main uncertainty in Debye temperature originates from the lattice parameter a and the transverse component of the sound velocity V_t which have equal sensitivity coefficients.
As for the Gruneisen parameter, the lattice parameter **alone seems to induce twice more variations** in γ than α, K_T or C_v. The latter however do not have null sensitivity coefficients, which signify that contrary to θ_D, which had one property with almost null sensitivity coefficient (V_l), **Gruneisen parameter is sensitive to all of the measured properties, from which it is deduced.**

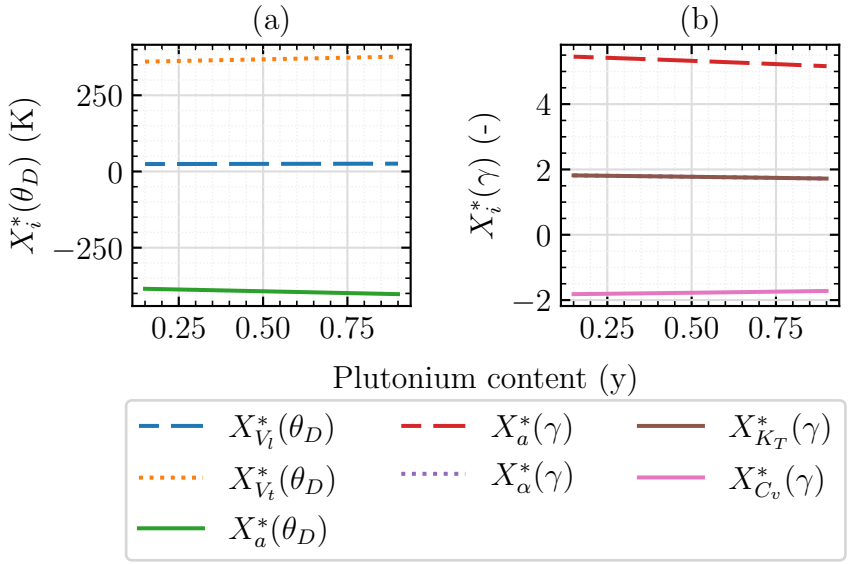

Figure 3.13: Variation with plutonium content, at $x = 0$, and $T = 1000$ K of the reduced sensitivity coefficients of the measured properties in the expression for (a): Debye temperature $X_i^*(\theta_D)$ and (b): Gruneisen parameter $X_i^*(\gamma)$.

3.2.6 Conclusion on the phonon contribution to thermal conductivity

To compute the phonon contribution to thermal conductivity, the semi-empirical temperature-variation $\lambda^{ph} = 1/(A + BT)$ was used.
To calculate A (extrinsic thermal resistivity) and BT (intrinsic thermal resistivity), the theoretical models of Ambegaokar [124] and Slack *et al.* [120] were used respectively. The latter were chosen for their low computational cost and their capacity of predicting the effect of plutonium and oxygen content.
Analysis of the magnitude of both extrinsic and intrinsic thermal resistivity has shown that, regardless of the impurity content, thermal resistivity is mainly due to phonon-phonon rather than to phonon-impurity interactions. However, the effect of oxygen and plutonium content

on thermal resistivity principally originates from the phonon-impurity term (*i. e.* A in $\frac{1}{A+BT}$). The latter could thus not be neglected, as do some authors [120].
Two important conclusions were made in this section, highlighting the existence of correlated plutonium-oxygen content effects:

1. Increasing deviation from stoichiometry, modifies the effect of plutonium content.
2. Plutonium content amplifies the effect of deviation from stoichiometry x.

Those correlated effects were explained by extrinsically created Pu^{3+} cations, when deviation from stoichiometry x becomes important.
Sensitivity analysis on the model parameters (see Section 3.2.5.3) allowed us to conclude that Debye temperature and Gruneisen parameter are the driving model parameters. The latter were calculated, using measured material properties. To reduce uncertainties in θ_D and γ, the following material properties should be measured with low uncertainties: lattice parameter a, transverse component of sound velocity V_t, thermal expansion α, isothermal bulk modulus K_T and heat capacity C_v.

3.3 Electron contribution to thermal conductivity

3.3.1 Introduction to heat transfer by electrons

Three mechanisms drive the heat transfer by electrons:

1. **Creation** of charge carriers
2. **Migration** of charge carriers through the solid
3. **Recombination** of charge carriers

A charge carrier can be a free electron (an electron, which no longer pertains to any nucleus), a free hole (a missing electron) or even the association of an electron (or a hole) with the crystal lattice distortion (*i. e.* a (quasi)particle called "polaron"). We distinguish three type of materials, depending on their charge carriers' number:

1. **Insulators**: no available charge carriers at low, nor at high temperature
2. **Semi-conductors and Mott insulators**: charge carriers are created with increasing temperature.
3. **Metals**: charge carriers are available at both low and high temperature.

The main parameter, determining the solids behavior with respect to the number of available charge carriers is the band gap energy H (see Figure 3.14). The latter separates the valence electrons (low energy states) from the conducting electrons (high-energy states).
In metallic materials, conducting electrons exist even at low temperatures.
In insulators, due to the important band-gap, electrons stay in the valence band.
In semi-conductors or Mott insulators, electrons overcome the band-gap if enough thermal energy is supplied. While transferring to the conduction band, the electrons leave "holes" in the valence band.

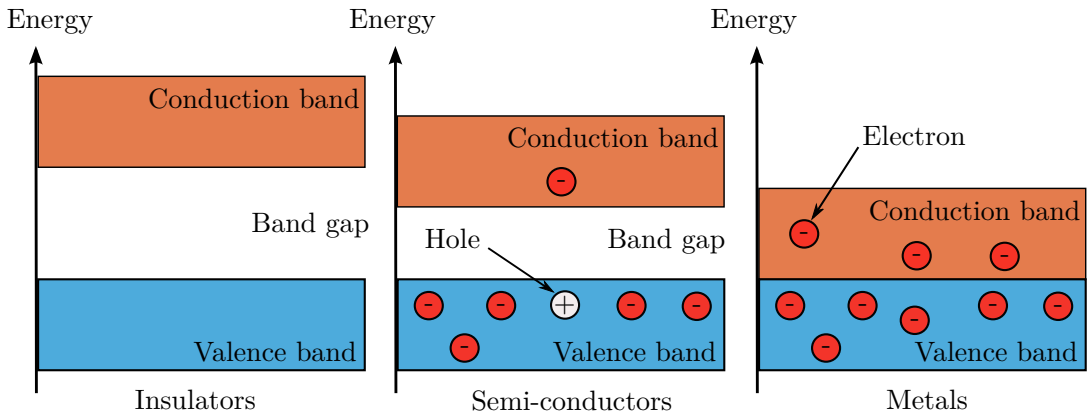

Figure 3.14: Illustration of the valence and conduction bands in metals, semi-conductors, insulators and Mott-insulators

Once created, charge carriers diffuse or "migrate" through the solid.
Charge carriers can either diffuse as "free" or "trapped" particles (see Figure 3.16).
In the former case, the carrier moves by tunneling, whereas in the latter case, by hopping. The free or trapped character of the electron is given by the band-width ΔW. The latter characterizes the electron orbitals' overlap. The higher the overlap, the broader the bands.
Carriers in broad bands have high kinetic energy. The latter thus induces low interactions with surrounding atoms, thus leaving the carrier as a free particle.
Because of their low overlapping capacity, contracted electron orbitals, like 5f orbitals in UO_2 or $U_{1-y}Pu_yO_{2-x}$ systems would form narrow bands. Carriers in narrow bands have low kinetic energy, which induces strong interactions with the surrounding lattice atoms.
Those electron-lattice interactions create lattice polarization and distortion (see Figure 3.15). The latter lowers the system's potential energy in the vicinity of the specific atomic site by a

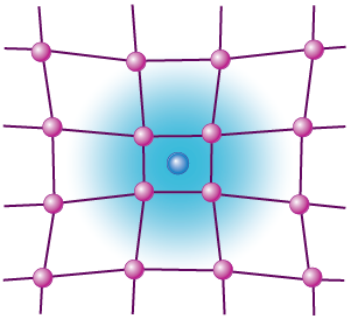

Figure 3.15: Illustration of a crystal lattice distortion induced by the presence of a negatively charged particle in the vicinity of a particular atomic site, from [142]

quantity E_p as opposed to that without crystal distortion (see Figure 3.16), thus producing a deep potential well, in which the charge carrier is trapped.

To escape from its trapped state, the charge is assisted by the surrounding atoms. The latter arrange themselves in specific configurations called "coincidence configurations (CC)". These lower the potential well, thus allowing the charge carrier to migrate. The migration is possible

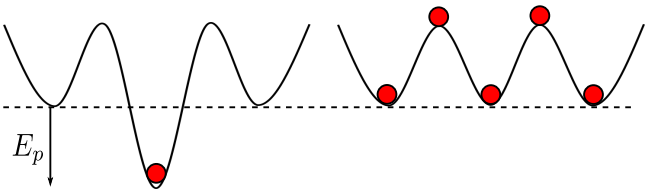

(a) Trapped electron (b) Free electron

Figure 3.16: Potential wells, felt by a free non-interacting charged particle (b) and by a trapped charge particle (b)

as long as the charge carrier overcomes the energy barrier called the "migration energy" E_m. The charge migrates together with its self-induced distortion. This particular association of a charge carrier and its self-induced crystal distortion is called a polaron.

The third and final process in heat transfer by electrons is charge carrier recombination. The latter characterizes an electron, which comes back to the valence band. During this process, the electron returns all the energy, stored during the creation and migration process, in the form of thermal energy.
Figure 3.17 illustrates the three processes in heat transfer by electrons in MOX: creation, migration and recombination.

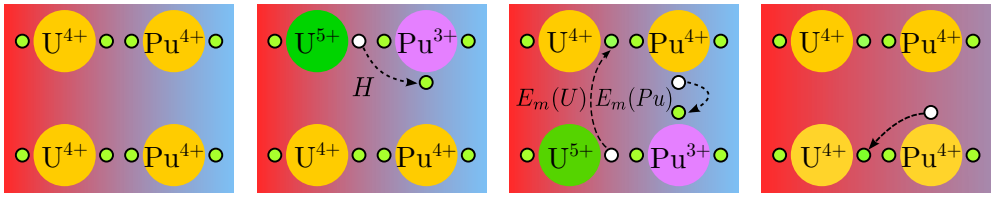

(a) Ground state (b) Creation (c) Migration (d) Recombination

Figure 3.17: Illustrative scheme, describing the three main processes in heat transfer by electrons, starting from MOX in its ground state (a), to creating charge carriers (b), then migrating (c) and finally recombining (d). The Pu^{3+} and U^{5+} polarons are in green and purple respectively. The "hole" is represented by a white circle and the electron by a green circle.

3.3.2 Modeling: state of the art

3.3.2.1 Semi-empirical approaches

Most models for the electronic contribution to thermal conductivity in actinide systems are based on the following semi-empirical equation:

$$\lambda^{el} = \frac{C}{T^n} e^{-\frac{E_a}{kT}} \tag{3.30}$$

where n can take several values ($n = -1, 2, 5/2$), depending on the authors, while C and E_a are fitted by the least-squares method using thermal conductivity experimental data. In this approach, the physical meaning of the "best-fit" parameters is not systematically investigated.

The choice of n is not justified. Table 3.5 summarizes n, C and E_a coefficients, reported for MOX fuel [3–5, 33].

Author (year)	$\boldsymbol{n}$	$\boldsymbol{E_a}$ (eV)	$\boldsymbol{C}$ ($\mathrm{W\,K^{n-1}\,m^{-1}}$)
Bonnerot (1986) [5]	-1	1.22	$2.4 \cdot 10^{-3}$
Duriez *et al.* (2000) [4]	2	1.16	$1.82 \cdot 10^{9}$
Kato *et al.* (2012) [3]	5/2	1.31	$1.54 \cdot 10^{11}$
Magni *et al.* (2020) [33]	2	1.47	$5.27 \cdot 10^{9}$

Table 3.5: Empirical n, E_a and C coefficients in Equation 3.30, reported for MOX fuel, based on thermal conductivity experimental data.

3.3.2.2 Price's model

We recall that MOX fuel is a semi-conductor, as no electrons occupy the conduction band at low temperatures [113, 143, 144]. Other more fundamental approaches use Price's model for a classical semi-conductor [145, 146]:

$$\lambda^{el} = \left(\frac{k}{e}\right)^2 T \left\{ (r+2)\left(\sigma_e^{el} + \sigma_h^{el}\right) + \frac{\sigma_e^{el}\sigma_h^{el}}{\sigma_e^{el} + \sigma_h^{el}} \left(2(r+2) + \frac{H}{kT}\right)^2 \right\} \tag{3.31}$$

where:

λ^{el} : electronic contribution to thermal conductivity ($\mathrm{W\,m^{-1}\,K^{-1}}$)
k : Boltzmann constant ($\mathrm{J\,K^{-1}}$)
e : elementary charge (C)
T : temperature (K)
σ_e^{el} : electrical conductivity due to electron diffusion ($\mathrm{S\,m^{-1}}$)
σ_h^{el} : electrical conductivity due to hole diffusion ($\mathrm{S\,m^{-1}}$)
H : band-gap (*i. e.* charge carrier creation energy) (J)

The r term represents the exponent of the energy in the expression for the carrier mean free path, whose value depends on the particular scattering mechanism (*i. e.* $r = 0$ for acoustic phonon scattering and $r = 1$ for optical phonon scattering) [147].
In the introduction, we saw that electron and hole diffusion, followed by their recombination are key elements in heat transfer.
Equation 3.31 can thus be re-written to clearly distinguish each contribution to heat transfer:

$$\lambda^{el} = \lambda_e^{el} + \lambda_h^{el} + \lambda_{amb}^{el} \tag{3.32}$$

where λ_e^{el} and λ_h^{el} are the elementary (Wiedemann-Franz) [148] contributions from electrons and holes respectively, written as follows:

$$\lambda_{e,h}^{el} = \left(\frac{k}{e}\right)^2 T(r+2)\sigma_{e,h}^{el} \tag{3.33}$$

Those reflect the **elementary migration processes** of electrons and holes.
λ^{el}_{amb} is the so-called ambipolar contribution, characterizing the **electron-hole recombination** [145–147]:

$$\lambda^{el}_{amb} = \left(\frac{k}{e}\right)^2 T \frac{\sigma^{el}_e \sigma^{el}_h}{\sigma^{el}_e + \sigma^{el}_h} \left(2(r+2) + \frac{H}{kT}\right)^2 \tag{3.34}$$

The $(r+2)$ term, represents the kinetic energy gain effect, during both migration and recombination.
Equation 3.31 is however a quite general expression for a normal broad-band semiconductor, thus treating the charge carriers as free moving charges. In the introduction, we saw that MOX fuel has contracted 5f orbitals, inducing high electron-lattice interactions. The electron does not migrate as a free particle, but rather as a polaron (trapped electron).

When considering polarons, the individual contributions of holes and electrons are set to zero (*i. e.* $\lambda_{e,h} = 0$ by setting $r + 2 = 0$), due to the absence of kinetic energy gain [147]. Indeed, only free particles would gain kinetic energy through their tunneling process in the conduction band.
When considering a trapped particle (polaron), heat transfer is solely driven by the ambipolar contribution, which by setting $r + 2 = 0$ is expressed as follows:

$$\boxed{\lambda^{el} = \lambda^{el}_{amb} = \left(\frac{k}{e}\right)^2 T \frac{\sigma^{el}_e \sigma^{el}_h}{\sigma^{el}_e + \sigma^{el}_h} \left(\frac{H}{kT}\right)^2} \tag{3.35}$$

3.3.2.3 Approach, used in this work

Equation 3.31 or 3.35 (depending whether the charger carrier is considered as a free or a trapped particle) is systematically used to assess thermal conductivity due to electrons in UO_2 [139, 147, 149–152].
For MOX, no such fundamental evaluation of λ^{el} has been reported in the literature. Most models for MOX fuel are based on the semi-empirical equation 3.30. Due to few experimental data at high temperatures and at high plutonium contents, no oxygen nor plutonium content effect was reported for the coefficients C and E_a in Equation 3.30 (see Table 3.5).

To better understand the effect of plutonium and oxygen content on thermal conductivity due to electrons, in this work, we use Equation 3.35. To apply this model to MOX fuel, it is necessary to know the electrical conductivity. To model this quantity for MOX fuel, a modified Heikes and Ure [153] model for ternary $U_{1-y}Pu_yO_{2-x}$ systems will be proposed (see Section 3.3.4).
Before this, we will briefly introduce Heikes and Ure's model for binary systems.

3.3.3 Electrical conductivity model for binary systems

In this work, we assume that electrical conductivity of MOX fuels is solely due to electronic defects: polarons. Other point defects, such as Frenkel or Schottky pairs were not considered. Indeed, the contribution of the latter to electrical conductivity was proven to be negligible in

other actinide systems [150, 152, 154].

Heikes and Ure's model can take two different forms, depending on the hopping nature of the polarons: adiabatic or non-adiabatic:

$$\sigma_{ad}^{el} = \frac{4e^2c(1-c)v_{0,opt}}{akT}e^{-\frac{E_m}{kT}} \tag{3.36}$$

$$\sigma_{nad}^{el} = \frac{2e^2c(1-c)J_{ov}^2}{a\hbar(kT)^{3/2}}e^{-\frac{E_m}{kT}} \tag{3.37}$$

where:

σ^{el}	: electrical conductivity ($\mathrm{S\,m^{-1}}$)
c	: fraction of polarons (-)
$(1-c)$	: fraction of available sites for hopping (-)
$v_{0,opt}$	: vibration frequency of the optical phonons ($\mathrm{s^{-1}}$)
a	: lattice parameter (m)
E_m	: migration energy of the polaron (J)
J_{ov}	: overlap integral (J)

The adiabatic or non-adiabatic hopping nature of the polarons is driven by the electron transfer timescale, relative to the that of the coincidence configurations (CC).
If the electron transfers faster than the CC, the migration process is called adiabatic, whereas if the electron transfers slower than than the CC, the process is non-adiabatic.
For further details on the physical origin of Equations 3.36 and 3.37, the reader may refer to Annex E.

Application to MOX fuels

To choose the correct form of the electrical conductivity equation for MOX fuels, we can calculate the adiabacity criterion, which according to Firsov and Lang [155] is written as follows:

$$\eta_{ad} = \frac{J_{ov}^2}{hv_{0,opt}\sqrt{E_m kT}} \tag{3.38}$$

$\eta_{ad} \gg 1$ for adiabatic hopping and $\eta_{ad} \ll 1$ for non-adiabatic hopping.
To our knowledge, no analytical, nor simulation results have been reported for the parameters, needed to calculate the adiabacity criterion for MOX fuel.
To make a first estimation of this criterion, multiple J_{ov}, $v_{0,opt}$ and E_m values were tested.
Figure 3.18 shows the calculated adiabacity criterion η_{ad} for four different migration energies, in the range $J_{ov} \in [0.02 - 0.09]$ eV and $v_{0,opt} \in [0.8 - 1.9] \times 10^{13}$ $\mathrm{s^{-1}}$. Those ranges were chosen, based on DFT+U calculations on PuO_2 (for E_m and J_{ov}) and $U_{1-y}Pu_yO_{2-x}$ systems (for $v_{0,opt}$) : $J_{ov} = 0.02$ eV, $E_m = 0.08$ in PuO_2 [144] and $v_{0,opt} = 1.713 \times 10^{13}$ in $U_{1-y}Pu_yO_{2-x}$ [113].

Values smaller than 1 (*i. e.* $\eta_{ad} < 1$) are generally observed, signifying non-adiabatic hopping.
Geneste *et al.* [144] found a value of $\eta_{ad} = 0.27$ for the adiabacity criterion associated with the

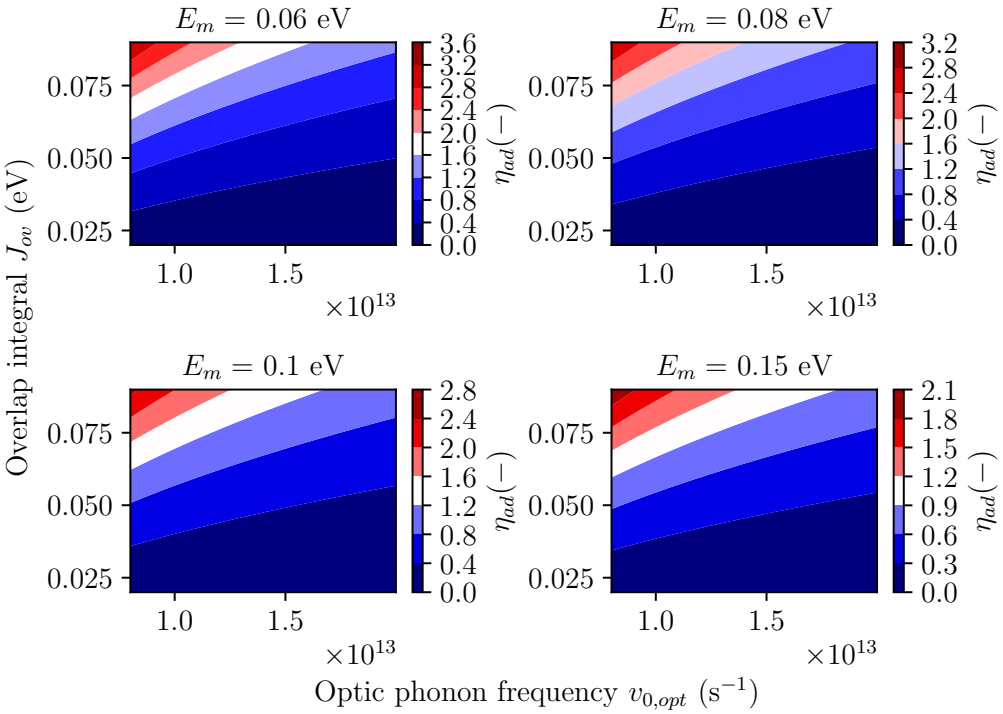

Figure 3.18: Adiabacity criterion calculated for four different migration energies and for values of J_{ov} ranging from 0.02 - 0.09 eV and $v_{0,opt}$ from 0.8×10^{13} to 1.9×10^{13} s^{-1}

Pu^{3+} polaron in pure PuO_2 system.
However, as reported by the authors, those values do not completely satisfy the adiabacity criterion, which needs to be much lower than 1 (*i. e.* $\eta_{ad} \ll 1$) in order to assume a non-adiabatic hopping.
Given the commentary, made by Geneste *et al.* and given the rather complex electrical conductivity model for a non-adiabatic hopping (*i. e.* involving the overlap integral J_{ov}), **in this work we make the assumption of adiabatic hopping**.

The electrical conductivity is therefore expressed as:

$$\sigma_{ad}^{el} = \frac{4e^2 c(1-c) v_{0,opt}}{akT} e^{-\frac{E_m}{kT}}$$

The *ad* subscript will be omitted from now on, for the sake of clarity.
We write $c = c_e + c_h$, to distinguish electrons e from holes h.

$$\sigma^{el} = \sigma_e^{el} + \sigma_h^{el} \tag{3.39}$$

In MOX fuel, the electrons are associated with Pu^{3+} polarons, and the holes with U^{5+} polarons. The available sites for hopping $(1-c)$ are therefore associated with the Pu^{4+} and U^{4+} cations. The reader may refer to Annex F for more information on the electronic states of the cations in MOX fuel.

Replacing e and h by Pu^{3+} and U^{5+}, therefore gives:

$$\sigma_{Pu}^{el} = \frac{4e^2 c_{Pu^{3+}}(1 - c_{Pu^{3+}} - c_{U^{5+}})v_{0,opt}}{akT} e^{-\frac{E_m}{kT}} = \frac{4e^2 c_{Pu^{3+}}(c_{Pu^{4+}} + c_{U^{4+}})v_{0,opt}}{akT} e^{-\frac{E_m}{kT}} \tag{3.40}$$

$$\sigma_{U}^{el} = \frac{4e^2 c_{U^{5+}}(1 - c_{Pu^{3+}} - c_{U^{5+}})v_{0,opt}}{akT} e^{-\frac{E_m}{kT}} = \frac{4e^2 c_{U^{5+}}(c_{Pu^{4+}} + c_{U^{4+}})v_{0,opt}}{akT} e^{-\frac{E_m}{kT}} \tag{3.41}$$

As shown in those equations, after directly applying Heikes and Ure's equation to ternary systems, the only distinction between the Pu^{3+} and U^{5+} polarons comes from their atomic fractions $c_{Pu^{3+}}$ and $c_{U^{5+}}$.
Both polarons are assumed to migrate with the same energy E_m. This observation leads to the first step in the modification of Heikes and Ure's model for ternary systems. In the following section, the three key elements into the proposal of a new model will be discussed.

3.3.4 Modified Heikes and Ure model for ternary systems

3.3.4.1 Migration energies

No analytical expression, nor simulation data for the polarons' migration energies have been found in the literature for MOX.
However, DFT+U calculations showed that the Pu^{3+} polaron's migration energy in PuO_2 [144] is different from that of the U^{5+} polaron in UO_2 [private com.]. That is $E_m(Pu) = 0.08$ eV and $E_m(U) = 0.28$ eV.
Furthermore, in another study of the polarons in a ternary $Mn_xFe_{3-x}O_4$ system, different migration energies have been reported for the Mn and Fe polarons [156, 157].
In this work, we will thus assume different migration energies for both polarons in MOX fuel: $E_m(U) \neq E_m(Pu)$. Equations 3.40 and 3.41 thus become:

$$\sigma_{Pu}^{el} = \frac{4e^2 v_{0,opt}}{akT} c_{Pu^{3+}}(c_{Pu^{4+}} + c_{U^{4+}}) e^{-\frac{E_m(Pu)}{kT}} \tag{3.42}$$

$$\sigma_{U}^{el} = \frac{4e^2 v_{0,opt}}{akT} c_{U^{5+}}(c_{Pu^{4+}} + c_{U^{4+}}) e^{-\frac{E_m(U)}{kT}} \tag{3.43}$$

If we further develop those equations, we can re-write both contributions, as being composed of like-element and mixed-element polaron hopping:

$$\sigma_{Pu}^{el} = \sigma_{Pu-Pu}^{el} + \sigma_{Pu-U}^{el} = \frac{4e^2 v_{0,opt}}{akT} \left(c_{Pu^{3+}} c_{Pu^{4+}} e^{-\frac{E_m(Pu)}{kT}} + c_{Pu^{3+}} c_{U^{4+}} e^{-\frac{E_m(Pu)}{kT}} \right) \tag{3.44}$$

$$\sigma_{U}^{el} = \sigma_{U-U}^{el} + \sigma_{U-Pu}^{el} = \frac{4e^2 v_{0,opt}}{akT} \left(c_{U^{5+}} c_{U^{4+}} e^{-\frac{E_m(U)}{kT}} + c_{U^{5+}} c_{Pu^{4+}} e^{-\frac{E_m(U)}{kT}} \right) \tag{3.45}$$

The like-element hopping characterizes a polaron, associated with an atom of type A hopping to another atom of the same type. On the opposite, mixed-element hopping describes a polaron of type A hopping to another atom of type B.
Once again, no distinction is made between the migration energies associated with like-element

and mixed-element hopping. That is, the Pu^{3+} polaron must overcome the same migration barrier to hop to another Pu^{4+} atom (*i. e.* like-element) as to a U^{4+} atom (*i. e.* mixed-element).
In MOX fuels, to our knowledge, no information on the hopping nature of the polarons is available in the literature. However, in $Mn_xFe_{3-x}O_4$ systems, Bhargava *et al.* [156, 157] have reported a clear difference between migration energies, associated with like-element and mixed-element hopping. This information leads to the second step into the modification of Heikes and Ure's model.

3.3.4.2 Like-element and mixed-element hopping

In this section, we assume different migration energies associated with like-element and mixed-element hopping.
In a more general way, let us notate the electrical conductivity due to hopping of polaron of type A as σ_A, which can be represented by a term involving a like-element hopping σ^{el}_{A-A} and a mixed-element hopping σ^{el}_{A-B} :

$$\sigma^{el}_A = \sigma^{el}_{A-A} + \sigma^{el}_{A-B} = \frac{\sigma^{el}_{0,A-A}}{T} e^{-\frac{E_m(A-A)}{kT}} + \frac{\sigma^{el}_{0,A-B}}{T} e^{-\frac{E_m(A-B)}{kT}} \tag{3.46}$$

where both the like-element and the mixed-element terms are associated with their proper like-element and mixed-element pre-exponential terms $\sigma^{el}_{0,A-A}$, $\sigma^{el}_{0,A-B}$ and migration barriers $E_m(A-A)$ and $E_m(A-B)$.
If we write the same equations for a B-type polaron, we obtain:

$$\sigma^{el} = \sigma^{el}_A + \sigma^{el}_B = \sigma^{el}_{A-A} + \sigma^{el}_{A-B} + \sigma^{el}_{B-B} + \sigma^{el}_{B-A} \tag{3.47}$$

Which can be put into a more generalized form:

$$\sigma^{el} = \sigma^{el}_{mix} + \sigma^{el}_{like} = \sum_{\substack{i=A,B \\ j=A,B \\ i\neq j}} \sigma^{el}_{i-j} + \sum_{i=A,B} \sigma^{el}_{i-i} = \sum_{\substack{i=A,B \\ j=A,B \\ i\neq j}} \frac{\sigma^{el}_{0,i-j}}{T} e^{-\frac{E_m(i-j)}{kT}} + \sum_{i=A,B} \frac{\sigma^{el}_{0,i-i}}{T} e^{-\frac{E_m(i-i)}{kT}} \tag{3.48}$$

Applying this equation to MOX, we obtain:

$$\sigma^{el} = \sigma^{el}_{mix} + \sigma^{el}_{like} = \sigma^{el}_{Pu-U} + \sigma^{el}_{U-Pu} + \sigma^{el}_{Pu-Pu} + \sigma^{el}_{U-U} \tag{3.49}$$

Mixed-element migration of Pu^{3+} leads to U^{3+} cations, and that of U^{5+} to Pu^{5+} cations. Catlow and Pyper [143] showed that Pu^{5+} is not a stable ionic state in MOX fuel. A mixed-element Pu-U hopping therefore is not likely to occur in MOX fuel.
U^{3+} states can be created at higher temperatures, by allowing a cationic disproportionation reaction between uranium atoms: $2U^{4+} \rightarrow U^{5+} + U^{3+}$, which requires an important amount of thermal energy (*i. e.* $H = 2$ eV). However, no evidence for the existence of a U^{3+} state, due to the migration of a Pu^{3+} polaron to U^{4+} has been reported in the literature.
In this work, as a first approximation, we also omit the probability of a mixed-element U-Pu hopping.

With those assumptions, both Pu-U and U-Pu mixed-element components are set to zero, yielding:

$$\sigma^{el} = \sigma^{el}_{Pu-Pu} + \sigma^{el}_{U-U} = \frac{4e^2 v_{0,opt}}{akT}\left(c_{Pu^{3+}} c_{Pu^{4+}} e^{-\frac{E_m(Pu-Pu)}{kT}} + c_{U^{5+}} c_{U^{4+}} e^{-\frac{E_m(U-U)}{kT}}\right) \tag{3.50}$$

From now on, for more clarity in notations, $E_m(Pu-Pu)$ and $E_m(U-U)$ will be written as $E_m(Pu)$ and $E_m(U)$. The same follows for σ^{el}_{Pu-Pu} and σ^{el}_{U-U}, which will be replaced by σ^{el}_{Pu} and σ^{el}_{U} respectively.

Equation 3.50 involves the fractional occupancy products $c_{Pu^{3+}} c_{Pu^{4+}}$ and $c_{U^{5+}} c_{U^{4+}}$. Those terms characterize the probabilities of Pu^{4+} and U^{4+} being the first neighbors to Pu^{3+} and U^{5+} respectively, and are only valid for an ideal solid solution. To account for a possible deviation from the ideal solid solution, the so-called short-range order parameter $\alpha_{i,i}$ can be introduced:

$$\sigma^{el,reg} = \sigma^{el,reg}_{Pu} = \sigma^{el,reg}_{U} = (1-\alpha_{Pu,Pu})\sigma^{el,id}_{Pu} + (1-\alpha_{U,U})\sigma^{el,id}_{U} \tag{3.51}$$

where the *id* and *reg* superscripts refer to the ideal and the regular solution, respectively. The order parameters $\alpha_{U,U}$ and $\alpha_{Pu,Pu}$ translate the probability of finding U-U and Pu-Pu pairs as first neighbors.
For further details on the origin of Equation 3.51, the reader may refer to Annex G.
Even though the model requires $\alpha_{U,U}$ and $\alpha_{Pu,Pu}$, the measure of the deviation from the ideal solid solution can be obtained by calculating $\alpha_{U,Pu}$, translating the probability of the U-Pu pair.

3.3.4.3 Order parameter $\alpha_{U,Pu}$ in MOX fuel

The order parameter $\alpha_{U,Pu}$ can be calculated by the theoretical approach, derived by Swalin [158]:

$$\alpha_{U,Pu} = 2y(1-y)\frac{u + j(X) + g(T)}{RT} \tag{3.52}$$

where y is plutonium content, R the perfect gaz constant ($\mathrm{J\,mol^{-1}\,K^{-1}}$), T temperature (K) and $u + j(X) + g(T)$, functions, which depend on both:

1. the excess entropy of mixing $\Delta S^{xs}_m = \Delta S^{reg}_m - \Delta S^{id}_m$ (*i. e.* the entropy of mixing of an ideal solid solution ΔS^{id}_m subtracted to that of the real solid solution (*i. e.* the regular solid solution ΔS^{reg}_m)).
2. enthalpy of mixing ΔH_m

through the following equations:

$$\Delta S^{xs}_m \cong |\alpha_{U,Pu}| R\left[y \ln y + (1-y)\ln(1-y)\right] - \left\{\frac{\partial}{\partial T}\left[12y(1-y)(1-\alpha_{U,Pu})g(T)\right]\right\} \tag{3.53}$$

$$\Delta H_m = 12y(1-y)(1-\alpha_{U,Pu})[u + j(X)] \tag{3.54}$$

To compute ΔS_m^{xs} and ΔH_m for MOX fuel, we performed *Thermo-Calc* calculations, using the *TAF-ID 1.3* version.
One observes that $\alpha_{U,Pu}$ depends on both $u + j(X)$ and $g(T)$, which themselves depend on $\alpha_{U,Pu}$. This implies to resolve a fixed-point problem $f(X) = X$ in which $X = \alpha_{U,Pu}$.
It should be mentioned that, ΔS_m^{xs} and ΔH_m, were calculated for a stoichiometric MOX (*i. e.* O/M = 2). To asses the effect of stoichiometry, new Thermo-Calc calculations should be provided for different stoichiometries. In this work, we considered the case $x = 0$.
Depending on the sign of α_{AB}, three configurations exist:

$$\begin{cases} \alpha_{AB} = 0, & \text{no deviation from the ideal solid solution, } P_B^{reg} = P_B^{id} \\ \alpha_{AB} < 0, & \text{A-B pairs are more likely to occur} \\ \alpha_{AB} > 0, & \text{A-A or B-B pairs are more likely to occur} \end{cases}$$

Figure 3.19 shows the results obtained for the order parameter $\alpha_{U,Pu}$.

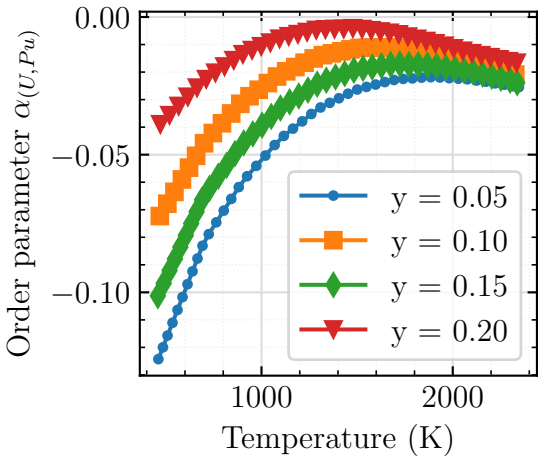

Figure 3.19: Order parameter $\alpha_{U,Pu}$ as obtained from the fixed-point problem resolution by use of thermodynamic data for stoichiometric MOX fuel, provided by Thermo-Calc calculations. The order parameter is plotted versus temperature for four different plutonium contents

The latter has a negative sign, meaning a preference for U-Pu pairs is observed rather than U-U or Pu-Pu types clustering. At $T = 500$ K, the order parameter is maximal. Increasing temperature decreases its value and thus decreases the deviation from the ideal solution. At approximately $T = 1500$ K, the short-range order parameter is close to 0. This observation leads to the conclusion that in stoichiometric MOX fuel, **the assumption of an ideal solid solution is legitimate**.

3.3.4.4 *Final expression and computation*

As shown in Figure 3.19, the deviation from the ideal solid solution is slight. The short-range order parameters can thus be neglected : $\alpha_{U,U} \approx 0$ and $\alpha_{Pu,Pu} \approx 0$. The electrical conductivity for a regular solid solution is thus equal to that of an ideal solid solution, recalled here:

$$\sigma^{el} = \frac{4e^2 v_{0,opt}}{akT}\left(c_{Pu^{3+}} c_{Pu^{4+}} e^{-\frac{E_m(Pu)}{kT}} + c_{U^{5+}} c_{U^{4+}} e^{-\frac{E_m(U)}{kT}}\right)$$

To compute electrical conductivity from this equation, we use:

1. the lattice parameter from Annex C.3
2. the optical phonons' vibration frequency, as calculated by DFT+U [113] : $v_{0,opt} = 1.713 \times 10^{13}$ s^{-1}

The fractional occupancy of the polarons $c_{U^{4+}}, c_{Pu^{4+}}$ and the cations $c_{U^{5+}}, c_{Pu^{3+}}$ can be calculated from the equilibrium rate constant of the disproportionation reaction, responsible for the polaron creation:

$$Pu^{4+} + U^{4+} \rightarrow Pu^{3+} + U^{5+}$$

The rate constant of this reaction is written as:

$$K_{pol} = \frac{c_{Pu^{3+}} c_{U^{5+}}}{c_{Pu^{4+}} c_{U^{4+}}} = \exp\left(-\frac{H}{kT} + \frac{S}{k}\right)$$

where H and S are the enthalpy and entropy of the reaction. The latter is related to polaron creation in MOX and thus its enthalpy corresponds to the band-gap energy.
The rate constant can further be developed, using $c_{Pu^{4+}} = y - c_{Pu^{3+}}$ and $c_{U^{4+}} = 1 - y - c_{U^{5+}}$, thus giving:

$$K_{pol} = \frac{c_{Pu^{3+}} c_{U^{5+}}}{(y - c_{Pu^{3+}})(1 - y - c_{U^{5+}})} = \exp\left(-\frac{H}{kT} + \frac{S}{k}\right) \tag{3.55}$$

To preserve crystal electroneutrality, the fractional occupancy of the polarons is also related to the deviation from stoichiometry x:

$$c_{Pu^{3+}} = c_{U^{5+}} + 2x \tag{3.56}$$

In MOX, to compensate for the two missing oxygen electrons, Pu^{4+} cations change their valence states to Pu^{3+} [143, 159–161].
Equations 3.55 and 3.56 constitute a system of equations, relating polarons' fractional occupancy to the deviation from stoichiometry x and the rate constant K_{pol}:

$$\begin{cases} \frac{c_{Pu^{3+}} c_{U^{5+}}}{(y - c_{Pu^{3+}})(1 - y - c_{U^{5+}})} = K_{pol} \\ c_{Pu^{3+}} = c_{U^{5+}} + 2x \end{cases}$$

The resolution of this equation system, gives the following expression for $c_{U^{5+}}$:

$$c_{U^{5+}} = \frac{K_{pol}(1-2x)+2x-\sqrt{\begin{array}{c}K_{pol}^2(4x^2-8xy+4x+4y^2-4y+1)+K_{pol}(-8x^2+8xy-\\4x-4y^2+4y)+4x^2\end{array}}}{2(K_{pol}-1)} \tag{3.57}$$

$c_{Pu^{3+}}$ is deduced from Equations 3.56 and 3.57. Finally, the computation of electrical conductivity can be done, using the following equation:

$$\boxed{\sigma^{el} = \frac{4e^2 v_{0,opt}}{akT}\left((c_{U^{5+}}+2x)(y-c_{U^{5+}}-2x)e^{-\frac{E_m(Pu)}{kT}} + c_{U^{5+}}(1-y-c_{U^{5+}})e^{-\frac{E_m(U)}{kT}}\right)} \tag{3.58}$$

where we identify the elementary plutonium and uranium contributions:

$$\boxed{\sigma_{Pu}^{el} = \frac{4e^2 v_{0,opt}}{akT}\left((c_{U^{5+}}+2x)(y-c_{U^{5+}}-2x)e^{-\frac{E_m(Pu)}{kT}}\right)} \tag{3.59}$$

$$\boxed{\sigma_{U}^{el} = \frac{4e^2 v_{0,opt}}{akT}\left(c_{U^{5+}}(1-y-c_{U^{5+}})e^{-\frac{E_m(U)}{kT}}\right)} \tag{3.60}$$

No data for the migration energies in MOX fuel has been reported in the literature.
The band-gap H was estimated in the work of Catlow and Pyper [143], but was not confirmed by other studies.
The polaron creation entropy S has not been estimated in the literature neither.
For those reasons, in the following sections, $H, S, E_m(Pu)$ and $E_m(U)$ will be considered as the model parameters and will estimated by inverse methods, using available experimental data on electrical conductivity of MOX systems.

3.3.5 Electrical conductivity experimental data on MOX fuels

The currently available experimental data on electrical conductivity of MOX fuels is summarized in Table 3.6

Author	Experimental technique	Temperature range (K)	Pu content (y)	O/M (2-x)	Nb. of points
Fujino *et al.* [159]	Four-point probe	220 - 1397	0.3; 0.5; 0.9	2	220
Schmitz *et al.* [162]		640 - 940	0.2	1.95 - 2	38
Kurihara *et al.* [163]		283 - 1065	0.189-0.4	1.95 ; 1.99	93
Yamashita *et al.* [164]		310 - 1328	0.05	2	36
				Total	***387***

Table 3.6: Available experimental data on electrical conductivity of MOX fuels

Electrical conductivity measurements are available for a quite important range of plutonium content and O/M ratios, showing the effect of both plutonium and oxygen content on electrical

conductivity of MOX.
However, for stoichiometric MOX fuels, there is quite an important lack of measurements covering plutonium contents higher than $y = 0.5$. Only a single data set is available for $y = 0.9$.
Apart from missing experimental data for high-plutonium MOX fuels, **the temperature range of the measurements is limited to [220-1397]** K. Schmitz' data allows to investigate the effect of stoichiometry. However, the measurements are limited to the range [640-940] K.
Therefore, the validation of the model is limited to low temperatures.

3.3.6 Inverse methods for estimating model parameters

So far, we have identified a theoretical model for the electrical conductivity of MOX fuels σ^{el} and experimental data. The model contains unknown parameters : $H, S, E_m(Pu)$ and $E_m(U)$. For sake of simplicity we will arrange those parameters in a vector $\boldsymbol{\beta} =< H, S, E_m(Pu), E_m(U) >$. Those parameters can be estimated using inverse methods [165, 166]. The latter consist of finding the optimal vector $\boldsymbol{\beta_{opt}}$, minimizing a certain quantity. The latter is often called the cost function and is related to the deviation of the measurements from the theoretical model.
To quantify this cost function, we will notate $y(t_i)$ the measurement at t_i and $f(t_i, \boldsymbol{\beta})$ the theoretical model at t_i for a given parameters vector $\boldsymbol{\beta}$. t is called the independent variable. In our case it represents the temperature. With those notations, the cost function is written as follows:

$$J(\mathbf{t}, \boldsymbol{\beta}) = \sum_{i}^{m} \left(y_i(t_i) - f_i(t_i, \boldsymbol{\beta})\right)^2 \tag{3.61}$$

where m is the number of measurements. To simplify notations, we can introduce the residuals $r_i(t_i) = y_i(t_i) - f_i(t_i, \boldsymbol{\beta})$. If we denote the residuals vector $\mathbf{r} = \mathbf{y} - \mathbf{f}(\mathbf{t}, \boldsymbol{\beta})$, we can write the matrix form of the cost function:

$$J(\mathbf{t}, \boldsymbol{\beta}) = \sum_{i}^{m} r_i(t_i)^2 = \mathbf{r^T r} \tag{3.62}$$

The minimization of this cost function consists of finding $\boldsymbol{\beta}_{opt}$, such that:

$$\boldsymbol{\beta_{opt}} = \arg[\min(J(\mathbf{t}, \boldsymbol{\beta}))] \tag{3.63}$$

To find $\boldsymbol{\beta_{opt}}$, the general strategy is to start from an "initial guess" vector $\boldsymbol{\beta}_0$ and generate $\boldsymbol{\beta}^k$ vectors such that $J(\boldsymbol{\beta}^{k-1}) > J(\boldsymbol{\beta}^k)$. This iterative process is repeated until a certain quality criterion on the cost function is satisfied.
The minimization process can sometimes lead to a local minimum, depending on the initial-guess vector. Generally, it is recommended to try multiple $\boldsymbol{\beta}_0$ vectors to avoid problems with local minimum.
To chose the appropriate $\boldsymbol{\beta}^k$ at each iteration, there are three main methods [165]:

1. Using only successive values of the cost function (dichotomy or relaxation methods)
2. Using the gradient of the cost function ∇J (first order methods)
3. Using both the gradient and the Hessian $H(J) = \nabla^2 J$ (second order methods)

In this work, we will use second order methods, as they are more robust and converge faster close to the optimal solution than first order methods.
Minimizing the cost function requires solving, for $\boldsymbol{\beta}$:

$$\forall t \geq 0, \forall j \in [1, m] : \frac{\partial J(\mathbf{t}, \boldsymbol{\beta})}{\partial \beta_j} = 0$$

No matter the optimization method (first or second order), it requires information about the first-order derivative of the model $f(t, \boldsymbol{\beta})$ with respect to each parameter β_j : $\frac{\partial f(\mathbf{t}, \boldsymbol{\beta})}{\partial \beta_j}$. This quantity corresponds to the sensitivity coefficient, already mentioned in Equation 3.28. Here, the model parameters are not all expressed in the same units. We thus use the reduced sensitivity coefficients (see Equation 3.29). Comparing the variation of those coefficients with the independent variable t (here the temperature T) can provide important information on the parameters' correlations [141, 165, 167]. The latter are of crucial importance when determining the parameters' standard deviations.

Sensitivity analysis on the model parameters

As shown in Figure 3.20, strong correlations exit between H and S, which can be partially explained by exiting linear dependencies between H and S or by the quasi-nullity of the sensitivity coefficient of either $E_m(Pu)$ at y = 0.1 or $E_m(U)$ at y = 0.9 and at low temperatures.

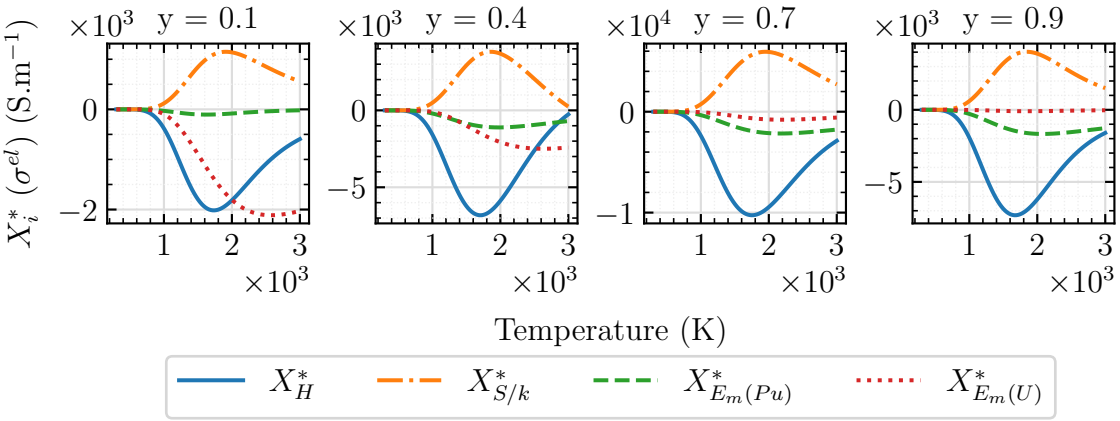

Figure 3.20: Variation with the independent variable (temperature) of the electrical conductivity model's reduced sensitivity coefficients, for four plutonium contents, at the stoichiometric composition $x = 0$

In addition to the detected correlations, we observe the driving model parameters: H and S, except for the case of y=0.1, where $E_m(U)$ becomes the driving parameter at temperatures higher than 2000 K.
When deviation from stoichiometry increases, the model parameter at temperatures below 1200 K, becomes the migration energy of the Pu polaron (see Figure 3.21).

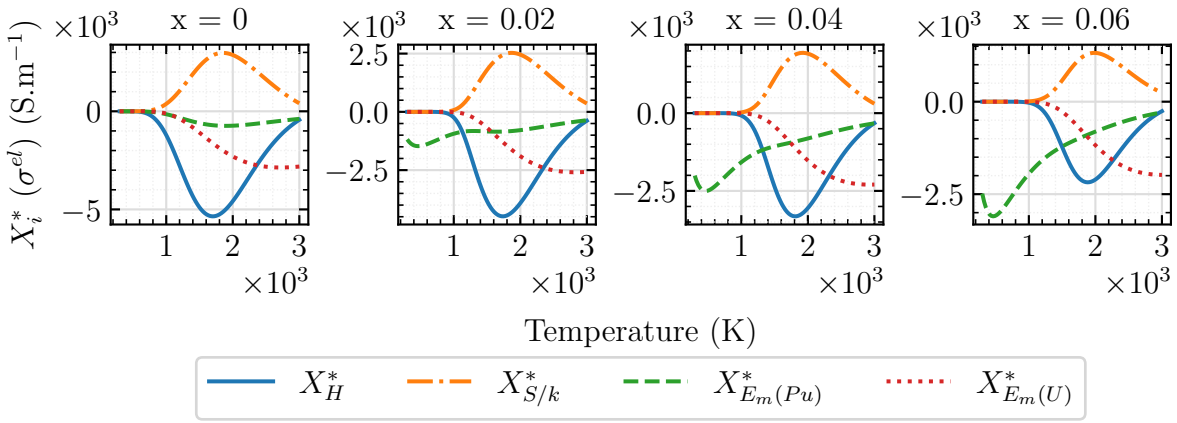

Figure 3.21: Variation with the independent variable (temperature) of the electrical conductivity model's reduced sensitivity coefficients, for four deviations from stoichiometry x, at y = 0.3

3.3.7 Parameter estimation

Optimization algorithm

To perform the parameters estimation, two different optimization algorithms were tested: the Levenberg-Marquardt algorithm (L-M) [168–170] and the Trust-Region-Reflective (TRR) [170].
Both algorithms use second-order methods to perform the cost function minimization. The differences in those two algorithms are slight. For more information about the comparison of those two algorithms, the reader can refer to [170]. The main advantage of the TRR algorithm, as opposed to L-M, lies in its capacity to perform constrained optimization (*i. e.* allows to restrain the optimized parameters to a range of physical values).

Three optimizations were performed:

1. **Unconstrained** optimization using the TRR algorithm (*i. e.* no physical bounds on the parameters are included)
2. **Constrained** optimization using the TRR algorithm (*i. e.* physical bounds on the parameters are included)
3. Optimization using the L-M algorithm (unconstrained optimization)

The estimated parameters obtained with each method are shown in Table 3.7. Despite the different results, obtained with the three methods, the model output seems to be the same for temperatures lower than approximately 1500 K (see Figure 3.22). The differences in model outputs start to be clear above 1500 K. Three different temperature profiles are observed. However, no experimental data is available at those temperatures to confirm which one is valid.

No matter the optimization method, H and S/k lie in a range of physical values (*i. e.* $H \in [1.09 - 3.51]$ eV and $S/k \in [3.15 - 9.35]$).

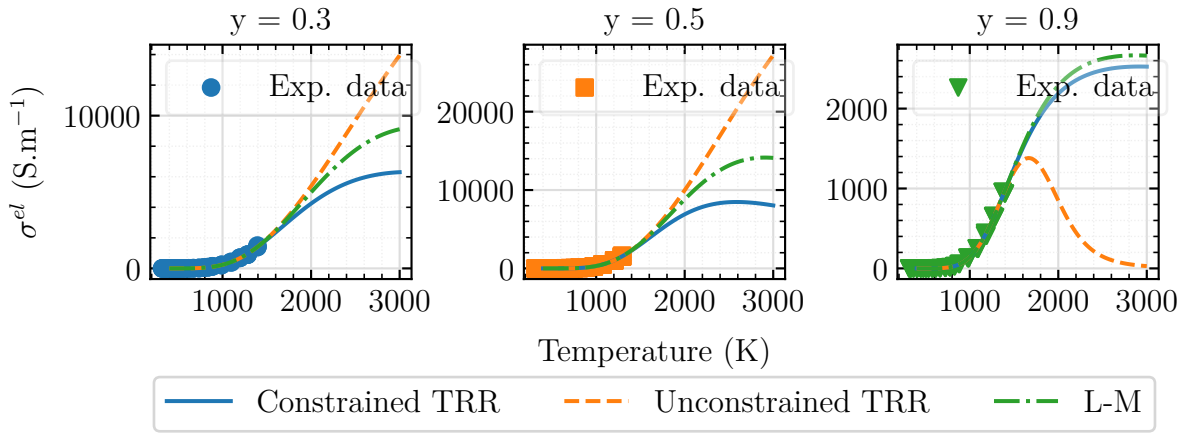

Figure 3.22: Optimization results obtained with three methods : constrained TRR, unconstrained TRR and L-M. The constrained TRR was performed with the following bounds : $H \in [0.5 - 1.5]$ eV, $\frac{S}{k} \in [2 - 12]$, $E_m(Pu) \in [0.04 - 0.5]$ eV, $E_m(U) \in [0.06 - 0.5]$ eV.

Parameter	H (eV)			$\frac{S}{k}$ (-)			$E_m(Pu)$ (eV)			$E_m(U)$ (eV)		
Pu content (y)	**0.3**	**0.5**	**0.9**	**0.3**	**0.5**	**0.9**	**0.3**	**0.5**	**0.9**	**0.3**	**0.5**	**0.9**
Constrained TRR	1.22	1.36	1.23	3.15	5.07	6.38	0.04	0.04	0.23	0.06	0.06	0.06
Unconstrained TRR	3.51	3.40	1.89	4.01	5.40	9.35	-1.15	-0.77	2.73	-0.87	-1.01	-0.21
L-M	1.79	1.83	1.09	3.93	5.37	5.59	-0.29	-0.02	0.21	-0.04	-0.22	0.41

Table 3.7: Optimization results, obtained with three methods for three plutonium contents. The constrained TRR was performed with the following bounds: $H \in [0.5-1.5]$ eV, $\frac{S}{k} \in [2-12]$, $E_m(Pu) \in [0.04 - 0.5]$ eV, $E_m(U) \in [0.06 - 0.5]$ eV

As for the migration energies, both unconstrained TRR and L-M give negative values.
The constrained TRR method identifies positive migration energies. However, these are systematically equal to the lower limits they were restricted to (*e. g.* $E_m(Pu) = 0.04$ eV whereas $E_m(Pu)$ was constrained to stay in $[0.04 - 0.5]$ eV).

Standard deviation of the estimation

Table 3.8 shows the relative errors, associated with the parameters, obtained with the unconstrained TRR method.
The relative errors associated with H and $\frac{S}{k}$ are relatively low, which could be explained by their high sensitivity coefficients.
However, the migration energies have excessively high standard deviations (> 622.2 %). This does not seem surprising, given their low sensitivity coefficients in the temperature range $[500 - 1500]$ K and the correlations involved.

Pu content (y)	0.3	0.5	0.9
$\frac{\sigma_H}{H}$ (%)	30.43	20.97	54.42
$\frac{\sigma_{S/k}}{S/k}$ (%)	179.01	76.69	76.68
$\frac{\sigma_{E_m(Pu)}}{E_m(Pu)}$ (%)	6177.17	2119.93	36.33
$\frac{\sigma_{E_m(U)}}{E_m(U)}$ (%)	2655.26	2817.87	622.20

Table 3.8: Relative standard deviations of the parameters, with the unconstrained TRR method.

Factor fixing

Given the correlations, making the estimation of the parameters difficult, we propose to proceed to factor fixing (FF).

At the stoichiometric composition, the FF will concern both migration energies, the sensitivity coefficients of which are almost null in the temperature range of the experimental data: $T \in [500 - 1380]$ K.
We will fix the migration energies to the values, calculated by DFT+U for PuO_2 [144] and UO_2 [private com.] systems respectively.
We thus make the following assumption: Pu^{3+} and U^{5+} **polarons migrate with the same energies in MOX system as in pure** PuO_2 and UO_2 systems.

At the hypostoichiometric composition, the FF will concern only the migration energy of the Uranium polaron, since $E_m(Pu)$ is the driving model parameter for $x > 0.01$.

Plutonium content dependency of the model parameters

The experimental data used for the optimization involves the measurements, performed in the work of Fujino *et al.* [159] for three plutonium contents in the range $y \in [0.3 - 0.9]$. The data of Yamashita *et al.* [164] ($y = 0.05$) and Schmitz [162] ($y = 0.2$) were not used because of unstable stoichiometry, during the measurements, reported by the authors.

The optimization yields a constant value of $S = 4k$, regardless of the plutonium content.
Figure 3.23 shows the optimized H parameter, together with DFT+U calculations on the band-gap energy in MOX fuel [private com.].
The H values estimated in this work show good consistency with the DFT+U results. The optimized values for H were fitted to the following equation:

$$H(y) = 0.6342y^{16.76} + 1.109 \tag{3.64}$$

This equation has been chosen to stay consistent with the profile of the DFT+U results.

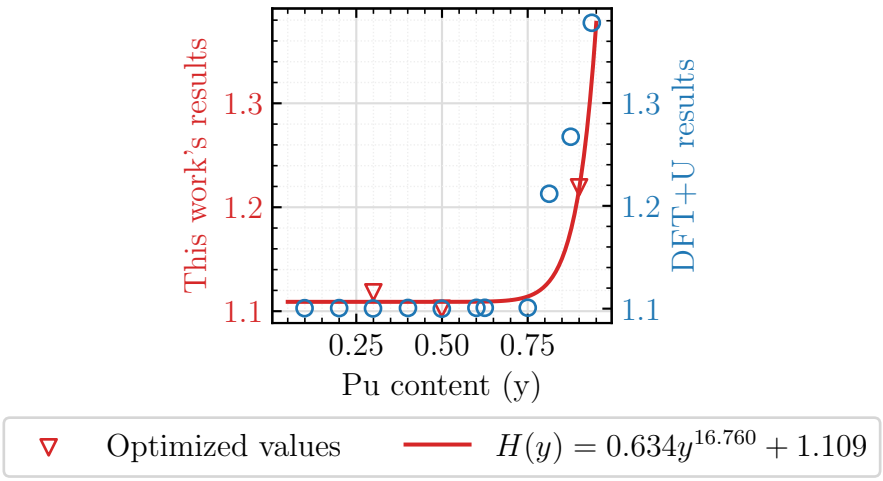

Figure 3.23: Evolution of the optimized H in this work (red triangles) and its fit to an equation of the type ($H(y) = ay^b + c$) (red solid line). This evolution is compared to DFT+U calculations (blue circles).

Oxygen content dependency of the model parameters

The measurements, used to provide the oxygen content dependency of the model parameters are those of Schmitz [162] on five different stoichiometries $x \in [0.01 - 0.05]$. The measurements of Kurihara *et al.* were not used in this study, because of the reported unstable stoichiometry during measurement cycles [163].
In this optimization, we assumed that the value of $S = 4k$ holds for a hypostoichiometric MOX fuel.

The optimization yielded a constant value for $E_m(Pu) = 0.3$ eV, whereas the enthalpy H showed a strong linear dependency of x. The variation of H with x was fitted to a linear equation:

$$H(x) = -6.989x + 0.9028 \tag{3.65}$$

Figure 3.24 shows the optimized $H(x)$, together with the measurements and the electrical conductivity model.

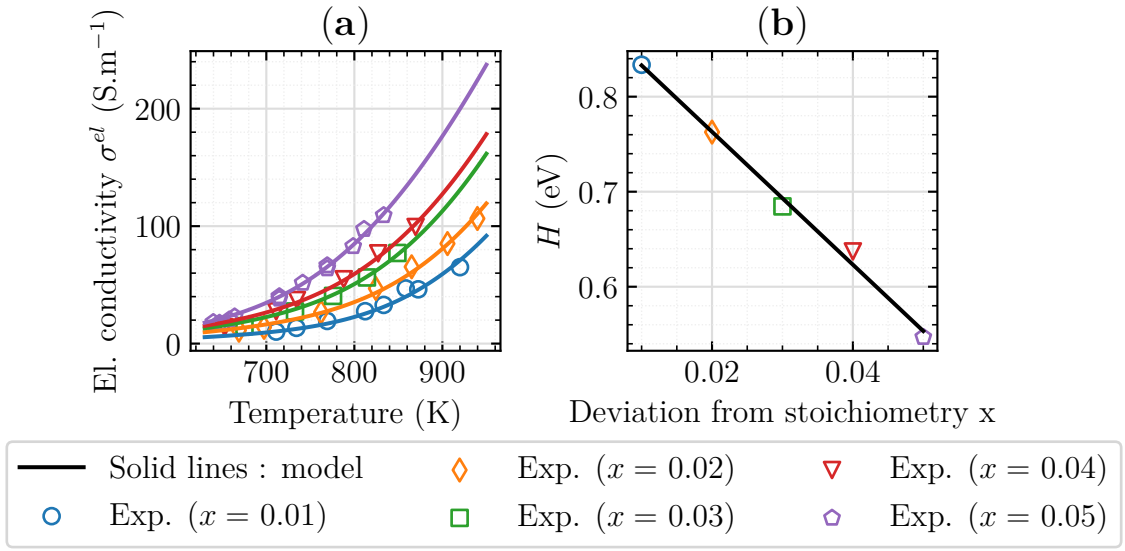

Figure 3.24: (a): Schmitz' hypostoichiometric experimental data [162] and the model (solid lines). (b): Variation of the estimated H with deviation from stoichiometry x

Summary on the estimation

Table 3.9 summarizes the estimated parameters and the assumptions, made to optimize them.

Parameter	x	Method	Assumption	Value
H (eV)	0 > 0	Optimization	-	$H(x=0) = 0.6342 \times y^{16.76} + 1.109$ $H(x>0) = -6.989x + 0.9028$
S (eV K^{-1})	0 > 0	Optimization	$S(x=0) = S(x>0)$	4k
$v_{0,opt}$ (s^{-1})	0 > 0	DFT+U [113]	$v_{0,opt}(x=0) = v_{0,opt}(x>0)$	1.714×10^{13}
$E_m(Pu)$ (eV)	0 > 0	DFT+U [144] Optimization	$E_m(Pu) = E_m(Pu)^{PuO_2}$ $E_m(Pu)(x=0) \neq E_m(Pu)(x>0)$	$E_m(Pu)(x=0) = 0.08$ $E_m(Pu)(x>0) = 0.30$
$E_m(U)$ (eV)	0 > 0	DFT+U [Private com.]	$E_m(U) = E_m(U)^{UO_2}$ $E_m(U)(x=0) = E_m(U)(x>0)$	0.28

Table 3.9: Summary of the parameter estimation

3.3.8 Computation of the electron contribution to thermal conductivity

Thermal conductivity due to electrons can be calculated, using:

$$\lambda^{el} = \left(\frac{k}{e}\right)^2 T \frac{\sigma_{Pu}^{el}\sigma_{U}^{el}}{\sigma_{Pu}^{el}+\sigma_{U}^{el}} \left(\frac{H}{kT}\right)^2$$

where:

$$\sigma_{Pu}^{el} = \frac{4e^2 v_{0,opt}}{akT}\left((c_{U^{5+}}+2x)(y-c_{U^{5+}}-2x)e^{-\frac{E_m(Pu)}{kT}}\right)$$

$$\sigma_{U}^{el} = \frac{4e^2 v_{0,opt}}{akT}\left(c_{U^{5+}}(1-y-c_{U^{5+}})e^{-\frac{E_m(U)}{kT}}\right)$$

$$c_{U^{5+}} = \frac{K_{pol}(1-2x)+2x-\sqrt{\begin{array}{c}K_{pol}^2(4x^2-8xy+4x+4y^2-4y+1)+K_{pol}(-8x^2+8xy-\\4x-4y^2+4y)+4x^2\end{array}}}{2(K_{pol}-1)}$$

$$K_{pol} = \exp\left(-\frac{H}{kT}+\frac{S}{k}\right)$$

where x: deviation from stoichiometry in $U_{1-y}Pu_yO_{2-x}$, y: plutonium content in $U_{1-y}Pu_yO_{2-x}$. For the model parameters $H, S, E_m(Pu), E_m(U)$ and $v_{0,opt}$ see Table 3.9. The electronic model is valid for $x < y/2$, similarly to the phonon model.

Plutonium content dependency

As shown in Figure 3.25 (c), at the stoichiometric composition ($x = 0$), the variation with plutonium content of total electrical conductivity follow the variation of the plutonium contribution σ_{Pu}^{el}.
This is caused by the differences in migration energy. Indeed, the migration energy of the uranium polaron is of 0.28 eV, whereas that of plutonium is of 0.08 eV. This implies higher contribution from the plutonium polaron to total electrical conductivity.
Increasing deviation from stoichiometry, also contributes to increase the plutonium contribution, due to the extrinsically created Pu^{3+} polarons.
The maximum of electrical conductivity is obtained at $y = 0.70$, for a stoichiometric MOX and at $y = 0.85$ for a non-stoichiometric MOX (*i. e.* here $x = 0.08$).

Thermal conductivity shows a slightly different variation with plutonium content. The former attains its maximum at $y = 0.45$, for a stoichiometric MOX, and $y = 0.55$ for a non-stoichiometric MOX (*i. e.* here $x = 0.08$). We therefore observe that electrical and thermal conductivity do not attain their maximum, at the same plutonium content value.
This is due to the proportionality of λ^{el} to the **product** $\sigma_{Pu}^{el} \times \sigma_{U}^{el} \times \frac{1}{\sigma^{el}}$ (see Equation 3.35). That is, if one polaron contribution to electrical conductivity (either σ_{Pu}^{el} or σ_{U}^{el}) is null, thermal conductivity will also be null. Therefore, even though at $x = 0.08$, the contribution from Pu^{3+} is at its maximum at $y = 0.85$, the contribution from U^{5+} is null.

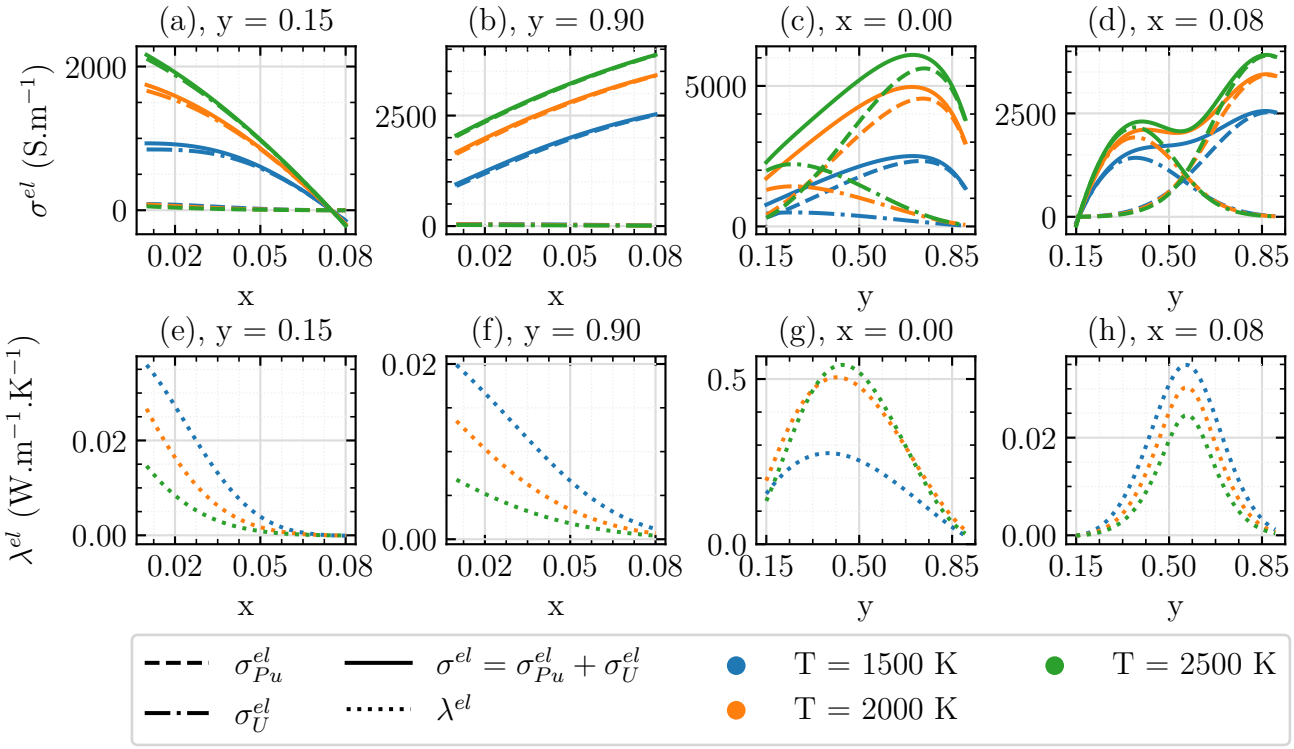

Figure 3.25: Variation of both electrical (a,b,c,d) and thermal conductivity (e,f,g,h) with both deviation from stoichiometry (a,b,e,f) and plutonium content (c,d,g,h).

.

This implies null thermal conductivity. Instead, thermal conductivity is at its maximum, where the product $\sigma^{el}_{Pu} \times \sigma^{el}_{U}$ exhibits its maximum (*i. e.* where both $\sigma^{el}_{Pu}(y)$ and $\sigma^{el}_{U}(y)$ curves cross each other).

Oxygen content dependency

The electrical conductivity variation with deviation from stoichiometry x depends on plutonium content: σ^{el} decreases with x for low plutonium contents and increases with x for high plutonium contents (see Figures 3.25 (a) and (b)).
Indeed, for low plutonium contents, $\sigma^{el} \approx \sigma^{el}_{U}$, whereas $\sigma^{el} \approx \sigma^{el}_{Pu}$, when plutonium content is high. Since the concentration of Pu^{3+} polarons increases with x, $\sigma^{el} \approx \sigma^{el}_{Pu}$ is also an increasing function of x. The opposite is observed for $c_{U^{5+}}$, which decreases with x.

Thermal conductivity, however decreases with x no matter the plutonium content. This is, once again, due to the thermal conductivity proportionality to the product of each polaron contribution to electrical conductivity.
λ^{el} further decreases with x due to its proportionality to the polaron enthalpy $\lambda^{el}(x) \propto H(x)^2$, which is a decreasing linear function of x (see Equation 3.65).

3.3.8.1 *Sensitivity analysis on the chemical composition*

The reduced sensitivity coefficients: $X_x^*(\lambda^{el}) = \frac{\partial \lambda^{el}}{\partial x} \cdot x$ and $X_y^*(\lambda^{el}) = \frac{\partial \lambda^{el}}{\partial y} \cdot y$ are shown in Figure 3.26.

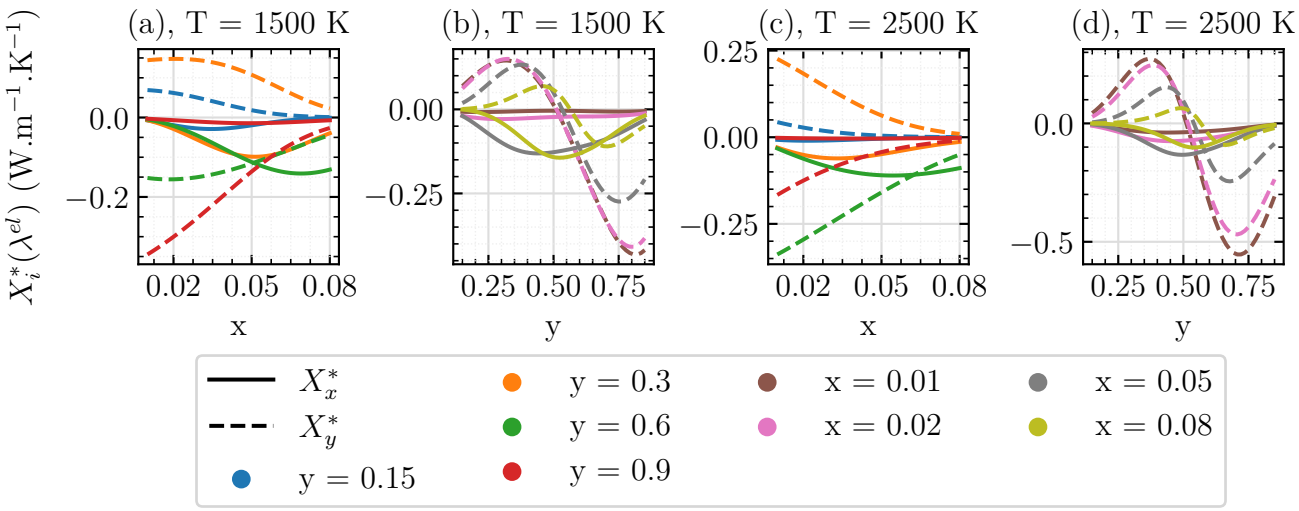

Figure 3.26: Variation of the electronic thermal conductivity model's reduced sensitivity coefficients $X_x^*(\lambda^{el})$ (solid lines) and $X_y^*(\lambda^{el})$ (dashed lines) with stoichiometry (a, c), and with plutonium content (b, d).

The electron contribution λ^{el} exhibits **more sensitivity to variations in plutonium content than to oxygen**, as in most cases, $|X_y^*| > |X_x^*|$.
This is the opposite to the thermal conductivity due to phonons λ^{ph}, which is more sensitive to variations in stoichiometry than to plutonium.
The model sensitivity to plutonium content is shown to decrease with deviation from stoichiometry. Indeed, increasing the deviation from stoichiometry increases the number of extrinsically created Pu^{3+} polarons, compared to the intrinsic ones. The Pu^{3+} contribution σ_{Pu}^{el} is, therefore more likely to be affected by the deviation from stoichiometry than by plutonium content.

3.3.9 Conclusion on the electron contribution to thermal conductivity

Thermal conductivity due to electrons was modeled by the ambipolar contribution (see Equation 3.35) in Price's initial model for a classical semi-conductor [145].

To compute λ^{el}, knowledge of the electrical conductivity σ^{el} and the polaron creation enthalpy H was required.
To model σ^{el}, the theoretical equation of Heikes and Ure was used for its success in describing electrical properties of oxide actinides [147, 149, 150, 152, 171] and other systems [172–175]. However, when applied to MOX, Heikes and Ure's model led to three essential observations:

1. any polaron (Pu or U) hops with the same migration energy
2. polarons can exhibit mixed-element and like-element hopping
3. MOX is an ideal solid solution

Literature data on MOX fuel [113] and other ternary systems [156, 157] proved that observations (1) and (2) are not likely to hold for MOX fuel. The model of Heikes and Ure for binary systems was thus modified. Observation (3) was however confirmed by calculating the short-range order parameter of MOX fuel, which showed **low deviations from the ideal solid solution.**

Due to missing experimental or simulated data on the model parameters, those were estimated by inverse methods, using available experimental data on electrical conductivity of MOX.
Sensitivity analysis showed strong correlations between the parameters, therefore yielding high standard errors, related to the parameter estimations.

The effect of both plutonium and oxygen content on electrical and thermal conductivity was studied. **The thermal conductivity variation with plutonium content is a parabola with a maximum, which depends on stoichiometry**: at $x = 0$ thermal conductivity reaches its maximum at $y = 0.45$, whereas for $x = 0.08$, it is reached for $y = 0.55$. The maximum of thermal conductivity is reached, where the product $\sigma^{el}_{Pu}(y) \times \sigma^{el}_{U}(y)$ exhibits its maximum. Deviation from stoichiometry contributes to decrease thermal conductivity, due to (1): a decreasing creation enthalpy with x, (2): a decreasing σ^{el}_{U} with x.

Sensitivity analysis on the chemical composition, led to the second remarkable conclusion: **the electronic contribution to thermal conductivity is more sensitive to variations in plutonium than to oxygen content**. Increasing the deviation from stoichiometry, however decreases the effect of plutonium content, due to the extrinsically created Pu^{3+} polarons, which are rather driven by the stoichiometry than by plutonium.

Now that both phonon and electron contributions to thermal conductivity have been studied, we will study the final contribution to thermal conductivity, considered in this work: radiative contribution (*i. e.* from photons).

3.4 Photon contribution to thermal conductivity

3.4.1 Introduction to heat transfer by photons

Let us recall the three different mode of heat transport in solids :

- **Conduction**: heat is transported by mutual molecule shocks, transmitting their kinetic energy from one to another.
- **Convection**: heat it transported generally between fluids. It associates the conduction and the mass transport and depends strongly on the fluid's flow velocity.
- **Radiation**: heat is transported, without any physical support, through electromagnetic waves. This heat transfer is extremely rapid (*i. e.* 300 000 $\mathrm{km\,s^{-1}}$ in void) .

In this section we are interested in the last mode of heat transport: radiation. At temperatures higher than the absolute zero ($T > 0$ K), every body emits electromagnetic waves. The latter cover a large spectral domain, with wavelengths from 10^{-14} m to 10^{6} m. Those resulting from a body's molecules' vibration are restricted to a spectral domain covering wavelengths from 10^{-7} m to 10^{-4} m (*i. e.* 0.1 µm to 100 µm). This spectral domain is also called "thermal radiation" domain. Media have multiple ways of interacting with an electromagnetic wave. A medium is defined as opaque, transparent or semi-transparent, depending on its behavior with respect to the electromagnetic wave traveling through it. We, thus define those media as follows:

- **Transparent**: the medium does not interact with the electromagnetic wave. The latter passes through without any trajectory or energy loss.
- **Opaque**: the medium "stops" the electromagnetic wave on its surface. In other words, this medium is such that the penetration distance of the electromagnetic wave is much smaller than a characteristic dimension of the medium. We, thus, consider, that all phenomena (absorption, reflection and emission) occur at the surface.
- **Semi-transparent** : the medium is such that the electromagnetic wave can travel a long distance before being absorbed. Here, absorption, reflection and emission are considered to be volumetric phenomena.

In the framework of this doctoral research, we are interested in the MOX fuel's behavior with respect to thermal radiation. MOX fuel is a semi-transparent medium and thus in the following sections, a particular attention is going to be made on the study of semi-transparent media.

3.4.2 Modeling: state of the art

3.4.2.1 Semi-empirical approaches

Most radiative thermal conductivity estimates for MOX fuel are based on the following semi-empirical equation [2, 176]:

$$\lambda^{rad} = DT^3 \tag{3.66}$$

where D is a constant, fitted to thermal conductivity experimental data by the least-squares method. To optimize the D constant, authors [2, 176] use thermal conductivity experimental data, from which they remove the phonon contribution, by fitting it to $1/(A + BT)$. They

thus consider that thermal conductivity at high temperature is only due to photons, and thus do not consider any electronic contribution. The physical meaning of D is therefore biased by the strong assumption that electrons do not contribute to thermal conductivity at high temperature. Furthermore, no stoichiometry, nor plutonium content effect is included.

Author (year)	$\boldsymbol{D}$ ($\mathrm{W\,K^{-4}\,m^{-1}}$)
Martin (1982) [176]	$78.90 \cdot 10^{-12}$
Philipponneau (2000) [2]	$76.38 \cdot 10^{-12}$

Table 3.10: Reported D constant in Equation 3.66 for MOX fuel [2, 176]

3.4.2.2 Rosseland approximation

Another approach to estimate radiative thermal conductivity is to use the optically thick limit of the radiative transport equation [177]:

$$\boxed{\lambda^{rad} = \frac{16 n^2 \sigma_B}{3\beta_R} \cdot T^3} \tag{3.67}$$

where:

n : refractive index of the media (-)
σ_B : Stefan-Boltzmann constant $= 5.67 \times 10^{-8}$ ($\mathrm{W\,m^{-2}\,K^{-4}}$)
β_R : mean Rosseland extinction coefficient ($\mathrm{m^{-1}}$)
T : temperature (K)

The mean extinction coefficient is the average of the spectral extinction coefficients denoted β_λ over the Planck distribution of the radiation and is calculated as follows:

$$(\beta_R)^{-1} = \frac{\int_0^\infty (\beta_\lambda)^{-1} \frac{d(n_\lambda^2 \varphi_\lambda^0)}{dT} d\lambda}{\int_0^\infty \frac{d(n_\lambda^2 \varphi_\lambda^0)}{dT} d\lambda} = \int_0^\infty \frac{1}{\beta_\lambda} \frac{\pi h^2 c^3}{2 n^5 \sigma_B \lambda^6 k T^5} \frac{\exp\left(\frac{hc}{n\lambda k T}\right)}{\left(\exp\left(\frac{hc}{n\lambda k T}\right) - 1\right)^2} d\lambda \tag{3.68}$$

Where:

β_λ : monochromatic extinction coefficient ($\mathrm{m^{-1}}$)
n_λ : monochromatic refractive index (-)
φ_λ^0 : black body's monochromatic emittance (m)
λ : wavelength (m)
c : speed of light in the medium ($\mathrm{m\,s^{-1}}$)
h : Planck constant (J s)
σ_B : Stefan-Boltzmann constant $= 5.67 \times 10^{-8}$ ($\mathrm{W\,m^{-2}\,K^{-4}}$)

The Rosseland approximation is valid for samples with thick optical lengths. The optical length is the product of the extinction coefficient and the geometrical length of the sample.

Bates [177] was the first to apply the Rosseland approximation for UO_2 in 1961. Since then, other subsequent studies on the application of the Rosseland approximation for UO_2 were reported [139, 147, 178–184].
Other authors [182, 183] have opposed the validity of this approximation while assessing the radiative thermal conductivity of mono-crystals. Viskanta *et al.* [182] used exact, gray radiative transfer calculations and concluded that the optically thick limit approximation for mono-crystals yielded results far more different than those obtained with the more rigorous transport equation. Indeed, mono-crystals have a low extinction coefficient. It is therefore difficult to obtain a thick optical length even with high geometrical sample lengths.
However, for poly-crystals scattering by grain boundaries make the extinction coefficient big enough to yield thick optical lengths and thus validating the Rosseland approximation [183].

3.4.2.3 Approach, used in this work

In the framework of this work, the thermal conductivity experimental data, used to validate the thermal conductivity model only covers poly-crystals. Given the validity of the Rosseland approximation for poly-crystals, to compute radiative thermal conductivity, we use Equation 3.67.

3.4.3 Computation of photon contribution to thermal conductivity

3.4.3.1 Refraction index

The refractive index n in equation 3.67 is considered to be diffuse (*i. e.* does not depend on wavelength), and temperature independent ($n_\lambda(T) \approx n$). Hyland [147] has mentioned the work of Bober *et al.* [184] on directional spherical reflectivity measurements of UO_2, from which it can be deduced that the refractive index of UO_2 is independent of both wavelength and temperature.
The refractive index n is, thus, estimated to the value of **2.25**.

3.4.3.2 Rosseland extinction coefficient

As the mean Rosseland extinction coefficient is an average value over the Planck distribution, one needs experimental data of the spectral extinction coefficient β_λ. Numerous measurements of the spectral extinction coefficient β_λ of UO_2 were reported in the literature [178, 179, 181, 184, 185]. Some of those measurements only cover mono-crystals of UO_2 [178, 185] and others cover also poly-crystals [179, 181, 184].
The spectral extinction coefficient β_λ is needed over the range of wavelengths: $0 < \lambda < \infty$. Measurements however could not be based on an infinite range. The evaluation of β_R should be restrained to a certain finite range of wavelengths.
Browning [178], reported the range, which allows a reliable estimate of β_R (see Table 3.11).
According to extinction coefficient measurements on UO_2 [178, 181, 185], $\lambda = 0.6$ µm corresponds to the absorption edge of UO_2, meaning that at $\lambda = 0.6$ µm, the extinction coefficient becomes infinite.
Therefore, to estimate β_R in a more accurate way, experimental data beyond the absorption

T (K)	$\boldsymbol{\lambda_{min}}$ (µm)	$\boldsymbol{\lambda_{max}}$ (µm)
300	1.12	63.1
1200	0.23	15.0
3000	0.09	6.3

Table 3.11: Finite wavelength range for the calculation of β_R, per temperature, reported by Browning [178]

edge is required.
As until 1980, the year of Browning's study, no experimental data beyond the absorption edge was available, Browning took an average value $\bar{\beta}(\lambda < 0.6\ \mu m)$ to calculate β_R. He proved that β_R strongly depends on $\bar{\beta}(\lambda < 0.6\ \mu m)$ for $T > 1000$ K.
In 1981, however, *Bober et al.* [184], made directional spherical reflectivity measurements on UO_2, in the range $\lambda < 0.6$ µm from which one can obtain a proper value of $\bar{\beta}(\lambda < 0.6\ \mu m)$ and a proper variation of the refractive index with both wavelength and temperature.
According to their work, $\bar{\beta}(\lambda < 0.6\ \mu m)$ **is of the order of 10^5** cm^{-1} independently of the temperature and it is shown that the refractive index is independent of the wavelength. Thus using the proper value of $\bar{\beta}(\lambda < 0.6\ \mu m)$ from Bober *et al.*'s work, Hyland [147] calculated the Rosseland mean extinction coefficient (see Table 3.12).
In this work, as no data on MOX fuel is available to our knowledge, **we make the assumption that Hyland's reported $\boldsymbol{\beta_R}$ stands for MOX fuel**. We fitted an empirical equation on $\beta_R(T)$ from Table 3.12:

$$\boxed{\beta_R(T) = 3.405 \cdot 10^{-6} \cdot T^{2.965} + 1.729 \cdot 10^4} \tag{3.69}$$

where β_R is given in (m^{-1}).
As mentioned by Hyland [147], the β_R values reported in Table 3.12 should be considered as lower limits for two reasons:

1. The spectral extinction coefficient measurements β_λ [178] from which β_R was deduced, **correspond to those at ambient temperature**. The temperature dependency of β_R (see Table 3.12) arises solely from averaging over the Planck distribution, which adds a T^5 term (see Equation 3.68)
2. The spectral extinction coefficient measurements β_λ [178] from which β_R was deduced were performed on **single crystals**, the absorbance of which is lower than that of poly crystals, due to the absence of scattering by grain boundaries.

Since radiative thermal conductivity is inversely proportional to β_R, underestimating β_R leads to overestimate λ^{rad}. **Estimates of $\boldsymbol{\lambda^{rad}}$ in this work correspond to possible upper**

T (K)	1000	1500	2000	2500	3000
$\boldsymbol{\beta_R}$ (cm^{-1})	190	275	385	570	865

Table 3.12: Mean Rosseland extinction coefficient, as calculated by Hyland [147], using *Bober et al.*'s value for $\bar{\beta}(\lambda < 0.6\ \mu m)$ [184]

limits.

3.4.4 Conclusion on the photon contribution to thermal conductivity

Radiative thermal conductivity was computed, using the Rosseland approximation (see Equation 3.67). The semi-empirical models were not considered in this work, as they are based on the unjustified assumption that electrons do not contribute to thermal conductivity at high temperature.

To compute λ^{rad}, we used refractive index data, reported for UO_2 in [184], and the mean Rosseland extinction coefficient, reported by Hyland [147], based on Bober *et al.*'s data for β_λ beyond the absorption edge (*i. e.* $\lambda < 0.6$ µm) [184].
None of these properties depend on oxygen, or plutonium content, as to our knowledge, no such experimental data was reported for MOX fuel.
Optical property measurements on MOX fuel were proposed in the framework of the *ESFR-SIMPLE* project.
This data will be used in the future to validate the assumption, used in this work that UO_2 and MOX systems have similar optical properties.

A particular attention should be payed to the mean Rosseland extinction coefficient β_R, which due to β_λ measurements, performed on single crystals and at ambient temperature, corresponds to its lower limits β_R^{min}. The latter thus lead to overestimate radiative thermal conductivity. A more accurate estimate of λ^{rad} would require spectral β_λ measurements for poly crystals and for different temperatures.

3.5 Computation of the thermal conductivity of (U,Pu)O_2

Total thermal conductivity is computed as follows:

$$\lambda = \underbrace{\frac{1}{\frac{\pi^2 a^3 \theta_D}{12(3-x)\overline{v_p}^2 h}\Gamma + \frac{\gamma_\infty^2 n_a^{2/3}}{B^* \overline{M} \theta_D^3 \overline{V_a}^{1/3}} \cdot T}}_{\lambda^{ph}} + \underbrace{\left(\frac{k}{e}\right)^2 T \frac{\sigma_{Pu}^{el}\sigma_U^{el}}{\sigma^{el}} \left(\frac{H \cdot 1.6 \cdot 10^{-19}}{kT}\right)^2}_{\lambda^{el}} + \underbrace{\frac{16 n^2 \sigma_B}{3\beta_R} \cdot T^3}_{\lambda^{rad}} \tag{3.70}$$

where:

- λ : thermal conductivity ($\mathrm{W\,m^{-1}\,K^{-1}}$)
- T : temperature (K)
- x : deviation from stoichiometry in $U_{1-y}Pu_yO_{2-x}$
- e : elementary charge $= 1.6 \cdot 10^{-19}$ (C)
- h : Planck constant $= 6.63 \cdot 10^{-34}$ (J s)
- k : Boltzmann constant $= 1.38 \cdot 10^{-23}$ ($\mathrm{J\,K^{-1}}$)
- σ_B : Stefan-Boltzmann constant $= 5.67 \times 10^{-8}$ ($\mathrm{W\,m^{-2}\,K^{-4}}$)
- a : lattice parameter (m), see Equation C.8 in Annex C.3
- θ_D : Debye temperature (K), see Equation 3.10 in Section 3.2.3.1
- $\overline{v_p}$: mean phonon velocity ($\mathrm{m\,s^{-1}}$), see Equation 3.11 in Section 3.2.3.2
- Γ : scattering cross section (-), see Equation 3.15 in Section 3.2.3.4
- γ_∞ : high-temperature Gruneisen parameter (-), derived by $\gamma_\infty = \gamma(\theta_D)$ with γ, given by Equation 3.14 in Section 3.2.3.3
- $\overline{M}$: mean atomic mass of the compound (here in $\mathrm{g\,mol^{-1}}$): $\frac{(1-y)M_U + yM_{Pu} + (2-x)M_O}{3}$
- $\overline{V_a}$: mean atomic volume (here in Å^3), $\overline{V_a} = \frac{(a \cdot 10^{10})^3}{4(3-x)}$, where a is the lattice parameter in (m)
- n_a : number of atoms per unit cell $= 4(3-x)$
- B^* : constant (-) given by Equation 3.24 in Section 3.2.4
- σ^{el} : total electrical conductivity $\sigma^{el} = \sigma_{Pu}^{el} + \sigma_U^{el}$ ($\mathrm{S\,m^{-1}}$), see Equation 3.58 in Section 3.3.4.4
- σ_{Pu}^{el} : plutonium contribution to electrical conductivity ($\mathrm{S\,m^{-1}}$), Equation 3.59, Section 3.3.4.4
- σ_U^{el} : uranium contribution to electrical conductivity ($\mathrm{S\,m^{-1}}$), Equation 3.60, Section 3.3.4.4
- H : creation enthalpy of the polarons (eV), see Table 3.9
- n : refractive index of the medium (-), see Section 3.4.3.1
- β_R : mean Rosseland extinction coefficient ($\mathrm{m^{-1}}$), see Equation 3.69 in Section 3.4.3.2

The model is valid for deviations from stoichiometry, such that $x < y/2$, where y is the plutonium content, and temperatures, above the Debye temperature: $T > \theta_D$.

3.5.1 Effect of temperature

We briefly recall the temperature variation of each term:

$$\lambda^{ph}(\boldsymbol{T}) \propto \boldsymbol{T}^{-1}$$

$$\sigma^{el}_{Pu}(\boldsymbol{T}),\ \sigma^{el}_{U}(\boldsymbol{T}) \text{ and } \sigma^{el}(\boldsymbol{T}) \propto \boldsymbol{T}^{-1}\exp(\boldsymbol{T}^{-1})$$

$$\lambda^{el}(\boldsymbol{T}) \propto \boldsymbol{T}\cdot\frac{\sigma^{el}_{Pu}(\boldsymbol{T})\times\sigma^{el}_{U}(\boldsymbol{T})}{\sigma^{el}(\boldsymbol{T})}\cdot\boldsymbol{T}^{-2} \propto \boldsymbol{T}^{-2}\exp(\boldsymbol{T}^{-1})$$

$$\lambda^{rad}(\boldsymbol{T}) \propto \boldsymbol{T}^{3}$$

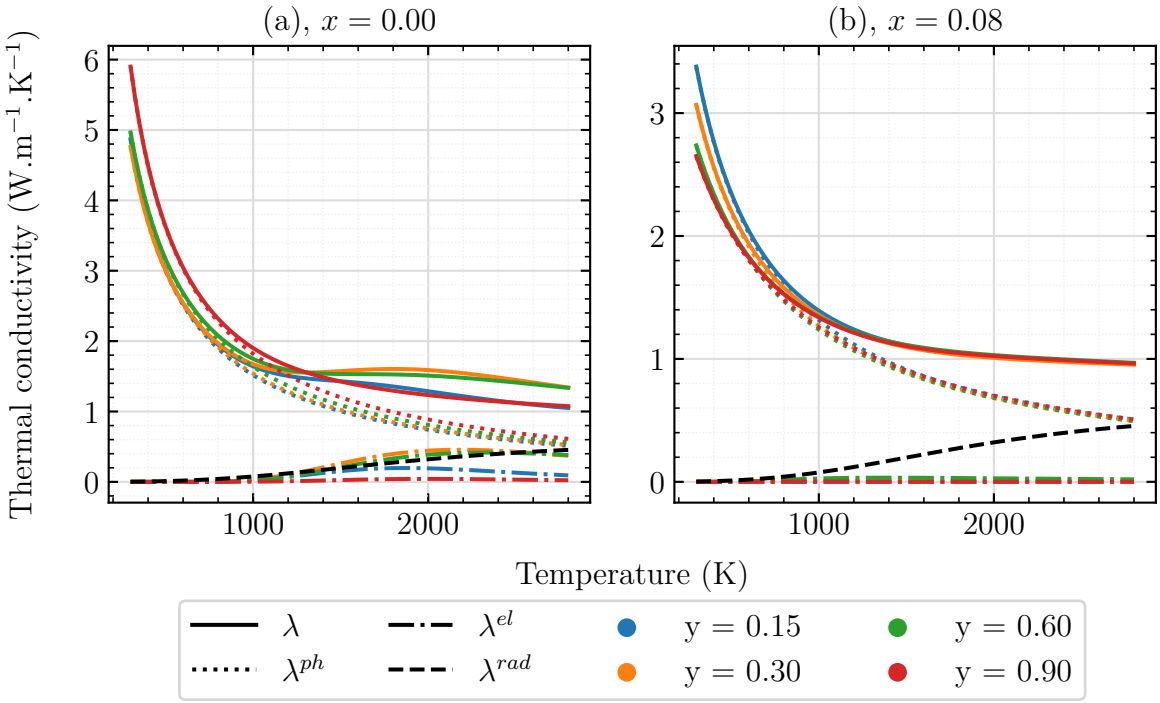

Figure 3.27: Variation with temperature, of the three elementary contributions λ^{ph} (dotted lines), λ^{el} (dash-dotted lines) and λ^{rad} (dashed lines), together with the total λ (solid lines).

As shown in Figure 3.27, regardless of the chemical composition, the phonon contribution to thermal conductivity is higher than both electron and photon contributions in the whole temperature region (*i. e.* here $T \in [\theta_D - 3000]$ K).
Even though, λ^{el} and λ^{rad} both increase with temperature, the phonon contribution decreases. This decrease thus compensates for the increase due to λ^{el} and λ^{rad}, therefore leading to a rather constant thermal conductivity at high temperature.

We also observe that the radiative thermal conductivity is comparable to the electronic one in the range $y \in [0.30 - 0.60]$ (*i. e.* in the range where the electronic contribution exhibits a maximum) and at $x = 0$. For plutonium contents outside this range, the radiative contribution is higher.
At $x = 0.08$ however, electronic thermal conductivity is close to 0 and radiative thermal

conductivity drives the temperature variation of thermal conductivity at high temperatures.

However, as mentioned in Section 3.4.3.2, due to a possible underestimation of the mean Rosseland coefficient, the radiative thermal conductivity, as computed in this work, might be overestimated.
In addition to an overestimation of the radiative contribution, there is another difficulty in making an accurate comparison of electronic and radiative contributions: **the uncertainty, associated with estimating the migration energies** $E_m(Pu)$ and $E_m(U)$ in the electronic term, due to missing electrical conductivity experimental data above 1400 K.

Confirmation for the uncertainties, related to the electronic term is the particular temperature profile of both electrical and thermal conductivity.
As shown in Figure 3.28, the electronic thermal conductivity term presents an inflection point, regardless of plutonium content.
This inflection point originates from the electrical conductivity profile.

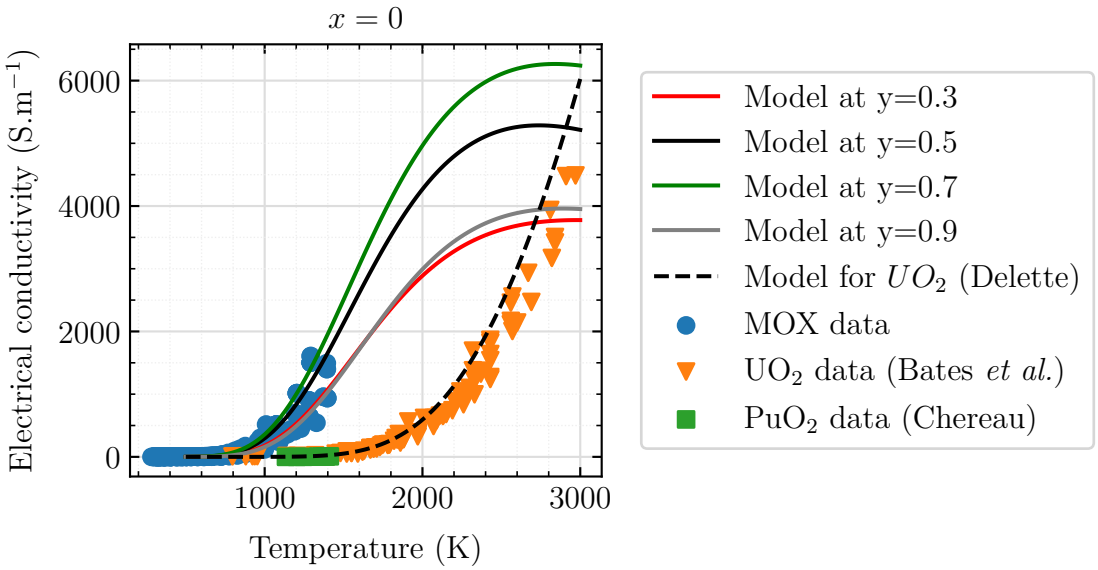

Figure 3.28: Electrical conductivity variation with temperature, as observed experimentally for MOX [159], UO_2 [181] and PuO_2 [186] and as modeled in this work (for MOX) and in the work of Delette *et al.* [152] (for UO_2).

Indeed, as shown in Figure 3.28, experimental data on electrical conductivity of MOX fuel, regardless of plutonium content, yield an importance increase in the range $T \in [900 - 1400]$ K. At those temperatures, both UO_2 and PuO_2 show zero electrical conductivity. It therefore does not seem impossible that an inflection point appears in the electrical conductivity temperature variation, since the latter exhibits a very rapid increase at low temperatures, which may be saturated at rather low temperatures (here around 1500 K).
To date, due to missing data at high temperatures, we could not confirm if the inflection point is driven by a real physical phenomenon or to modeling uncertainties, such as omitting the mixed-element Pu-U hopping term in the electrical conductivity model.
Indeed, a third contribution in the electrical conductivity model may compensate for the

inflection point effect. However, including Pu-U mixed element hopping also adds a supplementary model parameter: the migration energy of the Pu-U hopping.
This therefore adds further difficulties in optimization, given the low number of experimental data, covering only low temperatures.
This further justifies the need for electrical conductivity measurements at temperatures, which are not covered by the present data (*i. e.* T > 1380 K).

To further detail the discussion around the inflection point we need to mention the effect of the H parameter.
Indeed, we saw that thermal conductivity depends on electrical conductivity, but is also directly proportional to the polaron creation enthalpy H. The latter therefore not only appears in the expression for electrical conductivity, but is also an intrinsic parameter of the electronic thermal conductivity model.
If the electrical conductivity's temperature profile is responsible for the inflection point in $\lambda^{el}(T)$, the H parameter may contribute to further increase or decrease the amplitude of λ^{el}.
To illustrate this discussion, we plotted the temperature variation of both σ^{el} and λ^{el}, for different model parameters: $H \in [1 - 1.5]$ eV, $\frac{S}{k} \in [2 - 6]$, $E_m(Pu) \in [0.1 - 0.3]$ eV and $E_m(U) \in [0.1 - 0.3]$ eV (see Figure 3.29).

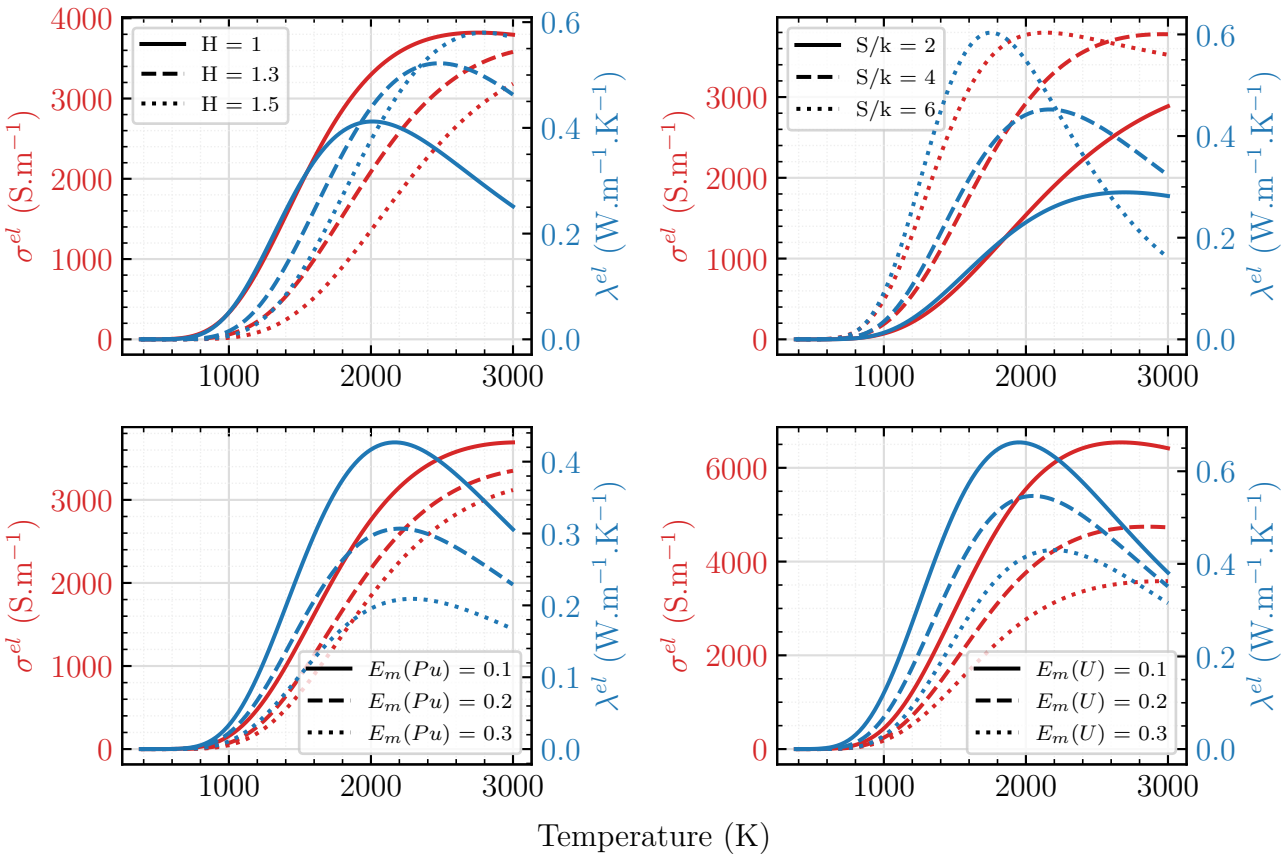

Figure 3.29: Electrical (in red) and thermal (in blue) conductivity variation with temperature, for different model parameters. The H, $E_m(Pu)$ and $E_m(U)$ parameters are expressed in eV, whereas S/k, where k is the Boltzmann constant, is unit-less.

The effect of $S, E_m(Pu), E_m(U)$ is the same on both electrical and thermal conductivity. That is, increasing the migration energies decreases both electrical and thermal conductivity, whereas increasing the polaron creation entropy S increases both σ^{el} and λ^{el}.
The effect of H is however different. Increasing H leads to a decrease in σ^{el}, but to an increase in λ^{el}.
We recall that H is the energy, needed for the polaron creation. Therefore, the lower H, the "easier" the polaron creation. However, thermal conductivity is due to the recombination of the polarons.
During recombination, the energy needed for the creation of the polarons is then transformed into thermal energy. Therefore, if polarons need less energy to be created, they will also supply less thermal energy during recombination.
This is why, thermal conductivity is directly proportional to the polaron creation energy.

As shown in Figure 3.29, increasing H leads to a shift of the inflection point to higher temperatures. Therefore, increasing H allows to yield a rather monotone increase in thermal conductivity. It does not however mean that the inflection point does not appear. It does appear, but at higher temperatures.

If increasing H allows to solve the inflection point problematic, in the temperature range $T \in [298 - 3000]$ K, it however shifts the electrical conductivity $\sigma^{el}(T)$ curve to the right. In other words, electrical conductivity would start its exponential increase at higher temperatures.
This however may not be consistent with electrical conductivity measurements, which show a great increase at rather low temperatures. This observation therefore highlights the difficulty in satisfying both (1): a monotone increase in thermal conductivity (*i. e.* without inflection point) and (2): consistency with electrical conductivity experimental data.
This difficulty will be described in details in the following chapter.

The capacity of the migration energies to "delay" the inflection point (*i. e.* to shift it to higher temperatures) is however less obvious. Indeed, as shown in Figure 3.29, the $E_m(Pu)$ and $E_m(U)$ parameters contribute to moderate the amplitude of both σ^{el} and λ^{el}, therefore shifting the curves up and down, but they do not seem to shift the curves to the right (*i. e.* to moderate the inflection point). The S parameter however can, together with H, contribute to shift the inflection point to higher temperatures.

It should be mentioned that the available semi-empirical models for the electronic thermal conductivity [3–6, 33] for MOX, do not show any inflection point.
Indeed, those models are calibrated using only thermal conductivity experimental data, since electrical conductivity is not an input property to those models.
Since experimental thermal conductivity does not show an inflection point, but rather a monotone increase with temperature, the semi-empirical models also show a monotone increase with temperature.
Nevertheless, in the next chapter it will be seen that the experimental temperature variation of thermal conductivity above 2200 K is associated with great uncertainties, due to the use of

a heat capacity model, valid only up to 2500 K.
Indeed, most measurements on thermal conductivity are based on thermal diffusivity measurements, multiplied by a heat capacity model and density. In the next chapter, we will see that the temperature variation of thermal conductivity above 2000 K is driven by the temperature variation of heat capacity, since thermal diffusivity shows a rather constant temperature dependency.
The unique use of thermal conductivity experimental data to provide empirical models for thermal conductivity, especially above 2200 K, can therefore lead to high modeling uncertainties, given the uncertainty on the heat capacity model.

3.5.2 Effect of chemical composition

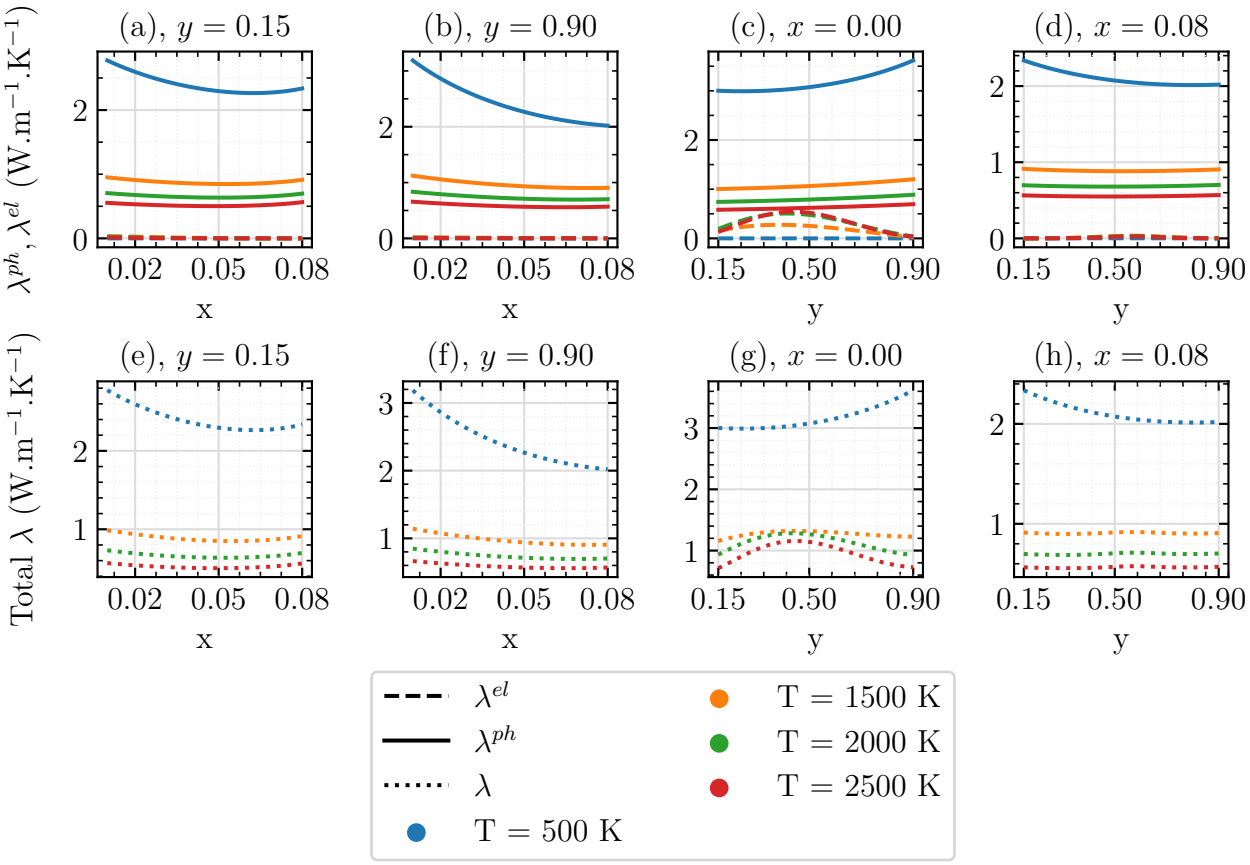

Figure 3.30: Variation of the phonon (solid lines) and electron (dashed lines) terms with deviation from stoichiometry (a, b) and plutonium content (c, d), together with the total thermal conductivity (dotted lines) (e,f,g,h).

After studying the particularity of the temperature variation of both electrical and thermal conductivity, here we will show the effect of chemical composition.
As shown in Figure 3.30, the variation of the total thermal conductivity with x is mostly driven by the phonon term's variations with x, regardless of the temperature.
Indeed, irrespective of temperature, the sensitivity of the phonon term on x is higher than that of the electron term.

Uncertainties in model predictions, **associated** with **stoichiometry** uncertainties are therefore mainly driven by the **phonon contribution** to thermal conductivity, regardless of the temperature.

On the other hand, the variation of λ with plutonium content depends on temperature. Increasing temperature, increases the electronic contribution and decreases the phonon one. The variation of λ^{el} with y thus drives the overall variation with y of λ, at high temperatures (*i. e.* $T > 1500$ K).
However, for temperatures lower than 1500 K, the electronic contribution is almost null. The overall variation of λ with plutonium content is thus mainly driven by the phonon contribution.

3.6 Identification of experimental data to reduce model uncertainties

In this chapter, we performed several sensitivity analysis on both chemical composition and model parameters. The former led to some **important conclusions in terms of model uncertainty reduction**.
Based on those conclusions, in this section we propose complementary experimental data to reduce uncertainties, associated with chemical composition, parameter estimation by inverse methods and material properties.

3.6.1 Uncertainties, associated with stoichiometry effect

Sensitivity analysis on the chemical composition effect on total thermal conductivity (see Figure 3.31), reveals that the sensitivity coefficient of λ^{ph} to stoichiometry x is higher than that of λ^{el}: $|X_x^*(\lambda^{ph})| > |X_x^*(\lambda^{el})|$. This holds even at high temperatures ($T = 2500$ K, where the phonon contribution is relatively low.
Furthermore, we also observe that **increasing plutonium content, increases the phonon model sensitivity to stoichiometry**, as already pointed out in Section 3.2.3.6.
Therefore, to reduce model uncertainties, due to stoichiometry, experimental data at low temperatures ($T < 1500$ K), on highly hypostoichiometric MOX fuel ($x > 0.05$) and high plutonium content $y > 0.3$ is required.

3.6.2 Uncertainties, associated with plutonium content effect

Contrary to the effect of stoichiometry, which mainly impacts the phonon term in the whole temperature range, the effect of plutonium depends on temperature.
At low temperatures, the variations with y of the total λ are driven by the phonon term, while at high temperatures, the electron term is responsible for the overall λ variations with y.
However, both phonon and electron terms' sensitivity to y **increases with plutonium content and decreases with deviation from stoichiometry.**
Most experimental data, used to provide semi-empirical thermal conductivity models are based on experimental data, covering low plutonium contents (*i. e.* $y \in [0.1 - 0.3]$)

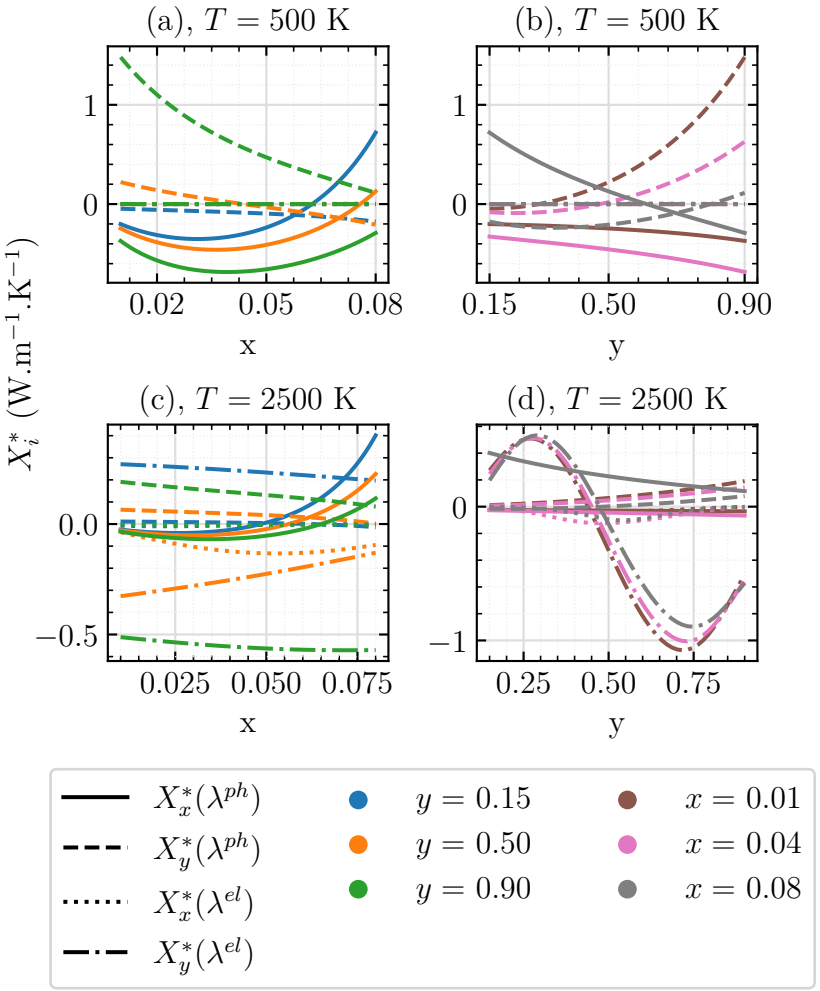

Figure 3.31: Comparison of the sensitivity coefficients of the electron and phonon terms on x and y. Their variations with x and y are plotted for $T = 500$ K and $T = 2500$ K at (a), (b) and (c), (d) respectively

[3, 4, 33, 107, 118, 122]. However, for low plutonium contents (no matter the deviation from stoichiometry), the effect of plutonium content is negligible to that of deviation from stoichiometry.
To decrease model uncertainty, related to the effect of plutonium content, experimental data on MOX fuels with high plutonium content and low deviation from stoichiometry should be provided and used to validate theoretical models or develop semi-empirical correlations.

3.6.3 Uncertainties, associated with parameter estimation

In the temperature range of the available electrical conductivity experimental data, the electrical conductivity model shows very low sensitivity to $E_m(Pu)$ and $E_m(U)$. Their estimation by inverse methods therefore leads to relative standard deviations of more than 2000 %. To reduce model uncertainties, associated with the migration energies, electrical conductivity **experimental data at high temperatures (*i. e.* $>$ 1500 K) is required**.

3.6.4 Uncertainties, associated with material properties

3.6.4.1 Phonon properties

As seen in Section 3.2.5.3, Debye temperature and Gruneisen parameter are the driving model parameters in the phonon term λ^{ph}. These were evaluated, using **measured material properties**: lattice parameter a, longitudinal and transverse components of the sound velocity V_l and V_t, thermal expansion α, isothermal bulk modulus K_T, heat capacity C_v.

Debye temperature and its associated material properties

Sensitivity analysis on those properties concluded that to reduce uncertainties, associated with **Debye temperature**, the lattice parameter and the transverse component of the sound velocity **should be determined with the highest precision**. The longitudinal component V_l does not seem to induce uncertainties in θ_D.
In this work, we used Hirooka and Kato's [126] empirical correlation for V_t, which is valid in the range $x \in [0 - 0.04]$ and $y \in [0 - 1]$. If this correlation covers the whole plutonium content range, stoichiometry is however limited to rather low deviations from stoichiometry.
To reduce uncertainties, associated with the effect of stoichiometry on V_t, experimental data, covering higher deviations from stoichiometry $\boldsymbol{x}$ are required.
As for the lattice parameter, *Kato et al.*'s experimental correlation was used in this work [187]. The latter is based on various measurements, covering the whole plutonium and oxygen content range of interest: $y \in [0 - 1]$ and $x \in [0 - 0.08]$.
Uncertainties, associated with the lattice parameter therefore should be low.

Gruneisen parameter and its associated material properties

The lattice parameter was shown to induce **twice more variations** in **Gruneisen parameter** than the other material properties, from which it was deduced (*i. e.* K_T, α, C_v). The latter however do not have null sensitivity coefficients, which shows that they also should be determined with high precision to avoid uncertainties in γ_∞.

3.6.4.2 Optical properties

To compute β_R from Equation 3.68, knowledge of the spectral extinction coefficient β_λ is needed. In this work, we used Hyland's vales for β_R, based on Browning's spectral β_λ measurements on UO_2.
However, the latter were performed on (1): single crystals and (2): correspond to those at ambient temperature. The β_λ values so-obtained therefore possibly underestimate the real β_λ. The radiative thermal conductivity, computed in this work, is therefore overestimated.
To make an accurate estimate of λ^{rad}, **spectral extinction coefficient** measurements on **poly crystals and for temperatures, other than the ambient temperature.** are required.

3.7 Conclusion and perspectives

In this chapter, we saw how chemical composition can affect thermal conductivity at both low (< 1500 K) and high temperatures (> 1500 K), through the use of low computational cost theoretical models.
The interest in using these models lies in their application, using known material properties: thermal expansion, bulk modulus, heat capacity, extinction coefficient *etc.*.
Even though the electronic contribution requires knowledge of more complex properties (*i. e.* the migration energies of the polarons or the creation enthalpy and entropy of the polarons), the use of inverse methods allowed to estimate the values of those parameters, using electrical conductivity experimental data.

This chapter revealed pioneering results, concerning the **correlated effects of plutonium and oxygen content on thermal conductivity**.
Plutonium content amplifies the effect of stoichiometry, on the phonon contribution to thermal conductivity. This was explained as being due to the Pu^{3+} cations, the fractional occupancy of which is proportional to the deviation from stoichiometry x, and the phonon scattering strength of which increases with plutonium content due to the increasing radius difference between the Pu^{3+} cation and the (U, Pu) sub-lattice with plutonium content.
Another reason for the correlated plutonium-oxygen content effect arises from how stoichiometry affects the plutonium content dependency of the phonon contribution. We showed that increasing deviation from stoichiometry, induced a shift of the plutonium content, at which thermal conductivity assumes a minimum, to higher plutonium content values.
That is, at $x = 0.08$, the minimum of the phonon thermal conductivity is observed around $y = 0.85$, whereas at $x = 0$, this minimum is situated around $y = 0.15$. This was, once again, explained by the Pu^{3+} cations, which drive the phonon scattering for high deviations from stoichiometry.
We saw that the correlated plutonium-oxygen content effects do not concern only the phonon contribution but also the electronic one. Indeed, increasing deviation from stoichiometry decreases the effect of plutonium content, due to the extrinsic creation of Pu^{3+} polarons, which outweighs the plutonium content-dependent intrinsic creation of Pu^{3+}.
We also saw that increasing deviation from stoichiometry increases the contribution of the plutonium polaron. The migration energy of the latter is of crucial interest to avoid uncertainties, related to modeling the effect of stoichiometry on electrical and thermal conductivity.
The importance of considering the correlated plutonium-oxygen content effects on thermal conductivity is crucial in fast reactor applications. Indeed, we saw that important plutonium and oxygen redistribution occurs due to high temperature radial gradient. Plutonium redistributes towards the center of the fuel pellet, whereas oxygen -to the fuel periphery. Modeling those correlated effects therefore allows to provide a more accurate estimate of the fuel local temperature. Semi-empirical approaches do not account for this effect and can therefore yield important uncertainties, when used in fuel performance codes to simulate FNR irradiations.

Sensitivity analysis on the chemical composition of both the phonon and electronic con-

tributions revealed that phonons are more sensitive to oxygen vacancies, whereas the polarons to plutonium content.
This chapter also highlighted the model sensitivity to the parameters. Through sensitivity analysis, we concluded that the phonon contribution is mainly driven by Debye temperature and Gruneisen parameter, whereas the electronic contribution by the creation enthalpy and entropy of the polarons. The importance of the migration energy of the polarons increases with temperature. Based on those observations, to reduce uncertainties, associated with the model parameters, supplementary experimental data was proposed in Section 3.6.4.1 for θ_D and γ and Section 3.6.3 for the migration energies.

This chapter reveled the uncertainties, associated with the electronic and radiative thermal conductivity.
Radiative thermal conductivity was shown to be underestimated, due to an overestimation of the mean Rosseland extinction coefficient. This led to the **perspective of performing extinction coefficient measurements on MOX fuels**.
On the other hand, due to missing electrical conductivity experimental data for temperatures higher than 1400 K, the temperature variation of both electrical and thermal conductivity conductivity is uncertain. This revealed one of the major perspectives of this chapter: **perform measurements of electrical conductivity at temperatures above 1380 K**.
Indeed, we observed a particular temperature variation of both electrical and thermal conductivity, involving an inflection point at rather low temperatures.
We showed that among the four electronic model parameters, the polaron creation enthalpy H **can contribute to deal with the inflection point problem by increasing its value**, therefore yielding an almost monotone increase of λ^{el} with temperatures.
We have also found that dealing with the inflection point problem can be accompanied by a reduction in the consistency of the electrical conductivity model with measurements.
In addition to identifying the main parameters, responsible for the inflection point, we also identified possible modeling uncertainties, such as assuming that mixed-element Pu-U hopping is not likely to occur. However, **adding another contribution also adds another model parameter: the migration energy of the Pu-U polaron.** To estimate the latter by inverse methods, the available electrical conductivity experimental data is not sufficient. This further confirms the need for supplementary experimental data above 1380 K.

3.8 Conclusion et perspectives du chapitre

Dans ce chapitre, nous avons vu comment la composition chimique peut affecter la conductivité thermique à la fois à basse (< 1500 K) et à haute température (> 1500 K), grâce à l'utilisation de modèles théoriques à faible coût de calcul. Il est intéressant d'utiliser ces modèles car leur application nécessite la connaissance de propriétés connues du combustible MOX: expansion thermique, module d'élasticité isostatique, capacité thermique, coefficient d'extinction *etc.*. Même si la contribution électronique nécessite la connaissance de propriétés plus complexes (*i. e.* les énergies de migration des polarons ou l'enthalpie et l'entropie de création des polarons), l'utilisation de méthodes inverses a permis d'estimer les valeurs de ces paramètres, en utilisant des données expérimentales de conductivité électrique.

Ce chapitre a révélé des résultats novateurs concernant les effets corrélés de la teneur en plutonium et en oxygène sur la conductivité thermique.
La teneur en plutonium amplifie l'effet de la stœchiométrie sur la contribution des phonons à la conductivité thermique. Ceci a été expliqué comme étant dû aux cations Pu^{3+}, dont la fraction est proportionnelle à l'écart à la stœchiométrie x, et dont la force de diffusion des phonons augmente avec la teneur en plutonium en raison de l'augmentation avec la teneur en plutonium de la différence de rayon ionique entre le cation Pu^{3+} et le sous-réseau (U, Pu). Une autre raison de l'effet corrélé de la teneur en plutonium et en oxygène tient à la manière dont la stœchiométrie affecte la dépendance à la teneur en plutonium de la conductivité phononique. Nous avons montré qu'un écart croissant par rapport à la stœchiométrie induit un déplacement de la teneur en plutonium, à laquelle la conductivité thermique atteint un minimum, vers des valeurs de teneur en plutonium plus élevées. C'est-à-dire qu'à $x = 0.08$, le minimum de la conductivité thermique des phonons est observé autour de $y = 0.85$, alors qu'à $x = 0$, ce minimum est situé autour de $y = 0.15$. Ceci s'explique, une fois de plus, par les cations Pu^{3+}, qui pilotent la diffusion des phonons pour des écarts importants à la stœchiométrie.
Nous avons vu que les effets corrélés de la teneur en plutonium et en oxygène ne concernent pas seulement la contribution des phonons mais aussi celle des électrons. En effet, l'augmentation de l'écart à la stœchiométrie diminue l'effet de la teneur en plutonium, en raison de la création extrinsèque de polarons Pu^{3+}, qui l'emporte sur la création intrinsèque de Pu^{3+} qui elle dépend de la teneur en plutonium. Nous avons également vu qu'une déviation croissante de la stœchiométrie augmente la contribution du polaron Pu^{3+}. L'énergie de migration de ce dernier est d'un intérêt crucial pour éviter les incertitudes liées à la modélisation de l'effet de la stœchiométrie sur la conductivité électrique et thermique.

L'importance de prendre en compte les effets corrélés de la teneur en plutonium et en oxygène sur la conductivité thermique est cruciale pour les applications dans les réacteurs à neutrons rapides. En effet, nous avons vu qu'une redistribution importante du plutonium et de l'oxygène se produit en raison d'un gradient radial de température élevé. Le plutonium se redistribue vers le centre de la pastille de combustible, tandis que l'oxygène se déplace vers la périphérie du combustible. La modélisation de ces effets corrélés permet donc de fournir une estimation plus précise de la température locale du combustible. Les approches semi-

empiriques ne tiennent pas compte de cet effet et peuvent donc donner lieu à d'importantes incertitudes lorsqu'elles sont utilisées dans les codes de performance des combustibles pour simuler des irradiations en RNR.

L'analyse de sensibilité à la composition chimique des contributions phononique et électronique a révélé que les phonons sont plus sensibles aux lacunes d'oxygène, tandis que les polarons sont plus sensibles à la teneur en plutonium. Sur la base de ces observations, des données expérimentales supplémentaires ont été proposées dans les sections 3.6.2 et 3.6.1 respectivement, afin de réduire les incertitudes du modèle associées à l'effet de la teneur en plutonium et en oxygène.

Ce chapitre a également mis en évidence la sensibilité du modèle aux paramètres. Grâce à l'analyse de sensibilité, nous avons conclu que la contribution des phonons est principalement déterminée par la température de Debye et le paramètre de Gruneisen, tandis que la contribution électronique est déterminée par l'enthalpie de création et l'entropie des polarons. L'importance de l'énergie de migration des polarons augmente avec la température.

Ce chapitre a révélé les incertitudes associées à la conductivité thermique électronique et radiative. Il a été démontré que la conductivité thermique radiative était sous-estimée, en raison d'une surestimation du coefficient d'extinction moyen de Rosseland. Cela a conduit à la **perspective d'effectuer des mesures du coefficient d'extinction sur les combustibles MOX**. D'autre part, en raison de l'absence de données expérimentales sur la conductivité électrique pour des températures supérieures à 1400 K, les variations en température de la conductivité électrique et thermique sont entachées d'incertitudes. Ceci a révélé l'une des principales perspectives de ce chapitre: **effectuer des mesures de la conductivité électrique à des températures supérieures à 1380 K**. En effet, nous avons observé une variation de température particulière de la conductivité électrique et thermique, impliquant un point d'inflexion à des températures assez basses (autour de 1850 K). Nous avons montré que parmi les quatre paramètres du modèle électronique, l'enthalpie de création de polarons H **peut contribuer à traiter le problème du point d'inflexion en augmentant sa valeur**, produisant ainsi une augmentation presque monotone de λ^{el} avec les températures, comme prédit par la plupart des modèles empiriques. Nous avons également constaté que si la gestion du problème du point d'inflexion permet de trouver une plus grande cohérence avec les modèles empiriques, elle peut conduire à une diminution de la cohérence du modèle de conductivité électrique avec les mesures associées. Outre l'identification des principaux paramètres responsables du point d'inflexion, nous avons également identifié des incertitudes de modélisation possibles, telles que l'hypothèse selon laquelle les sauts de Pu-U ne sont pas susceptibles de se produire. En effet, l'ajout d'une troisième contribution peut contribuer à augmenter l'amplitude de la conductivité électrique et thermique. Cependant, **l'ajout d'une autre contribution ajoute également un autre paramètre de modèle: l'énergie de migration, associée au saut Pu-U.** Pour estimer cette dernière par des méthodes inverses, les données expérimentales de conductivité électrique disponibles ne sont pas suffisantes. Cela confirme la nécessité de disposer de données expérimentales supplémentaires au-delà de 1380 K.

Chapter 4

Calibration and validation of the model on the available experimental data

Contents

Summary

In the previous chapter, we presented the thermal conductivity model for the MOX fuel matrix. In this chapter, we will proceed to the validation of this model, using the most up-to-data experimental data on thermal conductivity of MOX fuels, provided by CEA, OECD, IAEA, EU projects. This experimental data counts a total number of 6619 experimental (λ_i, T_i) points and is presented in the beginning of this chapter. Comparison with experimental measurements will reveal that the model, proposed in the previous chapter, systematically yields lower thermal conductivity values than measurements. This observation will lead to:

1. the introduction of an empirical factor in the expression for the phonon term of thermal conductivity
2. the simultaneous use of both electrical and thermal conductivity experimental data, to provide new electronic parameters, using a Bayesian multi-objective cost function. This optimization will show if electrical and thermal conductivity can be fitted at the same time, with physical parameters, which was one of the concerns in the previous chapter.
3. the optimization of a new Rosseland extinction coefficient on electronic thermal conductivity residuals $(\lambda^{el}_{exp} - \lambda^{el}_{mo})$, where exp and mo stand for experimental and model, respectively.

Those three points are covered in three separate sections. At the end of this chapter, a detailed comparison of the new thermal conductivity model with measurements will be done. This comparison will focus on the consistency of the model with measurements, regarding the temperature, plutonium and oxygen content variation of thermal conductivity. The comparison between this work and other reported work on thermal conductivity will also be covered. This chapter will be finished by a conclusion and some perspectives.

Résumé

Dans le chapitre précédent, nous avons présenté le modèle de conductivité thermique de la matrice du combustible MOX. Dans ce chapitre, nous allons procéder à la validation de ce modèle, en utilisant les données expérimentales les plus récentes sur la conductivité thermique des combustibles MOX, provenant du CEA, de l'OCDE, de l'AIEA et de l'UE. Ces données expérimentales comptent un nombre total de 6619 points expérimentaux (λ_i, T_i) et sont présentées au début de ce chapitre. La comparaison avec les mesures expérimentales révèlera que le modèle proposé dans le chapitre précédent donne systématiquement des valeurs de conductivité thermique inférieures aux mesures. Cette observation conduira à:

1. l'introduction d'un facteur empirique dans l'expression du terme phononique de la conductivité thermique
2. l'utilisation simultanée des données expérimentales de conductivité électrique et thermique, pour fournir de nouveaux paramètres électroniques, en utilisant une fonction de coût multi-objectif, basée sur le théorème de Bayes. Cette optimisation montrera si la conductivité électrique et la conductivité thermique peuvent être ajustées en même temps, avec des paramètres physiques, ce qui était l'une des préoccupations du chapitre

précédent.

3. l'optimisation d'un nouveau coefficient d'extinction de Rosseland sur les résidus de conductivité thermique électronique ($\lambda^{el}_{exp} - \lambda^{el}_{mo}$), où exp et mo signifient respectivement expérimental et modèle.

Ces trois points sont traités dans trois sections distinctes. A la fin de ce chapitre, une comparaison détaillée du nouveau modèle de conductivité thermique avec les mesures sera effectuée. Cette comparaison se concentrera sur la cohérence du modèle avec les mesures, en ce qui concerne la variation de la conductivité thermique en fonction de la température, de la teneur en plutonium et en oxygène. La comparaison entre ce travail et d'autres travaux sur la conductivité thermique sera également abordée. Ce chapitre se terminera par une conclusion et quelques perspectives.

4.1 Available experimental data on thermal conductivity of MOX fuels

The experimental data, used for the validation of the model is provided by:

1. CEA [private com.]: **3844** measurement points
2. IAEA/Therpro [188]: **1415** measurement points
3. EU-projects (ESNII+ [189, 190], ESFR-SMART [108], PUMMA [109]): **1020** measurement points
4. OECD/EGIFE [191–194]: **340** measurement points

making a total of **6619** measurement points (λ_i, T_i), covering:

- temperatures in the range $T \in$ [323.2–3000] K
- plutonium contents in the range $y \in$ [0–1]
- oxygen/metal ratios in the range $\mathrm{O/M} = 2 - x \in$ [1.9–2] (x, being the deviation from stoichiometry)
- porosity in the range $p \in$ [0.02–0.215]

Out of those 6619 measurement points, **586** are determined by **direct techniques** (radial heat flow technique) and **6033** by **indirect measurement techniques** (Angstrom, Cowan, LAF or CLASH) (see Annex H). Indirect measurements consist of measuring thermal diffusivity d, heat capacity C_p and density ρ, therefore providing a measure of thermal conductivity, through: $\lambda = \rho C_p d$. **Heat capacity measurements are not systematically provided along with thermal diffusivity measurements** to deduce thermal conductivity. Therefore, the 6033 indirect (λ_i,T_i) points have been obtained by multiplying **measured** thermal diffusivity, density and **calculated heat capacity**, based on Kopp law:

$$C_p^{\mathrm{U_{1-y}Pu_yO_{2-x}}} = (1-y)\cdot C_p^{\mathrm{UO_2}} + y\cdot C_p^{\mathrm{PuO_2}} - \frac{x}{2}\cdot C_p^{\mathrm{O_2}} \tag{4.1}$$

where the heat capacities of UO_2 and PuO_2 are calculated with the models, proposed by Konings *et al.* [195], based on the most up-to-date heat capacity experimental data on UO_2 and PuO_2 systems. $C_p^{\mathrm{O_2}}$ are calculated from the model, proposed in [4]. We recall those equations:

$$\begin{aligned} C_p(\mathrm{UO_2}) = \big(&247.1735 + 1.5976\cdot 10^{-1}\cdot T \\ &-1.3199\cdot 10^{-4}\cdot T^2 + 4.3162\cdot 10^{-8}\cdot T^3 - \tfrac{4.3278\cdot 10^6}{T^2}\big) \end{aligned} \tag{4.2}$$

$$\begin{aligned} C_p(\mathrm{PuO_2}) = \big(&127.8532 + 5.5151\cdot 10^{-1}\cdot T \\ &-4.6097\cdot 10^{-4}\cdot T^2 + 1.3145\cdot 10^{-7}\cdot T^3 - \tfrac{1.2591\cdot 10^6}{T^2}\big) \end{aligned} \tag{4.3}$$

and $C_p(\mathrm{O_2})$ (in $\mathrm{J\,kg^{-1}\,K^{-1}}$) from the model, proposed by *Duriez et al.* [4]:

$$\begin{aligned} C_p(\mathrm{O_2}) = \big(&27.85 + 8.53\cdot 10^{-3}\cdot T \\ &-204.54\cdot 10^{-8}\cdot T^2 + 19.32\cdot 10^{-11}\cdot T^3\big) \end{aligned} \tag{4.4}$$

To facilitate its use, the experimental data has been stored under a python object: dataframe (.h5 file), a .csv file and a .xlsx file. Each experimental data set is described by the following information (when available):

- Fuel's sample name
- Fuel's microstructure (porosity : open and closed, grain size, fabrication process)
- Fuel's chemical composition (Pu and Am content (if any Am), O/M ratio: before and after the measurements)
- Experimental technique used to measure thermal diffusivity or conductivity.
- Experimental technique used to measure the O/M ratio
- Atmosphere during the measurement
- Run cycle (heating or cooling)
- Number of runs on the same sample (if multiple heat cycles have been realized on the same sample)
- Reference and author of the experimental data set

Table 4.1 summarizes the general characteristics of the data.

Origin	Author	Experimental technique	Direct/Indirect method	Temperature range (K)	Pu content range (y)	O/M range (2–x)	Porosity range (%)	Nb. of points
CEA	Alessandri	LAF	Indirect	829.15–1748.15	0.0787–0.0787	1.998–1.998	5.5–5.5	11
	Bonnerot	LAF	Indirect	973–2473	0.05–1	1.967–2	2.8–21.5	344
	Duriez [4]	LAF	Indirect	404–2278.15	0.03–0.45	1.948–2	3.8–5.3	2307
	GACID	LAF	Indirect	541.97–1461.8	0.19–0.19	2–2	5–5	23
	LEFCA–CAPR–145	LAF	Indirect	743–2073	0.45–0.45	1.961–1.961	5.5–5.5	82
	Ottaviani	LAF	Indirect	729–1923	0.1752–0.275	1.94–1.96	2.7–3.2	139
	Otter	Angstrom	Indirect	373–1073	0.05–0.3	1.985–2	0–6.4	120
		Cowan	Indirect	1173–1973	0.05–0.3	1.985–2	0–6.4	135
		LAF	Indirect	2073–2973	0.05–0.3	1.985–2	0–6.4	150
	SCARABIX	LAF	Indirect	688–2129	0.214–0.214	1.982–1.982	4–4	92
	TRUMOX	LAF	Indirect	717.461–2045.63	0.25–0.65	1.98–2	4–5	51
	Van–Craeynest and Stora [58]	Angstrom	Indirect	325.7–1172	0.2–0.2	2–2	5–20	62
	Van–Craeynest and Weilbacher [106]	Angstrom	Indirect	323.2–1137	0.2–0.2	1.902–2	5–5	105
		Cowan	Indirect	1273–1973	0.2–0.2	1.945–1.996	5–5	43
		LAF	Indirect	2073–2173	0.2–0.2	1.994–1.996	5–5	4
	Weilbacher	LAF	Indirect	773–2973	0.05–1	1.9–2	5–5	176
							Total CEA	***3844***
EU projects	ESFR–SMART [108]	CLASH	Indirect	1740.2–2820.9	0.29–0.31	1.981–1.995	5.8–7.3	68
		LAF	Indirect	542.59–1519.4	0.29–0.31	1.995–1.995	5.8–7.3	58
	ESNII+ [189, 190]	CLASH	Indirect	1652.4–2881	0.24–0.45	1.971–2	4.8–6.9	131
		LAF	Indirect	541.57–1647.6	0.24–0.45	1.999–2	4.8–7.3	438
	PUMMA [109]	CLASH	Indirect	1668.5–2858.2	0.6–1	1.98–2	5–5	196
		LAF	Indirect	542.78–1634	0.6–0.7	1.98–2	5–5	129
							Total EU projects	***1020***
IAEA	ANL [196]	Radial heat flow	Direct	800–3000	0.2–0.2	1.9–2	5–5	21
	Elbel and Schmidt [197]	Cowan	Indirect	1048–1692	0.209–0.252	1.936–1.962	4.4–7.3	107
	Evans [198]	Radial heat flow	Direct	1141–1771	0.2–0.2	1.94–2	8.3–8.3	24
	Fukushima [98]	LAF	Indirect	691.2–1819	0.2–0.2	2–2	4.1–4.1	72
	Gibby [117, 122, 199, 200]	LAF	Indirect	360.2–1873	0.05–0.3	1.933–2	2–4.6	504
	Hetzler [201]	Radial heat flow	Direct	1075–2164	0.2–0.2	1.982–2	3.6–5.7	51
	Laskiewicz [202]	Radial heat flow	Direct	1076–2540	0.1–0.3	1.94–2	9–16	436
	Morimoto [192, 203, 204]	LAF	Indirect	872.467–1865.343	0.2–0.4	2–2	0–0	46
	Serizawa [78]	Cowan	Indirect	1099.901–2105.749	0.1–0.2	1.98–1.99	3.9–4.1	100
	Yamaguchi [205]	Radial heat flow	Direct	1073.2–2673.2	0.3–0.3	1.94–2	5–20	54
							Total IAEA	***1415***
OECD	Morimoto [191, 192]	LAF	Indirect	870.667–2249	0.2952–0.3	1.903–2	4.8–15.7	296
	Rao [206]	LAF	Indirect	673–1473	0.21–0.4	2–2	4–4	25
	Sengupta [193]	LAF	Indirect	915.862–1862.069	0.04–0.44	1.98–1.997	5–9.5	19
							Total OECD	***340***
							Total	***6619***

Table 4.1: General characteristics of the available experimental data on thermal diffusivity and conductivity of MOX fuels

4.2 Validation of the proposed thermal conductivity model

In this section, we proceed to the validation of the model, proposed in the previous chapter, using the above mentioned thermal conductivity experimental data.
This data is based on poly crystals and therefore is a measurement of the effective thermal conductivity λ^{eff} of the material. To deduce the thermal conductivity of the matrix λ_m, out of λ_{eff}, we use the Maxwell-Eucken porosity correction, recalled here [85, 86]:

$$\lambda_m = \lambda_{eff} \cdot \frac{1 + 0.5 \cdot p}{1 - p}$$

where p is the fractional porosity ($0 < p < 1$).
For the sake of notation clarity, the m subscript in λ_m will be omitted from now on. λ will therefore refer to the thermal conductivity of the (U,Pu)O_2 fuel matrix.

We recall from Chapter 2 that the Maxwell-Eucken's simplified equation has been chosen to stay consistent with spherical and dispersed pores, which accurately represents the porosity of MOX after fabrication, where porosity does not exceed $p = 0.05$. We shall mention that other microstructure effects have to be taken into account to properly deduce the thermal conductivity of the matrix out of thermal conductivity measurements: grain boundaries, grain size, dislocations, self-irradiation damage.
In this work, **those effects were not studied and therefore only the porosity effect was considered**.

Figure 4.1 shows the variation with temperature of the experimental data and our model, for multiple deviations from stoichiometry x. The model was plotted for a plutonium content of $\overline{y} = 0.21$, representing the **weighted** average plutonium content of the whole experimental data set: $\overline{y} = \frac{\sum_0^{n_y} n_i y_i}{\sum_0^{n_y} n_i}$, where n_i is the number of experimental points per plutonium content, y_i - the plutonium content and n_y - the number of plutonium contents.
As shown in Figure 4.1, the model underestimates the experimental data, at both low and high temperature, regardless of the deviation from stoichiometry x. Given those discrepancies, in the next section we will calibrate some of the model parameters to the available experimental data.

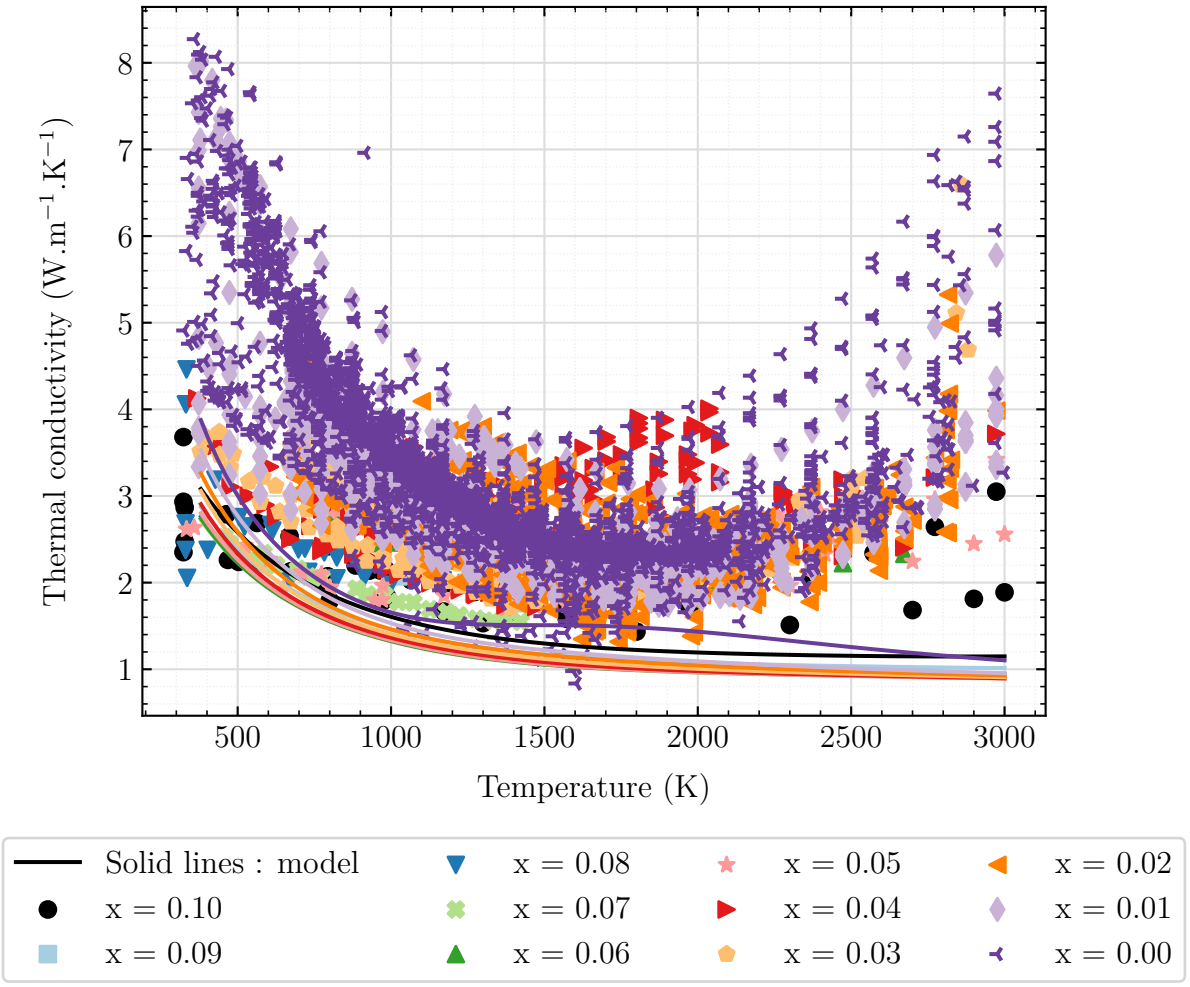

Figure 4.1: Variation with temperature of thermal conductivity of the (U,Pu)O_2 fuel matrix, for multiple deviations from stoichiometry $x = 2-O/M$, according to experimental data (markers) and to our model (solid lines). The model was shown for a plutonium content of $y = 0.21$, whereas the experimental data considers all plutonium contents (*i. e.* 6619 measurement points).

4.3 Calibration of the model for the phonon contribution to thermal conductivity and proposal of a modified model

We will firstly consider the discrepancies between the experimental data and the phonon term. We recall the phonon contribution to thermal conductivity:

$$\lambda^{ph} = \frac{1}{A + BT} = \frac{1}{\frac{\pi^2 a^3 \theta_D}{12(3-x)\overline{v_p}^2 h}\Gamma + \frac{\gamma_\infty^2 n_a^{2/3}}{B^* \overline{M} \theta_D^3 \overline{V_a}^{1/3}} \cdot T}$$

For the physical meaning of the parameters, see Equation 3.70.

In the previous chapter, we saw that the driving parameters in the phonon term are Debye temperature and Gruneisen parameter (see Section 3.2.5.3).
We deduced those parameters from measured properties. The latter were taken from the most up-to-date experimental data on MOX fuel [126, 127, 187, 207], confirming the accuracy of Debye temperature and Gruneisen parameter, calculated in this work.
Those parameters have an explicit physical meaning and therefore modifying them by introducing empirical factors does not seem appropriate.
The only term, the physical meaning of which, has never been clearly identified in subsequent reported work, is the B^* parameter in the expression for the intrinsic thermal resistivity BT.
This parameter was firstly reported by Leibfried and Schlomann [137] as a constant, then Julian [125] reported an error in their value, and proposed for B^* a Gruneisen parameter-dependent function (see Equation 3.24).
Given the discrepancies for this parameter, reported by different authors, the calibration of the phonon term will concern B^*, instead of the other model parameters, which have an explicit physical meaning.

The calibration of the phonon term therefore consists of introducing an empirical factor b_{emp}, which multiplies B^* as follows:

$$\lambda^{ph} = \frac{1}{A + \frac{\gamma_\infty^2 n_a^{2/3}}{\boldsymbol{b_{emp}} \cdot \boldsymbol{B^*} \overline{M} \theta_D^3 \overline{V_a}^{1/3}} \cdot T} \tag{4.5}$$

To obtain b, we firstly fitted the "experimental" A_{exp} and B_{exp} values to obtain an experimental evaluation of the phonon term λ_{exp}^{ph}, using thermal conductivity experimental data before $T =$ 1500 K (*i. e.* in the temperature range of the phonon contribution). Then b_{emp} was obtained, by solving for b_{emp} the following equation:

$$\frac{1}{A + \frac{\gamma_\infty^2 n_a^{2/3}}{\boldsymbol{b_{emp}} \cdot \boldsymbol{B^*} \overline{M} \theta_D^3 \overline{V_a}^{1/3}} \cdot T} = \lambda_{exp}^{ph} = \frac{1}{A_{exp} + B_{exp} \cdot T} \tag{4.6}$$

where A assumes its theoretical value.

Thermal conductivity experimental data, covering $x \in [0 - 0.1]$ allowed to obtain en empirical correlation of the experimental A_{exp} and B_{exp}, with x (see Figure 4.2).

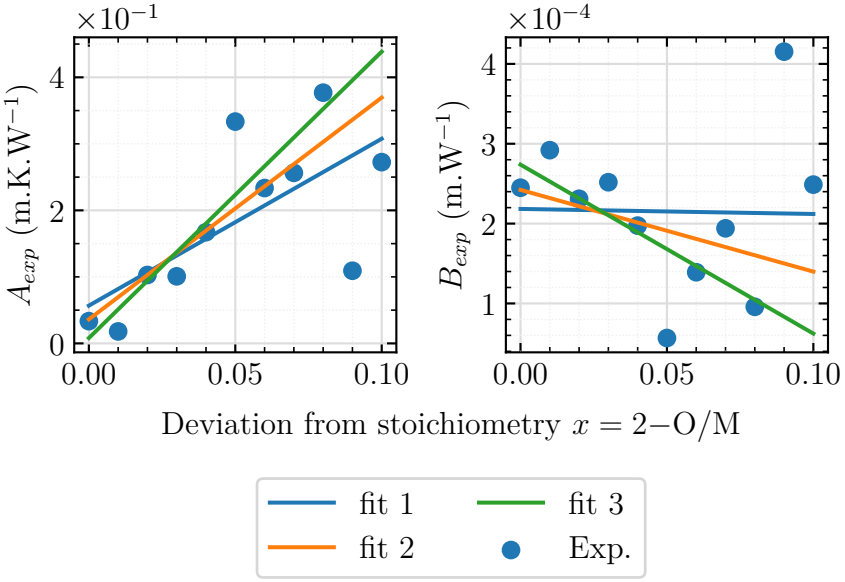

Figure 4.2: Variation with deviation from stoichiometry x (in $U_{1-y}Pu_yO_{2-x}$) of the optimized A_{exp} and B_{exp}, using thermal conductivity experimental data, before $T = 1500$ K. The lines correspond to the fits of $A_{exp}(x)$ and $B_{exp}(x)$. Three fits were performed - fit 1: all points considered, fit 2: without considering the point at x = 0.09, fit 3: without considering the points at x = 0.1 and x = 0.09.

No experimental correlation with plutonium content y was performed, since according to our sensitivity analysis (see Section 3.2.5.2), at relatively low plutonium contents (here $\overline{y} = 0.21$), the effect of stoichiometry is greater than that of plutonium content.

The optimization led to three $A_{exp}(x)$ and $B_{exp}(x)$ correlations, depending on the number of deviations from stoichiometry x, considered.
As shown in Figure 4.2, the optimized A_{exp} and B_{exp} show a quite steep linear increase and decrease respectively with x, until $x = 0.08$.
Considering the two points at $x = 0.09$ and $x = 0.1$ tend to lower the slope of the linear variations. For $B_{exp}(x)$, the slope is almost null, when the points at $x = 0.09$ and $x = 0.1$ are considered.
Indeed, very few measurements are available at $x = 0.09$ (**only 12 points**) and $x = 0.10$ (**only 48 points**) (see Table 6 in Annex I), thus leading to high uncertainties, associated with the estimation of A_{exp} and B_{exp} at those stoichiometries.
For this reason, we retain the correlations, without considering the points at $x = 0.09$ and $x = 0.1$, which yield the following $A_{exp}(x)$ and $B_{exp}(x)$ variations:

$$A_{exp}(x) = 4.3053 \cdot x + 8.0814 \cdot 10^{-3} \tag{4.7}$$

$$B_{exp}(x) = (-21.1577 \cdot x + 2.7384) \cdot 10^{-4} \tag{4.8}$$

where A_{exp} and B_{exp} are expressed in ($\mathrm{m\,K\,W^{-1}}$) and ($\mathrm{m\,W^{-1}}$) respectively.

Using Equations 4.7 and 4.8 for A_{exp} and B_{exp}, b_{emp} was obtained by solving Equation 4.6 for b_{emp}.
The solutions of this equation were both x and T-dependent, since our theoretical evaluation of A and B is both x and T dependent.
Those solutions were fitted to an empirical equation of the form:

$$b_{emp}(x,T) = f_1(x) \cdot T^6 + f_2(x) \cdot T^5 + f_3(x) \cdot T^4 + f_4(x) \cdot T^3 + f_5(x) \cdot T^2 + f_6(x) \cdot T + f_7(x) \tag{4.9}$$

where:

$$f_i(x) = p_1 \cdot x^6 + p_2 \cdot x^5 + p_3 \cdot x^4 + p_4 \cdot x^3 + p_5 \cdot x^2 + p_6 \cdot x + p_7 \tag{4.10}$$

with the p coefficients being tabulated in Table 4.2. The physical meaning of this correlation cannot be interpreted, since no explicit meaning was reported by Julian [125], or Leibfried and Schlomann [137] for the B^* parameter.
What, however, can be said is that computing b_{emp} at $x = 0$ and $T = 1000$ K, gives $\boldsymbol{b_{emp}(0, 1000) = 2.44}$.
This means that to obtain better consistency with the experimental estimation λ^{ph}_{exp} (at $x = 0$ and $T = 1000$ K), the B^* parameter, **given in the original model, must be multiplied by a factor of 2.44**.

	f_1	f_2	f_3	f_4	f_5	f_6	f_7
p_1	8.9187 $\cdot 10^{-13}$	-9.4066$\cdot 10^{-9}$	3.9736$\cdot 10^{-5}$	-8.5828$\cdot 10^{-2}$	9.9783$\cdot 10^{1}$	-5.8240$\cdot 10^{4}$	1.3181 $\cdot 10^{7}$
p_2	-3.6828 $\cdot 10^{-13}$	3.8820$\cdot 10^{-9}$	-1.6350$\cdot 10^{-5}$	3.5070$\cdot 10^{-2}$	-4.0312$\cdot 10^{1}$	2.3315$\cdot 10^{4}$	-5.2429$\cdot 10^{6}$
p_3	6.4486 $\cdot 10^{-14}$	-6.8219$\cdot 10^{-10}$	2.8795$\cdot 10^{-6}$	-6.1702$\cdot 10^{-3}$	7.0421	-4.0327$\cdot 10^{3}$	8.9919$\cdot 10^{5}$
p_4	-6.1139 $\cdot 10^{-15}$	6.5259$\cdot 10^{-11}$	-2.7828$\cdot 10^{-7}$	6.0280$\cdot 10^{-4}$	-6.9414$\cdot 10^{-1}$	3.9860$\cdot 10^{2}$	-8.8890$\cdot 10^{4}$
p_5	3.2049 $\cdot 10^{-16}$	-3.4695$\cdot 10^{-12}$	1.5073$\cdot 10^{-8}$	-3.3490$\cdot 10^{-5}$	3.9940$\cdot 10^{-2}$	-2.4035$\cdot 10^{1}$	5.5678$\cdot 10^{3}$
p_6	-7.9317$\cdot 10^{-18}$	8.7298$\cdot 10^{-14}$	-3.8825$\cdot 10^{-10}$	8.9368$\cdot 10^{-7}$	-1.1300$\cdot 10^{-3}$	7.6392$\cdot 10^{-1}$	-2.1183$\cdot 10^{2}$
p_7	4.3791 $\cdot 10^{-20}$	-4.8433$\cdot 10^{-16}$	2.1689$\cdot 10^{-12}$	-5.0407$\cdot 10^{-9}$	6.4854$\cdot 10^{-6}$	-4.4516$\cdot 10^{-3}$	3.7242

Table 4.2: p coefficients for the calculation of $f_i(x)$ in Equation 4.10.

We compared the A and B terms from this work (both theoretical and experimental) with those of the literature (see Figure 4.3).
Clear discrepancies are observed, between all reported empirical values for A.
Indeed, at the stoichiometric composition, $x = 0$, the extrinsic thermal resistivity is dispersed in the range $[0.02 - 0.06]$ $\mathrm{m\,K\,W^{-1}}$. Those discrepancies become even higher for higher deviations from stoichiometry. That is, at $x = 0.10$, $A \in [0.02 - 0.41]$ $\mathrm{m\,K\,W^{-1}}$.
Those disparities mostly originate from the available experimental data, used for the optimization of A on thermal conductivity experimental data.
For example, Inoue [107] only used measurements at $x = 0$ and $x = 0.02$, therefore highlighting the difficulties, related to the extrapolation of the model of Inoue to $x > 0.02$.
Magni *et al.* [33] predicts a surprisingly low value for A: 0.02 $\mathrm{m\,K\,W^{-1}}$. According to their

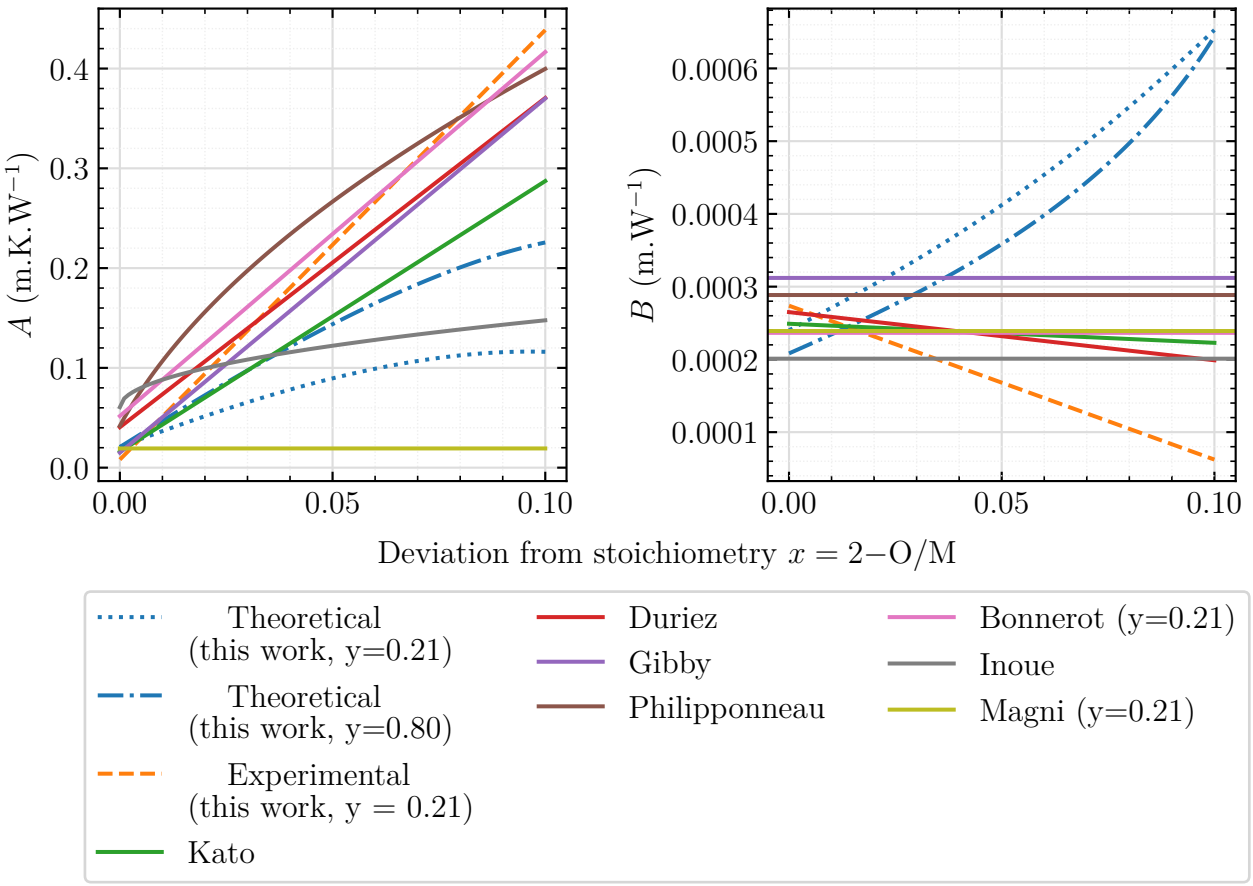

Figure 4.3: Variation of intrinsic B and extrinsic A thermal resistivity with deviation from stoichiometry x, according to this work (theoretical and experimental) and to empirical values, reported in the literature [2–5, 33, 107, 122]

model, the extrinsic thermal resistivity (*i. e.* due to phonon-impurity interactions) is therefore negligible to the intrinsic one (*i. e.* due to phonon-phonon interactions).

Indeed, important dispersion between the reported empirical values for B is also observed: $B \in [2 \cdot 10^{-4} - 4 \cdot 10^{-4}]$ m W^{-1}. Those discrepancies between the reported empirical values for both A and B highlight the sensitivity of empirical approaches to the experimental data, used for the calibration.

In this work, we performed the calibration of A_{exp} and B_{exp}, using all available experimental data, covering $x \in [0 - 0.1]$.
Our estimation for A seems consistent with the empirical values of Duriez *et al.* [4], Gibby [200] and Philipponneau [2].
As for B_{exp}, the least squares estimation showed a linear decrease with deviation from stoichiometry, which is consistent with the models of Kato *et al.* [3] and Duriez [4]. However, our linear decrease is more pronounced than that of Kato *et al.* and Duriez. This might be due to the use of less experimental data in other reported work and to the frequently limited range of x, covered by the data.

Another reason for the higher slope of our decreasing function is the fact that we did not consider the experimental points at $x = 0.09$ and $x = 0.10$, due to the low number of measurements at those stoichiometries. Indeed, as we showed in Figure 4.2, if $x = 0.09$ and $x = 0.10$ were taken into account, a rather constant variation of B_{exp} with x is observed, which seems to be more consistent with other empirical models.

The theoretical A value from Chapter 3 is plutonium content-dependent and is lower than the experimental A_{exp} one.
Those discrepancies could be explained by the phonon model driving parameters, which according to our sensitivity analysis from Chapter 3 are Debye temperature and Gruneisen parameter. To compensate for this possible underestimation of the extrinsic thermal resistivity A, the theoretical intrinsic thermal resistivity BT (from this chapter), yields higher values than the experimental value B_{exp}.
We observe that the theoretical B is a rather increasing function of the deviation from stoichiometry, whereas B_{exp} shows a decreasing function. Indeed, those discrepancies are not surprising given the intrinsic dependency of the theoretical B to deviation from stoichiometry, which originates from the model parameters' dependency on x: Debye temperature, lattice parameter and Gruneisen parameter.
Even though B_{exp} was used to calibrate the empirical factor b_{emp}, it does not change the intrinsic variation of B with x.

4.4 Calibration of the model for the electron contribution to thermal conductivity and proposal of a modified model

We recall the temperature-variation of the electronic thermal conductivity model:

$$\lambda^{el}(\mathbf{T}) = \left(\frac{k}{e}\right)^2 \mathbf{T} \frac{\sigma^{el}_{Pu}(\mathbf{T})\sigma^{el}_{U}(\mathbf{T})}{\sigma^{el}_{Pu}(\mathbf{T}) + \sigma^{el}_{U}(\mathbf{T})} \left(\frac{H}{k\mathbf{T}}\right)^2$$

where:

$$\sigma^{el}_{Pu}(\mathbf{T}) = \frac{4e^2 v_{0,opt}}{ak\mathbf{T}} \left((c_{U^{5+}}(\mathbf{T}) + 2x)(y - c_{U^{5+}}(\mathbf{T}) - 2x)e^{-\frac{E_m(Pu)}{k\mathbf{T}}}\right)$$

$$\sigma^{el}_{U}(\mathbf{T}) = \frac{4e^2 v_{0,opt}}{ak\mathbf{T}} \left(c_{U^{5+}}(\mathbf{T})(1 - y - c_{U^{5+}}(\mathbf{T}))e^{-\frac{E_m(U)}{k\mathbf{T}}}\right)$$

$$c_{U^{5+}}(\mathbf{T}) = \frac{K_{pol}(\mathbf{T})(1-2x) + 2x - \sqrt{\begin{array}{c} K_{pol}(\mathbf{T})^2(4x^2 - 8xy + 4x + 4y^2 - 4y + 1) \\ +K_{pol}(\mathbf{T})(-8x^2 + 8xy - \\ 4x - 4y^2 + 4y) + 4x^2 \end{array}}}{2(K_{pol}(\mathbf{T}) - 1)}$$

$$K_{pol}(\mathbf{T}) = \exp\left(-\frac{H}{k\mathbf{T}} + \frac{S}{k}\right)$$

where x: deviation from stoichiometry in $U_{1-y}Pu_yO_{2-x}$, y: plutonium content in $U_{1-y}Pu_yO_{2-x}$. For the model parameters $H, S, E_m(Pu), E_m(U)$ and $v_{0,opt}$ see Table 3.9.

In this section, we will focus on fitting the temperature-variation of thermal conductivity. Indeed, one of the most challenging points in the previous chapter was finding a plausible explanation for the inflection point in the $\lambda^{el}(T)$ curve. We concluded that this problematic can be treated by increasing the value of the H parameter in the model, but that at the same time, this might lead to decrease the consistency of the associated electrical conductivity model with measurements.

Since the H parameter has only been calibrated using electrical conductivity experimental data, in this chapter we propose to use thermal conductivity experimental data.

For each optimization, we systematically checked the ability of the newly identified parameters to describe the electrical conductivity measurements. Unfortunately, none of the estimated parameter sets was able to reproduce the correct experimental variation in electrical conductivity.

Figure 4.4 shows the inadequacy of the electrical conductivity model to reproduce experimental data, when parameters are optimized using only thermal conductivity data.

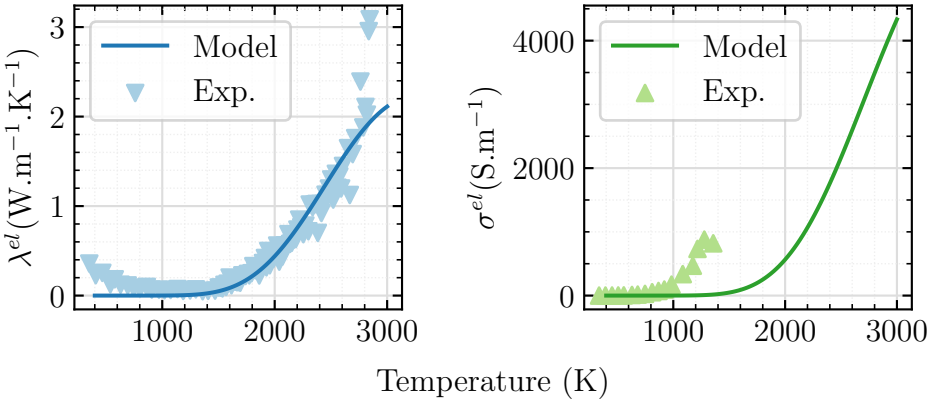

Figure 4.4: Sampled experimental thermal and electrical conductivity data, and their associated models. The models are evaluated at the estimated parameters, optimized on **thermal conductivity experimental data**, yielding: H = 2.80 eV, S/k = 7.73, $E_m(Pu)$ = 0.06 eV, $E_m(U)$ = 0.04 eV

On the opposite, when optimizing the parameters, using only electrical conductivity experimental data (as already done in the previous chapter), the associated thermal conductivity model fails to reproduce thermal conductivity experimental data (see Figure 4.5).

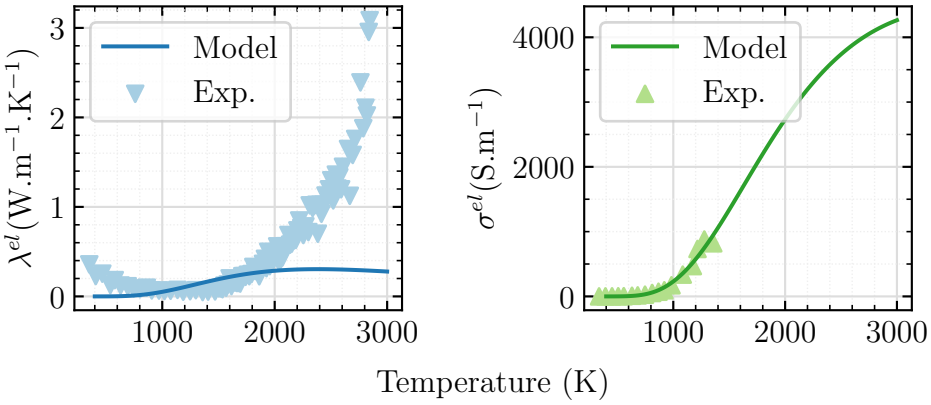

Figure 4.5: Sampled experimental thermal and electrical conductivity data, and their associated models. The models are evaluated at the estimated parameters, optimized on **electrical conductivity experimental data**, yielding H = 1.00 eV, S/k = 1.1, $E_m(Pu)$ = 0.06 eV, $E_m(U)$ = 0.08 eV

We therefore performed other optimizations, using a multi-objective cost-function, which considers thermal and electrical conductivity experimental data at the same time.
The thermal conductivity experimental data, used for the optimization was described in Annex J.
As shown in Figure 4.6, it is possible to fit thermal and electrical conductivity data at the same time. However, the physical sens of the parameters is not preserved. In particular we obtain negative migration energies for the polarons, which could not be physical. If now we extrapolated both electrical and thermal conductivity models with negative energies in the

Arrhenius functions, infinite values for λ and σ would be found at high temperatures. This is not acceptable if one is concerned with the predictive nature of the model outside of its fitting range.

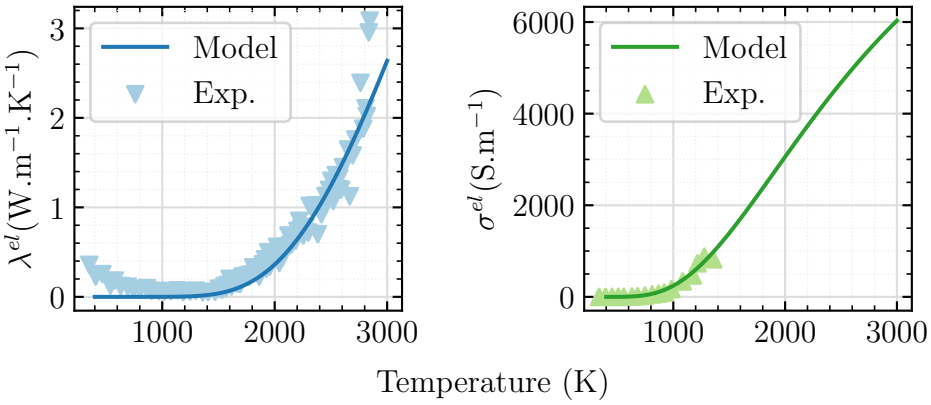

Figure 4.6: Sampled experimental thermal and electrical conductivity data, and their associated models. The models are evaluated at the estimated parameters, optimized on **both thermal and electrical conductivity experimental data**, yielding H = 10.05 eV, S/k = 1.43, $E_m(Pu) = -3.57$ eV, $E_m(U) = -4.47$ eV

In summary, we found that estimating model parameters using electrical conductivity measurements alone failed to reproduce experimental thermal conductivity data, and vice versa: using thermal conductivity measurements alone to estimate model parameters failed to achieve consistency with electrical conductivity measurements.
We also saw that optimizing both electrical and thermal conductivity at the same time, using a multi-objective cost function, is possible, but non-physical parameters are obtained.
In this thesis, the physical meaning of the model is our primary concern. Preserving the physical sens of the estimated parameters is key if we want to be able to extrapolate the model to a wide range of temperatures, plutonium and oxygen contents.
In order to find out if thermal and electrical conductivity measurements can be fitted with a set of physical parameters, we will use the Bayesian optimization approach.
With this approach, the cost function not only involves electrical and thermal conductivity data but also a prior information about the parameters. By prioritizing information about measurements over parameters and vice-versa, the Bayesian optimization enables us to find the best possible compromise between quality fits of thermal and electrical conductivity data and physical parameters.

4.4.1 Bayesian optimization

Bayesian optimization [208–211] is based on the Bayes theorem, the essential result of which is an additional term in the cost function J, as opposed to the classical least squares J^{LSQR}:

$$\boxed{J = J^{LSQR} + (\boldsymbol{\beta} - \boldsymbol{\beta}_{\text{ap}})^{\mathbf{T}} \mathbf{S}_{\mathbf{ap}}^{-\mathbf{1}} (\boldsymbol{\beta} - \boldsymbol{\beta}_{\text{ap}})} \tag{4.11}$$

where J^{LSQR} is the classical least-squares cost function characterizing the distance between the measurement $\mathbf{y}$ and the model output $\mathbf{f}(\mathbf{t}, \boldsymbol{\beta})$ (see Equation 3.61), $\boldsymbol{\beta}_{\text{ap}}$ is called the *a priori* parameters vector and $\mathbf{S_{ap}}$ the associated covariance matrix.
The Bayesian approach is based on the assumption that the probability density function of the parameters is a normal distribution: $N(\beta_{ap}, \sigma_\beta^2)$, with a mean value of β_{ap} and a standard deviation σ_β. Information about the characteristics of the normal distribution: β_{ap} and σ_β can originate from personal knowledge of the parameters: literature data, sensitivity analysis *etc.*

4.4.1.1 Cost function

In our case, since a simultaneous optimization using electrical and thermal conductivity experimental data will be performed, the J^{LSQR} term in Equation 4.11 will be composed of three cost functions:

1. J^{λ}, characterizing the difference between thermal conductivity experimental data and the electronic thermal conductivity model, evaluated at $x = 0, \overline{y} = 0.31$ (mean plutonium content of the high-temperature experimental data). Indeed, the effect of stoichiometry on thermal conductivity at high temperature is slight. In addition, the experimental data at high temperatures (*i. e.* $T > 2300$ K) is mainly composed of stoichiometric MOX fuels ($x = 0$). Furthermore, due to highly scattered experimental data at high temperatures, it is very difficult to observe the effect of plutonium. The weighted average plutonium content of the experimental data is $\overline{y} = 0.31$ (weighted by the number of experimental points per plutonium content). For those reasons, the model was evaluated at $x = 0, \overline{y} = 0.31$.
2. $J^{\sigma^{el}}_{x=0}$, characterizing the difference between electrical conductivity experimental data on stoichiometric MOX fuel, and the electrical conductivity model, evaluated at $x = 0$, $\overline{y} = 0.56$. Indeed, Fujino *et al.* [159] reported data for $y = 0.3, 0.5, 0.9$. This corresponds to a mean plutonium content of $\overline{y} = 0.56$.
3. $J^{\sigma^{el}}_{x>0}$, characterizing the difference between electrical conductivity experimental data on hypostoichiometric MOX fuel, and the electrical conductivity model, evaluated at $\overline{x} = 0.03$, $y = 0.2$. Indeed, Schmitz [162] reported data for $y = 0.2$ and $x \in [0.02 - 0.04]$, corresponding to a mean of $\overline{x} = 0.03$.

When building a global cost function J, out of elementary cost functions J^i, and especially when using Bayesian approach, which adds a supplementary term, one needs to **weight** each elementary cost function [208].
This weight depends on the particular problem. It can be composed of the number of measurement points, the mean of the experimental data or it can include hyper-parameters, which mathematically add more weight.
Here in particular, we deal with only 220 electrical conductivity measurement points, versus 6619 thermal conductivity points. In addition, electrical and thermal conductivity are not expressed in the same units. If the number of measurement points is not introduced in the cost function, the thermal conductivity cost function J^{λ} will naturally outweigh $J^{\sigma^{el}}_{x=0}$ and $J^{\sigma^{el}}_{x>0}$, due to the higher number of λ_i data, compared to σ_i.
For this reason, we need to normalize each elementary cost function by the associated number

of measurement points. We also need to normalize by the mean value of the experimental data set, as thermal and electrical conductivity are not expressed in the same units.
We also introduce mathematical hyper-parameters. Those will artificially add more weight to one cost function, as opposed to another, independently of the number of experimental points.

In this case, our J^{LSQR} cost function is therefore written as:

$$J^{LSQR} = \sum_j J^j = J^\lambda + J^{\sigma^{el}}_{x=0} + J^{\sigma^{el}}_{x>0} \tag{4.12}$$

where the elementary contributions J^j are expressed as:

$$J^j = \sum_i^{m_j} P_i^j \left(y_i^j - f_i^j(t_i^j, \beta)\right)^2 = \left(\mathbf{y^j} - \mathbf{f^j(t^j, \beta)}\right)^{\mathbf{T}} \mathbf{P^j} \left(\mathbf{y^j} - \mathbf{f^j(t^j, \beta)}\right) = \mathbf{r^j}^{\mathbf{T}} \mathbf{P^j r^j} \tag{4.13}$$

where j refers to the specific data set: thermal conductivity, electrical conductivity at $x = 0$ and $x > 0$ and:

- $\mathbf{r}$: residuals $= \mathbf{y} - \mathbf{f(t, \beta)}$
- $\boldsymbol{\beta}$: vector, containing the parameters to be optimized
- m : number of measurements
- $\mathbf{y}$: vector, with experimental data. The experimental electronic thermal conductivity λ^{el}_{exp} is deduced, by subtracting the experimental phonon contribution $\dfrac{1}{A_{exp} + B_{exp}T}$ from the total experimental thermal conductivity (see Equations 4.7 and 4.8 for A_{exp} and B_{exp}). Radiative thermal conductivity has been neglected here, due to its probable overestimation, mentioned in Section 3.4.4, Chapter 3.
- $\mathbf{t}$: vector, with the independent variable (*i. e.* here the temperature)
- $\mathbf{f}$: vector, containing the model. We recall that:

$$f^j = \begin{cases} \lambda^{el}(x = 0, \overline{y} = 0.31), & \text{if } j = \lambda \\ \sigma^{el}(x = 0, \overline{y} = 0.56), & \text{if } j = \sigma^{el}_{x=0} \\ \sigma^{el}(\overline{x} = 0.03, y = 0.2), & \text{if } j = \sigma^{el}_{x>0} \end{cases} \tag{4.14}$$

with σ^{el}, given by Equation 3.58 and λ^{el} by Equation 3.35

- $\mathbf{P^j}$: $(P^j_{ik})_{1 \leq i,l \leq m_j}$ is the $[m \times m]$ weighing diagonal matrix, where the diagonal elements are expressed as:

$$P^j_{ik} = p^m \cdot \frac{p^j}{\overline{\mathbf{y^j}} \cdot m_j} \tag{4.15}$$

where $\overline{\mathbf{y}^j}$ is the mean of the j-th experimental data set, p^m is an hyper-parameter, describing the weight of the measurements with respect to the Bayesian term and p^j are the elementary

hyper-parameters, expressed as:

$$p^j = \begin{cases} p^\lambda, & \text{if } j = \lambda \\ (1-p^\lambda)p^{\sigma^{el}}_{x=0}, & \text{if } j = \sigma^{el}_{x=0} \\ (1-p^\lambda)(1-p^{\sigma^{el}}_{x=0}), & \text{if } j = \sigma^{el}_{x>0} \end{cases} \tag{4.16}$$

In this formalism, we have two elementary hyper-parameters, describing:

1. the weight of thermal conductivity data, with respect to electrical conductivity: p^λ
2. the weight of stoichiometric electrical conductivity data, with respect to hypostoichiometric data: $p^{\sigma^{el}}_{x=0}$

The total cost function to be minimized is thus given by:

$$J = J^\lambda + J^{\sigma^{el}}_{x=0} + J^{\sigma^{el}}_{x>0} + J^\beta \tag{4.17}$$

where J^β is the supplementary term, originated from the Bayesian approach, expressed as:

$$J^\beta = (\boldsymbol{\beta} - \boldsymbol{\beta}_{\text{ap}})^{\mathbf{T}} \mathbf{P}^{\boldsymbol{\beta}} (\boldsymbol{\beta} - \boldsymbol{\beta}_{\text{ap}}) \tag{4.18}$$

where $\mathbf{P}^{\boldsymbol{\beta}} : (P^{\beta_l}_{ik})_{1 \leq i,k \leq n}$ is a $[n \times n]$ weighing diagonal matrix, with diagonal elements:

$$P^\beta_{ik} = (1 - p^m) \cdot \frac{1}{\sigma_{\beta_l} \cdot n} \tag{4.19}$$

where n is the number of parameters, p^m - the weight of the measurements with respect to the Bayesian term and σ_{β_l} - the standard deviation of the l-th *a priori* parameter.
The total cost function can be written in a more general way as:

$$J = (\mathbf{y} - \mathbf{f}(\mathbf{t}, \boldsymbol{\beta}))^{\mathbf{T}} \mathbf{P} (\mathbf{y} - \mathbf{f}(\mathbf{t}, \boldsymbol{\beta})) \tag{4.20}$$

where:

$\mathbf{t} : < \mathbf{t}^\lambda, \mathbf{t}^{\sigma^{\mathbf{el},0}}, \mathbf{t}^{\sigma^{\mathbf{el},>0}}, \mathbf{t}^\beta > \in \mathbb{R}^{m=m_\lambda + m_{\sigma^{el},0} + m_{\sigma^{el},>0} + n}$
$\mathbf{y} : < \mathbf{y}^\lambda, \mathbf{y}^{\sigma^{\mathbf{el},0}}, \mathbf{y}^{\sigma^{\mathbf{el},>0}}, \mathbf{y}^\beta > \in \mathbb{R}^{m=m_\lambda + m_{\sigma^{el},0} + m_{\sigma^{el},>0} + n}$
$\mathbf{f} : < \mathbf{f}^\lambda, \mathbf{f}^{\sigma^{\mathbf{el},0}}, \mathbf{f}^{\sigma^{\mathbf{el},>0}}, \boldsymbol{\beta} > \in \mathbb{R}^{m=m_\lambda + + m_{\sigma^{el},0} + m_{\sigma^{el},>0} + n}$
$\mathbf{P} : < \mathbf{P}^\lambda, \mathbf{P}^{\sigma_{\mathbf{el},0}}, \mathbf{P}^{\sigma_{\mathbf{el},>0}}, \mathbf{P}^{\boldsymbol{\beta}} >$, a $[m \times m]$ matrix, where $m = m_\lambda + m_{\sigma^{el},0} + m_{\sigma^{el},>0} + n$

The 0 and > 0 superscripts refer to stoichiometric $x = 0$ and hypostoichiometric $x > 0$ electrical conductivity experimental data.

4.4.1.2 Minimization algorithm

The minimization of this cost function was performed with the Marquardt-Levenberg algorithm, [168, 169], recalled here:

$$\boldsymbol{\beta}^{k+1} = \boldsymbol{\beta}^k - \lambda^k [\mathbf{X}(\boldsymbol{\beta}^k)^{\mathbf{T}} \mathbf{P} \mathbf{X}(\boldsymbol{\beta}^k) + \alpha^k \mathbf{I}]^{-1} \mathbf{X}(\boldsymbol{\beta}^k)^{\mathbf{T}} \mathbf{P} (\mathbf{y} - \mathbf{f}(\mathbf{t}, \boldsymbol{\beta}^k)) \tag{4.21}$$

where α is a penalization term, k the iteration and $\mathbf{X}$ the sensitivity matrix. For further details on **weighted least squares**, the reader may refer to Annex K.

4.4.2 Results

The optimization of the cost function was performed for multiple values of the hyper-parameters: $p^m \in [0-1]$, $p^\lambda \in [0-1]$ and $p^{\sigma^{el}}_{x=0} \in [0-1]$, as well as for different mean values of the normal *a priori* distributions β_{ap}.
The absolute standard deviations of the *a priori* normal distributions were chosen as follows: $\sigma_H = 1$ eV, $\sigma_{S/k} = 4$, $\sigma_{E_m(Pu)} = 0.2$ eV, $\sigma_{E_m(U)} = 0.2$ eV. Those standard deviations were chosen given the observed discrepancies on those parameters, reported in the literature.
Different starting $\boldsymbol{\beta}_0$ vectors were also tested. A total number of **21504 optimizations** were performed.
To assure a bijective cost function, both electrical and thermal conductivity experimental data were sampled every 55 K for $T < 1500$ K and 15 K for $T > 1500$ K.

4.4.2.1 Effect of the hyper-parameters on the cost function

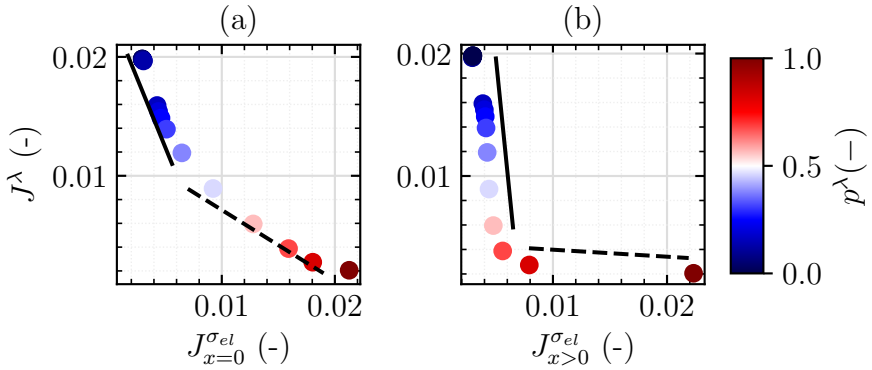

Figure 4.7: Variation of the thermal conductivity cost function J^λ with (a): $J^{\sigma^{el}}_{x=0}$ and (b): $J^{\sigma^{el}}_{x>0}$ obtained with $p^\lambda \in [0-1]$ and fixed $p^m = 0.95$, $p^{\sigma^{el}}_{x=0} = 0.6$. The values of p^λ are shown in the color bar.

When performing weighted least squares, a particular attention should be payed to the effect of the hyper-parameters (*i. e.* the weights) on the elementary cost functions. Excessive weighting of one cost function in particular can have serious repercussions on the other cost functions.
Figure 4.7 shows how increasing the weight of thermal conductivity experimental data (*i. e.* p^λ) impacts the three elementary cost functions in J^{LSQR}: J^λ, $J^{\sigma^{el}}_{x=0}$ and $J^{\sigma^{el}}_{x>0}$.
Increasing the weight of the thermal conductivity cost function p^λ until a certain critical value p^λ_{crit} induces a great decrease in J^λ, without necessarily penalizing the other elementary cost functions.
However, increasing p^λ beyond p^λ_{crit} results in only a slight decrease in J^λ, while the other cost functions are penalized considerably.
The $(J^\lambda, J^{\sigma^{el}}_{x=0})$ and $(J^\lambda, J^{\sigma^{el}}_{x=0})$ curves are therefore L-shaped. If one defines p^λ_{crit} as the value, at

which both slopes, forming the L-shape curve cross each other, we obtain different p^{λ}_{crit} values for the $(J^{\lambda}, J^{\sigma^{el}}_{x=0})$ and $(J^{\lambda}, J^{\sigma^{el}}_{x>0})$ curves: $p^{\lambda}_{crit} \approx 0.4$ and $p^{\lambda}_{crit} \approx 0.75$ respectively.
The steepness of the slopes before and after the critical value, are also not the same. The variation J^{λ} with $J^{\sigma^{el}}_{x=0}$ for $p^{\lambda} < p^{\lambda}_{crit}$ is less steep than J^{λ} with $J^{\sigma^{el}}_{x>0}$.
In other words, a decrease in J^{λ} is associated with a higher increase in $J^{\sigma^{el}}_{x=0}$ than in $J^{\sigma^{el}}_{x>0}$.

When performing optimization of a multi-objective cost function, the goal is to obtain a solution, where all elementary cost functions are at their minimum. However, this study shows that in our case minimizing J^{λ} is always followed by an increase in either $J^{\sigma^{el}}_{x=0}$ or $J^{\sigma^{el}}_{x>0}$ and thus finding a solution, where all cost functions are minimum is complex. We should thus search for a quality criterion, which despite the complex nature of the problem, will give the best possible solution.

4.4.2.2 Choice of a quality criterion

Given that decreasing J^{λ} can lead to a more significant increase in $J^{\sigma^{el}}_{x=0}$ than in $J^{\sigma^{el}}_{x>0}$, the quality criterion will be governed by the value of $J^{\sigma^{el}}_{x=0}$. The question is to know up to what maximum value $(J^{\sigma^{el}}_{x=0})_{max}$ we allow $J^{\sigma^{el}}_{x=0}$ to increase.

Criterion on the stoichiometric electrical conductivity residuals
To choose $(J^{\sigma^{el}}_{x=0})_{max}$, we referred to the systematic uncertainty in the electrical conductivity measurements.
The latter were performed, using the four-probe technique [159, 212, 213]. Mackey *et al.* performed systematic uncertainty analysis on the electrical conductivity, determined with the four-probe technique.
They estimated this uncertainty to be of ± 7 %, across any temperature. Furthermore, Fujino *et al.* (*i. e.* the author of the measurements we use for the optimization) did not report the porosity of the fuels [159]. Given the fabrication process of those fuels, to deduce the electrical conductivity of the material at 100 % of its theoretical density (*i. e.* σ^{el}_0), we assumed a porosity of 5 vol. %.
However, this value can be different by 5 ± 2 vol. %. According to Maxwell-Eucken's correction for porosity [85, 86]: $\frac{\sigma^{el}_p}{\sigma^{el}_0} = \frac{1-p}{1+0.5p}$, 2 vol. % of uncertainty on porosity induces a relative uncertainty of 3 % on electrical conductivity. Adding this uncertainty to the systematic experimental uncertainty of 7 % yields a total uncertainty on the measurements of 10 %.

In this manner, $(J^{\sigma^{el}}_{x=0})_{max}$ has been chosen, such that the electrical conductivity residuals $r^{\sigma^{el}_{x=0}}$ do not exceed the experimental uncertainty at the last measurement temperature, which is: $\boldsymbol{\Delta\sigma_{el}(T = 1357.4) = 820 \times 0.10 = 82}$ $\mathrm{S\,m^{-1}}$.
Indeed, most fits of electrical conductivity manage quite well to reproduce the data at low temperatures. The biggest discrepancies between the model and the data occur at the last measurement point. For this, the quality criterion is only based on the residuals at the last measurement temperature.

We thus search for $(J^{\sigma_{el}}_{x=0})_{max}$, such that the following criteria is met:

$$\boxed{r^{\sigma_{el}}_{x=0}(T^{\sigma_{el}}_{max}) < \Delta\sigma_{el}(T^{\sigma_{el}}_{max}) = 82 \quad \mathrm{S\,m^{-1}}} \tag{4.22}$$

Among all solutions, which satisfy criteria 4.22 we retain the one, with the minimum thermal conductivity cost function $(J^{\lambda})_{min}$.
The couple $\{(J^{\lambda})_{min}, (J^{\sigma_{el}}_{x=0})_{max}\}$ is thus the best compromise.

Multiple, $\{(J^{\lambda})_{min}, (J^{\sigma_{el}}_{x=0})_{max}\}$ solutions were found, depending on the physical meaning of the estimated parameters (see Table 4.3). Regardless of the cost functions, the identified

$\boldsymbol{H}$ (eV)	$\frac{\boldsymbol{S}}{\boldsymbol{k}}$ (-)	$\boldsymbol{E_m(Pu)}$ (eV)	$\boldsymbol{E_m(U)}$ (eV)	$\boldsymbol{(J^{\lambda})_{min}}$ (-)	$\boldsymbol{J^{\sigma_{el}}_{x>0}}$ (-)	$\boldsymbol{(J^{\sigma_{el}}_{x=0})_{max}}$ (-)	$\boldsymbol{p_m}$ (-)	$\boldsymbol{p_\lambda}$ (-)	$\boldsymbol{p^{\sigma_{el}}_{x=0}}$ (-)
1.7936	6.7877	0.2606	0.0004	0.0061	0.0510	0.0273	0.85	0.80	0.60
1.7951	7.3678	0.2611	0.0347	0.0070	0.0495	0.0293	0.80	0.80	0.60
1.6499	6.1139	0.2572	0.0403	0.0073	0.0619	0.0287	0.85	0.80	0.60
1.6608	6.5116	0.2554	0.0515	0.0074	0.0681	0.0256	0.80	0.80	0.60
1.4217	5.0808	0.2514	0.0946	0.0095	0.0847	0.0237	0.80	0.80	0.60
1.2805	3.9566	0.2561	0.1004	0.0114	0.0659	0.0205	0.80	0.80	0.55

Table 4.3: Estimated parameters, cost functions, and weighing hyper-parameters, satisfying the quality criterion.

$H, S/k, E_m(Pu)$ parameters yield physical values, when compared to the published data on those parameters for UO_2 and PuO_2 [144, 147, 152]. Furthermore, they do not exhibit drastic changes with the values of the cost functions.
On the other hand, the migration energy of the uranium polaron $E_m(U)$ can be in the range $[0.0004 - 0.1004]$ eV, therefore yielding strong variations with the cost functions.
To make a final decision, another quality criterion should be fixed, regarding the value of $E_m(U)$.

Criterion on the migration energy of the uranium polaron $E_m(U)$
As shown in Table 4.3, the variation of $(J^{\lambda})_{min}$ with $E_m(U)$ yields an almost constant value around 0.007 until $E_m(U) = 0.0515$ eV and then suddenly shifts to a higher value of almost 0.009 eV.
Given this sudden shift in $(J^{\lambda})_{min}$ after $E_m(U) = 0.0515$, and given that $E_m(U) = 0.0515$ eV is not that far from the migration energy of the plutonium polaron, reported by Geneste *et al.* [144] of $E_m(Pu) = 0.08$ eV in PuO_2, we retain the solution corresponding to $E_m(U) = 0.0515$ eV.

4.4.2.3 *Monte-Carlo simulation*

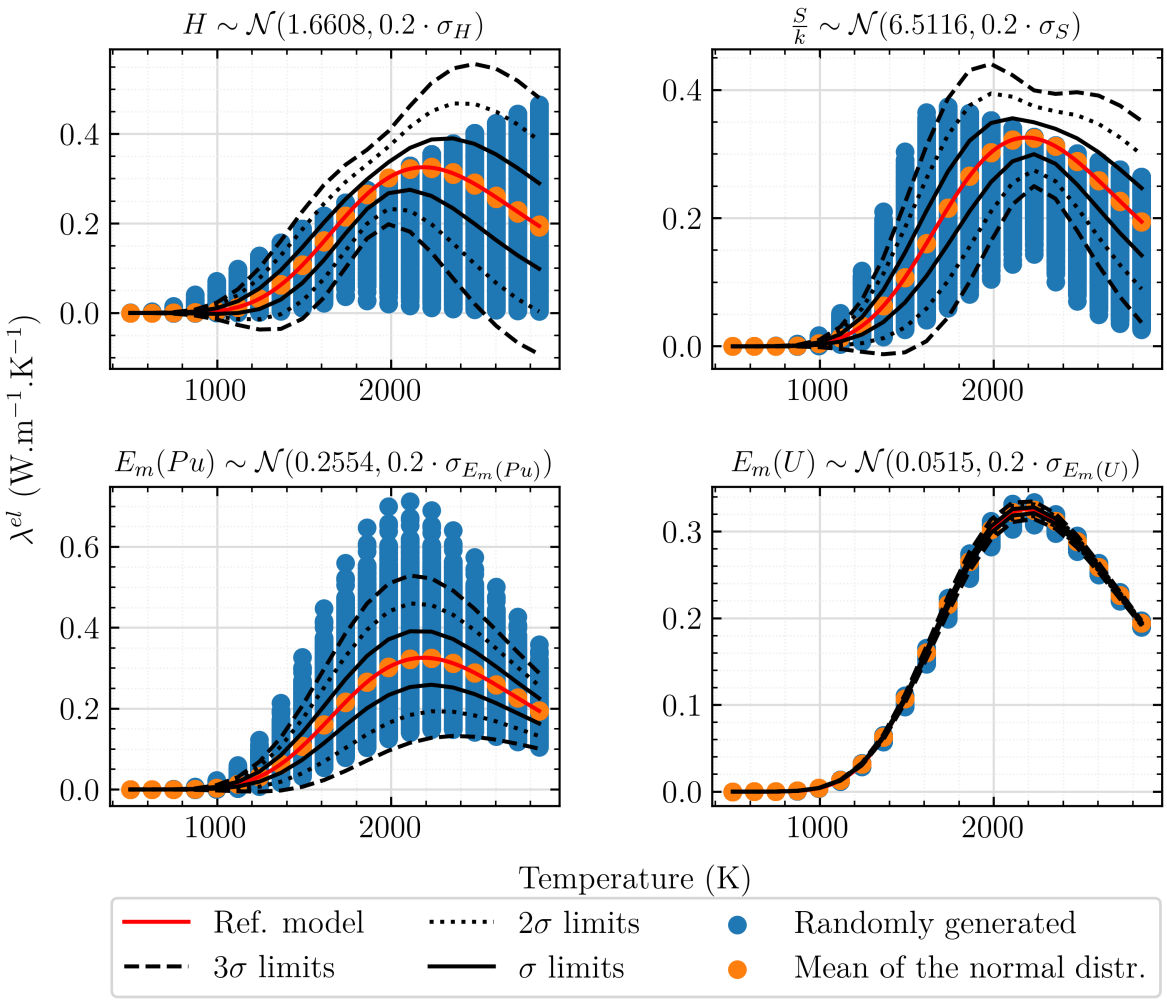

Figure 4.8: Variation with temperature of the electronic thermal conductivity term λ^{el}, as predicted by the model, evaluated in the estimated parameters (red solid line) and as generated by 10 000 Monte-Carlo simulation points (blue and orange circles).

The parameters, satisfying the quality criterion are therefore: $H = 1.6608$ eV, $S = 6.5116 \times k$ eV K^{-1}, $E_m(Pu) = 0.2554$ eV, $E_m(U) = 0.0515$ eV. The initial absolute standard deviations, assumed in the Bayesian normal distribution, were $\sigma_H = 1$ eV, $\sigma_{S/k} = 4$, $\sigma_{E_m(Pu)} = 0.2$ eV and $\sigma_{E_m(U)} = 0.2$ eV.
The Bayesian estimation, which satisfied the quality criterion was performed with a relatively low weight on the cost function, associated with the *a priori* parameters' information (*i. e.* $p^\beta = 1 - p^m = 0.2$, see Table 4.3).
To visualize the impact of a standard deviation of $0.2\sigma_i$ on each parameter, we performed Monte-Carlo simulations.
We generated four normal distributions $\mathcal{N}(\beta_i, 0.2\sigma_{\beta_i})$, where i refers to the i-th parameter, composed of 10 000 Monte Carlo points. The former are characterized by a mean, corresponding to the Bayesian estimation and a standard deviation of 20 % of the initial standard deviation, assumed in the Bayesian normal distribution.

For each of the 10 000 points, we plotted the model variation with temperature, together with the inverse model, evaluated in the nominal parameters (see Figure 4.8). For each temperature, the standard deviation σ was calculated and the σ, 2σ and 3σ limits plotted.

We observe that the standard deviation, induced by H, S/k and $E_m(Pu)$ is almost the same, with the difference that H generates the greatest standard deviation at high temperatures. As for the $E_m(U)$ parameter, no significant scattering in the Monte-Carlo (λ_i, T_i) points is observed, highlighting the quite low sensitivity of the electronic model to this parameter.
Those curves also show that the mean of the normal H and S/k distributions yields the highest electronic thermal conductivity value, especially in the range $T \in [1800 - 2200]$ K. In other words, deviating from the nominal H and S/k values, in this temperature range, can only lead to a decrease in λ^{el}.

4.4.2.4 Summary

Given the criteria, based on (1): the stoichiometric electrical conductivity residuals and (2): the value of $E_m(U)$, we retain the following solution for the electronic parameters:

$$\boxed{\begin{array}{l} H = 1.6608 \quad \text{eV} \\ S = 6.5116 \times k \quad \text{eV K}^{-1} \\ E_m(Pu) = 0.2554 \quad \text{eV} \\ E_m(U) = 0.0515 \quad \text{eV} \end{array}} \tag{4.23}$$

Those parameters can be used in Equation 3.58 for σ^{el} and Equation 3.35 to deduce electronic thermal conductivity λ^{el}.

Covariance of the estimator

The standard deviation of the estimation by the weighted least squares was not calculated.
Indeed, as shown in Figure 4.9, signed thermal conductivity residuals are observed- they are correlated with the independent variable (*i. e.* their mean value is not simply equal to 0, but is rather a temperature-dependent function).

When dealing with signed residuals, it is almost impossible to estimate the real standard deviation of the estimation [166, 214].
Indeed, the latter is the sum of a stochastic and a deterministic term (*i. e.* the modeling error): $\sigma_\beta = \sigma_\beta^{stoch} + \sigma_\beta^{det}$.
Since the residuals are signed in this case, the stochastic term is negligible to the deterministic one, the estimation of which is complex [214].
Therefore, calculating the standard deviation of the estimated parameters using covariance matrix (*i. e.* calculating the stochastic term, see Annex K) in this work could only lead to an overestimation of the real value.

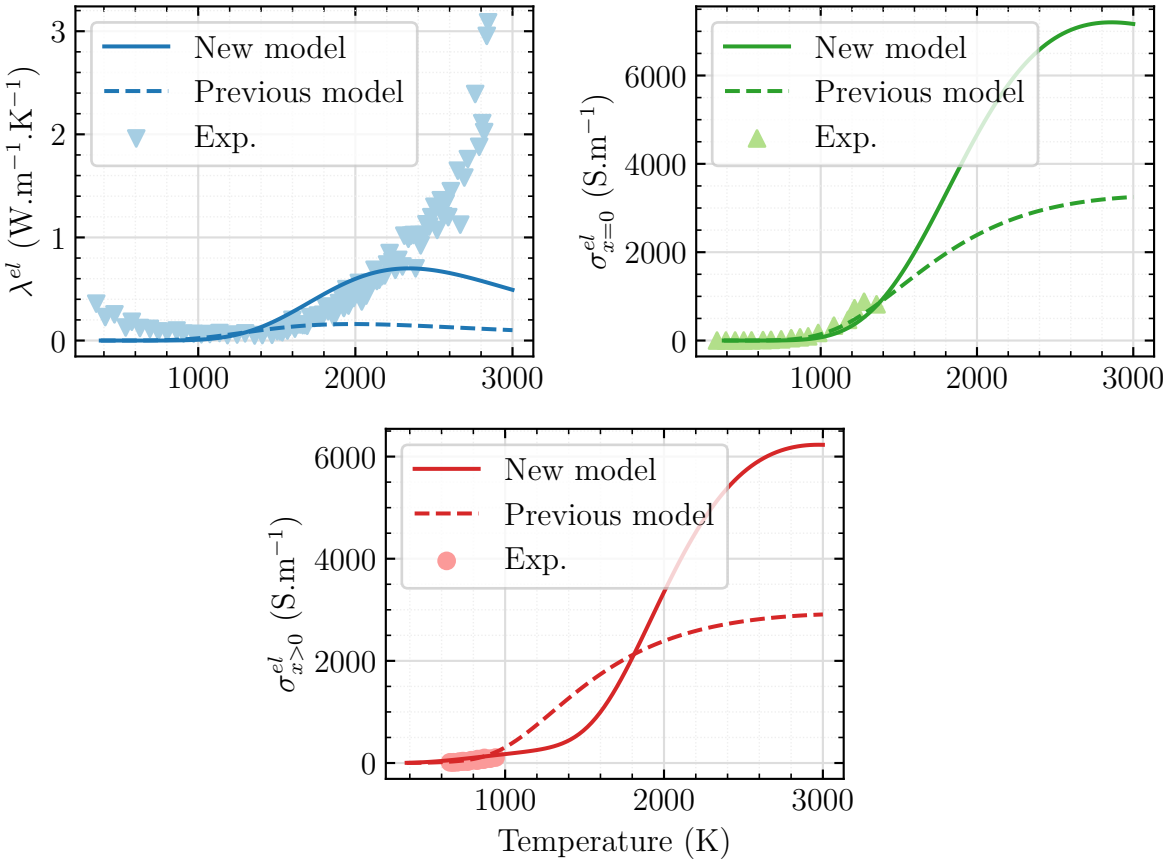

Figure 4.9: Sampled experimental data for thermal and electrical conductivity and the associated models. Both models were shown: the new, based on a Bayesian cost function (this chapter) and the old one, based on a classical least squares optimization on electrical conductivity data (from Chapter 3). The models are evaluated at the plutonium content, which represents the weighted average of the assocaited experimental data. That is, for λ^{el}, $\overline{y} = 0.31$, for $\sigma^{el}_{x=0}$, $\overline{y} = 0.56$, and for $\sigma^{el}_{x>0}$, $\overline{y} = 0.20$

Comparison with other reported work on the subject

We compared the new parameters with those, reported by several authors on UO_2 [147, 150, 152, 154, 215–217], PuO_2 [144, 218] and MOX [143, 159, 219, 220] (see Table 4.4). Literature data on UO_2 is scattered.

Most of the authors deduced the electronic parameters by fitting them to available electrical conductivity experimental data. The scattering in the reported values come from different experimental data, used by different authors.

For MOX systems, Kato *et al.* reported values for the polaron creation enthalpy H and entropy S, by fitting them (together with many other thermodynamic parameters) to oxygen potential experimental data, using a model for the defect structure of MOX [218–220]. Their values are higher than those found in this work. However the comparison between our work and theirs does not seem straightforward, due to (1): the complexity in providing a model for the defect structure of MOX fuel and (2): the sensitivity of the thermodynamic parameters to oxygen potential experimental data. Our value for H is however consistent with

Parameter	Pu content (y)				
	0	*0.2*	*0.5*	*0.7*	*1*
H (eV)	1.86 - 2.52	This work: 1.6608 Kato et al.: 2.9 [219, 220] Catlow et al.: 1.5 [143] Njifon et al. : 1.1 [113]	This work: 1.6608 Kato et al.: 2.9 [219, 220] Catlow et al.: 1.5 [143] Njifon et al. : 1.1 [113]	This work: 1.6608 Kato et al.: 2.9 [219, 220] Catlow et al.: 1.5 [143] Njifon et al. : 1.1 [113]	Kato et al. : 3.6 [220]
$\frac{S}{k}$ (-)	1-4.5	This work: 6.5116 Kato et al.: 10.5 [219, 220]	This work: 6.5116 Kato et al.: 12.86 [219, 220]	This work: 6.5116 Kato et al.: 11.10 [219, 220]	Kato et al. : 12.62 [220] Kato et al. : 10.22 [218]
$E_m(Pu)$ (eV)	-	This work: 0.2554 Fujino et al.: 0.8 [159]	This work: 0.2554 Fujino et al.: 0.8 [159]	This work: 0.2554 Fujino et al.: 0.8 [159]	0.08 [144]
$E_m(U)$ (eV)	0.12-0.31	This work: 0.0515 Fujino et al.: 0.53 [159]	This work: 0.0515 Fujino et al.: 0.53 [159]	This work: 0.0515 Fujino et al.: 0.53 [159]	-

Table 4.4: Summary of the electronic parameters from this work, and the literature on UO_2: [147, 150, 152, 154, 215–217], MOX [113, 143, 159, 219, 220], and PuO_2 [144, 218]

Pyper and Grant's estimation $H = 1.5$ eV, using Dirac-Fock techniques [143, 221] and not that different from the value, found by DFT$+U$ calculations on MOX fuel, $H = 1.1$ eV [113]. It should also be mentioned that our value for H is lower than those reported for UO_2 and PuO_2 systems, showing the non-linearity of the H parameter with plutonium content. It also shows that electronic defects (*i. e.* polarons) are more easily supplied in MOX than in UO_2 or PuO_2. This provides an explanation for the higher electrical conductivity of MOX, compared to UO_2 and PuO_2.

Neglecting Frenkel pairs

We recall that in this work, we did not take into account the effect of Frenkel pairs on neither electrical, nor thermal conductivity.

Indeed, their creation and migration energy, are both higher than those of the polarons [220]. Therefore Frenkel pairs have a negligible impact on electrical and thermal conductivity, compared to polarons.

This assumption has also been made in other published work on actinide systems [147, 150, 152, 159].

Dependency of the parameters on plutonium and oxygen content

The new electronic parameters, obtained in this chapter are different from those in Chapter 3. Especially plutonium and oxygen content are not included.

Indeed, in this optimization, we did not perform separate estimations per plutonium content, due to the very few measurement points per data set (*e. g.* only 18 points for $x = 0, y = 0.3$). Instead, we calculated the mean plutonium content of the whole experimental data set (*i. e.*

$\overline{y} = 0.56$ for σ^{el} and $\overline{y} = 0.31$ for λ^{el}) and proceeded to one unique optimization. The latter therefore uses more experimental data than the separate optimizations.
A part from the plutonium and oxygen content dependencies of the parameters, the new optimization yielded a higher value for the polaron creation enthalpy H, as opposed to that in the previous chapter: 1.66 eV, compared to 1.1 eV. This partially explains why the electronic contribution increased, as opposed to Chapter 3.

Global highlights and perspectives

Overall, through Bayesian optimization we showed that it was possible to fit thermal and electrical conductivity measurements at the same time, while conserving the physical meaning of the parameters.
This was the main issue in the beginning of this chapter, where through the use of a classical least squares cost function, the only way of fitting both properties was to accept negative and thus non-physical migration energies.
The Bayesian optimization however did not allow to fully describe the temperature variation of thermal and electrical conductivity. Indeed, electrical conductivity model exhibits an inflection point in the $\sigma^{el}(T)$ curve, which then is observed in $\lambda^{el}(T)$.
The observed residuals at $T > 2300$ K, due to the inflection point in $\lambda^{el}(T)$ led to the following question: could we compensate for those residuals by including a radiative contribution?!
Indeed, this optimization was performed by neglecting the radiative thermal conductivity due to its probable overestimation, caused by the underestimation of the Rosseland mean extinction coefficient (see Section 3.4.3.2).
In the following section, we will see if including radiative thermal conductivity will explain the thermal conductivity residuals.
However, instead of using the Rosseland extinction coefficient, as presented in Chapter 3, we will try to estimate a new value for β_R, based on the thermal conductivity residuals.

4.5 Explanation of the thermal conductivity residuals by a modified radiative contribution

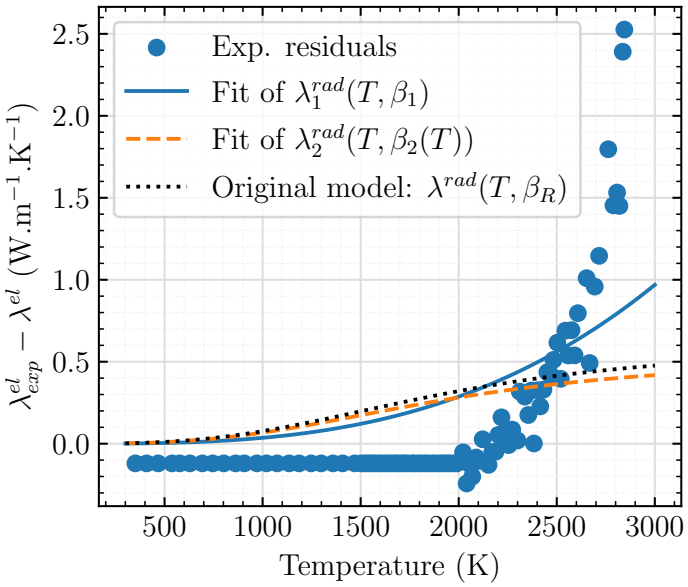

Figure 4.10: Fit of the experimental thermal conductivity residuals (blue circles) with two radiative contributions: considering a constant Rosseland extinction coefficient β_1 (blue solid line) and a temperature-dependent coefficient $\beta_2(T)$ (orange dashed line). The original radiative thermal conductivity model, as presented in Chapter 3 is also shown (black dotted line).

We tried to fit the experimental residuals, using the Rosseland approximation, with two different Rosseland extinction coefficients: a constant β_1 and the second a temperature-dependent $\beta_2(T)$:

$$\lambda_1^{rad}(T, \boldsymbol{\beta_1}) = \frac{16n^2\sigma_B}{3\boldsymbol{\beta_1}}T^3 \tag{4.24}$$

$$\lambda_2^{rad}(T, \boldsymbol{\beta_2(T)}) = \frac{16n^2\sigma_B}{3\boldsymbol{\beta_2(T)}}T^3 \tag{4.25}$$

where $\beta_2(T) = \beta_{emp} \cdot \beta_R(T)$, and β_{emp} - empirical factor, $\beta_R(T)$ - the expression in the original model (see Equation 3.69).
As shown in Figure 4.10, non of those equations allow to properly fit the thermal conductivity residuals at high-temperature.
Indeed, the residuals increase more rapidly than a physical $f(\frac{1}{\beta})T^3$ variation. Therefore neither of the two Rosseland extinction coefficients managed to fit the residuals with physical values.

The choice of a constant Rosseland extinction coefficient β_1 however seems more legitimate, given its greater consistency with the experimental residuals, compared to λ_2^{rad} or the original model λ^{rad}. We thus propose to use λ_1^{rad} with $\beta_1 = 42652.75$ m^{-1}.

It should be mentioned that fitting radiative thermal conductivity to the thermal con-

ductivity residuals is not a straightforward task.
Indeed, the residuals could be biased by the uncertainty in the heat capacity model, used to indirectly calculate thermal conductivity from thermal diffusivity experimental data.
As shown in Figure 4.11, the experimental thermal diffusivity variation with temperature is a rather decreasing function until approximately 2300 K, where it reaches a constant value until melting temperature.

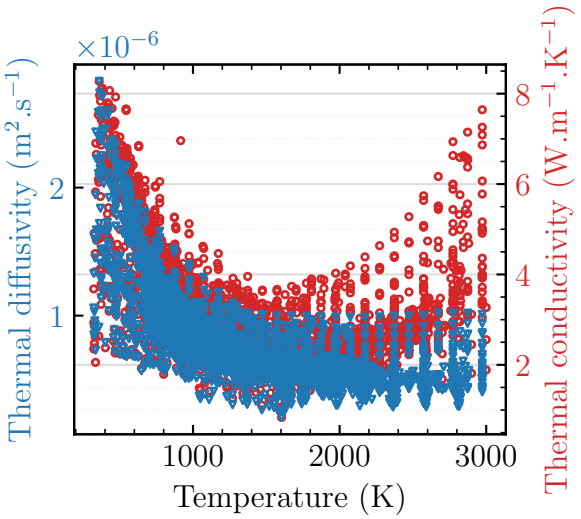

Figure 4.11: Experimental variation with temperature of thermal diffusivity (blue left axis) and thermal conductivity (red right axis). Thermal conductivity was deduced from experimental diffusivity and the heat capacity models for UO_2 and PuO_2 of Konings *et al.* [195] and for O_2 of Duriez *et al.* [4].

Experimental data on the heat capacity of MOX and other actinide oxides [195, 222], however show that heat capacity exhibits an important exponential variation with temperature. Given this exponential increase in heat capacity and the rather constant thermal diffusivity, the temperature variation of thermal conductivity therefore follows that of heat capacity.
This observation becomes further more curious when comparing indirectly measured thermal conductivity with direct thermal conductivity measurements.
The latter do not show any visible increase at high-temperatures, compared to indirect measurements (see Figure 4.12).
We conclude from this analysis that heat capacity modeling is of crucial interest to estimate accurately the temperature variation of indirectly measured thermal conductivity.

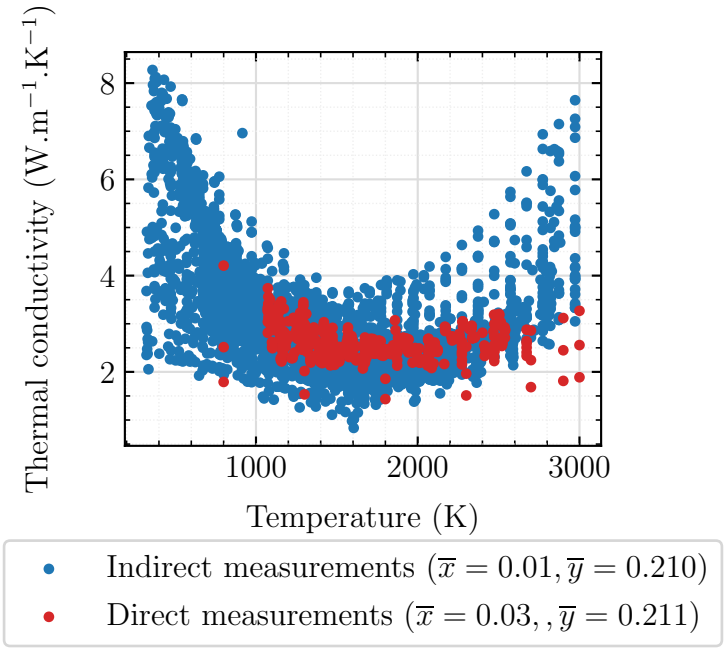

Figure 4.12: Comparison between direct and indirect thermal conductivity measurements. The average deviation from stoichiometry and plutonium content, weighted by the number of measurement points is also shown.

Effect of the heat capacity model, used to calculate thermal conductivity, from diffusivity experimental data.

We compared the effect of two heat capacity models on thermal conductivity outputs (see Figure 4.13).

The effect of both models on thermal conductivity is the same up to $T \approx 2200$ K. Above that temperature, the two heat capacity models yield clear differences in thermal conductivity: a factor of 3 at $T = 3000$ K.
In particular, using the model of Konings *et al.* induces higher thermal conductivity values than Fink (see Annex L for further details on this observation).
Indeed, as shown in Figure 4.13, our model is in better agreement with thermal conductivity, obtained by multiplying diffusivity by Fink's heat capacity model than by Konings *et al.*'s model.

Overall, regardless of the model (Konings *et al.* or Fink), the uncertainty in the heat capacity model of PuO_2 is high for temperatures above 2400 K (see Annex L).
Indeed, measurements above 2400 K are missing to confirm the extrapolation of the heat capacity models for PuO_2, above 2400 K.

As shown Figure 4.13, the experimental thermal conductivity residuals become important exactly at temperatures, where uncertainties associated with the heat capacity of PuO_2 are high (*i. e.* T > 2400 K).

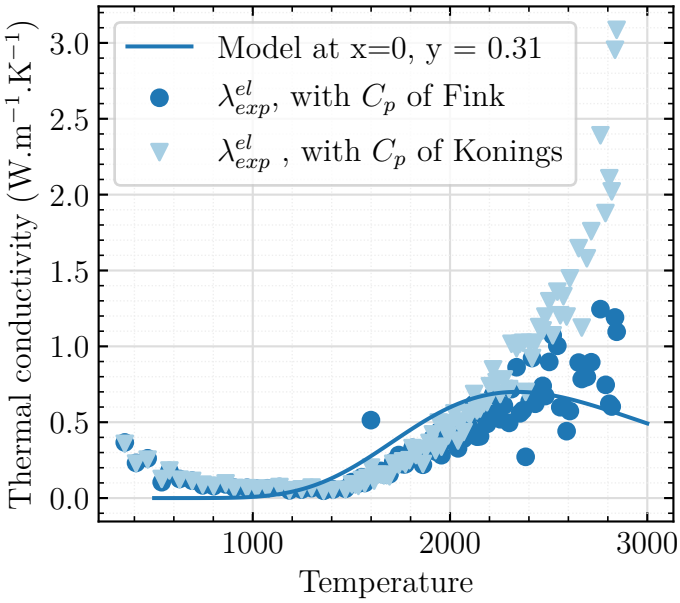

Figure 4.13: Comparison between our model and the experimental electronic thermal conductivity, deduced from: (1) the C_p model of Fink [223], based on enthalpy increment measurements on MOX fuel and (2) the Kopp model, deduced from the models for UO_2 and PuO_2 of Konings *et al.* [195] and for O_2 of Duriez *et al.* [4].

The variation with temperature of thermal conductivity in this temperature region will therefore remain uncertain until heat capacity measurements are performed on PuO_2 above 2400 K.
This therefore will allow to provide a more accurate estimate of the indirect measure of thermal conductivity.
Direct measurements above 2400 K are also required to check if indirect and direct thermal conductivity measurements yield the same value.

4.6 Summary on the modified thermal conductivity model

Now what we presented the modified thermal conductivity model and the uncertainties, associated with heat capacity, we summarize:

$$\lambda(\boldsymbol{T}) = \underbrace{\frac{1}{\frac{\pi^2 a^3 \theta_D}{12(3-x)\overline{v_p}^2 h}\Gamma + \frac{\gamma_\infty^2 n_a^{2/3}}{\boldsymbol{b_{emp}} \cdot B^* \overline{M} \theta_D^3 \overline{V_a}^{1/3}} \cdot \boldsymbol{T}}}_{\text{Modified } \lambda^{ph}} + \underbrace{\left(\frac{k}{e}\right)^2 \boldsymbol{T} \frac{\sigma_{Pu}^{el}(\boldsymbol{T})\sigma_U^{el}(\boldsymbol{T})}{\sigma^{el}(\boldsymbol{T})} \left(\frac{\boldsymbol{H} \cdot 1.6 \cdot 10^{-19}}{k\boldsymbol{T}}\right)^2}_{\text{Modified } \lambda^{el}} + \underbrace{\frac{16 n^2 \sigma_B}{3\boldsymbol{\beta_1}} \cdot \boldsymbol{T}^3}_{\text{Modified } \lambda^{rad}} \tag{4.26}$$

where the new empirical factors/electronic parameters are:

b_{emp} : empirical factor, given by Equation 4.9
H : 1.6608 eV (see Table 4.4)
β_1 : optimized Rosseland extinction coefficient = 42652.75 m^{-1}
$\sigma^{el} = \sigma_{Pu}^{el} + \sigma_U^{el}$: where,

$$\sigma_{Pu}^{el}(\mathbf{T}) = \frac{4e^2 v_{0,opt}}{ak\mathbf{T}} \left((c_{U^{5+}}(\mathbf{T}) + 2x)(y - c_{U^{5+}}(\mathbf{T}) - 2x) e^{-\frac{E_m(Pu)}{k\mathbf{T}}} \right)$$

$$\sigma_U^{el}(\mathbf{T}) = \frac{4e^2 v_{0,opt}}{ak\mathbf{T}} \left(c_{U^{5+}}(\mathbf{T})(1 - y - c_{U^{5+}}(\mathbf{T})) e^{-\frac{E_m(U)}{k\mathbf{T}}} \right)$$

$$c_{U^{5+}}(\mathbf{T}) = \frac{K_{pol}(\mathbf{T})(1-2x) + 2x - \sqrt{\begin{array}{c} K_{pol}(\mathbf{T})^2(4x^2 - 8xy + 4x + 4y^2 - 4y + 1) \\ +K_{pol}(\mathbf{T})(-8x^2 + 8xy - \\ 4x - 4y^2 + 4y) + 4x^2 \end{array}}}{2(K_{pol}(\mathbf{T}) - 1)}$$

$$K_{pol}(\mathbf{T}) = \exp\left(-\frac{H}{k\mathbf{T}} + \frac{S}{k}\right)$$

The new electronic parameters $H, S, E_m(Pu), E_m(U)$, optimized in this chapter are summarized in Table 4.4. For the other physical parameters (namely phonon parameters), the reader may refer to Equation 3.70 in Chapter 3.

4.7 Validation of the modified model

4.7.1 Validation data

To validate the model, we omitted a certain number of experimental data sets, which induced high data scattering, due to either self-irradiation damage, a non-negligible amount of americium or high porosity.
Indeed, our model does not account for porosity higher than 10 vol %., americium content or self-irradiation effects. The effect of those phenomena on thermal conductivity is detailed in Annex O.
Table 7 in Annex I summarizes the omitted experimental data.

4.7.2 Effect of temperature

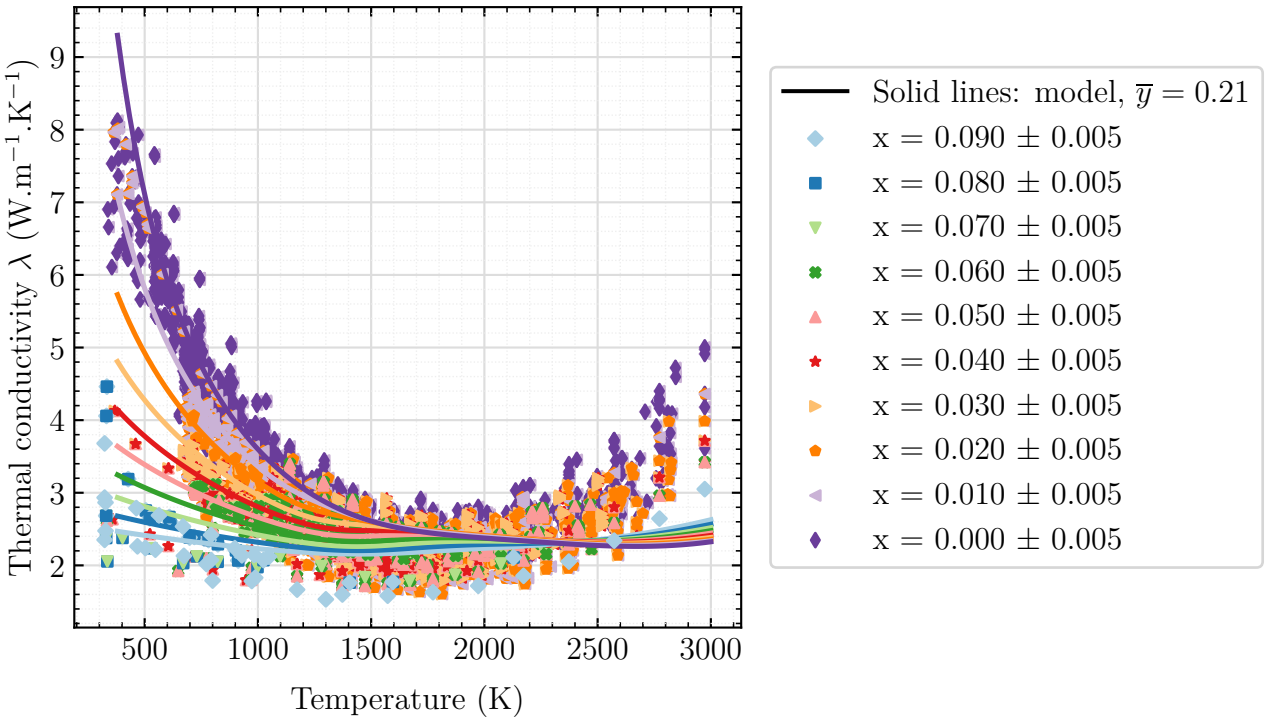

Figure 4.14: Experimental (colored markers) and modeled in this work (solid lines) variation with temperature.

As shown in Figure 4.14, our model correctly describes the temperature variation, regardless of the stoichiometry, until approximately $T = 2200K$, where the experimental values are higher than the predicted ones.

The variation with temperature of our model was also compared to the models of Kato *et al.* [3], Duriez *et al.* [4] and Philipponneau [2].
The phonon contribution to thermal conductivity, as predicted in this work seems consistent with Kato *et al.*. Philipponneau and Duriez *et al.* underestimate thermal conductivity at

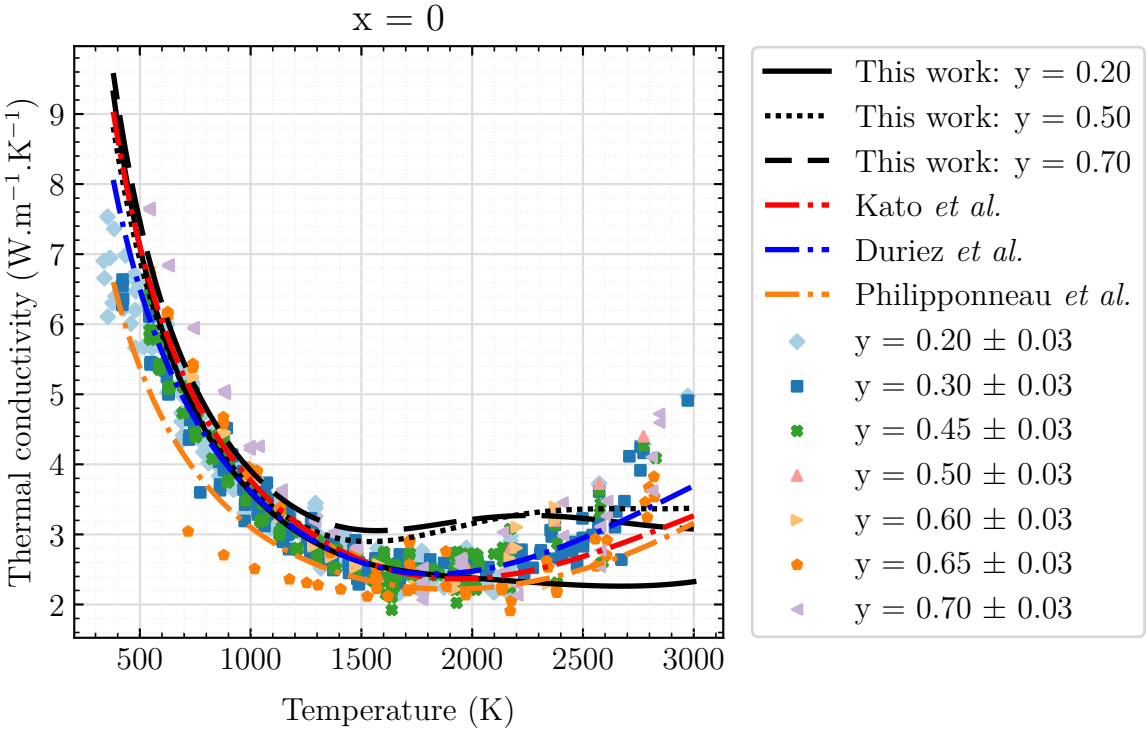

Figure 4.15: Experimental (colored markers) and modeled in this work (lines) variation with temperature for multiple plutonium contents $y \in [0.2 - 0.7]$, for $x \in [0 - 0.01]$. The models of Kato *et al.* [3], Duriez *et al.* [4] and Philipponneau [2] are also shown for comparison.

$T = 380$ K, respectively by 15 % and 40 %, compared to this work.
Discrepancies are also observed in the different electronic contributions to thermal conductivity. Indeed, the semi-empirical models all show a monotone increase in thermal conductivity at high temperatures. Those models do not use electrical conductivity to model thermal conductivity and are solely based on the experimental variation of thermal conductivity.
In our approach, thermal conductivity is a function of the electrical conductivity. In this chapter, we showed that to fit the electrical conductivity measurements with a monotone temperature function, non-physical parameters are required, which could not be considered in this work.
Those negative migration energies may not only be driven by uncertainties in experimental data, but also in the assumptions, made to provide the theoretical model. In particular, we recall that our model is based on the assumption that polarons can hope from atoms of the same type: U-U and Pu-Pu. If Pu-U hopping occurred, this would add an additional contribution in electrical conductivity, which could compensate for the negative migration energies.
In the state of the model, proposed in this work, if the physical meaning of the parameters is to be preserved, an inflection point appears in the $\sigma^{el}(T)$ curve and consequently in $\lambda^{el}(T)$, driven by the Arrhenius temperature function.

In addition to the inflection point, Figure 4.15 shows that the model at $y = 0.50$ and $y = 0.70$ yields higher values that the experimental data in the range $T \in [1600 - 2500]$ K.

Indeed, in the optimization we considered a mean plutonium content in the model, corresponding to the average plutonium content of the experimental data at high temperatures, weighted by the number of experimental points: $\overline{y} = 0.31$.
Due to the intrinsic parabolic variation with plutonium content of the model, it does not seem surprising that higher thermal conductivity is obtained in the range $y \in [0.50 - 0.70]$ than at $y = 0.30$.
However, it seems that the theoretical variation with y is more rapid than the experimental one, since the model predictions overestimate the experimental data.
Further details on this behavior will be given in the next section, where the theoretical variation with plutonium content will be compared to the experimental one.

4.7.3 Effect of plutonium content

In Chapter 3, we showed that the effect of plutonium content is different at low temperature (phonon term) and high temperature (electronic term).
To properly validate the theoretical variation with plutonium, it seems more appropriate to analyze those two temperature regions separately.
We will start by comparing our model with all available data then we will refine this comparison to specific data sets: EU projects (Section 4.7.3.2), Weilbacher, Bonnerot (Section 4.7.3.3).

4.7.3.1 Phonon term

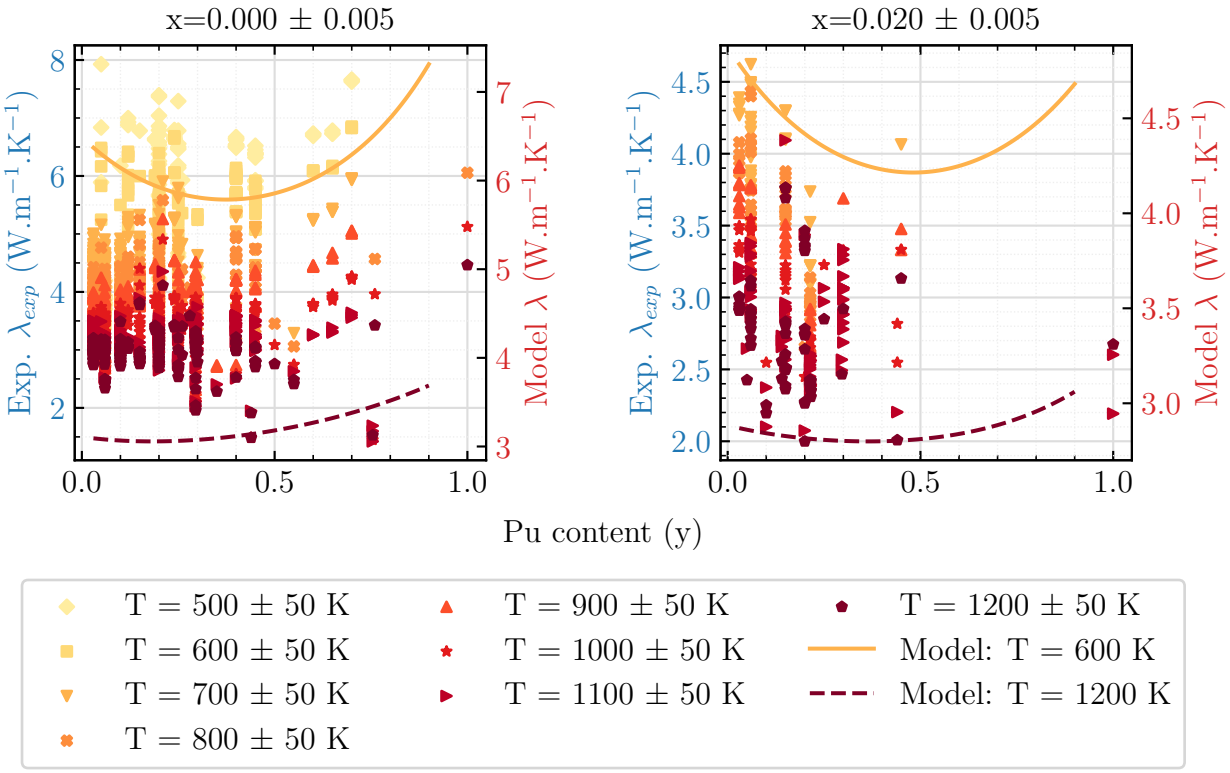

Figure 4.16: Experimental (left y-axis) and modeled (right y-axis) variation of thermal conductivity with plutonium content for $x = 0.000$ and $x = 0.020$, in the low temperature region (T $\in [500 - 1200]$ K)

As shown in Figure 4.16, the variation of the model with y at $T = 600K$ slightly decreases until $y = 0.45$ and then increases.
This plutonium content dependency therefore confirms our theoretical variation.
For stoichiometries different than $x = 0$, much less experimental data is available, thus making it difficult to validate the theoretical variation for $x > 0$.

Figure 4.16 also shows the correlated plutonium-oxygen content effect, mentioned in the previous chapter. Deviation from stoichiometry seems to change the variation of thermal conductivity with plutonium content, and especially the plutonium content at, which thermal conductivity exhibits a minimum.

4.7.3.2 *Electronic term: comparison with the data set of EU projects*

Experimental data for $T > 2000$ K is mainly provided by the EU projects.
As shown in Figure 4.17, the mean thermal conductivity per plutonium content shows a maximum at $y = 0.6$, no matter the temperature.

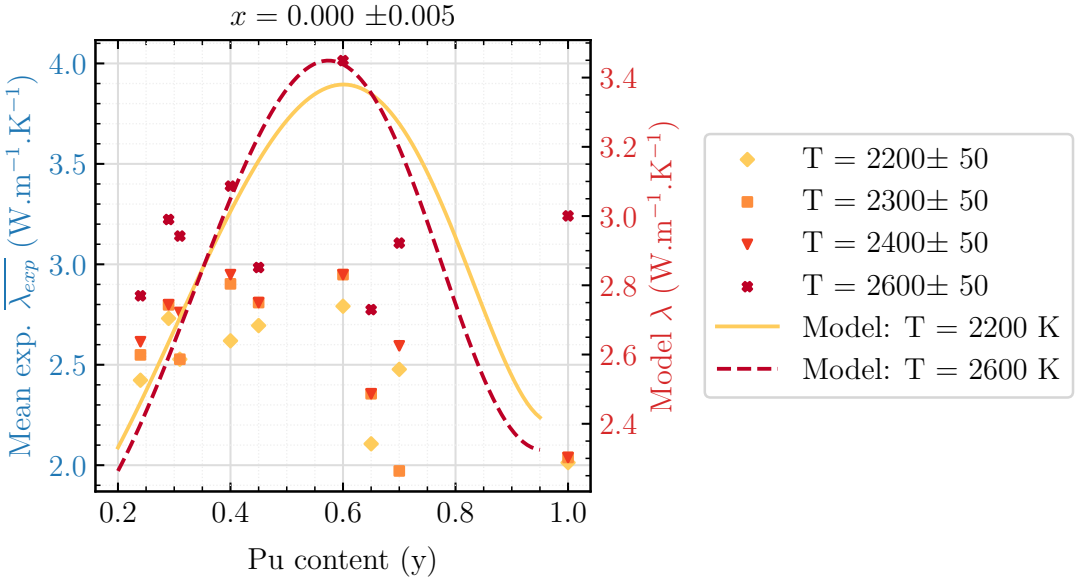

Figure 4.17: Experimental mean of thermal conductivity per plutonium content and temperature, (left y-axis) and modeled variation of thermal conductivity with plutonium content at the stoichiometric composition (right y-axis). The measurements are those of the European projects: PUMMA [109] ($y \in [0.6 - 1]$), ESNII+ [224] ($y \in [0.24 - 0.45]$), ESFR-SMART [108] ($y \in [0.29 - 0.31]$)

This observation is in agreement with the maximum, obtained with our model. The theoretical variation with y however seems more rapid than the experimental one. In particular, we observe that experimental thermal conductivity increases by 16 % between $y = 0.25$ and $y = 0.60$ at 2200 K, whereas our model predicts an increase of 35 %.
In other words, our parabolic plutonium content dependency is sharper than the experimental one.
This observation justifies why we saw, in Figure 4.15, that model predictions in the range $y \in [0.6 - 0.7]$ overestimate experimental data.
To flatten the theoretical parabolic variation with y, and thus obtain better consistency with the experimental variation, both $\sigma^{el}_{Pu}(y)$ and $\sigma^{el}_{U}(y)$ curves must be flattened.

As for the hypostoichiometric composition (see Figure 4.18), according the data set of the EU projects, at $x = 0.02$ the maximum of thermal conductivity takes place at $y = 0.40$, rather than at $y = 0.60$ as it was the case for $x = 0$. This shift of a thermal conductivity maximum to lower plutonium contents also occurs with our model, but not in such proportions. To clarify those particular tendencies, it bears analyzing the particular theoretical variation, predicted in this chapter.

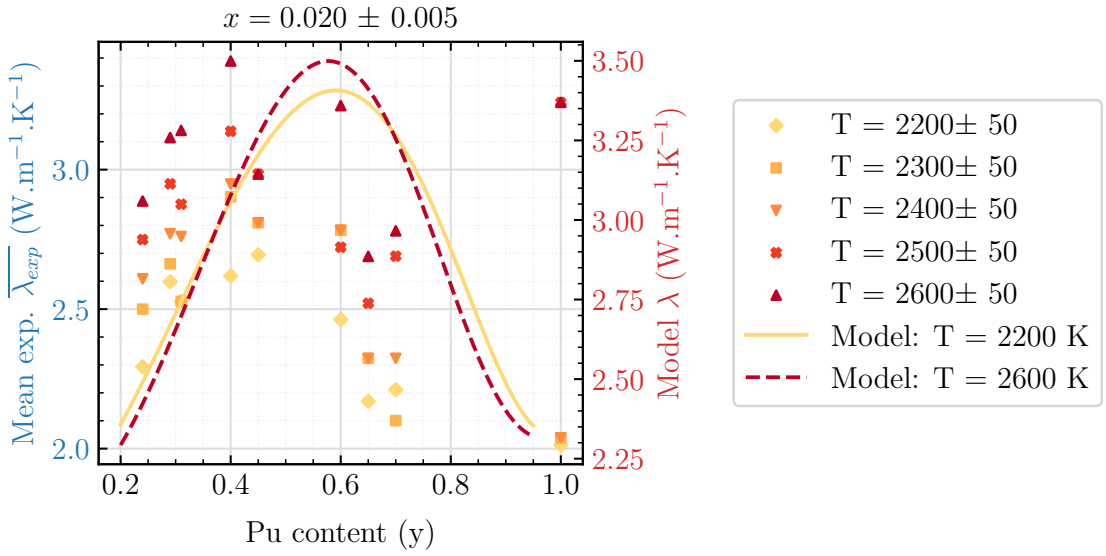

Figure 4.18: Experimental mean of thermal conductivity per plutonium content and temperature, (left y-axis) and modeled variation of thermal conductivity with plutonium content for $x = 0.02$ (right y-axis). The measurements are those of the European projects: PUMMA [109]($y \in [0.6 - 1]$), ESNII+ [224] ($y \in [0.24 - 0.45]$), ESFR-SMART [108] ($y \in [0.29 - 0.31]$)

Theoretical variation with plutonium content with the new parameters

The variation of the lattice parameter a with plutonium content has a negligible effect on the variation with y of the electrical conductivity.

If a plutonium content dependency is included in the polaron formation enthalpy H, the latter may have an impact on the overall plutonium content variation. As shown in Figure 4.19, the $\sigma^{el}_{Pu}(y)$ and σ^{el}_{U} curves at $x = 0$ are not symmetrical, thus yielding a maximum of electrical conductivity at $y \approx 0.30$ (rather than at $y = 0.50$ with the previous estimation).

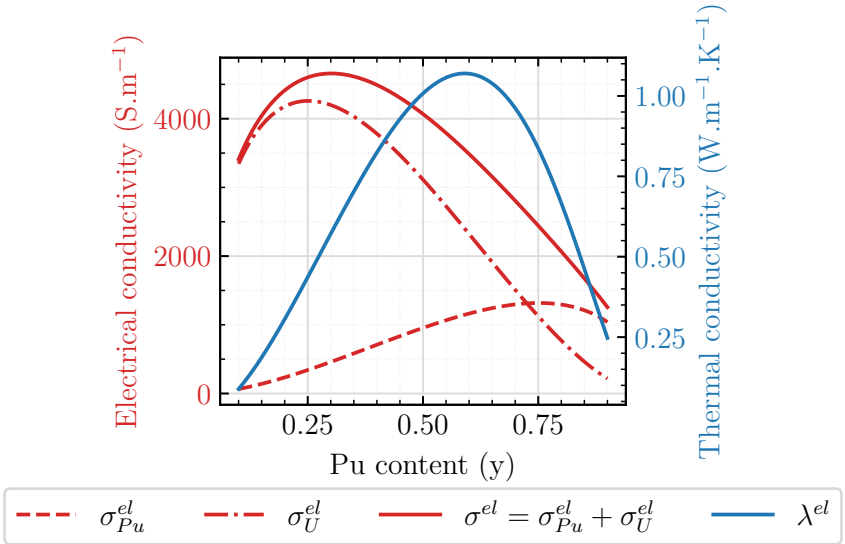

Figure 4.19: Electrical (red) and thermal (blue) conductivity variation with plutonium content at $x = 0$, $T = 2000$ K.

This asymmetry is explained by the different migration energy of the plutonium and uranium polarons: $E_m(Pu) = 0.2554$ eV $> E_m(U) = 0.0515$ eV.
The maximum electrical conductivity at $y = 0.30$, predicted in this work does not seem consistent with the electrical conductivity measurements, showing a maximum at rather $y = 0.50$.
Indeed, in the previous chapter, we performed separate optimizations per plutonium content and stoichiometry, therefore the model was able to reproduce the experimental maximum at $y = 0.50$. However, in this chapter we saw that our previous model was not able to reproduce the right temperature variation of thermal conductivity (see Figure 4.9).
We therefore privileged reproducing the right temperature variation, rather than the plutonium content one.
Furthermore, the previous variation of the model parameters with x and y was based on very few experimental data points, therefore highlighting the uncertainty of the estimated x and y dependencies.

The correlated plutonium content-stoichiometry effect needs also to be investigated with this new optimization. In the previous chapter, we showed that increasing deviation from stoichiometry induces a shift of the maximum of thermal conductivity to higher plutonium contents.
That is, at $x = 0$, the maximum was attained at $y = 0.50$, whereas at $x = 0.02$, the maximum shifted to $y = 0.56$. This shifting behavior was explained as being due to the increasing importance of the plutonium polaron's contribution σ^{el}_{Pu} with increasing x, due to extrinsically created Pu^{3+} in addition to the intrinsic Pu^{3+}.
In the new optimization, this shift is observed in the opposite way: increasing x tends to decrease the plutonium content, at which the maximum thermal conductivity is achieved (see Figure 4.20).

Indeed, this new optimization yielded a migration energy of the plutonium polaron 5 times higher than the uranium polaron. Therefore, the increase of the plutonium contribution due to x is not sufficient to compensate for the 5 times higher migration energy of Pu^{3+}, which tends to do the opposite: decrease its contribution, with respect to the U^{5+} polaron.
Nevertheless, this shift is very slight.
That is, in this optimization, the maximum thermal conductivity shifts from $y = 0.6$ at $x = 0$ to $x = 0.57$ at $x = 0.02$. This shift is not as important as the experimental one, yielding a maximum, which moves from $y = 0.60$ to $y = 0.40$ when deviation from stoichiometry goes from $x = 0.00$ to $x = 0.02$.
The maximum of thermal conductivity is mostly driven by the contribution from the plutonium polaron, as the latter increases with plutonium content. As shown in Figure 4.19, the plutonium contribution to electrical conductivity is lower than the uranium contribution, due to its lower migration energy.
Therefore, the increase in σ^{el}_{Pu} is less important than the decrease in σ^{el}_{U} with plutonium content. This "competition" between the plutonium and uranium contributions, therefore induces the maximum of thermal conductivity to take place at higher plutonium content values (*i. e.* here at $y = 0.60$ for a stoichiometric MOX).

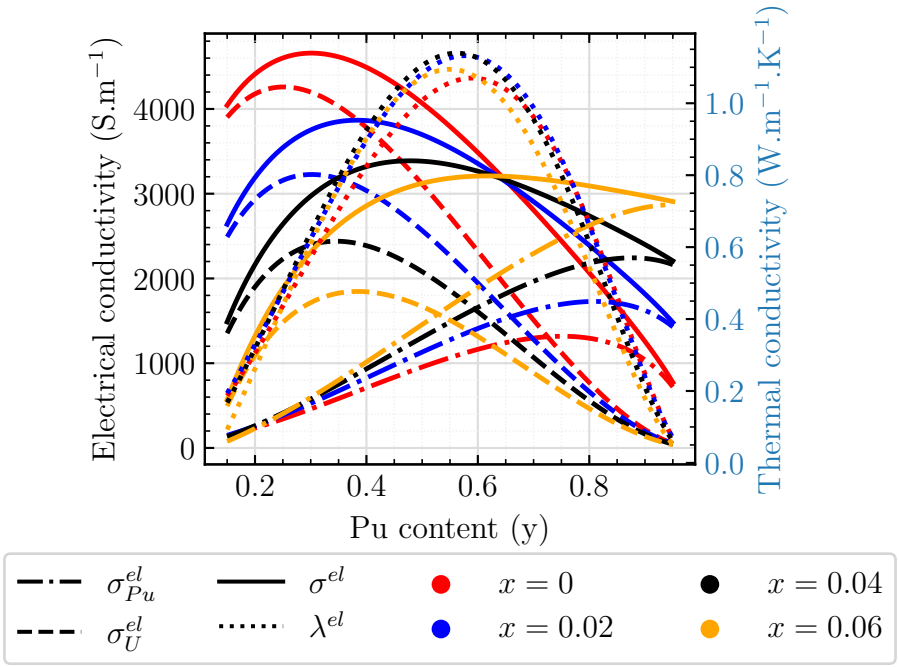

Figure 4.20: Electrical and thermal conductivity variation with plutonium content at $T = 2000$ K and four different deviations from stoichiometry.

If this maximum was to be shifted to lower plutonium contents (as it is experimentally observed at $x = 0.02$), the plutonium contribution had to be higher than the actual one, in order to outweigh the uranium contribution.
The increase in the contribution from the plutonium polaron to electrical conductivity can be achieved by decreasing its migration energy.

In this work, we optimized $E_m(Pu)$ on hypostoichiometric electrical conductivity data, since the sensitivity of the model to $E_m(Pu)$ was shown to increase with x.
We saw that decreasing $E_m(Pu)$ was accompanied with a decrease in the model consistency with the hypostoichiometric measurements. Therefore, if we seek to shift the plutonium content value, at which the maximum of thermal conductivity is obtained, to lower values, we will reduce the model's consistency with electrical conductivity measurements on hypostoichiometric MOX.
However, it should be mentioned that measurements on hypostoichiometric MOX fuel, used in the optimization were only based on the Schmitz' data set. Other measurements should be performed (and therefore included in the optimization) on hypostoichiometric MOX, in order increase the accuracy of estimation of $E_m(Pu)$.

We only discussed the plutonium polaron's migration energy, as being the only responsible for the maximum, because we searched to validate the experimental shift at $x = 0.02$.
Indeed, in hypostoichiometric MOX, the plutonium migration energy is the driving parameter. However, if one day, we recall into question the experimental maximum, obtained at $y = 0.60$ for the stoichiometric MOX, the migration energy of the uranium polaron should also be

investigated.
Indeed, for a stoichiometric MOX, decreasing $E_m(U)$ leads to increase the plutonium content, at which the maximum of thermal conductivity occurs.

This observation highlights the need for a **more accurate estimate of the migration energy of both polarons** if one seeks for a precise determination of the plutonium content value, at which thermal conductivity attains a maximum, regardless of the stoichiometry.

4.7.3.3 Comparison with literature reviews on the subject

It also bears comparing the plutonium content dependency, predicted in this work with other reported work on this subject.
As mentioned in the introduction, literature on the effect of plutonium content on thermal conductivity of MOX fuels, covering a wide range of plutonium contents is very limited.

In his doctoral research, Bonnerot [5] modeled the effect of plutonium on thermal conductivity, using experimental data on MOX fuels, in the range $y \in [0.05 - 0.3]$.
Among all reported work, to our knowledge, Bonnerot is the only author to take into account plutonium content in the electronic contribution to thermal conductivity.
However, the model proposed by Bonnerot takes a simple Arrhenius form, without any particular distinction between the polaron migration and creation energy. Instead, he uses the term "activation energy" of thermal conductivity and shows that this energy decreases in a monotone manner with plutonium content.
In Bonnerot's model, thermal conductivity exhibits a parabolic variation with y, with a maximum at $y = 0.15$ and $T = 2500$ K.
A quantitative comparison between our model and Bonnerot could not be done, given (1): the choice of a rather simple equation to fit thermal conductivity at high-temperature in Bonnerot's work and (2): the limited plutonium content range ($y \in [0.05 - 0.3]$) in his measurements, therefore limiting the validity of the model to only $y = 0.3$.

We compared our variation with Bonnerot's measurements in Figure 4.21. The data set of Bonnerot seems to yield a local minimum in the range $y \in [0.07 - 0.10]$.
Bonnerot however characterized those samples (namely at $y = 0.077$ and $y = 0.10$) and showed that this surprisingly low thermal conductivity value for those samples was due to a particular plutonium distribution over the (U, Pu) matrix.
Indeed, those samples presented some Pu-rich agglomerates. Those two fuels were therefore not considered in Bonnerot's model.
Two other samples, yielding surprisingly low thermal conductivity values were not considered in Bonnerot's study: those at $y = 0.45$ and $y = 0.75$. Indeed, those fuels were bi-phased at the fabrication and therefore were not totally representative of a monophased MOX matrix.
In fine, the plutonium content dependency in Bonnerot's model is based on fuels in the range $y \in [0.10 - 0.30]$. The maximum of thermal conductivity predicted by Bonnerot around $y = 0.15$ is however very complex to validate given the high discrepancy in the experimental data.

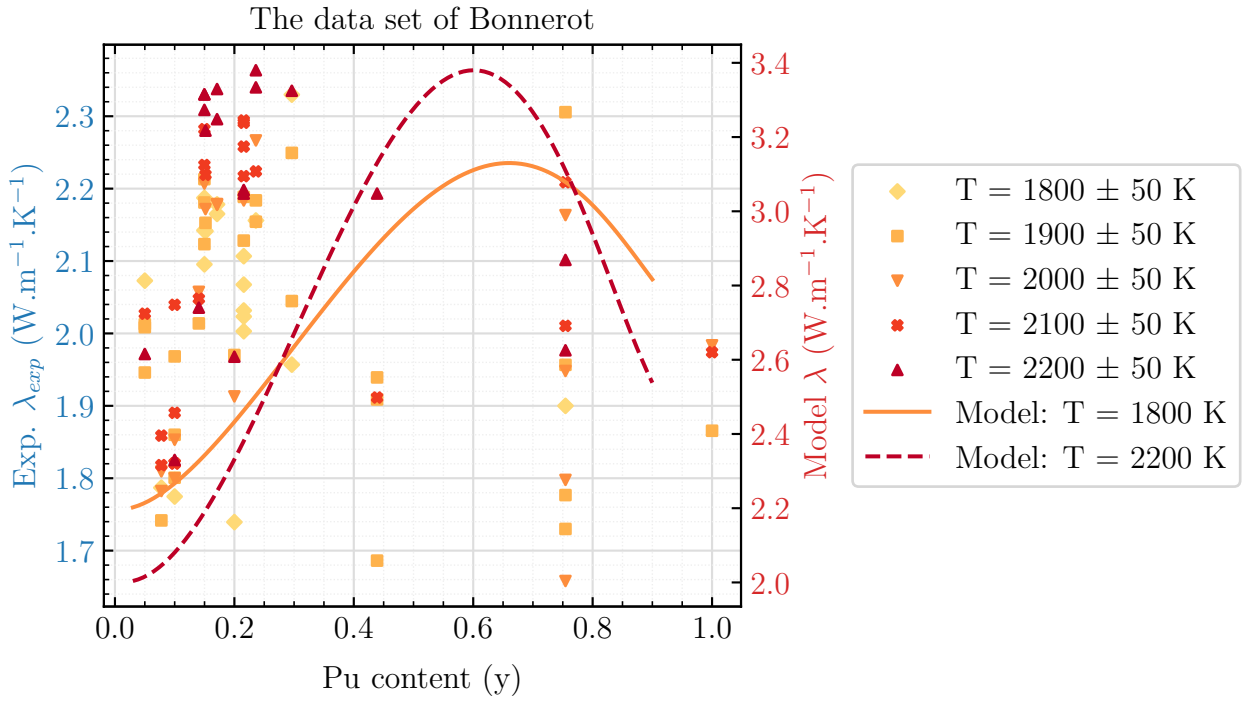

Figure 4.21: Experimental (from Bonnerot [5]) and modeled (in this work) plutonium variation of thermal conductivity at temperatures in the range $T \in [1800 - 2200]$ K

Weilbacher [6] also studied the effect of plutonium content on both phonon and electron contributions to thermal conductivity.
However, he did not propose a model for the effect of plutonium.
Indeed, he used quite the same equation as Bonnerot to represent the effect of electrons, but the fitted variation of what he also calls the activation energy was not modeled.
This may be caused by the fact that no physical equation could reproduce this variation. Weilbacher therefore did not conclude on the effect of plutonium content on the electronic term.
Another very curious observation from Weilbacher's data set is that plutonium content seems to impact both phonon and electron terms in the same way.
Indeed, as shown in Figure 4.22, the plutonium content variation of thermal conductivity, according to the data set of Weilbacher, seems to have the same form at $T = 800$ K and at $T = 2400$ K.

This observation is not consistent with our model, which shows a clear difference in the way plutonium content influences the contribution of phonons and electrons.
We observe in particular that in Weilbacher's data set, the maximum of thermal conductivity is achieved at $y = 0.15$, followed by a minimum at $y = 0.45$, regardless of temperature.
This observation is not consistent with both our model and the EU projects' data set, showing a maximum of thermal conductivity in the range $y \in [0.40 - 0.60]$.
Indeed, in our electronic model, the contribution from the plutonium polaron increases with plutonium content, whereas that of uranium decreases. Thermal conductivity due to electrons

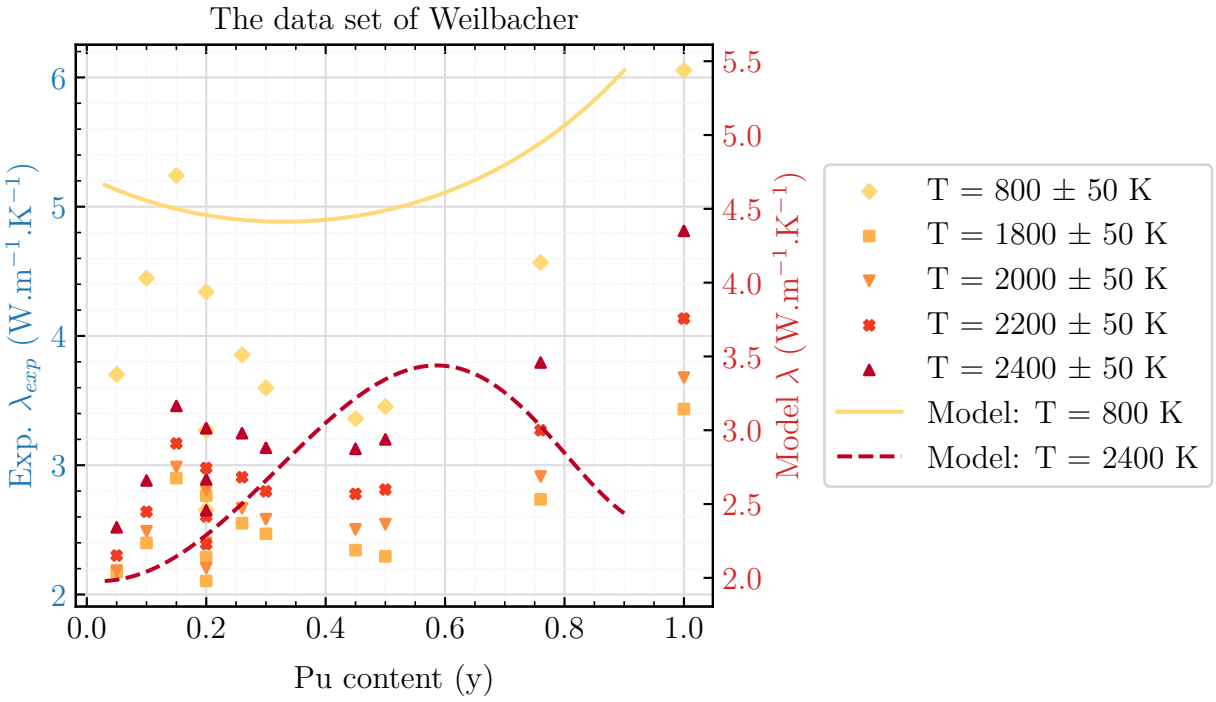

Figure 4.22: Experimental (from Weilbacher [6]) and modeled (in this work) plutonium variation of thermal conductivity at temperatures in the range $T \in [800 - 2400]$ K

is proportional to the product $\frac{\sigma^{el}_{Pu}\sigma^{el}_{U}}{\sigma^{el}}$. Therefore, since $\sigma^{el}_{Pu} \approx 0$ when $y < 0.15$ and $\sigma^{el}_{U} \approx 0$ when $y > 0.85$, the plutonium content profile of thermal conductivity is parabolic with a maximum, situated at approximately $y = 0.60$.
In order to be able to reproduce the particular variation with plutonium content, observed in the Weilbacher data set in the ranges $y \in [0.00 - 0.15]$ and $y \in [0.75 - 1.00]$:

1. the plutonium polaron's contribution at $y < 0.15$ should not be close to 0.
2. the uranium polaron's contribution at $y > 0.75$ should not be close to 0.

Those requirements are difficult to be achieved, since in those ranges: $y < 0.15$ and $y > 0.75$, the respective contributions from plutonium and uranium are almost zero.
Through the introduction of a percolation parameter in their model, Bhargava *et al.* [156, 157] showed that in their ternary $(Mn_x,Fo_{3-x})O_4$ system, the contribution from Mn and Fe should be set to zero when their respective atomic fraction is lower than 0.31.
Even though in this work, we do not include a percolation parameter in modeling, assuming a non-negligible contribution from the plutonium polaron when plutonium content is lower than $y < 0.15$ does not seem physical.
As for the minimum of thermal conductivity, observed at $y = 0.45$, under no circumstances can our model yield a minimum at that plutonium content.
Indeed, in the range $y \in [0.40 - 0.60]$, both contributions are different than zero and yield a maximal σ^{el}. Therefore, thermal conductivity will always assume its maximum in the range $y \in [0.40 - 0.60]$.
As to the phonon term, this work can partially reproduce the plutonium variation in Weilbacher's data set (at $T = 800$ K). In our phonon term, adding plutonium to a UO_2 system

can only lead to decrease thermal conductivity in the range $y \in [0.00 - 0.50]$ since foreign plutonium atoms act as phonon scattering centers.
This is consistent with the decreasing trend in Weilbacher's measurements in the range $y \in [0.15 - 0.50]$, but not with the observed increasing trend in the range $y \in [0 - 0.15]$. Our phonon model however confirms that thermal conductivity at $T = 800$ K increases in the range $y \in [0.50 - 1.00]$, as predicted by Weilbacher.

Other work mostly focus on the effect of plutonium at rather low temperatures (*i. e.* $T < 2000$ K).
Ikusawa *et al.* [225] measured thermal conductivity of MOX in the range $y \in [0 - 0.08]$ and provided a model for the phonon contribution, which shows a decreasing trend of thermal conductivity with y. This work is consistent with our model for the phonon contribution, which also shows a decreasing trend until $y = 0.45$. Ikusawa *et al.*'s model however could not be used above $y = 0.08$ due to its empirical nature.

Gibby [105] studied the effect of plutonium on MOX fuels with six different plutonium contents in the range $y \in [0.0 - 0.30]$ and one measurement on PuO_2.
The measurements were performed at temperatures lower than 1600 K, and the main conclusion of his work was that thermal conductivity decreases from $y = 0.00$ to $y = 0.30$.
The value for PuO_2 was higher than that of the MOX at $y = 0.30$. According to the model, proposed by Gibby, thermal conductivity decreases in the range $[0.00 - 0.60]$, then slightly increases until $y = 1.00$.
This is in agreement with the variation of the phonon term with y, predicted in this work.

Goldsmidth and Douglas [226] confirmed the decreasing trend, predicted by Gibby [105] in the range $y \in [0.00 - 0.30]$.

Serizawa *et al.* [78] showed that MOX fuels in the range $y \in [0.10 - 0.20]$ at temperatures below 1800 K did not show any particular plutonium content dependency. Indeed, their data was highly scattered, especially for temperatures below 1200 K, and therefore the plutonium content dependency may have been compensated by the experimental errors.

4.7.4 Effect of oxygen content

Both variations with deviation from stoichiometry, experimental and theoretical, yield a monotone decreasing function (see Figure 4.23).

Our model was also compared to that of Kato *et al.* [3] and showed good consistency.
As temperature increases, the effect of x is shown to be less important both by the experimental data and our model.
Indeed, in Chapter 3, we showed that increasing temperature increases the intrinsic phonon-phonon interactions (U-processes), compared to the extrinsic phonon-impurity ones. The U-processes processes were however shown to be less sensitive to deviation from stoichiometry than the phonon-impurity ones.

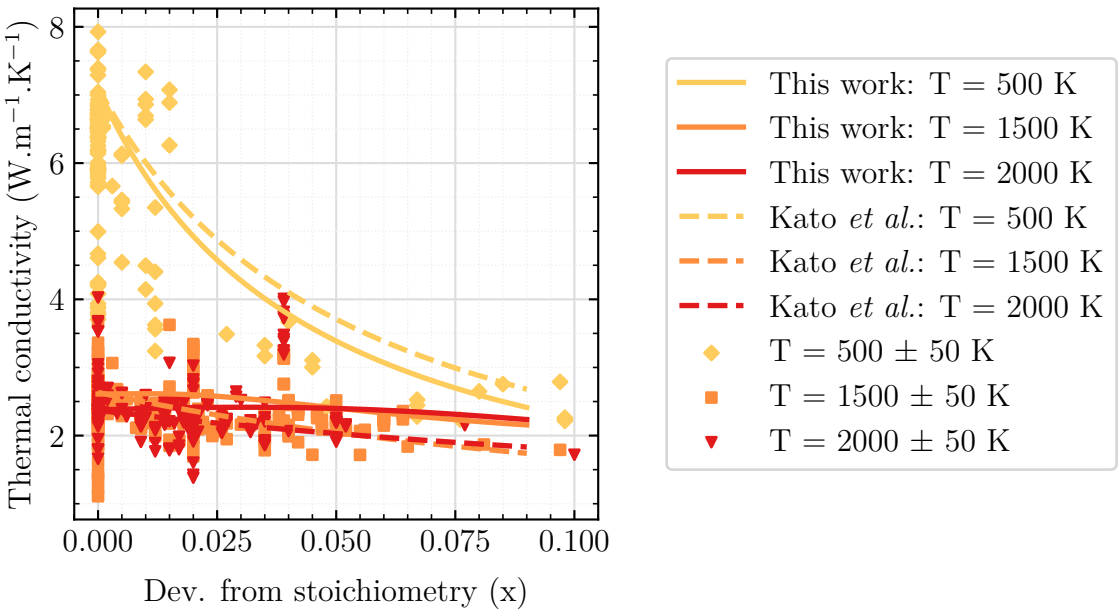

Figure 4.23: Experimental and theoretical variation with deviation from stoichiometry x of thermal conductivity. The model was plotted for a mean plutonium content of $\overline{y} = 0.21$, representing the weighted average plutonium content of the experimental data. The semi-empirical correlation with x of Kato *et al.* [3] was also plotted.

That is, the variation with stoichiometry of the physical parameters, describing the U-processes (*i. e.* mainly Debye temperature and Gruneisen parameter) does not affect the overall thermal conductivity variation, as much as the scattering cross section in the phonon-impurity term A. Furthermore, even at temperatures where polarons play an important role (*i. e.* $T > 2000$ K), the effect of stoichiometry is negligible, compared to the effect of plutonium content. This highlights the fact that even if a possible oxygen reduction of the sample occurs during thermal diffusivity measurements at high-temperatures, no significant impact on thermal conductivity would be expected.

As long as the correlated stoichiometry-plutonium content effect is concerned, the number of experimental measurements is not sufficient to confirm it.
Indeed, in the previous chapter, we saw that increasing plutonium content increases the effect of stoichiometry on the phonon contribution to thermal conductivity. This becomes however clear at extremely high plutonium contents (*i. e.* $y > 0.80$). Therefore, to conclude on this phenomenon, experimental measurements on MOX fuels with $y > 0.80$ are needed through a large range of stoichiometry values $x \in [0.00 - 0.10]$.

The variation of thermal conductivity with x, for $x > 0.05$ also needs supplementary measurements in order to confirm the model. Indeed, as observed in Figure 4.23, the number of measurements above $x = 0.05$ is very limited.

4.8 Conclusion and perspectives

This chapter was dedicated to compare theory and measurements.
The comparison included 6619 experimental thermal conductivity points, covering temperatures from room temperature to temperatures close to the melting temperature, plutonium contents in the range $y \in [0.00 - 1.00]$, deviations from stoichiometry in the range $x \in [0.00 - 0.10]$ and porosity fractions $p \in [0.00 - 0.21]$.
First, we compared the model, described in the previous chapter (*i. e.* Chapter 3) with measurements. We observed high discrepancies between the predicted variation with temperature of thermal conductivity and the measurements. We observed in particular that the previous model, systematically underestimated experimental thermal conductivity, regardless of the temperature.
Given the temperatures, achieved in FNR nominal conditions (*i. e.* $T > 1500$ K), it is of crucial importance to describe accurately the temperature variation of thermal conductivity.
For this, we calibrated some of the model parameters, using thermal conductivity experimental data, in order to increase the consistency between the model and experimental data. This calibration was done separately for the three contributions to thermal conductivity, considered here: phonon, polaron and photon.

The calibration of the phonon term consisted of adding an empirical factor in the expression for the intrinsic thermal resistivity B and in particular behind the constant B^*.
Indeed, no clear proof for the scientific meaning of this constant was reported in the literature [120, 137, 138]. We therefore chose to use thermal conductivity experimental data to calibrate this constant, instead of calibrating the other model parameters (*i. e.* Gruneisen parameter and Debye temperature), the physical meaning of which could not be recalled into question.
The calibration of this constant led to the conclusion that in order for the phonon term to describe correctly low temperature experimental data (*i. e.* $T < 1500$ K), the B^* constant in the initial model has to be multiplied by a factor of 2.44.

The calibration of the electronic term involved the estimation of the $(H, S, E_m(Pu)$ and $E_m(U))$ parameters. We therefore used thermal conductivity experimental data to provide a new estimation for those parameters, compared to that in the previous chapter.
However, the new parameter estimation, based solely on thermal conductivity experimental data failed to reproduce the electrical conductivity measurements.
Consequently, a second attempt was made for estimating those parameters, using both electrical and thermal conductivity data, based on a classical least-squares multi-objective cost function.
However, this optimization led to the conclusion that to accurately describe both electrical and thermal conductivity measurements, non-physical parameters had to be obtained (in particular negative migration energies for both polarons).
Aware of the importance of obtaining physical parameters, given the predictive nature of our model, we used Bayesian approach to find the best compromise between consistency of both electrical and thermal conductivity models with measurements, and physical parameters. With

this optimization approach, we:

1. obtained physical parameters, other that those of the previous chapter.
2. increased the amplitude of the electronic thermal conductivity, therefore increasing the consistency between the thermal conductivity model and the data, while preserving the consistency between the electrical conductivity model and the associated data.

Even though the consistency between the thermal conductivity model and the data was considerably increased, as opposed to the model proposed in the previous chapter, important residuals were however observed, especially for temperatures above 2300 K. Two main reasons for those discrepancies were identified:

1. Experimental uncertainties, related to the extrapolation of a heat capacity model for PuO_2, above its range of validity (*i. e.* above 2500 K).
2. Modeling uncertainties, related to the assumption of a like-element hopping nature of the polarons.

This analysis led to two essential perspectives of this chapter:

1. complete the already existing heat capacity data sets for PuO_2 [227–229] by measurements in the range T $\in [2400 - T_m]$, where m stands for melting.
2. perform new optimizations by including a third contribution in the electrical conductivity model, related to the possible Pu-U mixed-element hopping.

To compensate for the observed residuals at high-temperatures, we tried to fit those by a radiative T^3 contribution (*i. e.* from photons). The residuals increased more rapidly than T^3 with temperature and therefore no physical radiative term could fit the residuals.

Finally, we compared the new model to the data, not only in terms of temperature variation, but also of plutonium and oxygen content. The comparison in terms of plutonium content dependency led to the following conclusions:

1. Below 2000 K, regardless of stoichiometry, the plutonium content dependency, predicted in our model is consistent with the experimental data, showing a slightly **decreasing trend until $y = 0.45$**, followed by an **increase until $y = 1$**.
2. Above 2000 K, at the **stoichiometric composition** ($x = 0$), the predicted plutonium content variation of thermal conductivity is consistent with the measurements of the EU projects, covering the range $y \in [0.20 - 1.00]$. Both model and measurements show a **parabolic variation with a maximum around $y = 0.60$**.
3. Above 2000 K, at the **hypostoichiometric composition** (here $x = 0.02$), the data set of the EU projects shows a shift of the plutonium content value, at which the maximum is obtained, to lower plutonium contents: $y = 0.45$ (vs. $y = 0.60$ at $x = 0.00$). Our model also shows this shift, but not in such proportions. To obtain such shift with our model, **the migration energy of the plutonium polaron must be lowered**.
4. Overall, to accurately predict the plutonium content value, at which thermal conductivity attains a maximum, an accurate estimate of the migration energy of **both uranium and plutonium polarons** is required.

Given the need for an accurate estimate of those parameters, the following experimental measurements are needed:

1. Electrical conductivity measurements on **highly hypostoichiometric MOX fuels** (*i. e.* $x > 0.02$) and at temperatures **above 2000 K**. Those measurements will increase the estimation by inverse methods of the migration energy of the **plutonium polaron**.
2. Electrical conductivity measurements on MOX fuels with **very low plutonium contents** (*i. e.* $y \in [0.05 - 0.1]$) and temperatures **above 2000 K**. Those measurements will increase the estimation by inverse methods of the migration energy of the **uranium polaron**.

DFT $+U$ calculations can also be of interest in order to compare the results, obtained by inverse techniques and by more fundamental approaches.

4.9 Conclusion et perspectives du chapitre

Ce chapitre est consacré à la comparaison entre la théorie et les mesures. La comparaison a porté sur 6619 points de conductivité thermique expérimentale, couvrant des températures allant de la température ambiante à des températures proches de la température de fusion, des teneurs en plutonium dans l'intervalle $y \in [0 - 1]$, des écarts par rapport à la stœchiométrie dans l'intervalle $x \in [0 - 0.1]$ et des fractions de porosité $p \in [0 - 0.21]$.
Tout d'abord, nous avons comparé le modèle décrit dans le chapitre précédent (c'est-à-dire le chapitre 3) avec les mesures. Nous avons observé des écarts importants entre la variation théorique de la conductivité thermique en fonction de la température et les mesures. Nous avons observé en particulier que le modèle précédent sous-estimait systématiquement la conductivité thermique expérimentale, quelle que soit la température. Compte tenu des températures atteintes dans les conditions nominales des RNR (*i. e.* $T > 1500$ K), il est d'une importance cruciale de décrire avec précision la variation de la conductivité thermique en fonction de la température. Pour cela, nous avons calibré certains paramètres du modèle, en utilisant des données expérimentales de conductivité thermique, afin d'augmenter la cohérence entre le modèle et les données expérimentales. Ce calibrage a été effectué séparément pour les trois contributions à la conductivité thermique considérées ici: phonon, polaron et photon.

L'étalonnage du terme phononique a consisté à ajouter un facteur empirique dans l'expression de la résistivité thermique intrinsèque B et en particulier derrière la constante B^*. En effet, aucune preuve claire de la signification scientifique de cette constante n'a été publiée dans la littérature [120, 137, 138]. Nous avons donc choisi d'utiliser les données expérimentales de conductivité thermique pour calibrer cette constante, au lieu de calibrer les autres paramètres du modèle (*i. e.* paramètre de Gruneisen et température de Debye), dont la signification physique ne pouvait être remise en question. L'optimisation de cette constante a permis de conclure que pour que le terme phononique décrive correctement les données expérimentales à basse température (*i. e.* $T < 1500$ K), cette constante doit être multipliée par un facteur 2.44. L'étalonnage du terme électronique implique l'estimation des paramètres $(H, S, E_m(Pu)$ et $E_m(U))$. Nous avons donc utilisé les données expérimentales de conductivité thermique pour

fournir une nouvelle estimation de ces paramètres, comparée à celle du chapitre précédent. Cependant, la nouvelle estimation, basée uniquement sur les données expérimentales de conductivité thermique, n'a pas permis de reproduire les mesures de conductivité électrique. Par conséquent, une deuxième tentative d'estimation de ces paramètres a été faite, en utilisant à la fois les données de conductivité électrique et thermique. Cependant, cette optimisation a conduit à la conclusion que pour décrire avec précision les mesures de conductivité électrique et thermique, des paramètres non physiques devaient être obtenus (en particulier des énergies de migration négatives pour les deux polarons). Conscients de l'importance d'obtenir des paramètres physiques, étant donné la nature prédictive de notre modèle, nous avons utilisé une approche bayésienne pour trouver le meilleur compromis entre la cohérence des modèles de conductivité électrique et thermique avec les mesures, et les paramètres physiques. Grâce à cette approche d'optimisation, nous :

1. avons obtenu des paramètres physiques autres que ceux du chapitre précédent.
2. nous avons augmenté l'amplitude de la conductivité thermique électronique, augmentant ainsi la cohérence entre le modèle de conductivité thermique et les données, tout en préservant la cohérence entre le modèle de conductivité électrique et les données associées.

Même si la cohérence entre le modèle de conductivité thermique et les données a été considérablement améliorée, par rapport au modèle proposé dans le chapitre précédent, des résidus importants ont été observés, en particulier pour les températures supérieures à 2300 K. Deux raisons principales ont été identifiées pour expliquer ces divergences:

1. incertitudes expérimentales, liées à l'extrapolation d'un modèle de capacité thermique pour PuO_2, au-delà de son domaine de validité (*i. e.* au-dessus de 2500 K).
2. incertitudes de modélisation, liées à l'hypothèse que les polarons ne peuvent effectuer des sauts qu'entre atomes du même type: Pu-Pu et U-U.

Cette analyse a conduit à deux perspectives essentielles de ce chapitre:

1. compléter les ensembles de données déjà existants sur la capacité thermique de PuO_2 [227–229] par des mesures dans l'intervalle $T \in [2400 - T_m]$, où m représente la fusion.
2. Effectuer de nouvelles optimisations en incluant une troisième contribution dans le modèle de conductivité électrique, liée à l'éventuel saut d'éléments mixtes Pu-U.

Nous avons essayé d'expliquer les résidus observés à haute température, par une contribution radiative T^3 (*i. e.* des photons). En revanche, les résidus augmentent plus rapidement que T^3 avec la température et, par conséquent, aucun terme radiatif physique ne pouvait correspondre aux résidus.
Enfin, nous avons comparé le nouveau modèle aux données, non seulement en termes de variation en température, mais aussi en teneur en plutonium et en oxygène. La comparaison en termes de dépendance à la teneur en plutonium a conduit aux conclusions suivantes:

1. En dessous de 2000 K, quelle que soit la stœchiométrie, la dépendance à la teneur en plutonium, prédite dans notre modèle, est cohérente avec l'ensemble des données des projets de l'UE, montrant une légère **tendance à la baisse jusqu'à $y = 0,45$**, suivie d'une **augmentation jusqu'à $y = 1$**.

2. Au-dessus de 2000 K, à la **composition stœchiométrique** ($x = 0$), la variation théorique de la conductivité thermique en fonction de la teneur en plutonium est cohérente avec les mesures des projets de l'UE, couvrant la plage $y \in [0.2 - 1]$. Le modèle et les mesures montrent tous deux une variation **parabolique avec un maximum autour de $y = 0.6$**.
3. Au-dessus de 2000 K, à la **composition hypostoechiométrique** (ici $x = 0.02$), l'ensemble des données des projets de l'UE montre un déplacement de la valeur de la teneur en plutonium, à laquelle le maximum est obtenu, vers des teneurs en plutonium plus faibles: $y = 0.45$ (contre $y = 0.60$ à $x = 0$). Notre modèle montre également ce décalage, mais pas dans de telles proportions. Pour obtenir un tel décalage avec notre modèle, **l'énergie de migration du polaron de plutonium doit être plus faible**.
4. Globalement, pour prédire avec précision la valeur de la teneur en plutonium, à laquelle la conductivité thermique atteint un maximum, une estimation précise de l'énergie de migration de **des deux polarons** est nécessaire.

Étant donné la nécessité d'une estimation précise de ces paramètres, les mesures expérimentales suivantes sont nécessaires :

1. Mesures de la conductivité électrique sur des **combustibles MOX fortement hypostoechiométriques** (*i. e.* $x > 0.02$) et à des températures **supérieures à 2000 K**. Ces mesures permettront d'améliorer l'estimation, par des méthodes inverses, de l'énergie de migration du **polaron** Pu^{3+}.
2. Mesures de la conductivité électrique sur les combustibles MOX à **très faible teneur en plutonium** (*i. e.* $y \in [0.05 - 0.1]$) et à des températures **supérieures à 2000 K**. Ces mesures permettront d'améliorer l'estimation par des méthodes inverses de l'énergie de migration du **polaron** U^{5+}.

Les calculs DFT$+U$ peuvent également être intéressants afin de comparer les résultats obtenus par les techniques inverses et par des approches plus fondamentales.

Chapter 5

GERMINAL (V3) calculation of the INTA-2 experiment, using the thermal conductivity model, developed in this work

Contents

Summary

In this chapter, we will use the thermal conductivity model, developed in the previous chapter to simulate the fuel behavior during the INTA-2 irradiation experiment, using the fuel performance code *GERMINAL (V3)* of the software platform *PLEAIDES* (**P**late-forme **L**ogiciel pour les **E**lements **I**rradiés dans les **A**ssemblages, **D**emonstration, en **E**xpériminetation, ou en **S**ervice) [8].
The INTA-2 experiment was chosen in particular, since this irradiation provides thermocouple data and therefore allows to validate the calculated temperature.
The temperature at the fuel center (*i. e.* at the thermocouple position) is the only available observable for this experiment. Despite this fact, in this chapter, we will analyze the calculation results, concerning the main phenomena, occurring in the Beginning Of Life (BOL) of the fuel: thermal expansion and fuel-cladding gap closure.

Résumé

Dans ce chapitre, nous utiliserons le modèle de conductivité thermique développé dans le chapitre précédent pour simuler le comportement du combustible pendant l'expérience d'irradiation INTA-2, en utilisant le code de performance du combustible GERMINAL (V3) de la plate-forme logicielle PLEAIDES (**P**late-forme **L**ogiciel pour les **E**lements **I**rradiés dans les **A**ssemblages, **D**emonstration, en **E**xpériminetation, ou en **S**ervice) [8].
L'expérience INTA-2 a été choisie en particulier, car cette irradiation fournit des données de thermocouple et permet donc de valider la température calculée.
La température au centre du combustible (*i. e.* à la position du thermocouple) est la seule observable disponible pour cette expérience. Malgré cela, dans ce chapitre, nous analyserons les résultats de calcul concernant les principaux phénomènes qui se produisent au début de la vie du combustible: dilatation thermique et fermeture du jeu pastille-gaine.

5.1 General characteristics of the INTA-2 experiment

The **IN**strumented **T**est **A**ssembly 2 (INTA-2) experiment [107, 230–234] comprises 19 pins, including 16 instrumented pins, carrying MOX fuel, irradiated in the JOYO Mk-II reactor [232, 235, 236] in Japan for 7.2 JEPP (**J**our **E**quivalent **P**leine **P**uissance) in 1991.
In this experiment, 13 pins were equipped with a tungsten-rhenium type thermocouple, inserted into the central annular hole, measuring the fuel core temperature and 3 with thermocouples measuring the experimental assembly's coolant inlet and outlet temperatures (see Figure 5.1). The cladding was composed of austenitic steel [107]. Among those available, the I2208 pin was

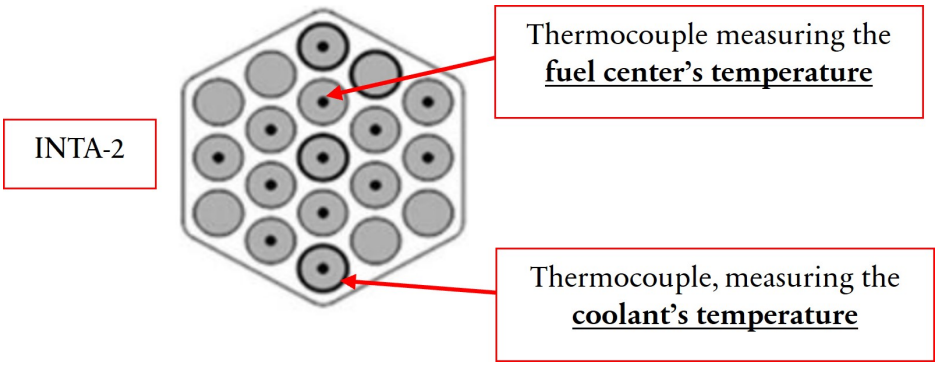

Figure 5.1: Schematic representation of the INTA-2's cross section of test fuel pin bundle [236]

selected as it was judged to have the lowest effect of fuel column and thermocouple eccentricity on the target temperature measurement. Details of the selected pin are shown in Table 5.1.

Characteristic	Value
Pellet inner diameter (mm)	1.916
Pellet outer diameter (mm)	6.546
Cladding inner diameter (mm)	6.704
Cladding thickness (mm)	0.40
Pu/(U+Pu) mass content (%)	18.89
Density (% th.d)	95.29
Oxygen/Metal ratio	1.96
Fissile column length (mm)	551.45
Upper plenum volume (cm^3)	20.0

Table 5.1: General characteristics of the pin I2208 of the INTA-2 experiment [107].

Irradiation of the INTA-2 assembly provides a direct measurement of the fuel core temperature. The latter can be used, together with the local linear power estimate, to validate the models included in *GERMINAL (V3)* for estimating the thermal regime in the fuel at the beginning of its life.
For the pin I2208, the thermocouple stopped working when the power exceeded $\approx 300\ W\,cm^{-1}$, *i. e.* after half a day's irradiation.

Irradiation time (days)	Linear power ($W\,cm^{-1}$)	Cladding outer temperature (°C)
0	0.00	350
0.042	10.42	359
0.084	37.52	374
0.126	63.07	388
0.168	91.72	400
0.210	97.44	402
0.252	109.26	407
0.294	138.30	420
0.336	164.91	432
0.378	185.40	441
0.420	221.76	457
0.462	252.62	470
0.504	275.51	479
0.546	302.90	491

Table 5.2: Irradiation conditions of the pin I2208

The temperature measurement is therefore not influenced by fuel restructuring, but only by early-life phenomena such as thermal expansion and relocation of fuel fragments during fracturing.
The pin is discretized into a single axial slice, to which the linear power and outer cladding temperature loads are applied, according to the data available in Table 5.2.

5.2 Presentation of GERMINAL

The *PLEIADES* simulation platform [8] was briefly introduced in Chapter 1. For more detailed information about *PLEIADES*, the reader may refer to [8]. In this section, we will briefly introduce some basic concepts in *GERMINAL* simulations.

5.2.1 Fuel pin geometry

The fuel pin geometry in *GERMINAL* is an axisymmetric $1D$ 1/2 representation (see Figure 5.2). This representation consists of dividing the fuel column into axial slices, within which a 1D radial meshing of the fuel pellet, the fuel-pellet gap and the cladding is created [7]. The radial meshing is axially located in the middle of the axial slice in question. The axial discretization can be composed of 10 to 40 slices. The number of slices generally depends on the fuel pin composition or its axial power. Radial meshing is refined as the fuel cladding is approached. This allows more accurate simulation of fuel behavior near the central hole. This radial meshing also allows to reduce simulation time cost, while maintaining high result precision.

5.2.2 Thermal analysis

GERMINAL is a thermo-mechanical fuel performance code. For further information on the mechanical modeling, the reader may refer to [7].
In this study, we are particularly interested in the impact of thermal conductivity on fuel temperature. Thermal analysis is performed, using Finite Elements computation with the CAST3M solver [237].
The Fourier's law is used to compute the temperature inside the fuel pin [7]:

$$\rho C_p \frac{\partial T}{\partial t} = \mathrm{div}(\lambda \overrightarrow{\mathrm{grad}\, T}) + S \tag{5.1}$$

where:

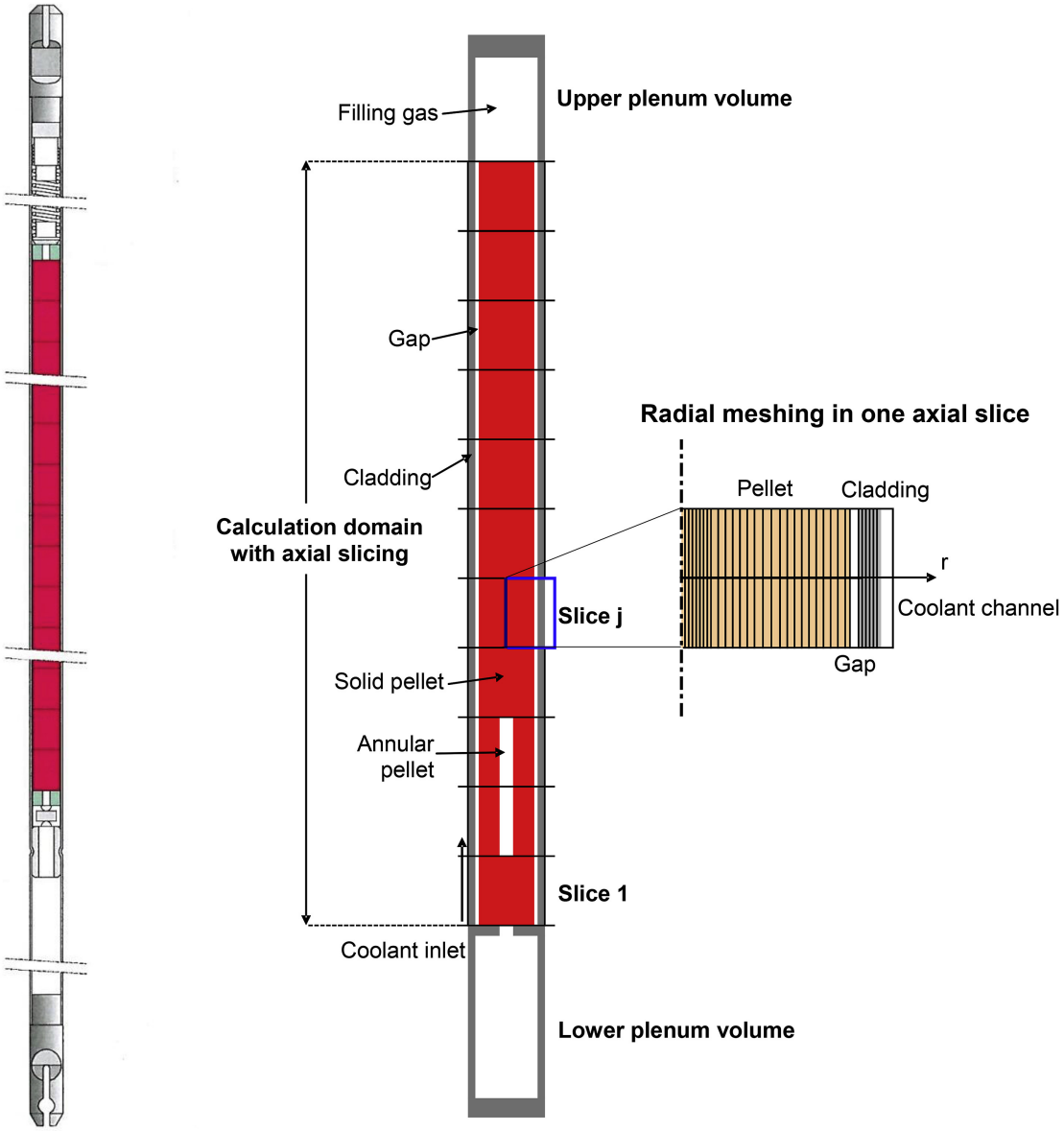

Figure 5.2: 1D 1/2 fuel pin representation used by GERMINAL [7]

ρ : density of the material ($\mathrm{kg\,m^{-3}}$)
C_p : heat capacity of the material ($\mathrm{J\,kg^{-1}\,K^{-1}}$)
S : volume power density ($\mathrm{W\,m^{-1}}$)
λ : thermal conductivity of the material ($\mathrm{W\,m^{-1}\,K^{-1}}$)
T : temperature (K)

The volume power density is driven by the fission reaction [7]:

$$S(r,z,t) = \left(\sum_i \varepsilon_{f_{\mathrm{X_i}}} \times \sigma_{f_{\mathrm{X_i}}} \times c_{\mathrm{X_i}}(r,z,t) \times N_A \right) \times \phi_n(r) \times \bar{\Phi}_n(z,t) \tag{5.2}$$

where:

$\varepsilon_{f_{\mathrm{X_i}}}$: fission energy of the X_i isotope (J)
$\sigma_{f_{\mathrm{X_i}}}$: one-group fission cross-section of the X_i isotope ($\mathrm{m^2}$)
$c_{\mathrm{X_i}}(r,z,t)$: local concentration of the X_i isotope at the time t. ($\mathrm{mol\,m^{-3}}$)
$\phi_n(r)$: local value of the radial normalized neutron flux shape (-)
$\bar{\Phi}_n(z,t)$: average neutron flux in the fuel section at the considered axial location, at the time t ($\mathrm{neutrons.m^{-2}\,s^{-1}}$)

The boundary condition, in steady-state conditions is a Dirichlet condition, imposing cladding outer temperature [7].
The latter is determined by the local temperature of the coolant, the heat transfer coefficient between the cladding and the coolant and the local heat flux, driven by the fuel power.
For further details on thermal analysis in *GERMINAL*, the reader my refer to [7, 8].

5.3 Simulation of the INTA-2 experiment with GERMINAL (V3)

In this section we will present the simulation results.
Two simulations were performed. One, using the thermal conductivity model, developed in this work, and the other, using the reference thermal conductivity model, used in *GERMINAL (V3)*, which is the model of Kato *et al.* [3].

The *V3* version of *GERMINAL* was used in this work, instead of *V2* because the newest version of GERMINAL uses the most up-to-date fuel properties reported for MOX fuel [EGIFE international fuel properties catalog: *to be published*].
For example, the reference thermal conductivity model in *GERMINAL (V2)* is that of Philipponneau [2]. In the previous chapter (see Figure 4.15), the latter was shown to yield lower values than both our model and that of Kato *et al.* [3].
We already identified a possible reason for this underestimation- the use of (1): a low number of experimental points for the calibration of the empirical model and (2): the use of old measurements, which were shown to be, for most of them, statistical outliers, compared to other experimental data.
Using Philipponneau's model may therefore lead to an overestimation of the fuel temperature

and thus lead to an underestimation of the fuel melting margin.
The latter is a crucial parameter for nuclear safety evaluations and therefore should be determined with precision. For further details on the differences between the *V2* and *V3* versions of *GERMINAL*, the reader may refer to [7, 8].

5.3.1 Axial and radial discretization

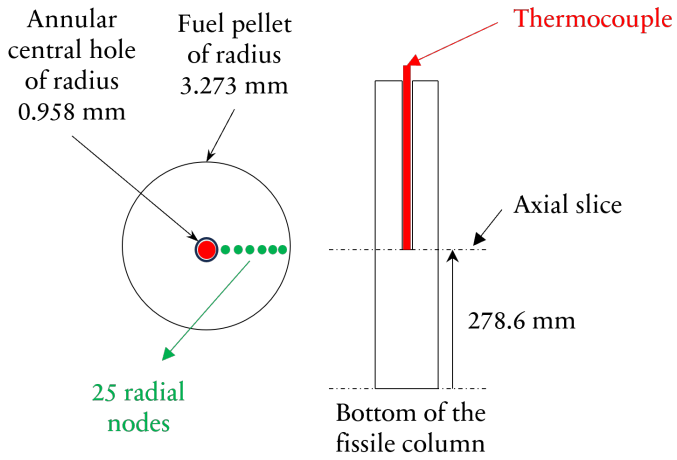

Figure 5.3: Scheme of the axial and radial discretizations in the *GERMINAL (V3)* simulation of the INTA-2 experiment

To simulate the INTA-2 experiment, the fuel geometry was divided into one 2.88 mm long axial slice, with a radial meshing, composed of 25 nodes (see Figure 5.3). The position of the axial slice was chosen to stay consistent with the thermocouple measurement position: at 278.60 mm from the bottom of the column.

5.3.2 Results

The burn-up in this experiment is low (*i. e.* 0.003 % FIMA). Phenomena, related to fission gas production or actinide migration therefore did not occur. INTA-2 is therefore a **B**eginning-**O**f-**L**ife (BOL) experiment. The BOL phenomena mainly concern fuel thermal expansion, fuel fragmentation relocation and oxygen redistribution. The simulation did not show any plutonium redistribution due to the relatively low temperatures (*i. e.* maximum 1750 K at the fuel center). The results will therefore concern fuel temperature, fuel-cladding gap and oxygen redistribution. Other experimental data, a part from fuel temperature, is not available for this experiment. The comparison with measurements will therefore concern only the fuel center temperature.

5.3.2.1 Fuel temperature

As shown in Figure 5.4, the calculated fuel temperature with the thermal conductivity model of Kato *et al.* is in perfect agreement with the thermocouple data. Indeed, the INTA-2 thermocouple data, was used to calibrate some empirical models, used in *GERMINAL (V3)*,

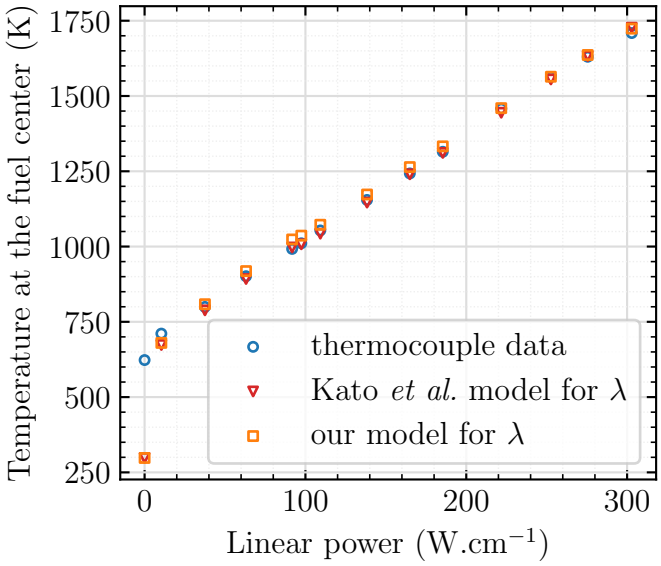

Figure 5.4: Calculated (void red triangles and orange squares) fuel temperature at the center of the pellet (*i. e.* at the thermocouple position) and measured temperature (blue circles), as a function of the linear power, at the axial position of 278.60 mm, from the bottom of the column.

related to BOL phenomena: namely the model for the fuel relocation [private com.]. This calibration was performed, using the thermal conductivity model of Kato *et al.* [3].
It therefore does not seem surprising that the calculated temperature, using the model of Kato *et al.*, is consistent with the measured temperature.
However, the model, developed in this work was not used to calibrate *GERMINAL (V3)* and yet Figure 5.4 shows that consistency between calculated and measured temperature is also obtained, using our thermal conductivity model.
This observation highlights the accuracy of our model in describing the fuel temperature in the BOL.

It should also be mentioned that the differences in calculated temperature, using the model of Kato *et al.* and ours are negligible (*i. e.* < 1 %). Indeed, in the previous chapter (see Figure 4.15), we showed that our model is consistent with Kato *et al*, in what concerns the phonon contribution to thermal conductivity.
In the temperature range of the INTA-2 experiment $T \in [630 - 1750]$ K, thermal conductivity is driven by phonons. This explains why both our model and that of Kato *et al.* yield similar fuel temperatures.

What is, however, different between Kato *et al.* and this work is the modeling of thermal conductivity at temperatures, where the contribution from polarons and photons become important.
In particular, Kato *et al.* does not account for plutonium or oxygen content.
However, in other FNR irradiations (*e. g.* NESTOR-3 [24, 25], PAVIX [110], TRABANT [112], CAPRIX [111]), plutonium redistribution occurs, together with fuel temperatures, attaining

2500 K in the fuel center.
In this configuration, Kato *et al.* can therefore under or overestimate the fuel temperature, since plutonium content is not taken into account in their model.
Our model does take plutonium content into account and can therefore be used to simulate the effect of plutonium redistribution on fuel temperature.
In this work, we chose the INTA-2 experiment to perform a first validation of our model, since INTA-2 provides thermocouple data.
In future work, our model can be used to simulate other FNR irradiations and examine the consistency with measurements of not only fuel temperature, but also JOG thickness, fission gas retention and release or fuel-cladding gap distance.

Radial fuel temperature profile

The radial fuel temperature distribution was also shown in Figure 5.5, showing a decreasing function with the radial position $\frac{r}{R}$, where R is the fuel external radius. This distribution function follows the resolution of the conduction equation [7]. The oxygen/metal ratio's variation is

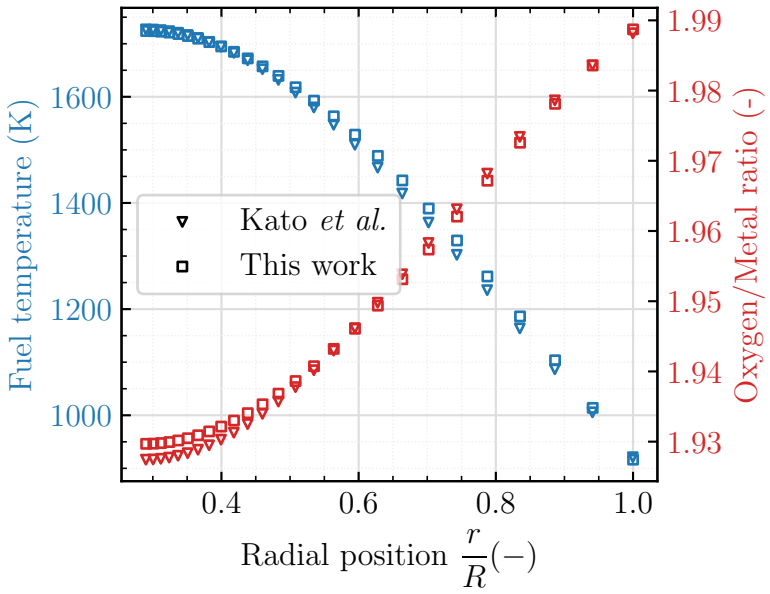

Figure 5.5: Variation of both calculated fuel temperature (blue) and oxygen/metal ratio (red) with the radial position on the pellet $\frac{r}{R}$ where R is the fuel external radius. The void triangles and squares represent respectively the results, obtained with the Kato *et al.* model for λ [3] and with our model. Those results correspond to the maximum linear power in INTA-2: 302.90 W cm^{-1}.

also shown. We observe that oxygen radially redistributes towards the fuel pellet's periphery. Thermal conductivity increases as the oxygen-to-metal ratio rises. Consequently, the radial temperature profile is a consequence of both the conduction equation, and the oxygen redistribution.
This observation also highlights the importance in considering the effect of O/M ratio in thermal conductivity modeling.
Once again, we observe good consistency in radial temperature profile, obtained with Kato *et*

al. and our model.
Indeed, not only did we show consistency in the temperature variation of the phonon term, predicted by our model and that of Kato *et al.* (see Figure 4.15), but also in its Oxygen/Metal variation (see Figure 4.23).
Therefore, the consistency of the results, obtained with the two models is further more justified.

5.3.2.2 Fuel-cladding gap

The fuel-cladding gap is a parameter of crucial interest, since it exhibits drastic changes at the very first moments of the irradiation, which can have important impact on fuel temperature (up to 300-400 K) [238].
In the very beginning of the irradiation (at $t = 0$ s), the gap is filled with helium, which was shown to have a negligible thermal conductivity to that of the fuel.
The gap exhibits fast closure due to two main BOL phenomena: fuel thermal expansion, as well as fuel fragmentation and relocation (see Figure 5.6). Figure 5.7 shows the variation with

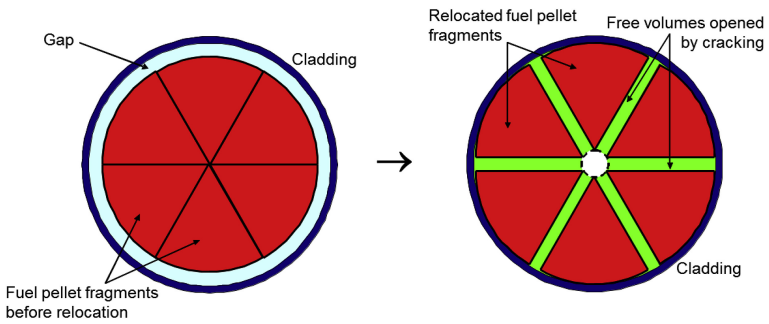

Figure 5.6: Fuel fragmentation (on the left) and relocation (on the right) [7]

linear power of the fuel-cladding gap, together with the fuel external radius and the cladding internal radius.
Under fuel external radius, one should understand the radius, after thermal expansion and fragment relocation.
We observe a very rapid increase in the fuel external radius, showing the effect of both thermal expansion and relocation, and on the other side a rather slow cladding expansion.
This leads to a rather fast gap closure. The gap is however not completely closed (*i. e.* it remains 18.3 µm of gap). Indeed, the maximum linear power in the INTA-2 experiment is not high enough to observe a complete closure of the gap. Another reason for the remaining 18.3 µm may originate from the fuel's roughness.
Figure 5.8 provides further evidence of the contribution of fragmentation and fuel relocation to gap closure, showing a correlation between gap closure and decreasing geometric density. The latter, accounts for both closed porosity (*i. e.* fabrication porosity) and fuel cracks (fragmentation).
In this irradiation, temperature is not high enough to activate the fabrication pores' migration towards the fuel center and therefore the decrease in geometrical density from the fabrication density (*i. e.* 95.29 % th.d) to 92 % th.d is due to fuel fragmentation.

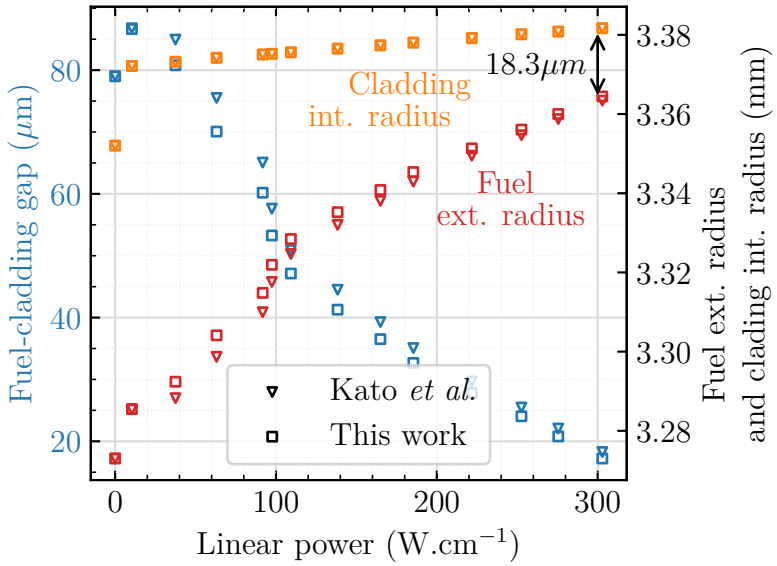

Figure 5.7: Calculated fuel-cladding gap (in blue, left y-axis), fuel external radius (in red, right y-axis), and cladding internal radius (in orange, right y-axis) as a function of the linear power, with both our model (squares) and the Kato *et al.* [3] (triangles) model for thermal conductivity.

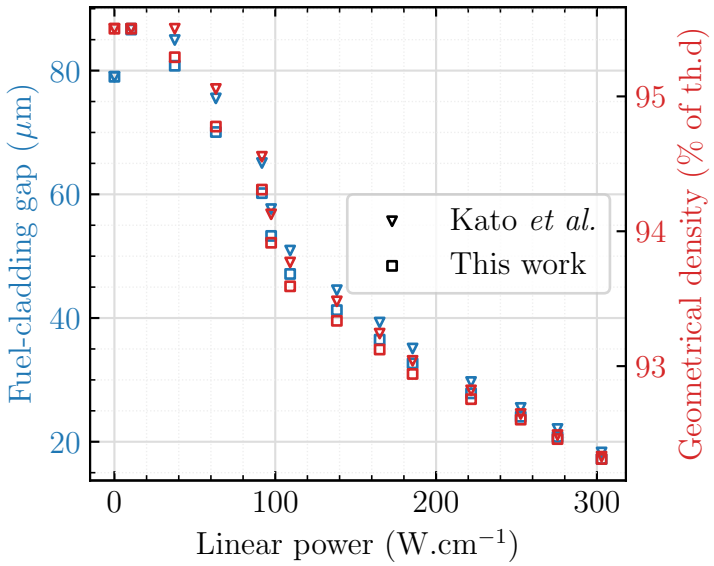

Figure 5.8: Calculated fuel-cladding gap (in blue) and geometrical density (*i. e.* accounting for closed (fabrication pores) and opened porosity: fuel fragmentation) (in red), as a function of the linear power, with both our model (squares) and the Kato *et al.* [3] (triangles) model for thermal conductivity.

5.4 Conclusion and perspectives

In this chapter, we showed that the thermal conductivity model, developed in this work, can be implemented into the fuel performance code *GERMINAL (V3)* due to its simple functional form, in terms of temperature, plutonium and oxygen content dependency.
This model is however based on physical foundations and therefore gathers two essential advantage: physically justified extrapolation to all temperatures, plutonium and oxygen contents of interest for FNR MOX fuels and low computational cost.
Those two criteria are essential for fuel performance codes, since these should be based on physical models, but at the same time, calculation time should be as low as possible.
This chapter therefore showed that this model is of great interest for fuel performance codes.

Simulating the INTA-2 irradiation experiment was a strategic choice, as this experiment provides thermocouple data and can therefore be used to validate the consistency of the calculated fuel temperature with the measured temperature. We showed that using the thermal conductivity, developed in this work led to perfect agreement between calculated fuel temperature at the pellet's center and thermocouple data. This observation highlighted the accuracy of this model in describing fuel temperature at the BOL.

We also compared fuel temperature results, obtained with our thermal conductivity model and that of Kato *et al.* [3], which is the reference thermal conductivity model, used in *GERMINAL (V3)*.
This comparison showed that the simulation results with both our model and Kato *et al.*, were similar (*i. e.* differences of less than 0.1 % for fuel temperature).
Those similarities were explained in terms of consistency between both our phonon thermal conductivity term and that of Kato *et al.*., which in the temperature range of the INTA-2 experiment (*i. e.* $T \in [630 - 1750]$ K) is the driving thermal conductivity term.
Differences in simulation results, with those two models are expected to appear for other FNR irradiation experiments, where temperatures are higher than 1750 K.
Above that temperature, the contribution of polarons and photons becomes important. In the previous chapter, we showed that, at high temperatures, plutonium content affects thermal conductivity in a significant manner (*i. e.* 35 % of increase from $y = 0.20$ to $y = 0.60$).
Given the plutonium redistribution, occurring in FNR MOX at high temperatures, uncertainties in the local fuel temperature are expected if plutonium content is not taken into account in thermal conductivity modeling. Kato *et al.* neglects this effect.
Performing GERMINAL simulations on FNR irradiations, achieving high temperatures (*e. g.* NESTOR-3 [22, 24], CAPRIX [111], PAVIX [110], TRABANT [112]) can therefore provide evidence for the differences in calculated fuel temperature with a Pu content-dependent model (our model) and Kato *et al.*.
This constitutes the main perspective of this chapter.

5.5 Conclusion et perspectives du chapitre

Dans ce chapitre, nous avons montré que le modèle de conductivité thermique, développé dans ce travail, peut être mis en œuvre dans le code de performance du combustible *GERMINAL (V3)* en raison de sa forme fonctionnelle simple, en termes de dépendance à la température, au plutonium et à la teneur en oxygène. Ce modèle est cependant basé sur des fondements physiques et présente donc deux avantages essentiels: une extrapolation physiquement justifiée à toutes les températures, teneurs en plutonium et en oxygène intéressantes pour les combustibles MOX RNR et un faible coût de calcul. Ces deux critères sont essentiels pour les codes de performance des combustibles, puisqu'ils doivent être basés sur des modèles physiques, mais en même temps, le temps de calcul doit être aussi faible que possible. Ce chapitre a donc montré que ce modèle présente un grand intérêt pour les codes de performance des combustibles.

La simulation de l'expérience d'irradiation INTA-2 était un choix stratégique, car cette expérience fournit des données de thermocouple et peut donc être utilisée pour valider la cohérence entre la température calculée du combustible et la température mesurée. Nous avons montré que l'utilisation de la conductivité thermique, développée dans ce travail, conduisait à un accord parfait entre la température calculée du combustible au centre de la pastille et les données du thermocouple. Cette observation a mis en évidence la précision de ce modèle dans la description de la température du combustible en début de vie.

Nous avons également comparé les résultats de la température du combustible, obtenus avec notre modèle de conductivité thermique et celui de Kato *et al.* [3], qui est le modèle de conductivité thermique de référence, utilisé dans *GERMINAL (V3)*. Cette comparaison a montré que les résultats des simulations avec notre modèle et celui de Kato *et al.* étaient similaires (*i. e.* différences inférieures à 0.1 % pour la température du combustible). Ces similitudes s'expliquent par la cohérence entre notre modèle de conductivité thermique phononique et celui de Kato *et al.*, qui, dans la gamme de températures de l'expérience INTA-2 (*i. e.* $T \in [630 - 1750]$ K), est le terme de conductivité thermique déterminant. Des différences dans les résultats de simulation, avec ces deux modèles, devraient apparaître pour d'autres expériences RNR, où les températures sont supérieures à 1750 K. Au-dessus de cette température, la contribution des polarons et des photons devient importante. Dans le chapitre précédent, nous avons montré qu'à haute température, la teneur en plutonium affecte la conductivité thermique de manière significative (*i. e.* 35 % d'augmentation de $y = 0.2$ à $y = 0.6$). Compte tenu de la redistribution du plutonium, qui se produit dans le MOX RNR à des températures élevées, des incertitudes sur la température locale du combustible sont attendues si la teneur en plutonium n'est pas prise en compte dans la modélisation de la conductivité thermique. Kato *et al.* néglige cet effet.
La réalisation de simulations *GERMINAL* sur des irradiations RNR, atteignant des températures élevées (*e. g.* NESTOR-3 [22, 24], CAPRIX [111], PAVIX [110], TRABANT [112]) peut donc fournir des preuves des différences de température du combustible calculée avec un modèle dépendant de la teneur en Pu (notre modèle) et Kato *et al.*. Ceci constitue la principale perspective de ce chapitre.

General conclusion and perspectives

The main goal of this work was to provide a physical understanding about the effect of temperature, plutonium and oxygen content, microstructure (mainly porosity), and irradiation on thermal conductivity.
Most reported modeling approaches are based on semi-empirical equations, fitted to thermal conductivity experimental data. However, those approaches are limited by the number of experimental data, and the ranges of temperature, plutonium and oxygen content, covered by the data. In addition, experimental measurements are subject to considerable dispersion, particularly at very high temperatures (*i. e.* above 2200 K). As a result, semi-empirical models are subject to considerable uncertainty when it comes to describing thermal conductivity at high temperatures.

Through physical modeling, we managed to avoid difficulties in extrapolating semi-empirical models beyond their experimental range of validity. In particular, we avoided issues, related to the unknown effect of plutonium content beyond $y \in [0.10 - 0.30]$, and especially in the high-temperature region (*i. e.* above 2200 K). The model, proposed in this work, covers the whole range of temperatures (T), plutonium (y) and oxygen (x) contents, which are of interest for FNR MOX fuels: T $\in [298 - 2800]$ K, $y \in [0.05 - 0.95]$, and $x \in [0.00 - 0.10]$.

In this work, we showed that plutonium content is of crucial importance in thermal conductivity modeling, contrary to what previous authors reported [2–5]. We especially showed that thermal conductivity above 2200 K (*i. e.* the electronic contribution) exhibits **a maximum** at a **plutonium content value, situated in the range $y \in [0.45 - 0.60]$**. This range depends on the oxygen stoichiometry of the fuel, therefore highlighting the **correlated plutonium-oxygen content effect**.
That is, decreasing the oxygen stoichiometry of the fuel tends to decrease the plutonium content, at which the maximum of thermal conductivity is obtained. This observation is both predicted by our model and verified experimentally, using the most up-to-date measurements on MOX fuels, covering plutonium contents in the range $y \in [0.24 - 1.00]$, provided by the European projects: ESNII+ [224], ESFR-SMART [108] and PUMMA [109].
A real challenge in this work was to find an accurate description of the temperature variation of thermal conductivity, especially for temperatures above 2000 K. We saw, in particular, an inflection point in thermal conductivity, situated at around $T = 2200$ K. Above this

temperature, important discrepancies with measurements were observed. Four main reasons were identified for those discrepancies:

1. **Extrapolation** of the heat capacity model for PuO_2 [239], used to indirectly determine thermal conductivity using thermal diffusivity experimental data, **beyond its domain of validity** (*i. e.* above 2500 K).
2. Missing **electrical conductivity experimental data** above 1400 K, to provide an accurate estimate of the **electronic model parameters** by inverse methods, independently of thermal conductivity experimental data.
3. Missing **extinction coefficient experimental data** on MOX fuel, to provide an accurate estimate of the **radiative contribution** to thermal conductivity, independently of thermal conductivity experimental data.
4. Assuming that both U and Pu polarons exhibit **like-element hopping**.

Once all the above-mentioned experimental data have been collected and a third contribution to the electrical conductivity model has been added, from a possible mixed-element Pu-U hopping, the Bayesian optimization cost function, developed in this work, can again be used to provide new model parameters. The four points mentioned above constitute **four major areas for progress**, with a view to improving consistency between the predicted temperature variation of thermal conductivity and measurements.

This work has also improved our understanding of the effects of irradiation on thermal conductivity, particularly in the case of FNR MOX fuels irradiated at high burn-up rates (*i. e.* the NESTOR-3 fuel). We saw that using Lucuta's thermal conductivity model, based on PWR UO_2 **SIM**ulated **F**els (SIMFuels) yields important discrepancies when compared to experimental data on FNR MOX fuels.
We improved the physics of the Lucuta model, by introducing a parameter, which is intrinsic to the irradiated fuel matrix: the atomic fraction of fission products.
The main challenge in modeling was to answer the question: why do we measure higher thermal conductivity at the MFP region (irradiated at 13 % FIMA) than at the TFC axial region (irradiated at 8 % FIMA). We therefore managed to show that porosity is a key element in explaining those differences.
This work therefore led to the proposition of an internship, the goal of which was to perform FFT calculations on microstructures, generated by image analysis on metallographies of the NESTOR-3 fuel. This internship study confirmed the conclusion of our work, that **porosity explains the differences** in thermal conductivity between the two axial regions.
Another perspective of our work was to perform **thermal conductivity measurements on FNR MOX SIMFuels**, to confirm our model for the thermal conductivity of the irradiated fuel matrix. Those measurements will be performed on the FNR MOX SIMFuels, fabricated and characterized in the thesis of Rafael Caprani [38], in the framework of a new doctoral research, starting this year.

In this work, we showed that our model can be implemented into the fuel performance code *GERMINAL* of the *PLEIADES* simulation software. The simulation on the INTA-2 irradiation experiment showed that temperature predictions, using the thermal conductivity,

developed in this work, were consistent with the thermocouple measurements.

Conclusion générale et perspectives

L'objectif principal de ce travail était de fournir une compréhension physique de l'effet de la température, de la teneur en plutonium et en oxygène, de la microstructure (principalement la porosité) et de l'irradiation sur la conductivité thermique. La plupart des approches de modélisation publiées dans la littérature sont basées sur des équations semi-empiriques, ajustées aux données expérimentales de conductivité thermique. Toutefois, ces approches sont limitées par le nombre de données expérimentales et par les plages de température et de teneur en plutonium et en oxygène couvertes par les données. De plus, les mesures expérimentales sont entachées d'importante dispersion, en particulier à très haute température (*i. e.* au-dessus de 2200 K). Par conséquent, les modèles semi-empiriques sont entachés d' incertitudes élevées quant à leur capacité à décrire la conductivité thermique à très haute température.

Grâce à l'approche physique, que nous avons utilisée dans cette thèse, nous avons réussi à éviter les difficultés liées à l'extrapolation des modèles semi-empiriques au-delà de leur domaine de validité expérimentale. En particulier, nous avons évité les problèmes liés à l'effet inconnu de la teneur en plutonium au-delà de $y \in [0.1 - 0.3]$, et en particulier dans la région à haute température (*i. e.* au-dessus de 2200 K). Le modèle proposé dans ce travail couvre toutes les domaines en température (T), teneur en plutonium (y) et en oxygène (x), qui présentent un intérêt pour les combustibles MOX RNR : T $\in [298-2800]$ K, $y \in [0.05-0.95]$, and $x \in [0-0.1]$.

Dans ce travail, nous avons montré que la teneur en plutonium est d'une importance cruciale dans la modélisation de la conductivité thermique, contrairement à ce que les auteurs précédents avaient affirmé. Nous avons notamment montré que la conductivité thermique présente **un maximum** à une **valeur de la teneur en plutonium, située dans l'intervalle $y \in [0.45 - 0.6]$**. Cette plage dépend de la stœchiométrie de l'oxygène du combustible, ce qui met en évidence l'effet **corrélé de la teneur en plutonium et en oxygène**. En d'autres termes, la diminution de la stœchiométrie en oxygène du combustible tend à diminuer la teneur en plutonium, à laquelle la conductivité thermique est maximale. Cette observation est à la fois prédite par notre modèle et vérifiée expérimentalement, en utilisant les mesures les plus récentes sur les combustibles MOX, couvrant les teneurs en plutonium dans la plage $y \in [0,24 - 1]$, fournies par les projets européens : ESNII+ [224], ESFR-SMART [108] et PUMMA [109].

Un véritable défi dans ce travail a été de trouver une description précise de la variation en température de la conductivité thermique, en particulier pour les températures supérieures à 2000 K. Nous avons vu, en particulier, un point d'inflexion dans la conductivité thermique, situé à environ $T = 2200$ K. Au-dessus de cette température, d'importantes divergences avec les mesures ont été observées. Quatre raisons principales ont été identifiées pour expliquer ces écarts :

1. **Extrapolation** du modèle de capacité thermique pour PuO_2 [239], utilisé pour déterminer indirectement la conductivité thermique à l'aide des données expérimentales de diffusivité thermique, **au-delà de son domaine de validité** (*i.e.* au-dessus de 2500 K).
2. **Manque de données expérimentales de conductivité électrique** au-dessus de 1400 K, pour fournir une estimation précise des**paramètres du modèle électronique** par des méthodes inverses, indépendamment des données expérimentales de conductivité thermique.
3. Manque de **données expérimentales sur le coefficient d'extinction** du combustible MOX, afin de fournir une estimation précise de la **contribution radiative** à la conductivité thermique, indépendamment des données expérimentales sur la conductivité thermique.
4. En supposant que les polarons U et Pu présentent **des sauts entre atomes du même type**.

Une fois que toutes les données expérimentales susmentionnées auront été collectées et qu'une troisième contribution au modèle de conductivité électrique aura été ajoutée, provenant d'un éventuel saut de Pu-U à éléments mixtes, la fonction de coût de l'optimisation bayésienne, développée dans ce travail, pourra à nouveau être utilisée pour fournir de nouveaux paramètres de modèle. Les quatre points mentionnés ci-dessus constituent **quatre domaines majeurs de progrès**, en vue d'améliorer la cohérence entre la variation de température prédite de la conductivité thermique et les mesures.

Ces travaux ont également permis de mieux comprendre les effets de l'irradiation sur la conductivité thermique, en particulier dans le cas des combustibles MOX FNR irradiés à des taux de combustion élevés (*i.e.* le combustible NESTOR-3). Nous avons constaté que l'utilisation du modèle de conductivité thermique de Lucuta, basé sur les combustibles MOX FNR UO_2 **SIM**ulated **F**els (SIMFuels), produit des divergences importantes par rapport aux données expérimentales sur les combustibles MOX FNR. Nous avons amélioré la physique du modèle Lucuta en introduisant un paramètre intrinsèque à la matrice du combustible irradié : la fraction atomique des produits de fission. Le principal défi de la modélisation était de répondre à la question suivante : pourquoi mesure-t-on une conductivité thermique plus élevée dans la région MFP (irradiée à 13 *at.*%) que dans la région axiale TFC (irradiée à 8 *at.*%). Nous avons donc réussi à montrer que la porosité est un élément clé dans l'explication de ces différences. Ce travail a donc conduit à la proposition d'un stage, dont le but était de réaliser des calculs FFT sur des microstructures, générées par analyse d'images sur les métallographies du combustible NESTOR-3. Cette étude de stage a confirmé la conclusion de notre travail, à savoir que la porosité explique les différences de conductivité thermique entre les deux régions axiales. Une autre perspective de notre travail était d'effectuer des **mesures de conductivité thermique sur les combustibles MOX FNR SIMFuels**, afin de confirmer notre modèle de conductivité

thermique de la matrice du combustible irradié. Ces mesures seront effectuées sur les SIMFuels FNR MOX, fabriqués et caractérisés dans la thèse de Rafael Caprani [38], dans le cadre d'une nouvelle recherche doctorale, qui débutera cette année.

Dans ce travail, nous avons montré que notre modèle peut être mis en œuvre dans le code de performance des combustibles *GERMINAL* du logiciel de simulation *PLEIADES*. La simulation de l'expérience d'irradiation INTA-2 a montré que les prévisions de température, utilisant la conductivité thermique développée dans ce travail, étaient cohérentes avec les mesures du thermocouple.

Annexes

A State of the art on the effect of porosity on thermal conductivity of nuclear oxide fuels

A.1 Empirical correlations

Some authors developed empirical correlations for the variation of thermal conductivity with porosity, using experimental data on fuels with different porosity [58, 59]. Those correlations are temperature-dependent and take the following form: $F_p(T) = 1 - (a - b \times 10^{-3} \cdot (T - 273)) \cdot p$, where p is the fractional porosity ($0 < \mathrm{p} < 1$) and T- the temperature. Brandt and Neuer [59] reported $a = 2.60$ and $b = -0.50$ for UO_2 fuels, whereas Van-Craeynest and Stora [58]: $a = 2.58$ $b = -0.58$ for MOX fuels, valid for $T \in [323 - 1273]$ K.

A.2 Formulations based on series slabs or parallel tubes

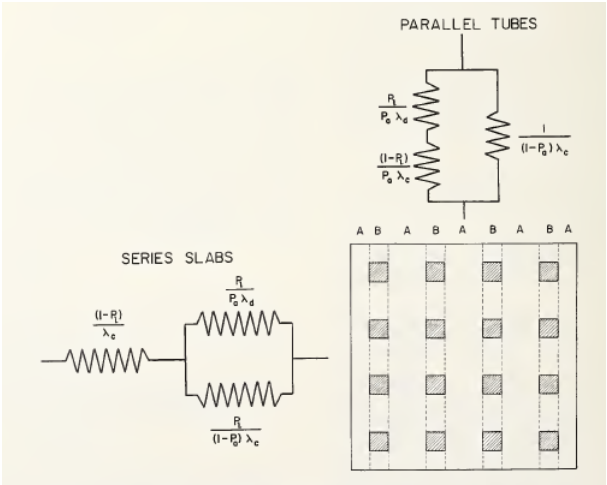

Figure A.1: Illustrative scheme of the series slabs and parallel tubes concepts [63]

Other formulations use the concept of series slabs and parallel tubes (see Figure A.1). In both concepts, the material is composed of two layers: one containing only the matrix, and the other, containing both matrix and a second phase (here pores). The layers are either considered as thin slabs perpendicular to the heat flux (series slabs) or long tubes, parallel to the heat

flux (parallel tubes). Applying the Kirchoff law for both cases, and approximating the pores to phases with zero thermal conductivity, the effective thermal conductivity of the material is expressed as:

$$\frac{\lambda_p}{\lambda_m} = \begin{cases} 1-p, & \text{in the series slabs concept} \\ 1-p+p^{3/2}, & \text{in the parallel tubes concept} \end{cases} \tag{A.1}$$

where λ_p and λ_m are the thermal conductivity of the porous material and the thermal conductivity of the fuel matrix, respectively (*i. e.* at the theoretical density).
Loeb formulation [52] is based on the series slabs concept, but instead of treating pores as phases with zero thermal conductivity, Loeb assesses the pore thermal conductivity and yields the following expression:

$$\frac{\lambda_p}{\lambda_m} = 1 - \alpha \times p \tag{A.2}$$

where α is a factor, which depends on (1) shape, size and orientation of the pores, with respect to the heat flux, (2) temperature and (3) emissivity of the material. In most literature reviews [53–56], α is considered as an empirical factor, due to the difficulty in evaluating (1), (2) and (3).
In addition, those concepts are known to either overestimate (series slabs) or underestimate (parallel tubes) the effective thermal conductivity, due to their idealized way of representing the material's behavior with respect to heat flux [63].

A.3 Maxwell-Eucken's formulation

Maxwell-Eucken [85, 86, 95] proposed a formula for n dispersed phases of volume fractions v_i, in a matrix, where λ_i is the thermal conductivity of the i-th dispersed phase:

$$\frac{\lambda_p}{\lambda_m} = \frac{1 + 2\sum_{i=1}^{n} v_i \frac{1-\frac{\lambda_m}{\lambda_i}}{1+2\frac{\lambda_m}{\lambda_i}}}{1 - \sum_{i=1}^{n} v_i \frac{1-\frac{\lambda_m}{\lambda_i}}{1+2\frac{\lambda_m}{\lambda_i}}} \tag{A.3}$$

The most common form of this equation is:

$$\frac{\lambda_p}{\lambda_m} = \frac{1-p}{1+0.5\cdot p} \tag{A.4}$$

which is based on two essential assumptions: (1) pores are spherical and have zero thermal conductivity, (2) pores are sufficiently isolated to avoid superposition of stray fields, caused by different pores (*i. e.* pores should be isolated). The validity of assumption (2) is therefore limited to small porosity fractions. However, according to Ondraceck and Schulz [54], the amount of porosity is not the only criterion, which has to be met to confirm the validity of assumption (2). Indeed, the distance between the pores should also be taken into account. According to Underwood [240], the mean distance between the pores $\overline{d}$ is directly proportional to the mean pore size $\overline{L}$:

$$\overline{d} = \overline{L} \cdot \frac{1-p}{p} \tag{A.5}$$

where p is the fractional porosity. In other words, for the same porosity fraction, the mean distance between the pores increases with pore size. Assumption (2) is therefore more accurate for large pores than for small pores [54]. Assumption (1) is based on the pore shape and thermal conductivity. To overcome limitations of Equation A.4 due to this assumption, Marino [60] used Fricke's method [67], which replaces the 0.5 in Equation A.4 by a geometrical factor β.

A.4 Fricke's formulation

Fricke also based its formula on a dilute dispersion of pores (*i. e.* assumption (2) in Maxwell-Eucken's formula), but takes into account pores with different size, shape and thermal conductivity. The generic form of this equations is:

$$F_p = \frac{\lambda_p}{\lambda_m} = \frac{1-p}{1+\beta \cdot p} \tag{A.6}$$

where β is a geometrical factor, depending on fractional porosity, pore shape, size and thermal conductivity. For further details on this equation, the reader may refer to Annex B.

A.5 Ondraceck and Schulz's formulation

In a literature review, Ondraceck and Schulz questioned the use of Fricke's formula. The reason for this is that Fricke used Ohm's law, which is an "integrated form of the general field equation, restricted to special presuppositions, not fulfilled in the present work". [54] Ondraceck and Schulz [54–56] proposed another formulation, based on Niesel's equation for two phased materials [66]:

$$\begin{aligned}
1-p &= \left(\frac{\lambda_m}{\lambda}\right)^m \frac{\lambda_{pores}-\lambda}{\lambda_{pores}-\lambda_m}\left(\frac{\lambda+n\lambda_{pores}}{\lambda_m+n\lambda_{pores}}\right)^q; \\
m &= \frac{F(1-2F)}{1-(1-F)\cos^2\alpha-2F\left(1-\cos^2\alpha\right)}; \quad n = \frac{1-(1-F)\cos^2\alpha-2F\left(1-\cos^2\alpha\right)}{2F\left(1-\cos^2\alpha\right)+(1-F)\cos^2\alpha}; \\
q &= \frac{F(1-2F)}{1-(1-F)\cos^2\alpha-2F\left(1-\cos^2\alpha\right)} + \frac{(1-F)2F}{2F\left(1-\cos^2\alpha\right)+(1-F)\cos^2\alpha} - 1.
\end{aligned} \tag{A.7}$$

where λ_{pores} is the thermal conductivity of the pores, α- the angle between the axis of revolution of the pore (ellipsoid) and the heat flux, and F- a shape factor. These parameters are defined as:

1. $F = 1$, $\cos^2\alpha = 0$ for an infinite thin disc
2. $F = 0.33$, $\cos^2\alpha = 0.33$ for a sphere
3. $F = 0.5$, $\cos^2\alpha = 1$ for an infinite thin cylinder

B Fricke's porosity correction

Fricke's method consists of giving the expression for the conductivity of an aggregate containing a dilute dispersion of ellipsoids of conductivity K_1 distributed randomly in a matrix of conduc-

tivity K_2 (see Figure B.2). Now if we consider the second phase to be a pore, we then will use the following notations: λ_1=λ_{pores} and λ_2=λ_m.
Now, with those notations, the Fricke's equation becomes:

$$\lambda_p = \lambda_m + \frac{2P(\lambda_{pores} - \lambda_p)}{3(1-p)} \sum_{i=a,b,c} \frac{1}{2 + abcL_i(\frac{\lambda_{pores}}{\lambda_m} - 1)} \tag{B.1}$$

Where :
$-p$: fractional porosity (0<p<1)
$-\lambda_p$: thermal conductivity of the porous media
$-\lambda_m$: thermal conductivity of the fuel matrix (i. e. at the theoretical density)
$-\lambda_{pores}$: thermal conductivity of the pores
$-a, b, c$: semi-axes of the ellipsoid
$-L_i$ for $i = a, b$ are given by:

$$L_a = \int_0^\infty \frac{1}{(a^2+s)^{3/2}(b^2+s)}\, ds \tag{B.2}$$

$$L_b = \int_0^\infty \frac{1}{(b^2+s)^{2}(a^2+s)^{1/2}}\, ds \tag{B.3}$$

For practical purposes, equation B.1 will be re-written using the following notation $\Lambda = \frac{\lambda_{pores}}{\lambda_m}$
With this notation, equation B.1 becomes :

$$\lambda_p = \lambda_m + \frac{2p(\lambda_{pores} - \lambda_p)}{3(1-p)} \sum_{i=a,b,c} \frac{1}{2 + abcL_i(\Lambda - 1)} \tag{B.4}$$

Now, in our study we only take into account **spherical pores**. Thus in the case where **a=b=c**, the summation term becomes:

$$\sum_{i=a,b,c} \frac{1}{2 + abcL_i(\Lambda - 1)} = \frac{3}{2 + a^3L_a(\Lambda - 1)} \tag{B.5}$$

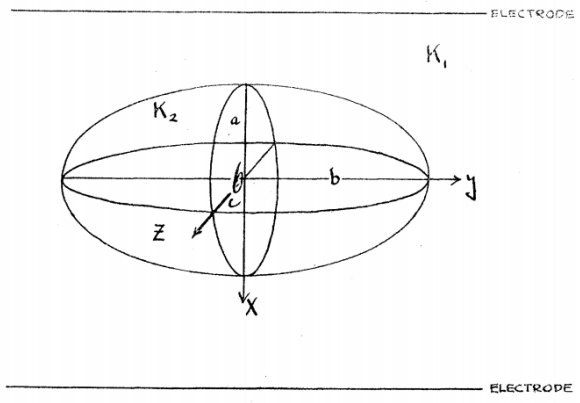

Figure B.2: Ellipse with conductivity K_2 in a solid matrix with conductivity K_1

Where, equation B.2 becomes:

$$L_a = \int_0^\infty \frac{1}{(a^2+s)^{3/2}(b^2+s)}\,ds = \int_0^\infty \frac{1}{(a^2+s)^{5/2}}\,ds = \frac{2}{3a^3} \tag{B.6}$$

By incorporating equation B.6 and B.5 into B.4, Fricke's equation becomes:

$$\lambda_p = \lambda_m + \frac{3p(\lambda_{pores} - \lambda_p)}{(1-p)(2+\Lambda)} \tag{B.7}$$

From this equation, we calculate the ratio $\frac{\lambda_p}{\lambda_m}$:

$$\frac{\lambda_p}{\lambda_m} = \frac{(1-p)(2+\Lambda) + 3p\Lambda}{(1-p)(2+\Lambda) + 3p} \tag{B.8}$$

Now we want to re-write this expression in order to compare it with the expression of Maxwell-Eucken which is of the following form:

$$\frac{\lambda_p}{\lambda_m} = \frac{1-p}{1+\beta p} \tag{B.9}$$

Now we solve the following equation in order to determine the expression for β :

$$\frac{1-p}{1+\beta p} = \frac{(1-p)(2+\Lambda) + 3p\Lambda}{(1-p)(2+\Lambda) + 3p} \tag{B.10}$$

The solution of the equation yields an expression for β as follows:

$$\boxed{\beta = -\frac{p(1-\Lambda) + 4\Lambda - 1}{2p(\Lambda-1) + 2 + \Lambda}} \tag{B.11}$$

Maxwell-Eucken's formula is mostly known under the following form:

$$\frac{\lambda_p}{\lambda_m} = \frac{1-p}{1+0.5p} \tag{B.12}$$

This formulation is valid for spherical pores and the assumption is made, as said in the previous section, that the conductivity of the pores is negligible ($\lambda_{pores} = 0$, *i. e.* $\Lambda = 0$).

Now if we calculate β from expression B.11 for $\lambda_{pores} = 0$, or $\Lambda = 0$ we obtain:

$$\beta(\Lambda = 0) = -\frac{p(1-\Lambda) + 4\Lambda - 1}{2p(\Lambda-1) + 2 + \Lambda} = 0.5 \tag{B.13}$$

The formulation of β for the case where the conductivity of the pores is neglected (*i. e.* $\Lambda = 0$) is thus in agreement with the Maxwell-Eucken's formulation for spherical pores. Now, another correction factor is known in literature as:

$$\frac{\lambda_p}{\lambda_m} = \frac{1-p}{1+2p} \tag{B.14}$$

Thus, in this formulation, the β term is simply replaced by $\beta = 2$. Now, if we try to seek for the physical meaning of this term, we refer ourselves to equation B.11 and thus resolve the

following equation:

$$2 = -\frac{p(1-\Lambda)+4\Lambda-1}{2p(\Lambda-1)+2+\Lambda} \tag{B.15}$$

The resolution of this equation yields a Λ value of :

$$\Lambda = \frac{\lambda_{pores}}{\lambda_m} = \frac{p-1}{p+2} \tag{B.16}$$

However, if we calculate the Λ value obtained by this equation for a porosity of 5 %, we obtain a value of :

$$\Lambda = \frac{0.05-1}{0.05+2} = -0.46341 < 0 \tag{B.17}$$

Physically, this could not be possible because it would mean that $\Lambda = \frac{\lambda_{pores}}{\lambda_m}$ is a negative value, thus assuming that the conductivity of the pores or the conductivity of the solid matrix is negative.

The approximation of $\beta = 2$ cannot, thus, be considered in our study.

C Physical properties, used to calculate the phonon contribution to thermal conductivity

C.1 Sound velocity in the medium

The sound velocity in the medium V_s can be expressed as a function of its longitudinal V_l and transverse V_t components as follows:

$$V_s = \left(3\left(\frac{1}{V_l^3}+\frac{2}{V_t^3}\right)^{-1}\right)^{1/3} \tag{C.1}$$

Where:

V_l : Longitudinal sound velocity in the medium ($\mathrm{m\,s^{-1}}$)
V_t : Transverse sound velocity in the medium ($\mathrm{m\,s^{-1}}$)

The components V_l and V_t have been measured for MOX fuel [126], for plutonium contents ranging from y=0 to y=1, O/M ratios ranging from 1.96 to 2 and densities ranging from 85 to 95 % from the theoretical density (*i. e.* 85 - 95 % dth). The longitudinal and traverse sound velocities can be expressed as a function of the plutonium content y, deviation from stoichiometry x and pores fraction p as follows:

$$V_l = 5358(1-0.7279\cdot x)(1+0.040\cdot y)(1-1.3172\cdot p) \tag{C.2}$$

$$V_t = 2750(1-0.8945\cdot x)(1+0.043\cdot y)(1-0.8945\cdot p) \tag{C.3}$$

Table 4: Ionic radii of the cations, used to calculate the lattice parameter

Ion	r_i ($\times 10^{-9}$ m)
U^4+	0.1001
Pu^4+	0.0960
O^2-	0.1368

C.2 Volumetric thermal expansion coefficient

The volumetric thermal expansion coefficient can be calculated by the following equation:

$$\alpha = 3\left(\frac{LTE}{T - T_0}\right) = 3\left(\frac{\Delta L}{L_0(T - T_0)}\right) \tag{C.4}$$

Where L_0 is the initial length of the sample at $T = T_0$. In the following sections, we will take $T_0 = 300K$. LTE is the linear expansion given by:

$$LTE = \frac{\Delta L}{L_0} = a_0 + a_1 T + a_2 T^2 + a_3 T^3 \tag{C.5}$$

And a_i coefficients are given by [127]:

$$a_i = b_0 + b_1 y + b_2 x + b_3 y^2 + b_4 x^2 + b_5 yx \tag{C.6}$$

Where x is the deviation from stoichiometry and y is the plutonium content. The coefficients b_i are given for every a_i value in Table 3 [127]

	b_0	b_1	b_2	b_3	b_4	b_5
$a_0.10^{-3}$	-2.8809	0.0301	-4.3954	0.0156	-15.1759	2.5642
$a_1.10^{-6}$	9.5024	-0.1864	15.8173	-0.0229	7.6258	-7.5789
$a_2.10^{-10}$	2.0894	2.9483	-19.9227	-1.0355	73.8931	11.6442
$a_3.10^{-13}$	4.4096	-1.4263	23.5638	0.0251	-54.751	-14.418

Table 3: Coefficients for the calculation of the linear expansion

C.3 Lattice parameter

The lattice parameter a_0 at ambient temperature, for MOX fuel has been measured [187] and thus can be expressed by the following equation:

$$a_0 = \frac{4}{\sqrt{3}}\left[\left((1-y)r_{U^{4+}} + y r_{Pu^{4+}}\right)(1 + 0.112x) + r_{O^{2-}}\right] \tag{C.7}$$

Where r_{Pu}^{4+}, r_U^{4+} and r_O^{2-} are the respective ionic radii of the cations [98] , given in Table 4. The temperature dependency of the lattice parameter $a(T)$ can be deduced using thermal expansion (see C.2) as follows:

$$a(T) = a_0 * (1 + LTE) \tag{C.8}$$

where LTE is given by C.5.

C.4 Isothermal bulk modulus

The isothermal Bulk modulus was calculated using:

$$K_T(T) = \Big[(203.66 \cdot (1-y) + 225.63 \cdot y) \cdot (1 - 1.88625x) \\ \cdot (1.02179 - 5.97137 \cdot 10^{-5} \cdot T - 4.30682 \cdot 10^{-8} \cdot T^2)\Big] \cdot 10^9 \tag{C.9}$$

C.5 Heat capacity at constant volume

Heat capacity at constant volume C_v has been deduced from heat capacity at constant pressure C_p, using:

$$C_v = C_p - V_m T \alpha^2 K_T \tag{C.10}$$

where

C_v : heat capacity at constant volume ($\mathrm{J\,mol^{-1}\,K^{-1}}$)
V_m : molar volume $= \frac{a^3 \cdot N_a}{4}$ ($\mathrm{m^3}$) with a, calculated by Equation C.8 and $N_a = 6.02 \cdot 10^{23}$
C_p : heat capacity at constant pressure ($\mathrm{J\,mol^{-1}\,K^{-1}}$), see Equations C.11 - C.14
T : temperature (K)
α : volumetric thermal expansion coefficient ($\mathrm{K^{-1}}$), see Equation C.4
K_T : isothermal bulk modulus (Pa), see Equation C.9

Heat capacity at constant pressure C_p has been calculated for MOX fuel using Kopp law:

$$C_p(\mathrm{U_{1-y}Pu_yO_{2-x}}) = (1-y)C_p(\mathrm{UO_2}) + yC_p(\mathrm{PuO_2}) - \frac{x}{2}C_p(\mathrm{O_2}) \tag{C.11}$$

where $C_p(\mathrm{UO_2})$ and $C_p(\mathrm{PuO_2})$ are given (in $\mathrm{J\,mol^{-1}\,K^{-1}}$) by the most recent models, recommended by *Konings et al.* [239]:

$$C_p(\mathrm{UO_2}) = \Big(247.1735 + 1.5976 \cdot 10^{-1} \cdot T \\ -1.3199 \cdot 10^{-4} \cdot T^2 + 4.3162 \cdot 10^{-8} \cdot T^3 - \tfrac{4.3278 \cdot 10^6}{T^2}\Big) \cdot 0.270 \tag{C.12}$$

$$C_p(\mathrm{PuO_2}) = \Big(127.8532 + 5.5151 \cdot 10^{-1} \cdot T \\ -4.6097 \cdot 10^{-4} \cdot T^2 + 1.3145 \cdot 10^{-7} \cdot T^3 - \tfrac{1.2591 \cdot 10^6}{T^2}\Big) \cdot 0.270 \tag{C.13}$$

and $C_p(\mathrm{O_2})$ (in $\mathrm{J\,mol^{-1}\,K^{-1}}$) from the model, proposed by *Duriez et al.* [4]:

$$C_p(\mathrm{O_2}) = \Big(27.85 + 8.53 \cdot 10^{-3} \cdot T \\ -204.54 \cdot 10^{-8} \cdot T^2 + 19.32 \cdot 10^{-11} \cdot T^3\Big) \cdot 0.270 \tag{C.14}$$

D Scattering cross section

The scattering cross section parameter Γ characterizes the phonon scattering strength of each sub-lattice (*i. e.* the cationic (U, Pu) and the anionic (O) sub-lattices), which for MOX is

written:

$$\Gamma = \frac{1}{3}\left(\frac{\overline{M_{(U,Pu)}}}{\overline{M}}\right)^2 \Gamma_{(U,Pu)} + \frac{2}{3}\left(\frac{\overline{M_O}}{\overline{M}}\right)^2 \Gamma_O \tag{D.1}$$

where $\overline{M_{U,Pu}}$ and $\overline{O}$ are the mean atomic masses of the (U, Pu) and O sub-lattices, expressed as:

$$\overline{M_{U,Pu}} = (1-y)M_U + yM_{Pu} \tag{D.2}$$

$$\overline{M_O} = \frac{2-x}{2}M_O \tag{D.3}$$

$\overline{M}$ is the mean atomic mass of the compound (MOX):

$$\overline{M} = \frac{1}{3}\overline{M_{U,Pu}} + \frac{2}{3}\overline{M_O} \tag{D.4}$$

and $\Gamma_{(U,Pu)}$ and Γ_O are the phonons scattering strength due to disorder in the (U, Pu) and O sub-lattices, expressed as:

$$\Gamma_{(U,Pu)} = \Gamma_U + \Gamma_{Pu} \tag{D.5}$$

$$\Gamma_O = \Gamma_{O_v} \tag{D.6}$$

where Γ_U, Γ_{Pu} and Γ_{O_v} are the contributions from disorder, associated with adding U and Pu into the (U,Pu) sub-lattice and O_v (oxygen vacancies) into the O sub-lattice. Incorporating equations D.2 - D.6 into D.1, we can write:

$$\Gamma = 3\left(\frac{(1-y)M_U + yM_{Pu}}{(1-y)M_U + yM_{Pu} + (2-x)M_O}\right)^2 (\Gamma_{U^{4+}} + \Gamma_{Pu^{4+}} + \Gamma_{Pu^{3+}}) + \frac{3}{2}\left(\frac{(2-x)M_O}{(1-y)M_U + yM_{Pu} + (2-x)M_O}\right)^2 \Gamma_O$$

To calculate $\Gamma_{U^{4+}}, \Gamma_{Pu^{4+}}, \Gamma_{Pu^{3+}}$ and Γ_O, we will use a modified version of Equation 3.7. recalled here:

$$\Gamma_i = f_i\left\{\left(\frac{M_i - \overline{M_{sub}}}{\overline{M_{sub}}}\right)^2 + 2\left[\left(\frac{G_i - \overline{G_{sub}}}{\overline{G_{sub}}}\right) - 6.4\gamma_\infty\left(\frac{r_i^{host} - \overline{r_{sub}}}{\overline{r_{sub}}}\right)\right]^2\right\}$$

where:

- f_i : atomic fraction of the i-th point defect
- M_i : atomic mass of the i-th point defect ($\mathrm{kg\,m^{-1}}$)
- r_i^{host} : atomic radius of the i-th point defect in the host lattice (m)
- G_i : average stiffness constant of the nearest neighbor bonds of defect atoms to the host lattice atoms (Pa)
- $\overline{G_{sub}}$: average stiffness constant of the host sub-lattice (Pa)
- $\overline{M_{sub}}$: mean atomic mass of the host sub-lattice ($\mathrm{kg\,mol^{-1}}$)
- $\overline{r_{sub}}$: mean ionic radii of the host sub-lattice (m)
- γ_∞ : High-temperature limit of the acoustic phonon mode Gruneisen parameter

As the term $\frac{G_i-\overline{G_{sub}}}{\overline{G_{sub}}}$ represents the influence of the force coupling misfit, it can be estimated by comparing the Young modulus of the PuO_2 and UO_2 solid solutions. From Kato's work on the mechanical properties of PuO_2 and UO_2, the Young modulus of both solid solutions do not differ from more than 10 %. As shown by Wan *et al.* [241] in their article on the effect of point defects on the thermal transport properties of $La_xGd_{1-x}Zr_2O_7$, $\frac{G_i-\overline{G_{sub}}}{\overline{G_{sub}}}$ can be neglected. Equation 3.7, thus reduces to:

$$\Gamma_i = f_i \left\{ \left(\frac{M_i - \overline{M_{sub}}}{\overline{M_{sub}}} \right)^2 + 2 \left[6.4\gamma_{\infty,ac} \left(\frac{r_i^{host} - \overline{r_{sub}}}{\overline{r_{sub}}} \right) \right]^2 \right\} \tag{D.7}$$

According to the elastic continuum "sphere in whole" model [242], when an impurity atom is introduced into a host lattice, its ionic radius changes. Eshelby [242] derived a relation between the ionic radius of the impurity atom in its own lattice r_i and that in the host lattice r_i^{host}. The term $\frac{r_i^{host}-\overline{r_{sub}}}{\overline{r_{sub}}}$ can be expressed by the following relation:

$$\frac{r_i^{host} - \overline{r_{sub}}}{\overline{r_{sub}}} = \left(\frac{r_i - \overline{r_{sub}}}{\overline{r_{sub}}} \right) \frac{1+\nu}{3(1-\nu)} \tag{D.8}$$

where ν is the Poisson ratio of the host matrix (*i. e.* of MOX fuel). This relation has been derived, based on the assumption of similar elastic properties between PuO_2 and UO_2 and their solid solutions. [207]. Incorporating Equation D.8 into D.7, we can write:

$$\Gamma_i = f_i \left\{ \left(\frac{M_i - \overline{M_{sub}}}{\overline{M_{sub}}} \right)^2 + \epsilon \left(\frac{r_i - \overline{r_{sub}}}{\overline{r_{sub}}} \right)^2 \right\} \tag{D.9}$$

where ε is given by:

$$\varepsilon = \frac{2}{9} \left(6.4 \times \gamma_\infty \left(\frac{1+\nu}{1-\nu} \right) \right)^2 \tag{D.10}$$

where ν can be expressed by the longitudinal V_l (see equation C.2 in Annex C.1) and transverse V_t (see equation C.3 in Annex C.1) components of the sound velocity V_s:

$$\nu = \frac{V_l^2 - 2V_t^2}{2V_l^2 - V_t^2} \tag{D.11}$$

$\Gamma_{U^{4+}}, \Gamma_{Pu^{4+}}, \Gamma_{Pu^{3+}}$ and Γ_O can thus be computed using the modified Equation D.9.

E Electrical conductivity model for binary systems

Heikes and Ure's electrical conductivity model is based on two equations [153]:

1. **Nernst-Einstein equation for ionic diffusion : electrical conductivity σ^{el} is a function of the charge carriers mobility μ**

$$\sigma^{el} = en\mu \tag{E.1}$$

where:

μ : mobility of the charge carrier ($m^2\,V^{-1}\,s^{-1}$)
e : elementary charge (C)
n : number density of charge carriers (m^{-3})

The polaron's mobility is expressed as that of ionic species (*i. e.* involving a diffusion coefficient D):

$$\mu = \frac{e}{kT} * D \tag{E.2}$$

where k is the Boltzmann constant ($J\,K^{-1}$) and D- the diffusion coefficient ($m^2\,s^{-1}$).

2. **Random walk model : the diffusion coefficient D is a function of the effective polaron hopping frequency ξ_{eff}**:

$$D = g a_p^2 \xi_{eff} \tag{E.3}$$

where:

g : geometric factor containing the number of possible jumps (*i. e.* the number of nearest neighbors in fluorite systems $Z = 12$) normalized by the 6 main directions (3D solid). This geometrical factor is thus equal to $\frac{Z}{6}$.
a_p : distance of the polaron jump. For small polaron hopping : $a_p = \frac{a}{\sqrt{2}}$ (m) where a is the lattice parameter
ξ_{eff} : Effective hopping frequency (s^{-1})

The effective hopping frequency ξ_{eff} have two different expressions, depending on the polaron migration regime (adiabatic or non-adiabatic).

Effective hopping frequency ξ_{eff}
The effective hopping frequency ξ_{eff} is expressed as a function of the elementary hopping frequency ξ_0 as follows [153]:

$$\xi_{eff} = \xi_0(1 - c) \tag{E.4}$$

where (1-c) is the fraction of available sites for hopping (*i. e.* the atomic sites which do not contain a charge carrier). The elementary hopping frequency is characterized by three parameters: optic phonon frequency $v_{0,opt}$, migration energy E_m and overlap integral J_{ov}. The former represents the coincidence configurations' timescale, while the migration energy - the energy, needed to overcome the potential wall. The overlap integral J_{ov} is proportional to the conduction bandwidth ΔW. The electrons' kinetic energy increases with ΔW. Based on the overlap integral J_{ov}, one could thus define an electron transfer time t_{el}, which is inversely proportional to J_{ov} (*i. e.* $t_{el} \propto \frac{\hbar}{J_{ov}}$ where $\hbar$ is the reduced Planck constant). One can also define a timescale related to the coincidence configurations t_{CC}. The latter is inversely proportional to the optic phonons mean frequency $t_{CC} \propto v_{0,opt}^{-1}$. Two possible phenomena can occur based on the values of t_{el} and t_{CC}:

1. Electrons transfer **faster** than coincidence configurations : $\boldsymbol{t_{el} \ll t_{CC}}$
2. Electrons transfer **slower** than coincidence configurations: $\boldsymbol{t_{el} \gg t_{CC}}$

The first case characterizes the "adiabatic" migration. In this case, the elementary hopping frequency of the polaron ξ_0 is an Arrhenius function of the migration energy E_m and the optic phonon frequency $v_{0,opt}$:

$$\xi_{0,ad} = v_{0,opt} e^{-\frac{E_m}{kT}} \tag{E.5}$$

The second case characterizes the "non-adiabatic' migration. The hopping probability in this case is written as:

$$\xi_{0,nad} = \frac{J_{ov}^2}{2\hbar}\sqrt{\frac{\pi}{E_m kT}} e^{-\frac{E_m}{kT}} \tag{E.6}$$

Firsov and Lang [155] derived an adiabacity criterion η_{ad}:

$$\eta_{ad} = \frac{J_{ov}^2}{h v_{0,opt}\sqrt{E_m kT}} \tag{E.7}$$

$\eta_{ad} \ll 1$ for non-adiabatic hopping and $\eta_{ad} \gg 1$ for adiabatic hopping.
By incorporating equations E.5 and E.6 for adiabatic and non-adiabatic hopping respectively, into equation E.4, the effective hopping frequency of the polarons is thus given in both the adiabatic and the non-adiabatic hopping regimes:

$$\xi_{eff,ad} = (1-c)\xi_{0,ad} = (1-c) v_{0,opt} e^{-\frac{E_m}{kT}} \tag{E.8}$$

$$\xi_{eff,nad} = (1-c)\xi_{0,nad} = (1-c)\frac{J_{ov}^2}{2\hbar}\sqrt{\frac{\pi}{E_m kT}} e^{-\frac{E_m}{kT}} \tag{E.9}$$

In summary, the effective hopping frequency thus represents the polaron hopping probability, driven by four events:

1. Vibration of surrounding atoms, leading to **coincidence configurations**, driven by the optic phonon mean frequency $\boldsymbol{v_{0,opt}}$
2. Overcoming the **migration barrier**, driven by the migration energy $\boldsymbol{E_m}$
3. Controlling the **electron transfer time**, driven by the overlap integral $\boldsymbol{J_{ov}}$
4. Having enough **available sites** for the charged carrier to hop, driven by $\boldsymbol{1-c}$

Final expression for the electrical conductivity of binary systems

Using equations E.2 for μ, E.3 for D, E.4 for ξ_{eff}, E.5 for $\xi_{0,ad}$, and E.6 for $\xi_{0,nad}$, and knowing that $a_p = \frac{a}{\sqrt{2}}$ and $g = 2$, one obtains the following equations:

$$\mu_{ad} = \frac{e a^2 (1-c) v_{0,opt}}{kT} e^{-\frac{E_m}{kT}} \tag{E.10}$$

$$\mu_{nad} = \frac{e a^2 (1-c) J_{ov}^2}{2\hbar (kT)^{3/2}} e^{-\frac{E_m}{kT}} \tag{E.11}$$

Using equation E.1 to relate mobility and conductivity, and knowing that the number density of electrons n can be expressed as the total number density of cations N by $n = Nc = \frac{4c}{a^3}$, with

c being fraction of charge carriers, the final expression for the electrical conductivity in both regimes becomes:

$$\sigma_{ad}^{el} = \frac{4e^2c(1-c)v_{0,opt}}{akT}e^{-\frac{E_m}{kT}} \tag{E.12}$$

$$\sigma_{nad}^{el} = \frac{2e^2c(1-c)J_{ov}^2}{a\hbar(kT)^{3/2}}e^{-\frac{E_m}{kT}} \tag{E.13}$$

F Electronic states of the Pu and U atoms in MOX fuel

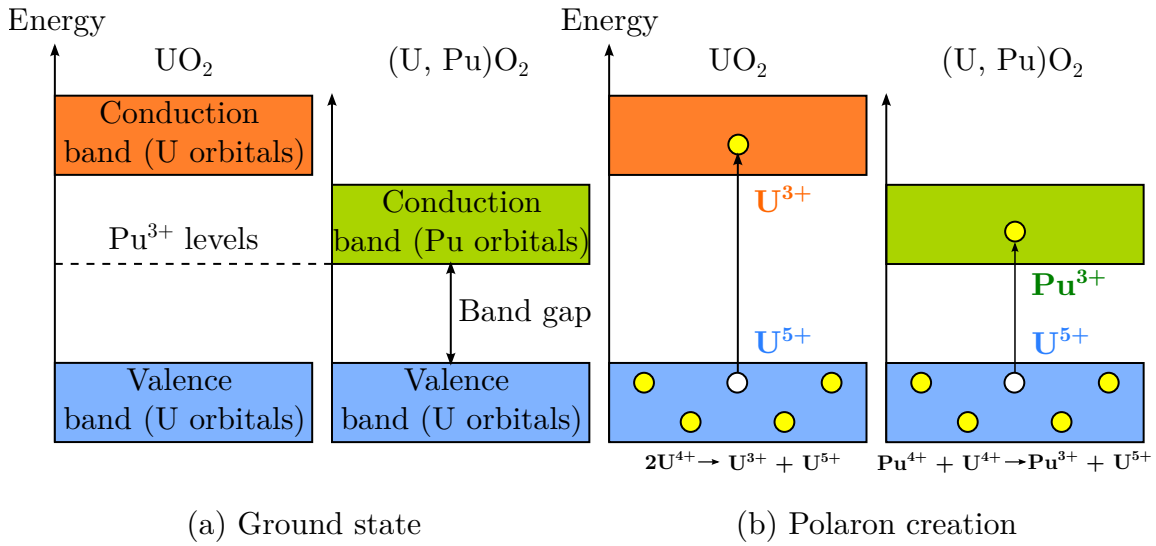

(a) Ground state (b) Polaron creation

Figure F.3: Illustrative scheme of (a): the electronic structure of UO_2 and $U_{1-y}Pu_yO_{2-x}$ at ground state and (b): the polaron creation process with the associated disproportionation reactions.

Figure F.3 shows the band structure of both UO_2 and $U_{1-y}Pu_yO_{2-x}$ systems. At their ground state, the uranium and plutonium atoms in stoichiometric MOX fuel are present under the valence state of 4+. The band-gap of UO_2 was measured experimentally and calculated by DFT+U and is in the range [2 - 2.5] eV [6, 147, 150, 152, 215–217, 243]. In $U_{1-y}Pu_yO_{2-x}$, the presence of Pu^{3+} energy levels, reduces the band-gap, as opposed to UO_2 [143]. Indeed, the fourth ionization potential of Pu is 1.8 eV higher than that of U^{4+} [143]. For this reason, in MOX fuel Pu^{4+} cations will trap electrons from the valence band (i. e. U^{4+}), thus forming Pu^{3+}. The following disproportionation reaction thus takes place (see Figure F.3 b):

$$Pu^{4+} + U^{4+} \rightarrow Pu^{3+} + U^{5+} \tag{F.1}$$

Catlow reported a value of 1.5 eV for the band-gap in MOX [143]. The Pu^{3+} levels have a lower energy than U^{5+}, and thus are more easily accessible. However, if enough thermal energy is supplied to the system, some U^{4+} valence electrons can occupy the U^{5+} levels rather than the Pu^{3+} ones. This leads to the same cation disproportionation reaction as in UO_2 system:

$$2U^{4+} \rightarrow U^{5+} + U^{3+}$$

The so-created U^{3+} ions will be completely consumed by the Pu^{4+}, leading to the following reaction [143]:

$$Pu^{4+} + U^{3+} \rightarrow Pu^{3+} + U^{4+} \tag{F.2}$$

Finally the oxidation states of the cations in $U_{1-y}Pu_yO_{2-x}$ fuel are: Pu^{3+} and Pu^{4+} for Pu, and U^{5+} and U^{4+} for U. From the above-mentioned reactions, the electrons in $U_{1-y}Pu_yO_{2-x}$ are associated with plutonium atoms (*i. e.* the Pu^{3+} polarons), whereas the holes with uranium atoms (*i. e.* the U^{5+} polarons). The MOX cationic sub-lattice can thus described by the following structural unit:

$$\underbrace{\left\{(Pu^{4+})_{c_{Pu^{4+}}}, (Pu^{3+})_{c_{Pu^{3+}}}\right\}}_{c_{Pu}=y}\underbrace{\left\{(U^{4+})_{c_{U^{4+}}}, (Pu^{3+})_{c_{Pu^{3+}}}\right\}}_{c_U=1-y} \tag{F.3}$$

where c_i with $i = Pu^{3+}, Pu^{4+}, U^{5+}, U^{4+}$ are the fractional occupancy of the cations.

G Electrical conductivity expression for a regular solid solution

We recall that in the case of an ideal solid solution, electrical conductivity is expressed as:

$$\sigma^{el} = \sigma^{el}_{Pu-Pu} + \sigma^{el}_{U-U} = \frac{4e^2 v_{0,opt}}{akT}\left(c_{Pu^{3+}}c_{Pu^{4+}}e^{-\frac{E_m(Pu-Pu)}{kT}} + c_{U^{5+}}c_{U^{4+}}e^{-\frac{E_m(U-U)}{kT}}\right) \tag{G.1}$$

From now on, for more clarity in notations, $E_m(Pu-Pu)$ and $E_m(U-U)$ will be written as $E_m(Pu)$ and $E_m(U)$.

Equation G.1 involves the fractional occupancy products $c_{Pu^{3+}}c_{Pu^{4+}}$ and $c_{U^{5+}}c_{U^{4+}}$. Those terms characterize the probabilities of Pu^{4+} and U^{4+} being the first neighbors to Pu^{3+} and U^{5+} respectively. Those probabilities come from the polaron hopping frequency expression, recalled here (see Annex E):

$$\xi_{eff} = (1-c)v_{0,opt}e^{\frac{E_m}{kT}}$$

This equation only stands for an ideal solid solution. We can rewrite this equation in a more general form as:

$$\xi^{id}_{eff} = P^{id}v_{0,opt}e^{\frac{E_m}{kT}} \tag{G.2}$$

where the *id* superscript stands for "ideal solution".

Indeed, the probability of an atom B being first neighbor to A, in an ideal solid solution, denoted P^{id}_B is simply equal to its fractional occupancy: $P^{id}_B = c_B$.

In a regular solid solution (*i. e.* a real solid solution), this probability, P^{reg}_B differs from P^{id}_B by a factor of $1-\alpha_{AB}$:

$$P^{reg}_B = (1-\alpha_{AB})P^{id}_B \tag{G.3}$$

The factor α_{AB} is called the short-range order parameter, measuring how far the solution deviates from the ideal solid solution.

We thus can define the effective frequency of a polaron of type B, hopping to an atom of type

A in a regular solid solution:

$$\xi_{eff,B}^{reg} = P_B^{reg} v_{0,opt} e^{\frac{E_m}{kT}}$$

Using Equation G.3, and knowing that $P_B^{id} = c_B$ we write:

$$\xi_{eff,B}^{reg} = P_B^{id}(1-\alpha_{AB}) v_{0,opt} e^{\frac{E_m}{kT}} = c_B(1-\alpha_{AB}) v_{0,opt} e^{\frac{E_m}{kT}} \tag{G.4}$$

Since, in this work, we omitted the existence of mixed-element U-Pu and Pu-U hopping, we need to define α_{AA} and α_{BB} order parameters. The effective like-element hopping frequency of the Pu^{3+} polaron in a regular solid solution can thus be written as:

$$\xi_{eff,B}^{reg} = c_{Pu^{3+}}(1-\alpha_{Pu,Pu}) v_{0,opt} e^{\frac{E_{m(Pu)}}{kT}}$$

The same analogy is done for the U^{5+} polaron. The electrical conductivity due to Pu^{3+} like-element hopping in a regular solid solution differs by that in ideal solid solution by $(1-\alpha_{Pu,Pu})$:

$$\sigma_{Pu}^{el,reg} = (1-\alpha_{Pu,Pu})\sigma_{Pu}^{el,id}$$

The total electrical conductivity in a regular solid solution is thus:

$$\sigma^{el,reg} = \sigma_U^{el,reg} + \sigma_{Pu}^{el,reg} = (1-\alpha_{Pu,Pu})\sigma_{Pu}^{el,id} + (1-\alpha_{U,U})\sigma_U^{el,id} \tag{G.5}$$

The "*id*" superscript has been added to distinguish the ideal from the regular solid solution. It will be omitted from now on, to stay consistent with the previous notations σ_{Pu}^{el} (see Equation 3.44) and σ_U^{el} (see Equation 3.45), in which the "ideal" solid solution was implicit. In the next section, the deviation from an ideal solid solution in MOX will be estimated by calculating the $\alpha_{U,Pu}$ parameter. The latter can be used to deduce also $\alpha_{U,U}$ and $\alpha_{Pu,Pu}$.

H Experimental techniques used to measure thermal conductivity of nuclear fuels

In this section, the most widely used experimental techniques to measure thermal conductivity of nuclear fuels will be introduced. The main goal of this section is to quantify the systematic uncertainties, associated with each experimental technique.
Thermal conductivity can be measured both by steady-state and transient techniques (see Table 5). It is beyond the scope of this work to focus on each of them. The focus is on those, used to measure the thermal conductivity of nuclear fuels: the radial heat flow method [244], the Angstrom method [245, 246], the Cowan method [247], the LAF method [248] and the CLASH method [249].

H.1 Direct methods

The direct measurement methods, consist in directly measuring the observable (i. e. the thermal conductivity in this case). The mostly used direct method to measure thermal conductivity of MOX fuels is a steady-state method: the radial heat flow technique.

Steady-state	Absolute technique Comparative technique Radial heat flow method Parallel conductance method Angstrom method Cowan method
Transient (frequency-domain)	Pulsed power technique
Transient (time-domain)	Hot-wire method LAser Flash (LAF) method Continuous-wave LAser Surface Heating (CLASH) method Transient plane source (TPS) method

Table 5: Experimental techniques, used to measure thermal conductivity of solids [246]

H.1.1 Radial heat flow technique

While other steady state techniques use a longitudinal arrangement of samples, the radial heat flow technique is based on cylindrical samples (see Figure H.4) [244]. The interest in this geometry is to prevent radiation heat losses at high temperatures, which can cause uncertainties in the determination of the heat flow through the sample.

Measurement principle

The measurement principle consists in heating a cylindrical sample of height H in its center to generate a radial heat flow Q. Once a steady-state radial temperature gradient is established, two thermocouples, placed at two radial positions r_1 and r_2, measure T_1 and T_2. Using Fourier's law for conduction in a cylinder, the thermal conductivity is calculated:

$$\lambda = \frac{Q \ln(r_2/r_1)}{2\pi H(T_2 - T_1)} \tag{H.1}$$

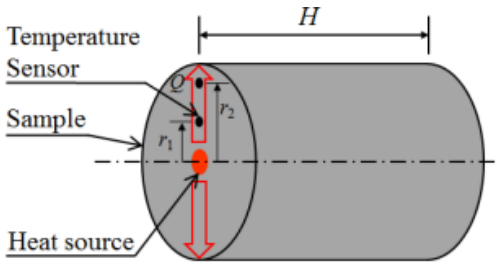

Figure H.4: Radial heat flow technique method [244]

Measurement uncertainties

Considering Eq. H.1, the relative uncertainty in λ has been estimated in [202].

H.2 Indirect methods

The indirect methods consist in measuring thermal diffusivity d, heat capacity C_p and density ρ (i. e. other properties), yielding an indirect measure of the thermal conductivity by the relation $\lambda = \rho C_p d$. Some measurement techniques (the LAF and CLASH for example) allow a simultaneous measure of both heat capacity and thermal diffusivity. However, the uncertainties in the heat capacity, determined by those techniques, can be quite important. This will be covered in more details in Section H.2.3, when introducing the LAF method. The heat capacity is, most of the time, determined by calorimetry, as it provides a more accurate measure. Heat capacity and thermal diffusivity aren't systematically measured together. As it will be seen in Section 4.1, there are much more measurements of thermal diffusivity than of heat capacity. For this reason, authors generally measure thermal diffusivity and to determine the thermal conductivity, they use empirical models for heat capacity, based on the available data.

H.2.1 Angstrom method

Measurement principle

The measurement consists in applying a sinusoidal heat wave on one of the extremities of the sample (point S in Figure H.5). Two thermocouples, separated by L are placed at distances X_1 and X_2 from the heating source. The phase delay dt between the temperature waves, at X_1 and X_2, as well as the amplitudes A_1, A_2 of temperature waves are measured. Knowing the period t of the temperature wave, the thermal diffusivity d is thus calculated [246]:

$$d = \frac{\pi L^2}{t \cdot dt \cdot \ln\left(\frac{A_1}{A_2}\right)} \tag{H.2}$$

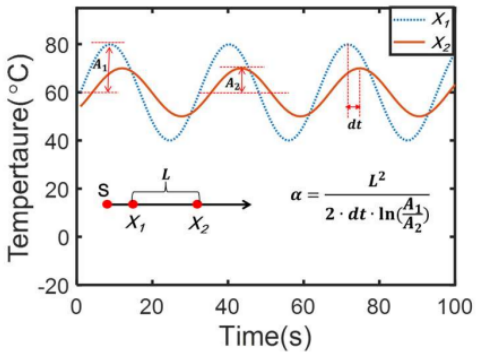

Figure H.5: Scheme of the Angstrom method [246]

Measurement uncertainties

From Eq. H.2, we can write:

$$\frac{\Delta d}{d} = 2\frac{\Delta L}{L} + \frac{\Delta t}{t} + \frac{\Delta dt}{dt} + \left(\frac{\Delta A_1}{A_1} + \frac{\Delta A_2}{A_2}\right) \ln\left(\frac{A_1}{A_2}\right) \tag{H.3}$$

The relative uncertainties, related to the wave period t, the phase delay dt, the sample length L and the amplitudes A_1, and A_2 have been estimated in : $\frac{\Delta t}{t} = 0.60\%$, $\frac{\Delta dt}{dt} = 3.0\%$, $\frac{\Delta L}{L} = 2.50\%$, $\frac{\Delta A_1}{A_1} = 0.15\%$,$\frac{\Delta A_2}{A_2} = 0.62\%$. Knowing $A_1 = 16.6$ cm and $A_2 = 4$ cm (values from thermal diffusivity measurements in [ref Otter, SEAMA 145]), the relative uncertainty on the thermal diffusivity with the Angstrom method is thus:

$$\boxed{\frac{\Delta d}{d} \approx 9\%}$$

H.2.2 Cowan method

Measurement principle

In this method, the sample is bombarded on one face by a beam of electrons [247] (see Figure H.6). The sample is heated in a manner to produce a sinusoidal thermal wave on the front face of the sample. Similarly to the Angstrom method, the phase delay dt of the heat wave between the front and the rear face of the sample is measured by a phasemeter and the thermal diffusivity is deduced [247]:

$$d = \frac{\pi f L^2}{dt^2} \tag{H.4}$$

where f is the wave frequency and L the sample length.

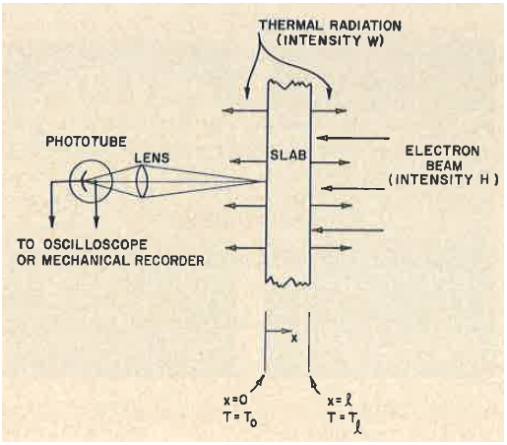

Figure H.6: Scheme of the Cowan method [247]

Measurement uncertainties

From Eq. H.4, we can write:

$$\frac{\Delta d}{d} = 2\frac{\Delta L}{L} + \frac{\Delta f}{f} + 2\frac{\Delta dt}{dt} \tag{H.5}$$

The relative uncertainties, related to the sample length, the wave frequency and the phase delay have been estimated as $\frac{\Delta L}{L} = 0.38\%$, $\frac{\Delta f}{f} = 1.66\%$ and $\frac{\Delta dt}{dt} = 0.94\%$ [private com.]. The relative

uncertainty on the thermal diffusivity with the Cowan method is thus:

$$\boxed{\frac{\Delta d}{d} \approx 3\%}$$

H.2.3 Laser Flash (LAF) method

The LAF method is the most widely used method for measuring thermal properties [248]. In 1998, Sheindlin [248] published an article with some advances in the use of the LAF technique and especially for the specific case of actinide fuels. As it will be seen in Section 4.1, 94 % of the available experimental data on thermal conductivity of MOX fuels has been realized by the LAF experimental technique. The latter is used to measure thermal properties on both fresh and irradiated fuel samples.

Measurement principle

The measurement principle of the LAF method consists in sending a short laser pulse (a few ms) on one side of the sample. The pulse induces a thermal wave through the material. An infra-red detector detects the evolution of the temperature with time, on the opposite side of the sample. Thermograms (i. e. $T = f(t)$ curves) are obtained and are interpreted to deduce thermal diffusivity (see Figure H.7). The interpretation of the thermograms and thus the deduction of thermal diffusivity depend on the particular resolution of the heat transfer equation. Depending especially on the boundary conditions (conduction and radiation heat losses), numerous resolutions of the heat transfer equation have led to different equations for the thermal diffusivity: Parker [250], Clark and Taylor [251], Cowan [247], Cape and Lehman [252], Degiovanni [253]. The differences in those equations are mostly due to different theoretical treatments of radiation heat losses. The most widely used equation for thermal diffusivity is that of Parker, as it the fastest way to calculate thermal diffusivity [250]:

$$d = 0.1388 \cdot \frac{L^2}{t_{1/2}} \tag{H.6}$$

where L is the sample thickness and $t_{1/2}$ the time, at which half of the temperature rise was reached. This equation, however, considers adiabatic boundary conditions, which are complicated to achieve in experimental conditions. More sophisticated theoretical models are used nowadays [248], based on more physical boundary conditions. Those models allow a simultaneous measure of heat capacity C_p and thermal diffusivity d to deduce thermal conductivity λ:

$$d = \bar{d} L_0^2 \vartheta(T)^2 \tag{H.7}$$

$$C_p = \frac{\bar{Q}\varepsilon}{T_0 \rho_0 L_0} \vartheta(T)^2 \tag{H.8}$$

$$\lambda = \frac{\bar{d} L_0 \bar{Q} \varepsilon \vartheta(T)}{T_0} \tag{H.9}$$

where $\overline{d}$ (in s^{-1}) and T_0 are two, out of 5 parameters, of the equation $T = f(t)$, used to fit the thermograms, L_0 (in m) and ρ_0 the sample width and density at ambient temperature, ε the emissivity, $\vartheta(T) = 1 + \alpha(T)$, with α the thermal expansion (in K^{-1}) and $\bar{Q}$ the energy delivered by the laser.

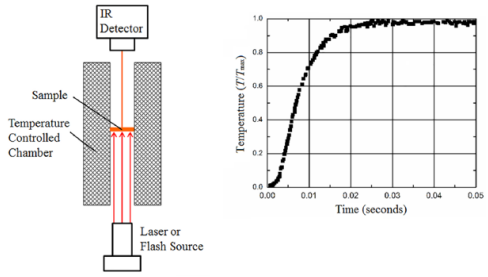

Figure H.7: Scheme of the LAF method [244]

An extension to the classical laser flash method: CLASH (Continuous-wave LAser Surface Heating)

The classical laser flash method uses a furnace to heat the sample to the desired measurement temperature. The maximum temperature, that can be reached with this method is generally limited by the furnace. At JRC-Karlsruhe, the measurements with the classical LAF method do not exceed 1650 K.

In 1999, a new configuration of the laser flash method was proposed by Musella [249], called the CLASH method (Continuous-wave LAser Surface Heating). In this technique, the heating source is the laser itself. The latter is used for both heating the sample to the desired measurement temperature and producing a pulse on one side of the sample (see Figure H.8). This technique allows thermal property measurements up to the melting temperature. Irradiated fuel samples, however, cannot be measured, due to the irregular form of the irradiated samples, which can be difficult to hold. Another obstacle to use the CLASH method for thermal property measurements on irradiated samples is the temperature range. No measurements below 1600 K can be obtained by the CLASH method, due to the sensibility of the pyrometers. At high temperatures however (*i. e.* above 1600 K), irradiated fuel samples go through important microstructure changes, mainly cracks, and thus cannot be measured.

Another advantage of the CLASH method, compared to the classical LAF one, apart from the ability to realize measurements at high temperatures (> 1600 K) is the rapidity in achieving the desired measurement temperature. The latter could take several minutes (sometimes 1 hour) to be achieved with the classical LAF method, as the heating is done in a furnace, compared to several seconds with the CLASH technique.

The main disadvantage of the CLASH method are the less temperature stability and the higher noise level on the thermograms. The temperature signals' quality can be improved by increasing the laser pulses' power, but this can damage the fuel samples.

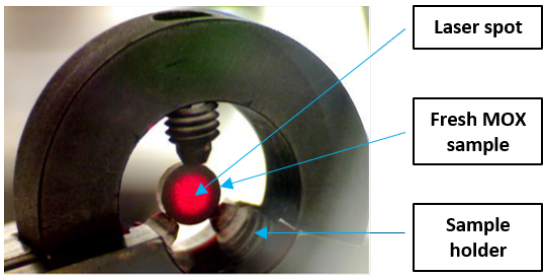

Figure H.8: Fresh MOX fuel sample in the CLASH apparatus at JRC-Karlsruhe. [254]

Measurement uncertainties

In this section, we discuss the systematic uncertainties, related to the simultaneous measure of heat capacity and thermal diffusivity, to deduce thermal conductivity, by use of equations H.7, H.8 and H.9:

$$\frac{\Delta d}{d} = \sqrt{\sigma_{\bar{d}}^2 + 4\left(\frac{\Delta L}{L}\right)^2 + 4\left(\frac{\Delta \vartheta}{\vartheta}\right)^2} \tag{H.10}$$

$$\frac{\Delta C_p}{C_p} = \sqrt{\left(\frac{\Delta \bar{Q}}{\bar{Q}}\right)^2 + \left(\frac{\Delta \varepsilon}{\varepsilon}\right)^2 + \sigma_{T_0}^2 + \left(\frac{\Delta \rho}{\rho}\right)^2 + \left(\frac{\Delta L}{L}\right)^2 + 4\left(\frac{\Delta \vartheta}{\vartheta}\right)^2} \tag{H.11}$$

$$\frac{\Delta \lambda}{\lambda} = \sqrt{\sigma_{\bar{d}}^2 + \sigma_{T_0}^2 + \left(\frac{\Delta L}{L}\right)^2 + \left(\frac{\Delta \bar{Q}}{\bar{Q}}\right)^2 + \left(\frac{\Delta \varepsilon}{\varepsilon}\right)^2 + \left(\frac{\Delta \vartheta}{\vartheta}\right)^2} \tag{H.12}$$

The uncertainties, related to the fitted parameters $\bar{d}$ and T_0 : $\sigma_{\bar{d}}$ and σ_{T_0} depend on the quality of the fit. The later depends on the specific LAF apparatus. For example, at the JRC-Karlsruhe, the standard deviation of the fitted parameters is close to 1% on fresh fuel samples. However, for irradiated fuel samples, this deviation can go up to 5%. One possible explanation for this higher standard deviation could be the capacity of the theoretical model to fit the thermograms. Indeed, the model is based on a resolution of the heat equation for a perfect cylindrical geometry. This geometry hypothesis stands for fresh fuel samples. However, irradiated fuel samples with perfect cylindrical form are complicated to obtain. Figure H.9 shows an irradiated sample fragment (Myosotis fuel) in the LAF apparatus at JRC-Karlsruhe. As observed on the figure, the sample's geometry strongly deviates from that of a cylinder. As for the uncertainties, related to the other parameters, typical values for those uncertainties have been given in [249]: $\frac{\delta L}{L} = 1\%$, $\frac{\delta \vartheta}{\vartheta} = 1\%$, $\frac{\delta \rho}{\rho} = 1\%$, $\frac{\delta \varepsilon}{\varepsilon} = 5\%$, $\frac{\delta \bar{Q}}{\bar{Q}} = 3\%$. The uncertainty on the emissivity was calculated, based on emissivity measurements on UO_2 samples in [184].

If one considers 1% of standard deviation on the fitted $\bar{d}$ and T_0 parameters for fresh fuel samples and 5% on irradiated fuel samples, the total uncertainties, calculated from Eqs. H.10-H.12 are: $\frac{\Delta d}{d} = 3\%$, $\frac{\Delta C_p}{C_p} = 6.4\%$, $\frac{\Delta \lambda}{\lambda} = 6.2\%$ for fresh samples and $\frac{\Delta d}{d} = 5.7\%$, $\frac{\Delta C_p}{C_p} = 8.1\%$, $\frac{\Delta \lambda}{\lambda} = 9.3\%$ for irradiated samples.

As it can be deduced from those values, the uncertainty on heat capacity is higher than on diffusivity. This is due to high uncertainties on $\bar{Q}$ and ε (3% and 5% respectively). This uncertainty analysis, however, takes only into account systematic errors and does not cover uncertainties, related to chemical composition and microstructure changes during thermal measurements at high temperatures (*i. e.* sample reduction, vaporization, micro-cracks).

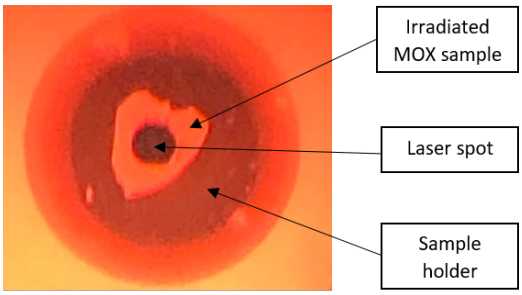

Figure H.9: Irradiated sample fragment (Myosotis fuel) in the LAF apparatus at JRC-Karlsruhe

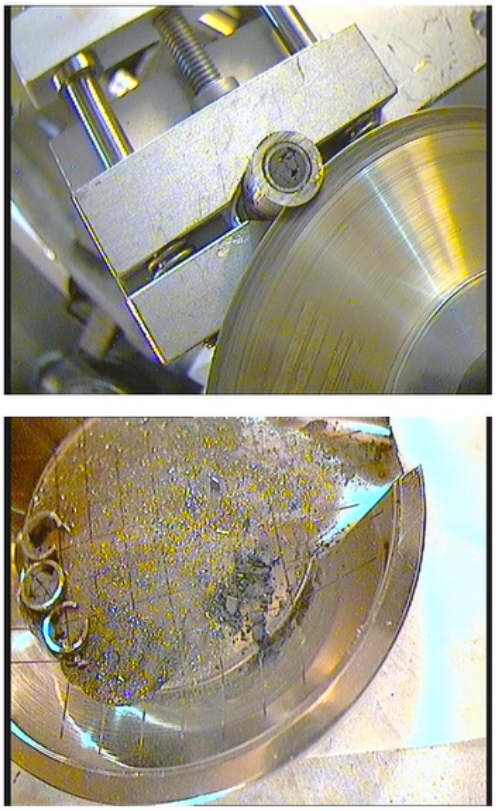

Figure H.10: Cutting of irradiated MOX fuel sample (Pavix) at JRC-Karlsruhe

I Thermal conductivity experimental data

O/M = 2-x (-)	Pu (y)	Author	Porosity (-)	Number of points	T_{min} (K)	T_{max} (K)
1.9	0.2	ANL [196]	0.05	7	800	3000
		Weilbacher [6]	0.05	12	773	2973
1.902	0.2	Van-Craeynest and Weilbacher [106]	0.05	9	323.2	988.2
1.903	0.2	Van-Craeynest and Weilbacher [106]	0.05	10	323.2	1049
	0.3	Morimoto [204]	0.069	10	884.459	1764.527
1.913	0.2952	Morimoto [192]	0.072	4	1024.7	2129
1.915	0.2	Van-Craeynest and Weilbacher [106]	0.05	8	331.2	913.2
1.919	0.3	Morimoto [204]	0.066	10	874.324	1766.216
1.92	0.2	Van-Craeynest and Weilbacher [106]	0.05	6	330.2	903.2
1.923	0.2952	Morimoto [192]	0.066	6	1246.097	2194.796
1.924	0.2	Van-Craeynest and Weilbacher [106]	0.05	8	330.2	998.2
1.933	0.25	Gibby [122]	0.044	22	457.2	1423
1.935	0.2952	Morimoto [192]	0.07	7	1098	2248
1.936	0.244	Elbel and Schmidt [197]	0.054	22	1048	1686
1.94	0.2	Evans [198]	0.083	6	1183	1681
		Elbel and Schmidt [202]	0.09	40	1163	1621
	0.275	Ottaviani [private com.]	0.027	39	731	1338
	0.3	Yamaguchi [205]	0.05	9	1073.2	2673.2
1.944	0.3	Morimoto [204]	0.058	10	874.324	1766.216
1.945	0.2	Van-Craeynest and Weilbacher [106]	0.05	6	1373	1873
	0.2952	Morimoto [192]	0.069	7	1100.7	2249
1.948	0.15	Duriez [4]	0.044	71	720.15	2238.15
	0.2	Van-Craeynest and Weilbacher [106]	0.05	3	333.2	971.2
1.95	0.2	ANL [196]	0.05	7	800	3000
		Evans [198]	0.083	6	1141	1621
		Elbel and Schmidt [202]	0.09	117	1099	2472
		Weilbacher [6]	0.05	12	773	2973
1.952	0.2	Van-Craeynest and Weilbacher [106]	0.05	6	358.2	947.2
1.953	0.252	Elbel and Schmidt [197]	0.044	22	1055	1682
1.954	0.225	Elbel and Schmidt [197]	0.048	23	1053	1670
1.955	0.25	Gibby [122]	0.044	22	429	1473
1.958	0.2	Van-Craeynest and Weilbacher [6]	0.05	7	1273	1873
	0.209	Elbel and Schmidt [197]	0.046	19	1072	1692
1.96	0.1752	Ottaviani [private com.]	0.032	100	729	1923
	0.2	Elbel and Schmidt [202]	0.16	80	1076	2515
		Van-Craeynest and Weilbacher [106]	0.05	6	368.2	1065
		Weilbacher [6]	0.05	12	773	2973
	0.3	Yamaguchi [205]	0.05	9	1073.2	2673.2
1.961	0.3	Morimoto [204]	0.061	10	899.662	1764.527
	0.45	LEFCA-CAPR-145 [private com.]	0.055	82	743	2073
1.962	0.252	Elbel and Schmidt [197]	0.073	21	1055	1678
1.965	0.1	Duriez [4]	0.04	106	666.263	1992.15
			0.042	64	718.15	2203.15
	0.2	Elbel and Schmidt [197]	0.131	40	1083	2523
			0.145	40	1086	2503
	0.25	Gibby [122]	0.044	23	378.2	1473
1.967	0.2818	Bonnerot [5]	0.053	25	1043	2363

O/M = 2-x (-)	Pu (y)	Author	Porosity (-)	Number of points	T_{min} (K)	T_{max} (K)
1.968	0.1	Duriez [4]	0.042	73	728.15	2278.15
1.97	0.2	Van-Craeynest and Weilbacher [6]	0.05	9	1273	1973
1.971	0.4	ESNII+	0.059	14	2049	2881
1.973	0.1	Duriez [4]	0.042	84	712.15	2278.15
	0.25	Gibby [122]	0.044	23	397.2	1473
1.974	0.15	Duriez [4]	0.044	55	710.15	2153.15
	0.2	Bonnerot [5]	0.046	24	1048	2223
1.976	0.2157	Bonnerot [5]	0.045	19	1123	2263
1.977	0.06	Duriez [4]	0.038	91	716.15	2213.15
1.978	0.05	Bonnerot [5]	0.061	15	1053.2	2273.2
	0.2962		0.069	18	1083	2273
1.979	0.06	Duriez [4]	0.038	72	714.15	2233.15
	0.1405	Bonnerot [5]	0.052	20	1068	2163
1.98	0.15	Serizawa [78]	0.04	37	1099.901	2082.357
	0.1516	Bonnerot [5]	0.032	16	973	2473
	0.2	Bonnerot [5]	0.099	18	1143	2273
		Evans [198]	0.083	6	1156	1771
		Serizawa [78]	0.039	24	1134.988	2105.749
		Weilbacher [6]	0.05	12	773	2973
	0.24	ESNII+	0.054	22	2039.3	2700
	0.25	TRUMOX	0.045	9	996.691	2045.63
	0.3	Elbel and Schmidt [202]	0.09	49	1145	1719
		Yamaguchi [205]	0.05	9	1073.2	2673.2
			0.1	9	1073.2	2673.2
			0.2	9	1073.2	2673.2
	0.44	Sengupta [193]	0.05	10	975.117	1813.15
	0.45	TRUMOX	0.05	9	717.461	1480.486
	0.6	PUMMA	0.111	42	1606.3	2821.1
	0.65	PUMMA	0.172	32	1578.6	2825.2
	0.7	PUMMA	0.096	34	1622.4	2815.5
1.981	0.29	ESFR-SMART	0.058	24	1740.2	2557.2
1.982	0.1498	Bonnerot [5]	0.037	27	1073	2243
	0.2	Hetzler [201]	0.036	9	1188	2086
			0.052	4	1215	1421
			0.057	11	1175	2009
	0.214	SCARABIX	0.04	92	688	2129
	0.3	Morimoto [204]	0.058	10	918.243	1771.284
1.983	0.03	Duriez [4]	0.039	73	710.902	2260.35
	0.1	Bonnerot [5]	0.057	28	1023	2193
	1	Bonnerot [5]	0.071	11	1123	2138
1.984	0.15	Duriez [4]	0.044	67	693.15	2223.15
	0.2157	Bonnerot [5]	0.037	18	1093	2243
1.985	0.0777	Bonnerot [5]	0.061	19	1133	2293
	0.1841	Otter	0.04	81	373	2973
1.986	0.06	Duriez [4]	0.038	113	685.15	2048.15
			0.049	108	684	2047
	0.1	Duriez [4]	0.042	67	717.15	2198.15
		Elbel and Schmidt [202]	0.09	40	1232	2540
	0.171	Bonnerot [5]	0.028	18	1083	2203
1.988	0.1837	Otter	0.04	81	373	2973

O/M = 2-x (-)	Pu (y)	Author	Porosity (-)	Number of points	T_{min} (K)	T_{max} (K)
	0.184	Otter	0.04	81	373	2973
1.99	0.1	Serizawa [78]	0.041	39	1134.988	2051.947
	0.2	Gibby [117]	0.04	60	363.2	1870
		Weilbacher [6]	0.05	12	773	2973
	0.236	Bonnerot [5]	0.062	15	1226	2253
	0.25	Gibby [122]	0.044	23	406.2	1480
1.991	0.06	Duriez [4]	0.038	95	679.15	1954.15
	0.1		0.04	203	653	2273
1.992	0.65	TRUMOX	0.04	10	718.021	1708.527
1.994	0.2	Van-Craeynest and Weilbacher[106]	0.05	9	1373	2173
1.995	0.2	Van-Craeynest and Weilbacher [106]	0.05	10	358.2	1014
	0.29	ESFR-SMART	0.058	60	542.59	2687.1
	0.31		0.073	42	549.02	2820.9
1.996	0.2	Van-Craeynest and Weilbacher [106]	0.05	16	1273	2173
1.997	0.04	Sengupta [193]	0.095	9	915.862	1862.069
	0.2	Van-Craeynest and Weilbacher [106]	0.05	6	377.2	977.2
1.998	0.0787	Alessandri	0.055	11	829.15	1748.15
	0.45	Duriez [4]	0.039	78	693	2138
1.999	0.2	Van-Craeynest and Weilbacher [106]	0.05	5	386.2	883.2
	0.4	ESNII+	0.059	79	541.57	2594.7
	0.03	Duriez [4]	0.039	99	676.15	1996.15
			0.049	140	680	2081
	0.05	Gibby [199]	0.03	20	374.153	1496.825
		Otter	0.064	27	373	2973
		Weilbacher [6]	0.05	12	773	2973
	0.059	Duriez [4]	0.053	85	663	2174
	0.06		0.038	100	404	1770
			0.049	141	680	2069
	0.1	Duriez [4]	0.04	64	669	2066
			0.042	149	674.15	2219.15
		Otter	0.021	27	373	2973
		Weilbacher [6]	0.05	12	773	2973
	0.12	Gibby [199]	0.03	54	368.92	1473.566
	0.15	Duriez [4]	0.044	109	677.15	2043.15
		Otter	0.021	27	373	2973
		Weilbacher [6]	0.05	12	773	2973
	0.19	GACID	0.05	23	541.97	1461.8
	0.2	ANL [196]	0.05	7	800	3000
		Evans [198]	0.083	6	1143	1710
		Fukushima [98]	0.041	72	691.2	1819
		Gibby [199]	0.02	28	425.087	1479.602
		Gibby [117]	0.046	78	360.2	1780
		Hetzler [201]	0.045	18	1075	2164
			0.048	9	1167	2001
		Elbel and Schmidt [202]	0.09	30	1291	1593
		Otter	0	27	373	2973
		Van-Craeynest and Stora [58]	0.05	15	354	1172
			0.14	14	340.7	1172
			0.16	15	335.3	1166
			0.2	18	325.7	1170

O/M = 2-x (-)	Pu (y)	Author	Porosity (-)	Number of points	T_{min} (K)	T_{max} (K)
		Van-Craeynest and Weilbacher [106]	0.05	28	337.2	1137
		Weilbacher [6]	0.05	12	773	2973
	0.21	Rao [194]	0.04	8	673	1473
	0.24	ESNII+	0.054	71	543.78	2818.5
	0.25	Gibby [199]	0.03	38	459.604	1480.672
		Gibby [122]	0.044	82	416.2	1873
	0.26	Otter [private com.]	0.055	27	373	2973
		Weilbacher [6]	0.05	12	773	2973
	0.28	Rao [194]	0.04	8	773	1473
	0.2952	Morimoto [203]	0.048	20	916.667	1769.667
			0.052	20	871.667	1773
			0.058	20	874.333	1770
			0.06	10	871.667	1773
			0.062	10	900.667	1764
		Morimoto [192]	0.063	10	872	1774
		Morimoto [203]	0.064	10	872	1774
			0.066	10	875	1764.333
			0.069	10	882.333	1764
			0.074	10	899.667	1770
			0.08	10	885.333	1772.333
			0.083	12	874.333	1766
			0.088	10	892	1765
			0.1	10	902	1770.333
			0.104	10	902	1770.333
			0.113	10	870.667	1765
			0.128	10	902.333	1766
			0.157	10	883	1765.667
	0.3	Gibby [199]	0.03	31	420.869	1488.846
		Morimoto [204]	0.064	10	870.946	1774.662
		Otter	0.025	27	373	2973
		Weilbacher [6]	0.05	12	773	2973
		Yamaguchi [205]	0.05	9	1073.2	2673.2
	0.35	TRUMOX	0.05	10	931.393	2017.114
	0.4	ESNII+	0.052	48	541.57	1612.7
			0.059	113	541.57	1661.5
		Rao [194]	0.04	9	673	1473
	0.439	Bonnerot [5]	0.215	19	1043.15	2270
	0.45	ESNII+	0.048	68	545.36	2828.9
			0.069	54	545.1	1653.4
			0.073	100	544.15	1647.6
		Weilbacher [6]	0.05	11	773	2773
	0.5	Weilbacher [6]	0.05	11	773	2773
	0.55	TRUMOX	0.05	13	730.248	1657.536
	0.6	PUMMA	0.03	54	546.92	2858.2
	0.65	PUMMA	0.04	62	543.98	2822.9
	0.7	PUMMA	0.042	63	542.78	2844.7
	0.7545	Bonnerot [5]	0.179	34	1050	2220
	0.76	Weilbacher [6]	0.05	11	773	2773
	1	Weilbacher [6]	0.05	11	773	2773
		PUMMA	0.05	38	1570	2793

Table 6

x (-)	y (-)	p (-)	T (K)	λ at $T = 450 \pm 70$ $(W.m^{-1}.K^{-1})$	λ at $T = 850 \pm 70$ $(W.m^{-1}.K^{-1})$	λ at $T = 2830 \pm 70$ $(W.m^{-1}.K^{-1})$	Author	Reason for omitting
0	0.2952	0.058	All		2.70		Morimoto et al. [203]	Presence of Am High grain size
0	0.2952	0.062			3.04			
0	0.2952	0.066			2.30			
0	0.2952	0.069			2.19			
0	0.25	0.044		4.84			Gibby [122]	High grain size
0.01	0.25	0.044		4.47				Alpha self-irradiation effects
0	0.06	0.038		4.19			Duriez et al. [4]	High grain size
0	0.55	0.05			2.75		TRUMOX [private com.]	
0	0.20	0.16		5.47	3.32		Van-Craeynest and Stora [58]	High porosity
0	0.20	0.20		4.51	3.16			
0	0.20	0.05		4.21	3.17		Van-Craeynest and Weilbacher [106]	Statistical outlier
0	0.439	0.215					Bonnerot [5]	High porosity Bi-phased material
0	0.15	0.05			4.40		Weilbacher [6]	Statistical outlier
0	0.40	0.04			2.73		Rao et al. [194]	Statisical outlier
0.005	0.31	0.073	T>2800			6.58	ESFR-SMART (sample: CAPRA-4)	Partial fuel melting
0.029	0.40	0.059	T>2800			6.59	ESNII+ (sample: TRABANT40-HY)	
0	0.60	0.03	T>2800			6.62	PUMMA (sample: PUMMA60-OM)	
Whole experimental data set							Otter	Systematically higher thermal conductivity
Whole experimental data set							LEFCA-CAPR-145	Systematically higher thermal conductivity

Table 7: Omitted experimental data for the calibration and validation of the thermal conductivity model

J Experimental data, used for the optimization of the multi-objective cost function

The electrical conductivity experimental data, used in this optimization includes: Fujino *et al.*'s experimental data [159] for $x = 0$ (and $y = 0.3, 0.5, 0.9$) and Schmitz' experimental data [162] for $x > 0, y = 0.2$. The optimization included electrical conductivity experimental data on hypostoichiometric due to the high sensitivity of the electrical conductivity model to $E_m(Pu)$ for $x > 0$ (see Figure 3.21). Including electrical conductivity experimental data for $x > 0$ therefore increases the accuracy of the estimation of $E_m(Pu)$.

As for thermal conductivity, some experimental data had to be omitted, due to surprisingly high thermal conductivity values.

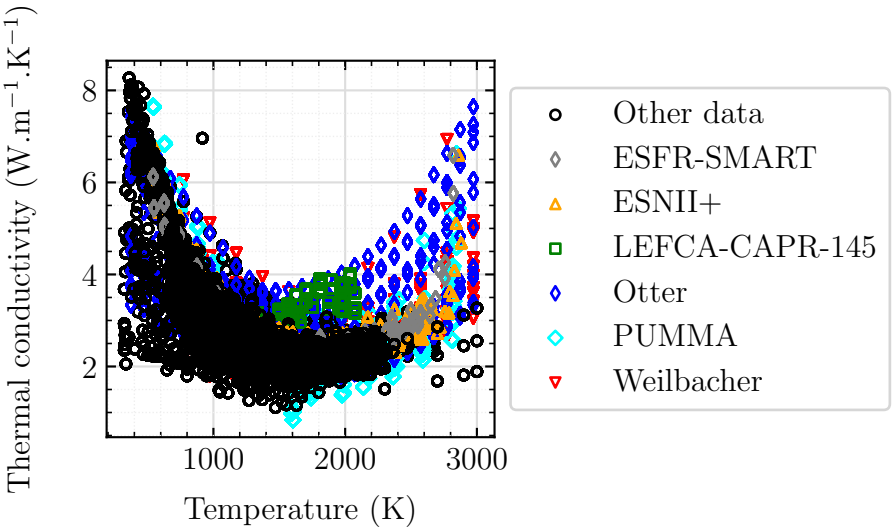

Figure J.11

As shown in Figure J.11, high temperature (*i. e.* T > 2000 K) experimental data is mainly provided by Otter [private com.], Weilbacher [6], and EU projects (PUMMA, ESNII+, ESFR-SMART). Otter's measurements show systematically higher values than those from the European projects, even for temperatures lower than $T < 2000$ K and regardless of the plutonium content. Indeed, Otter's measurements were done in 1977, using the Laser Flash technique, but to interpret the thermograms and thus deduce thermal diffusivity, they use Parker's correction [255]. As mentioned in Section H.2.3, other more sophisticated methods to interpret thermograms are used in the European projects' data set. Given the systematic overestimation of thermal conductivity in Otter's measurements, as opposed to those from the European projects, Otter's data was not considered in this optimization.

Some experimental points from the European projects were also omitted. Those concern the measurements, close to the melting temperature (*i. e.* close to 2850 K), where a possible partial fuel melting could occur and thus lead to a rapid increase in thermal conductivity.

The experimental data set, from LEFCA-CAPR-145 also showed higher values than most data for $T \in [1500 - 2000]$ K and thus were not considered in this optimization. Indeed, in this temperature region ($T \in [1500 - 2000]$ K), numerous experimental data exist: 2049 measurements. LEFCA-CAPR-145's data set (47 points) therefore only represents 2 % of the measurements. If we exclude the systematically high Otter values, the LEFCA-CAPR-145 data can be considered as a statistical outlier, given that the majority of the data yields up to 2 times lower thermal conductivity.

Table 7 in Annex I summarizes the omitted experimental data for the calibration of the electronic contribution, together with some other experimental data, omitted for the validation of the thermal conductivity model, which will be done in the following sections.

The thermal conductivity experimental data, used for the calibration of the electronic model therefore counts 6132 measurement points.

K Weighted least squares

We consider here the following cost function, originated from the Bayesian approach:

$$J = J^{\lambda} + J^{\sigma^{el}}_{x=0} + J^{\sigma^{el}}_{x>0} + J^{\beta} \tag{K.1}$$

Considering the elements, given in Section 4.4 of Chapter 4, we can write the total cost function in a matrix form as follows:

$$J(\mathbf{t}, \boldsymbol{\beta}) = (\mathbf{y} - \mathbf{f}(\mathbf{t}, \boldsymbol{\beta}))^{\mathbf{T}} \mathbf{P} (\mathbf{y} - \mathbf{f}(\mathbf{t}, \boldsymbol{\beta})) \tag{K.2}$$

The minimization of this function requires resolving :

$$\forall t \geq 0, \forall j \in [1, m_{\beta}] : \frac{\partial J(\mathbf{t}, \boldsymbol{\beta})}{\partial \beta_j} = 0 \tag{K.3}$$

The matrix form of this equation is written as follows:

$$-2\mathbf{X}^{\mathbf{T}} \mathbf{P} (\mathbf{y} - \mathbf{f}(\mathbf{t}, \boldsymbol{\beta})) = 0 \tag{K.4}$$

where $\mathbf{X}$ is the sensitivity matrix, containing the first derivatives of the inverse model $\mathbf{f}$ with respect to the parameters β:

$$X_{ij} = \frac{\partial f_i(t_i, \boldsymbol{\beta})}{\partial \beta_j} \tag{K.5}$$

In the case of a non-linear model with respect to the parameters, no explicit solution of equation K.4 could be obtained. One needs to use iterative methods. One of the most widely used algorithms is the Newton iterative algorithm, expressed as follows:

$$\boldsymbol{\beta}^{k+1} = \boldsymbol{\beta}^{k} - \lambda^{k} [\mathbf{H}(J(\boldsymbol{\beta}^{k}))]^{-1} \nabla J(\boldsymbol{\beta}^{k}) \tag{K.6}$$

where λ^k is a relaxation coefficient, ∇ and $\mathbf{H}$ are the gradient and Hessian matrices, involving the first and second order derivatives of the inverse model with respect to the parameters. To calculate the Hessian, a great amount of calculation time is required as second order derivatives are included. Therefore, in most cases, the "Gauss-Newton" approximation is used, which consists in neglecting the second order derivatives. The Gauss-Newton iterative method thus yields:

$$\boldsymbol{\beta}^{k+1} = \boldsymbol{\beta}^{k} - \lambda^{k} [\mathbf{X}(\boldsymbol{\beta}^{k})^{\mathbf{T}} \mathbf{P} \mathbf{X}(\boldsymbol{\beta}^{k})]^{-1} \mathbf{X}(\boldsymbol{\beta}^{k})^{\mathbf{T}} \mathbf{P} (\mathbf{y} - \mathbf{f}(\mathbf{t}, \boldsymbol{\beta}^{k})) \tag{K.7}$$

The matrix $\mathbf{X}^{\mathbf{T}}\mathbf{P}\mathbf{X}$ is called the information matrix, which should be invertible, thus satisfying $\det(\mathbf{X}^{\mathbf{T}}\mathbf{P}\mathbf{X}) \neq 0$. However, most of the time, the inverse models present an ill-conditioned information matrix, which has a determinant of zero. The inversion of ill-conditioned information matrices can be done by regularization. Combining the Tikhonov penalization to regularize the information matrix and the Gauss-Newton iterative method, the Marquardt-Levenberg algorithm is obtained:

$$\boxed{\boldsymbol{\beta}^{k+1} = \boldsymbol{\beta}^{k} - \lambda^{k} [\mathbf{X}(\boldsymbol{\beta}^{k})^{\mathbf{T}} \mathbf{P} \mathbf{X}(\boldsymbol{\beta}^{k}) + \alpha^{k} \mathbf{I}]^{-1} \mathbf{X}(\boldsymbol{\beta}^{k})^{\mathbf{T}} \mathbf{P} (\mathbf{y} - \mathbf{f}(\mathbf{t}, \boldsymbol{\beta}^{k}))} \tag{K.8}$$

where α is a penalization term.

K.1 Covariance matrix of the estimator

Now we notate $\mathbf{y(t)} - \mathbf{f(t, \boldsymbol{\beta})} = \boldsymbol{\epsilon}\mathbf{(t)}$, where $\boldsymbol{\epsilon}\mathbf{(t)}$ is treated as a stochastic variable, called white noise (i. e. uncorrelated with $\mathbf{t}$) with zero mean :

$$\mathbb{E}(\epsilon) = 0; \mathrm{cov}(\boldsymbol{\epsilon}) = \sigma^2 \mathbf{I_m}$$

where $\mathbb{E}$, cov, σ are the expectancy, covariance, standard deviation of the white noise respectively and $\mathbf{I_m}$ the $m \times m$ identity matrix. The variance matrix of the estimator is calculated as follows:

$$\mathbf{cov}(\hat{\boldsymbol{\beta}}) = \mathbb{E}\left[(\hat{\boldsymbol{\beta}} - \mathbb{E}(\hat{\boldsymbol{\beta}}))(\hat{\boldsymbol{\beta}} - \mathbb{E}(\hat{\boldsymbol{\beta}}))^{\mathbf{T}}\right] \tag{K.9}$$

Knowing that $\mathbb{E}(\hat{\boldsymbol{\beta}}) = \boldsymbol{\beta}$ and substituting $\hat{\boldsymbol{\beta}} - \boldsymbol{\beta}$ by its expression:

$$\boxed{\mathbf{cov}(\hat{\boldsymbol{\beta}}) = (\mathbf{X^T P X})^{-1}\mathbf{X^T P}\mathbb{E}(\boldsymbol{\epsilon}\boldsymbol{\epsilon}^{\mathbf{T}})\mathbf{P X}(\mathbf{X^T P X})^{-1}} \tag{K.10}$$

As ϵ is supposed uncorrelated, $\mathbb{E}(\boldsymbol{\epsilon}\boldsymbol{\epsilon}^{\mathbf{T}})$ is a diagonal $m \times m$ matrix, $\mathbb{E}(\boldsymbol{\epsilon}\boldsymbol{\epsilon}^{\mathbf{T}}) = (E_{jk})_{1 \leq j,k \leq m}$, such that:

$$E_{jk} = \begin{cases} 0, & \text{if } j \neq k \\ \sigma^2_{\lambda}, & \text{if } j = k \leq m_{\lambda} \\ \sigma^2_{\sigma_{el}}, & \text{if } m_{\lambda} < j = k \leq m_{\sigma} \\ \sigma^2_{\beta_1}, & \text{if } j = k = \dim(m) - (\dim(n) - 1) \\ \sigma^2_{\beta_2}, & \text{if } j = k = \dim(m) - (\dim(n) - 2) \\ \vdots & \vdots \\ \sigma^2_{\beta_n}, & \text{if } j = k = \dim(m) \end{cases}$$

The variance-covariance matrix of the estimator $\mathbf{cov}(\hat{\boldsymbol{\beta}})$ is thus a symmetric $n \times n$ matrix, containing the variance of the parameters $\mathrm{var}(\hat{\beta}_j)$ on the diagonal indices and the covariance between the parameters $\mathbf{cov}(\hat{\beta}_j, \hat{\beta}_k)$ on the off-diagonal indices. This matrix allows to build the so-called hybrid matrix, which contains the relative standard deviation of the parameters on its diagonal indices and the correlation coefficients ρ_{jk} on its off-diagonal indices:

$$V_{hyb}(\hat{\beta}) = \begin{bmatrix} \frac{\sqrt{\mathrm{var}(\hat{\beta}_j)}}{\hat{\beta}_j} & \rho_{jk} & \cdots \\ & \frac{\sqrt{\mathrm{var}(\hat{\beta}_k)}}{\hat{\beta}_k} & \cdots \\ sym & & \ddots \end{bmatrix}$$

L Commentary on the heat capacity model of PuO_2

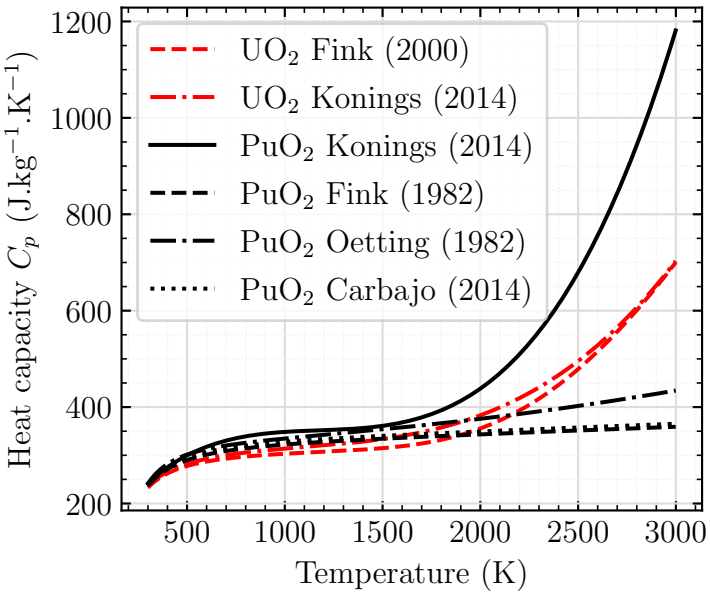

Figure L.12: Heat capacity variation with temperature for UO_2, according to Fink [87] and Konings *et al.* [195] and for PuO_2, according to Konings *et al.* [195], Fink [87], Oetting [227] and Carbajo *et al.* [79]

We compared different models, reported for both UO_2 and PuO_2. All those models are semi-empirical and are based either on direct heat capacity measurements or on the derivation of enthalpy increment measurements with respect to the temperature: $C_p = \frac{\partial H}{\partial T}$, where H is the enthalpy and T the temperature.
As shown in Figure L.12, good agreement is obtained between the models of Fink [87] and Konings *et al.* [195], concerning UO_2. Indeed, numerous experimental data for UO_2 were reported in the literature [256–263], covering the whole temperature range of interest, $T \in [380 - T_m]$, where T_m is the melting temperature.
However, for PuO_2, large discrepancies are observed between the model, proposed by Konings *et al.* and other models, especially for temperatures higher than 2000 K. A factor of 3 is observed at 3000 K, between the model of Konings *et al.* and other models (Fink [87], Oetting et al. [227] and Carbajo et al. [79]).

Indeed, to our knowledge, only three measurement data sets exist for heat capacity of PuO_2 [227–229]. Ogard [228] measured the enthalpy increment of PuO_2 from 1500 K to 2715 K and fitted an equation for the heat capacity. However, in Ogard's work, the four measurement points, covering $T \in [2470 - 2715]$ K were not considered in the fitting, because "a very prominent positive deviation of the results were present" (*i. e.* the measurements showed a very rapid increase after T=2370 K). No further scientific explanation for omitting those four measurements was given by the author. Oetting [227] measured enthalpy increment from 353.9 K to 1610.7, thus completing the temperature range, which was not covered in Ogard's work. Oetting also fitted a heat capacity equation to both his measurements and those of Ogard

[228] and Kruger and Savage [229]. However, instead of using all measurements, Oetting also omitted the four measurement points of Ogard, covering $T \in [2470 - 2715]$ K. Unlike Ogard, Oetting explained why those points were not considered in his model. According to Oetting, what may have caused the surprisingly rapid increase in the enthalpy increment measurements of Ogard is the interaction of the tungsten capsule with the PuO_2 samples. Konings *et al.* [195] instead used all available experimental data for PuO_2, including the four measurement points, which were omitted by both the original author of the measurements and Oetting. Those four measurement points showing a rapid increase after $T = 2370$ K, considered in Konings et al.'s work, therefore seem to be the reason for the differences in heat capacity models for PuO_2.

Given the obvious debate about whether the high-temperature measurement points in Ogard's work should be considered to fit a heat capacity empirical model, the exact temperature variation of the heat capacity of PuO_2 after T=2370 K, is uncertain. As we saw in Figure 4.10, the thermal conductivity residuals become important above approximately $T = 2200$ K, which is exactly the temperature range, in which uncertainties in heat capacity of PuO_2 are high.

We also compared the consistency of the heat capacity Kopp law with measurements on MOX fuels [25, 108, 109, 194, 222, 224, 228, 264, 265]. Those measurements are composed of enthalpy increment measurements [194, 222, 228, 264], which were derived with respect to temperature to obtain heat capacity, or direct heat capacity measurements [25, 108, 109, 224, 265].

M Comparison of models with heat capacity measurements on MOX fuels

This comparison was done, using both Fink [87] and Konings *et al.* [195] models for UO_2 and PuO_2, as well as the O_2 heat capacity from Duriez *et al.* [4].
As shown in Figures M.13 and M.14, both Fink and Konings *et al.*'s predictions underestimate the experimental heat capacity from PUMMA's measurements. The maximum deviation of Fink's model with respect to the measurements of PUMMA is of approximately 344 %, whereas that of Konings et al. is of ≈ 150 %. The consistency of the Konings et al.'s model with PUMMA's measurements on high plutonium content MOX fuels, is therefore better than that of Fink. In addition, Konings *et al.*'s model is in better agreement than Fink with the measurements of ESFR-SMART [108] and ESNII+ [224] ($y \in [0.24 - 0.45]$).
On the other side, Konings *et al.* overestimate heat capacity with respect to other measurements, especially those of Affortit [265] ($x \in [0 - 0.17]$) and Ogard [228] (maximum deviation of 88 %). The consistency of Fink's model with respect to those measurements is greater than that of Konings *et al.*, showing a maximum deviation of only 18 %.

It is however delicate to say which model better predicts heat capacity of MOX fuels, given the high experimental data scattering, especially at very high temperatures (T > 2500 K). Indeed, in the EU projects' data set (PUMMA, ESFR-SMART and ESNII+), heat capacity was measured simultaneously with thermal diffusivity, using the CLASH technique

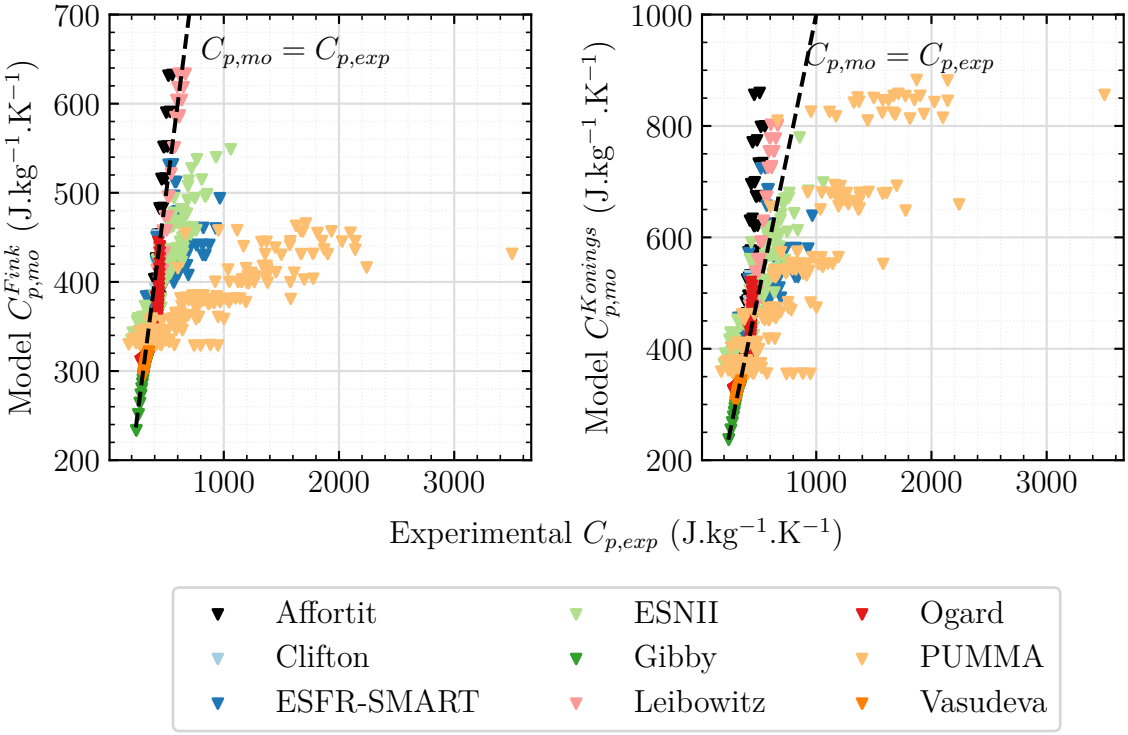

Figure M.13: Modeled vs. experimental heat capacity. The model is the Kopp law with both the models of Fink and Konings *et al.* for UO_2 and PuO_2. To correct for oxygen hypostoichiometry, we used the C_p model for O_2, given in Duriez et al.'s work [4]. The measurements are those of Affortit [265] ($y = 0.20$ and $y = 0.75$), Clifton [264] ($y = 0.20$), Leibowitz [222] ($y = 0.2$), Ogard [228]($y = 0.2$), Vasueva [206] ($y \in [0.35 - 0.45]$), PUMMA ($y \in [0.6 - 0.7]$), ESFR-SMART ($y \in [0.29 - 0.31]$) and ESNII+ ($y \in [0.24 - 0.45]$).

[249, 266] (see Section H.2.3). Numerous reviews on the uncertainties, related to thermal diffusivity and heat capacity measurements with laser flash techniques, were reported in the literature [267–271]. Most of those reviews report a systematic uncertainty of $[3 - 5]$ % for thermal diffusivity and $[7 - 10]$ % for heat capacity. The higher uncertainty in heat capacity originates from the need for a precise evaluation of the absorbed energy by the sample, which in most cases is very complex to evaluate [270]. This is however an estimation of solely the systematic uncertainty. Vlahovic *et al.* [266] measured thermal diffusivity of UO_2 samples by the CLASH method and mentioned that data scattering at high-temperatures is greater than the systematic errors. This led to the conclusion that other factors, such as microstructural changes, occurring at those temperatures (T>2500 K) contribute more than systematic errors to the total experimental standard deviation. Figure M.15 shows how a shift in experimental data scattering is observed after 2500 K on thermal conductivity of UO_2 [108, 256, 266], which is most certainly due to microstructural changes in the samples. The increasing standard deviation of the experimental data with temperature is also observed in the heat capacity measurements of the EU projects (see Figure M.14). The experimental heat capacity standard deviation goes from 91 J kg^{-1} K^{-1} at $T \approx 1900$ K, to 403 J kg^{-1} K^{-1} at $T \approx 2500$ K and finally 615 J kg^{-1} K^{-1} at $T \approx 2850$ K. Further investigation needs to be done to explain the discrepancies in both thermal diffusivity and heat capacity data. Using Scanning Electron

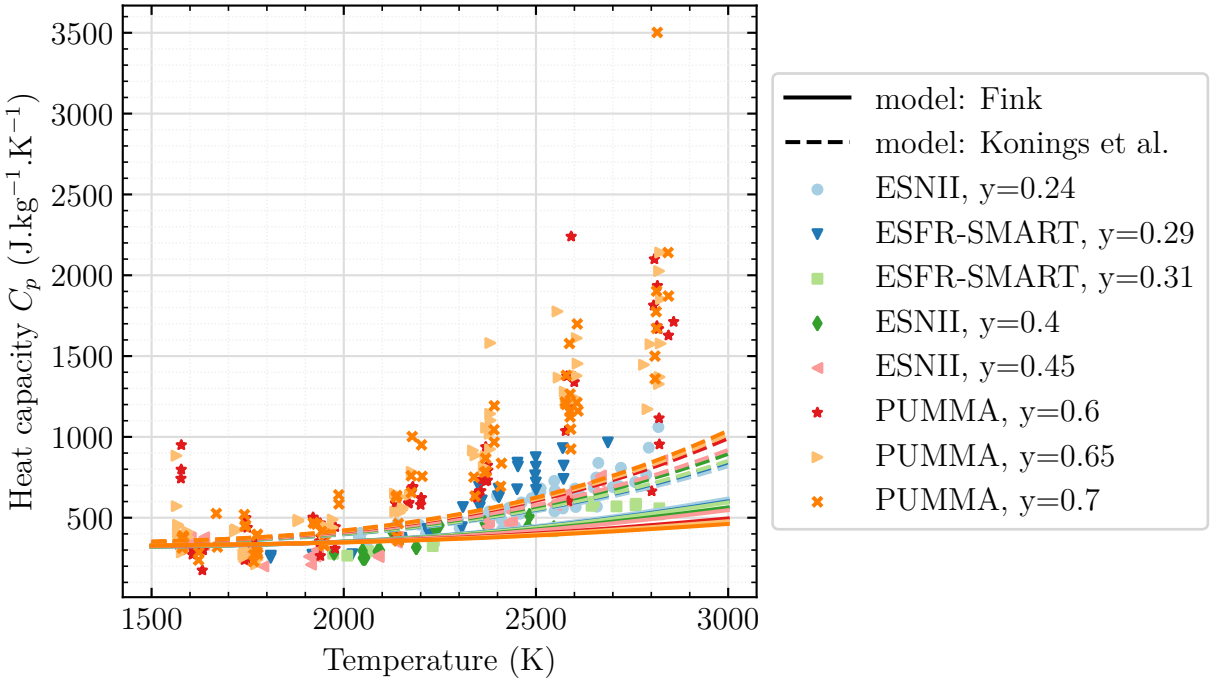

Figure M.14: Temperature variation of heat capacity, as modeled by Fink [87] and Konings *et al.* [239] and as measured by the EU projects.

Microscopy (SEM), Vlahovic *et al.* [266] showed that a strong re-crystallization of the sample occurred after heating at very high temperatures (i. e. $T = 2850$), which may explain data scattering at those temperatures. Indeed, this phenomenon leads to nonparallel front and rear surfaces, which therefore contradicts one of the assumptions in the model, used to fit the thermograms. In addition to data noise at extremely high temperatures (i. e. here 2850 K), we observe that data is also scattered for temperatures, lower than 2850 K. **Performing systematic characterization** (*e. g.* SEM) of the samples **after each laser pulse** in the range $T \in [2500 - 2850]$ may therefore allow to observe whether data scattering at $T = 2500$ occurs because of microstructural changes in the samples or because of uncertainties, which are intrinsic to the experimental technique (instability of the temperature baseline, neglecting the temperature variation of the emissivity *etc.*).

The purpose of this analysis was to highlight the difficulty in explaining the thermal conductivity residuals, observed in Figure 4.10, given the uncertainty in the heat capacity model, used to calculate thermal conductivity from thermal diffusivity data.

We recall that in addition to indirectly measured thermal conductivity, our experimental data base also counts direct measurements. Even though such data is more complex to provide, and is thus associated with higher uncertainties, it bears comparing them to the indirect measurements. This comparison can further clarify the uncertainty in the indirect determination of thermal conductivity due to heat capacity.

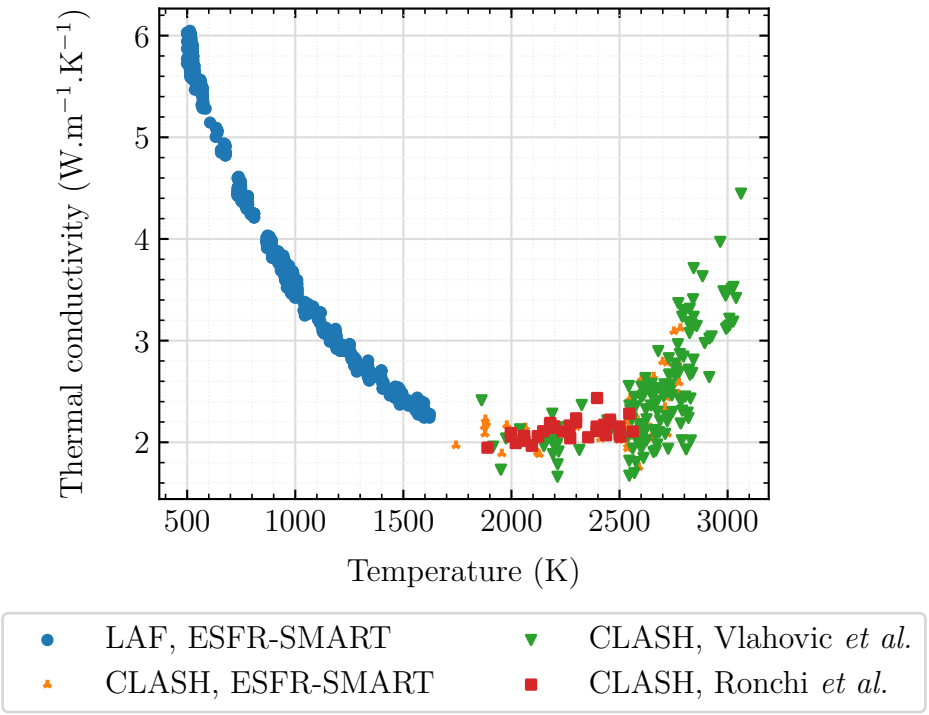

Figure M.15: Experimental variation with temperature of thermal conductivity of UO_2, according to the ESFR-SMART measurements (using LAF and CLASH techniques), Ronchi *et al.* [256] (CLASH) and Vlahovic *et al.* (CLASH) [266]. Thermal conductivity is deduced from experimental thermal diffusivity, density and the heat capacity model of Konings *et al.* for UO_2 [195].

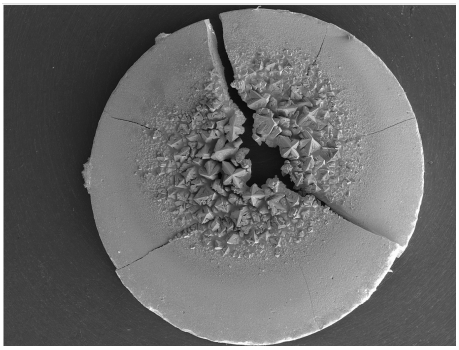

Figure M.16: SEM image of the UO_2 sample, after thermal diffusivity measurement at $T = 2850$ K. [266]

N Comparison between direct and indirect thermal conductivity experimental data

As shown in Figure N.17, the direct measurements yield lower thermal conductivity values than indirect measurements, especially for temperature above 2500 K. The average deviation from stoichiometry of the direct measurements is not the same as the indirect measurements. However, as already mentioned in Chapter 3 and as it will be experimentally confirmed later

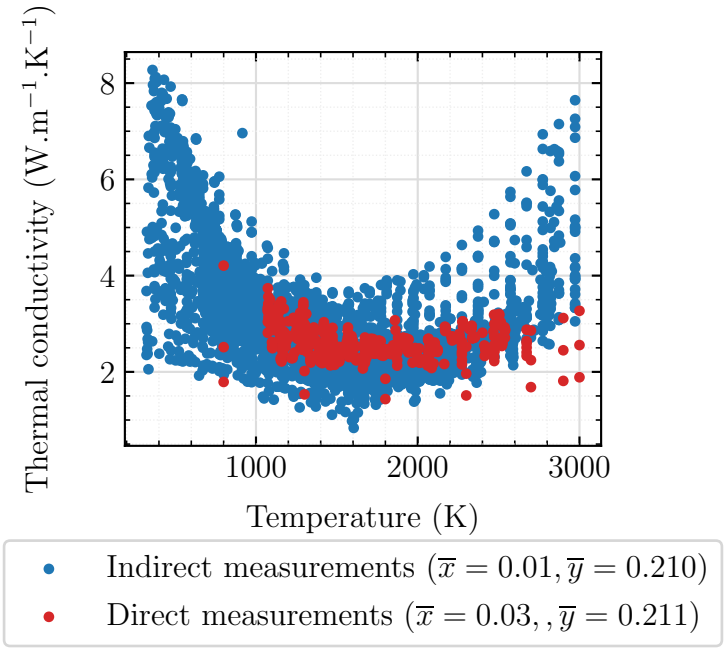

Figure N.17: Comparison between direct and indirect thermal conductivity measurements. The average deviation from stoichiometry and plutonium content, weighted by the number of measurement points is also shown.

in this chapter (see Section 4.7.4), the effect of stoichiometry at high temperatures is slight. Therefore, the different mean stoichiometry is unlikely to be the reason for the lower thermal conductivity, observed in the direct measurements. The latter does not show such an important thermal conductivity upswing at high temperatures, compared to the indirect measurements. This comparison gives more insight into the validity of the heat capacity model. However, this analyze is only qualitative, because most direct measurements do not exceed 2500 K. Only a couple of measurements go above that temperature. Given that the uncertainty in the use of the PuO_2 heat capacity model of Konings *et al.* [195] increases after T=2500 K, the direct measurements could not provide a quantitative validation of the indirect measurements.

O Possible explanation for discrepancies in thermal conductivity experimental data below 1500 K

In addition to high data scattering above 2500 K, important data scattering is also observed below 1500 K. Thermal conductivity data at $x = 0$ and below 1500 K, is dispersed in the range range $[4 - 8]$ W m^{-1} K^{-1}. In the following section, we will identify the possible reasons for those discrepancies. For some experimental data sets, no explicit scientific explanation could be provided, because of missing information.

The majority of the experimental data yields values close to 8 W m^{-1} K^{-1}. Some data sets however yield surprisingly low values: Duriez *et al.* [4], Van-Craeynest and Weilbacher [106], Van-Craeynest and Stora [58], Gibby [199], TRUMOX [private com.]. Some data sets

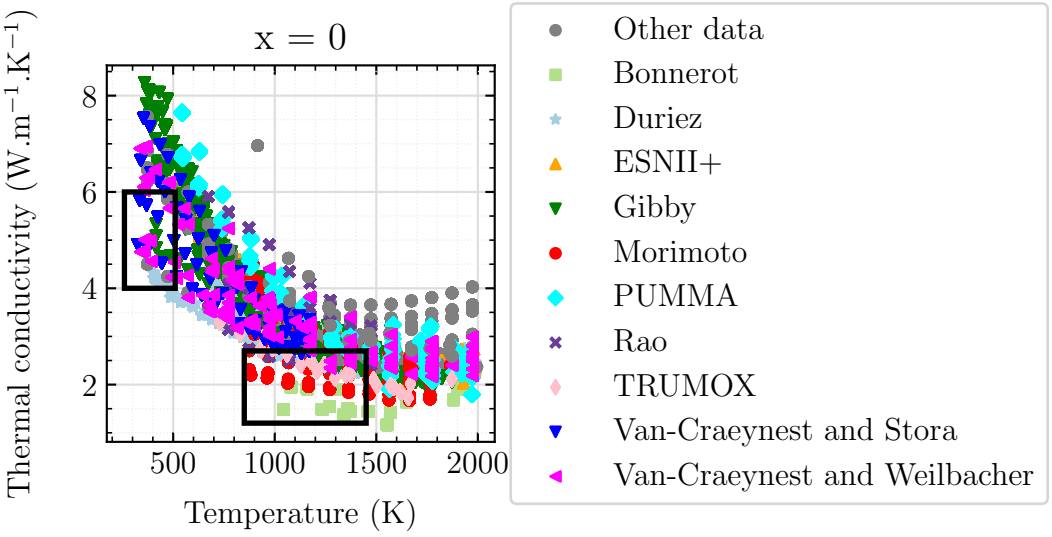

Figure O.18: Experimental variation of thermal conductivity with temperature, according to [4, 5, 58, 106, 109, 191, 192, 194, 203, 203, 224] and [private com.]

also show discrepancies, compared to the rest of the data, at T $\in [1000 - 1500]$ K: Morimoto *et al.* [191, 192, 203, 204], Bonnerot [5].

O.1 Effect of self-irradiation

One of the phenomena responsible for discrepancies in thermal conductivity experimental data could be self-irradiation damage [225, 272–274]. The latter characterizes the lattice defects due to alpha decay in nuclear fuels. Indeed, alpha decay leads to atomic displacements in the fuel lattice (i. e. atoms moving from their normal lattice positions) [273], which contributes to decrease thermal conductivity [225]. Alpha decay occurs in the first moments of fuel fabrication. Self-irradiation effects therefore increase with the elapsed time from fuel fabrication. Therefore the decrease in thermal conductivity due to alpha decay increases with storage time [225]. It should be mentioned that self-irradiation damage should not be confused with radiation damage, caused by in-pile irradiation. Indeed, irradiation in reactor causes supplementary lattice damage, due to the displacement of atoms, induced by the neutrons colliding with fissile atoms. Those damage therefore contribute to further decrease thermal conductivity during irradiation. Staicu *et al.* [273] mentioned that, to properly evaluate the self-irradiation (*i. e.* from alpha decay) effects on thermal conductivity, fresh fuels (*i. e.* unirradiated) should be used instead of irradiated ones, since the latter contain self-irradiation damage and damage, caused by irradiation in reactor.

Ikusawa *et al.* [225] proposed a model for self-irradiation effects on thermal conductivity of MOX fuels, based on thermal conductivity experimental data on MOX fuels with different storage time. According to their model, the decrease in thermal conductivity due to self-irradiation is characterized by storage time, isotopic composition, decay constant and temperature. Self-irradiation damage recovers with increasing temperature [37]. Ikusawa *et al.* showed that the thermal conductivity decrease of the alpha-damaged MOX fuel, with respect to the "recovered" MOX fuel, is of the order of 43 % at T=550 K, for a MOX fuel, stored for $\approx$ 1334 days.

To apply this model, precise knowledge of the time storage of the fuel is needed. Since such information is not systematically provided, in this work, we did not take into account self-irradiation damage, when extracting the thermal conductivity of the matrix out of thermal conductivity experimental data. However, our experimental data base accounts for the type of measurement cycle (*i. e.* heating or cooling). A general practice in fuel property measurements is to measure thermal conductivity when heating the sample and then to measure it again when cooling the sample. Indeed, as already mentioned, self-irradiation damage recovers with increasing temperature. Therefore measuring thermal conductivity during a cooling cycle (once a first heating cycle has already been performed), allows to recover self-irradiation damage. According to heating and cooling measurements in Ikusawa *et al.*'s work on alpha-decay damaged MOX fuels, at approximately $T = 1100$ K, heating and cooling cycles yield the same thermal conductivity. Lucuta *et al.* [32] proposed a model for the effect of radiation damage on thermal conductivity, but in their model, account is taken of both alpha-decay damage and damage from irradiation in reactor. In their model, at about $T = 1000$ K, all radiation damage is recovered. To avoid self-irradiation effects in thermal conductivity measurements

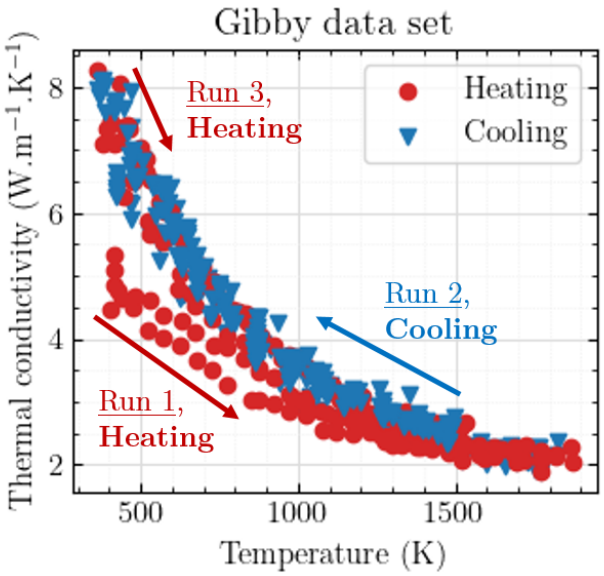

Figure O.19: Experimental variation of thermal conductivity with temperature, according to Gibby's experimental data set [200] at heating (in red) and cooling (in blue).

on fresh MOX fuels, it is important to perform a first heating cycle and then use the cooling cycle or a second heating cycle to extract the "undamaged" fuel's thermal conductivity. A clear observation of the heating and cooling cycles is made in Gibby's experimental data set (see Figure O.19). Thermal conductivity at around 400 K during the first heating cycle is almost twice lower than thermal conductivity at the cooling cycle or the second heating cycle. This may be caused by self-irradiation effects, because of a possible long time storage of the MOX fuels.

In most experimental data sets, information about whether the measurement corresponds to a heating or cooling cycle is not provided. It is therefore difficult, for most data sets, to conclude whether the lower thermal conductivity values can be explained by self-irradiation damage. The measurements, coming from the European projects correspond all to cooling cycles and data scattering is low, since self-irradiation damage is not observed. Figure O.20 shows that Gibby's experimental data set at the cooling and the second heating cycle is consistent with the measurements of the EU projects.

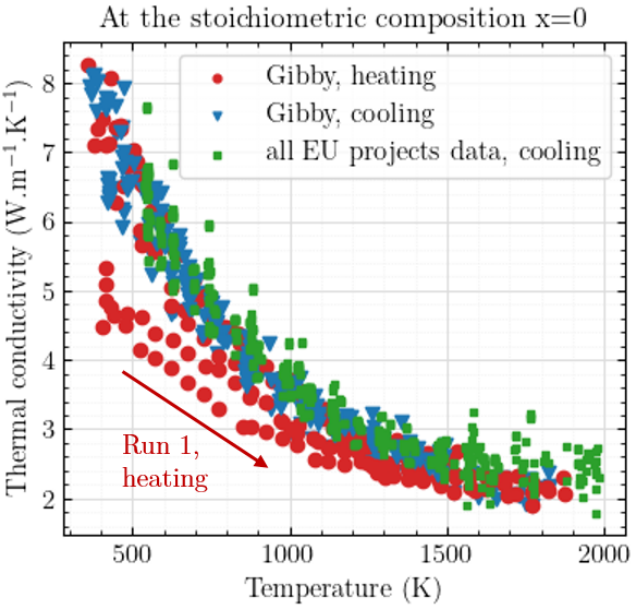

Figure O.20: Experimental variation of thermal conductivity with temperature, according to Gibby's experimental data set [122] at heating (in red) and cooling (in blue) and to the EU projects [108, 109, 224].

O.2 Americium content and high porosity

Some of the other data, yielding lower thermal conductivity values, compared to the rest of the data, could be explained by either the presence of a non negligible concentration of americium or high porosity.

Figure O.21 shows the experimental variation of thermal conductivity with temperature, at the stoichiometric composition (*i. e.* $x = 0$) and for different porosity fractions. We observe that most of the measurements, where $p = 0.05$ yield the same value with a relatively low standard deviation. Two exceptions are observed: the data of Van-Craeynest and Weilbacher [106] and that of TRUMOX [private com.]. Another fuel at $p = 0.07$ yields relatively low values, compared to the rest: the data of Morimoto *et al.* [203]. The reason for this discrepancy may come from the relatively high amount of americium in their fuel (3 %). Indeed, americium originates from the beta-decay of plutonium. Americium therefore is naturally present in MOX fuel [1]. Similarly to the effect of alpha-decay damage on thermal conductivity, the concentration of americium in MOX fuel increases with storage time. Am

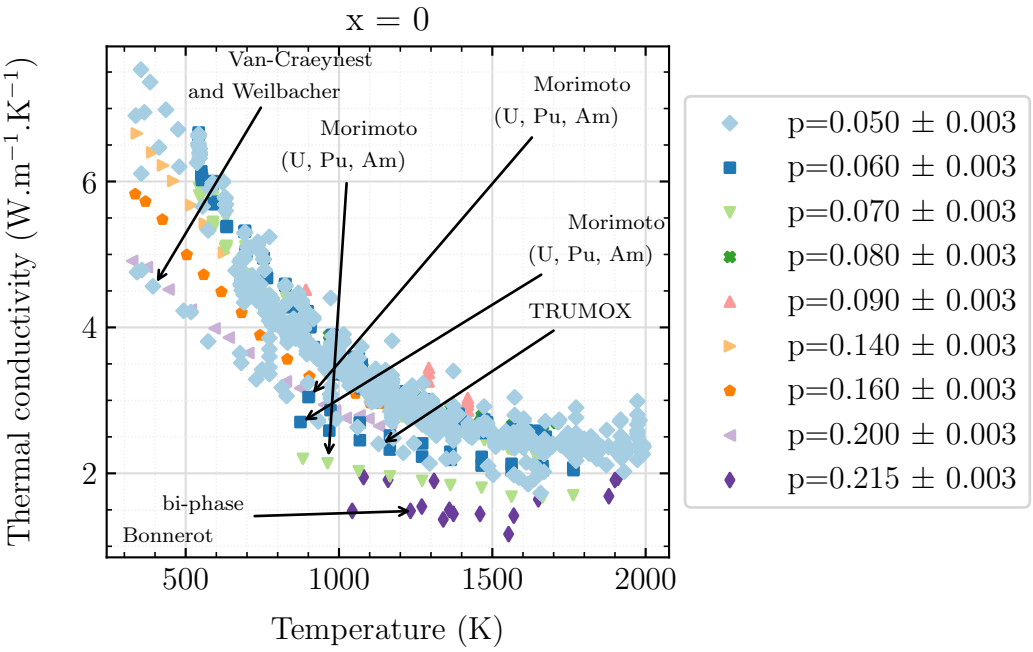

Figure O.21: Experimental variation of thermal conductivity with temperature for different porosity fractions.

has been proven to decrease thermal conductivity [203] and can therefore contribute to the observed discrepancies in thermal conductivity experimental data.

The rest of the data, yielding lower values compared the data at $p = 0.05$ could be explained by high porosity: the measurements at $p = 0.16$ and $p = 0.20$. This may be caused by the inadequacy of Maxwell-Eucken's porosity correction (used in this work) to calculate the matrix thermal conductivity out of effective thermal conductivity, when the porosity exceeds a certain value. Indeed, as already mentioned in Chapter 2, Maxwell-Eucken's formula is based on the assumption of diluted pores, which for $p > 0.10$ is no longer the case, since percolation begins to form, leading to open porosity [54–56]. This observation highlights the need for a proper analytical porosity correction model, when dealing with MOX fuels, exceeding $p = 0.10$. We also recall that to further develop this analysis, the porosity is not the only criteria. Information such as the pore shape and its orientation, as opposed to heat flux should also be provided.

O.3 Other explanations

As observed in Figure O.21, the data sets of Van-Craeynest and Weilbacher (at $p = 0.05$ and $y = 0.2$) [106], TRUMOX (at $p = 0.05$ and $y = 0.35; y = 0.55$) [private com.] and Bonnerot [5] (at $p = 0.215$ and $y = 0.44$) also yield lower thermal conductivity values, compared with the rest of the data.

The reason for the discrepancies, caused by Bonnerot's data set at $p = 0.215$ and $y = 0.44$ may

originate from both (1): high porosity ($p = 0.215$) and (2): bi-phased microstructure, reported in [5]. Bonnerot therefore did not account for this experimental data set, when proposing a thermal conductivity model [5]. The same follows for the experimental data set at $y = 0.75$, where bi-phased microstructure was observed.

The discrepancies caused by the data set of Van-Craeynest and Weilbacher at $p = 0.050$ and $y = 0.2$ could not be interpreted due to missing information about the fuel characteristics, in particular its microstructure or about the measurement cycle: heating or cooling. Indeed, Van-Craeynest and Weilbacher observed those discrepancies in their original paper [106], but could not provide a scientific explanation. The same follows for the TRUMOX fuel, which systematically yields lower values, but no reason for this could be identified due to missing supplementary information about fuel and measurement characteristics.

The EU projects' data set is composed of the most up-to-date measurements on MOX fuels, obtained with a physically and mathematically rigorous method to extract thermal diffusivity from thermograms [248]. The measurements always correspond to cooling cycles, which allows to avoid any self-irradiation damage. The MOX fuels, used for the measurements are single phased with a homogeneous spatial distribution of plutonium. The plutonium content of the fuels also covers the whole range of interest for FNR applications: $y \in [0.24 - 1]$. As a consequence, the EU projects' data set can be used as a reference thermal conductivity data set.

Figure O.22 shows that the following data sets: Vasudeva Rao *et al.* (at $y = 0.40$), Van-Craeynest and Weilbacher (at $y = 0.2$), Duriez *et al.* (at $y = 0.06$) and TRUMOX (both at $y = 0.35$ and $y = 0.5$) yield twice lower thermal conductivity than the EU projects' data set, at approximately 800 K. Those discrepancies could not be explained by plutonium content, since the EU projects' cover $y \in [0.24 - 1]$. The discrepancies are higher at low temperatures (i. e. $T < 1200$ K). We can also observe that the whole data set of Duriez *et al.* (i. e. covering $y \in [0.03 - 0.15]$) systematically gives lower thermal conductivity values than the EU projects. The available information about the measurements of Duriez *et al.* [4] does not allow to identify the reason for those discrepancies. A possible explanation could be the different methods to extract thermal diffusivity from thermograms, used in Duriez *et al.* and the EU projects.

O.4 Synthesis and conclusions

We saw that an experimental dispersion of the order of 200 % is observed on thermal conductivity data, at the stoichiometric composition. We saw that this dispersion could not be explained by differences in plutonium content, since the EU projects' data set covers a wide range of plutonium contents, y $\in [0.24 - 1]$, within which the dispersion is way lower than 200 %. For some experimental data sets, we managed to give a hypothetical explanation for the discrepancies: self-irradiation damage, invalidity of the porosity correction model for high porosity or the presence of a non-negligible amount of americium. For other experimental data sets, a plausible scientific explanation for the discrepancies could not be provided, due to missing supplementary information about either the fuel microstructure (open, closed porosity,

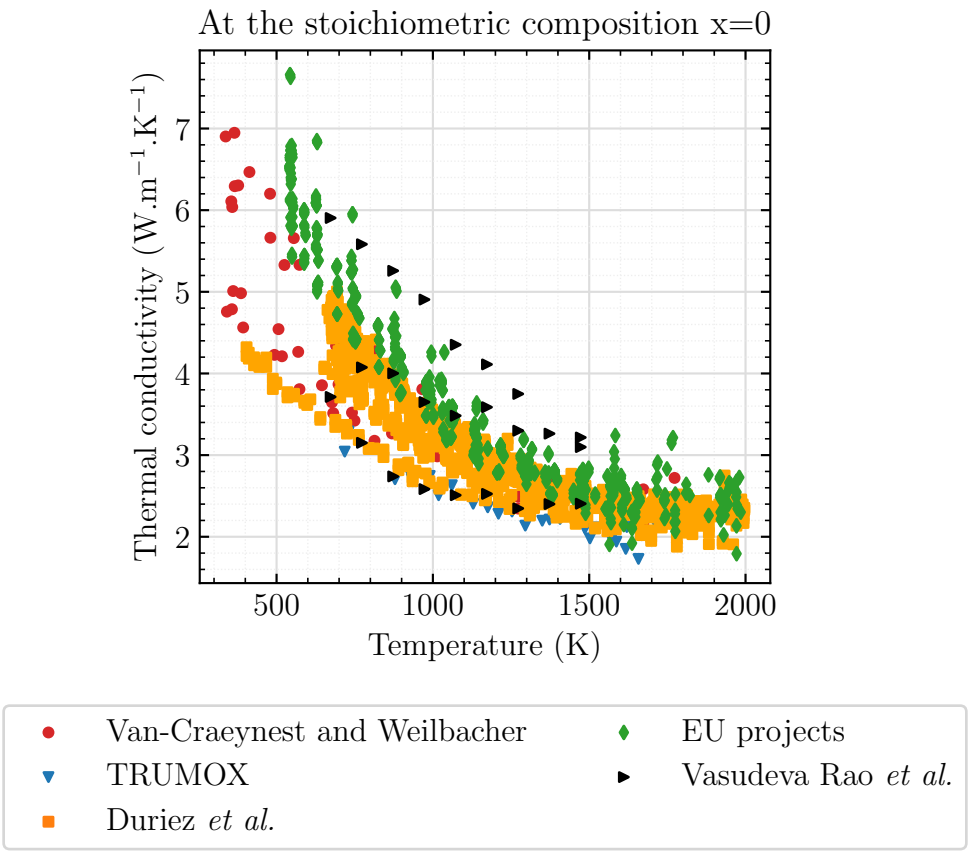

Figure O.22: Experimental variation of thermal conductivity with temperature, according to Van-Craeynest and Weilbacher [106], TRUMOX [private com.], Duriez *et al.* [4], Vasudeva Rao *et al.* [206] and EU projects [108, 109, 224].

crystal phases) or the measurement characteristics (heating or cooling cycles).

Overall, this analysis allowed us to observe how factors, other than plutonium and oxygen content or temperature can impact thermal conductivity in a significant manner. It was outside the scope of this work to focus on the effect of self-irradiation damage, high porosity or americium content on thermal conductivity. Ideally those phenomena have to be taken into account in thermal conductivity modeling, given their important impact. However, most of the time, the information, required to model them is missing in publications. For example, to develop a new model for the effect of self-irradiation damage or to simply use the model, proposed by Ikusawa *et al.* [225] or Staicu *et al.* [273], information about the fuel storage time is needed. This information is not provided in most papers. The same follows for the effect of americium. In most work, the americium content, present in the fuels is not characterized.

Other factors, such as grain boundaries, can also impact thermal conductivity. Indeed, in this work, as it was mentioned in Chapter 2, no analytical model has been identified for the effect of grain boundaries. Since no correction for grain boundaries is applied, the effective thermal conductivity (*i. e.* the measured one) intrinsically accounts for grain boundaries. This therefore adds a supplementary difficulty in extracting the fuel matrix thermal conductivity out

of effective thermal conductivity measurements. To provide the most accurate experimental estimate of thermal conductivity of the fuel matrix, measurements **must be performed on single crystals**.

In summary, to avoid issues, related to the interpretation of thermal conductivity due to radiation damage, americium content or grain boundaries, **thermal conductivity measurements should be performed**:

1. **at cooling**, once a first heating cycle has been performed. Heating until 1100 is sufficient, according to the model of Ikusawa *et al.* to recover self-irradiation damage. However, further heating the sample can lead to a reduction of the sample, therefore modifying its oxygen content at cooling. This is due to the MOX phase diagram.
2. on fuels, which have **not been stored for a long time after fabrication**. The latter increases both self-irradiation damage and americium content.
3. on single crystals.

List of Figures

List of Tables

List of Abbreviations

MOX	**M**ixed-**OX**ide
O/M	**O**xygen/**M**etal
SIMFUel	**SIM**ulated **FU**el
FP	**F**ission **P**roduct
FMP	**F**ive **M**etal **P**recipitates
GP	**G**rey **P**hase
FIMA	**F**ission per **I**nitial **M**etal **A**tom
PWR	**P**ressurized **W**ater **R**eactor
FNR	**F**ast **N**eutron **R**eactor
BOL	**B**eginning **O**f **L**ife
EOL	**E**nd **O**f **L**ife
MFP	**M**aximum **F**lux **P**lane
TFC	**T**op of the **F**issile **C**olumn
PIE	**P**ost-**I**rradiation **E**xamination
JOG	**J**oint **O**xyde-**G**aine
ROG	**R**éaction **O**xyde-**G**aine
FCCI	**F**uel **C**ladding **C**hemical **I**nteraction
SIMS	**S**econdary-**I**on **M**ass **S**pectrometry
EPMA	**E**lectron **P**robe **M**icro **A**nalysis
SEM	**S**canning **E**lectron **M**icroscopy
TEM	**T**ransmission **E**lectron **M**icroscopy
LSQR	**L**ea**S**t-**S**qua**R**es
FF	**F**actor **F**ixing
OAT	**O**ne **A**t a **T**ime

INTA-2 **IN**strumented **T**est **A**ssembly 2

JEPP **J**our **E**quivalent **P**leine **P**uissance

PLEIADES **P**late-forme **L**ogiciel pour les **E**lements **I**rradiés dans les **A**ssemblages, **D**emonstration, en **E**xpériminetation, ou en **S**ervice

Bibliography

[1] Pauline Fouquet-Métivier. *Study of the influence of americium on thermodynamic and structural properties of (U,Pu)O2±x mixed oxides*. Theses, Université Paris-Saclay, June 2022.

[2] Y Philipponneau. Thermal conductivity of $(U, Pu)O_2$, mixed oxide fuel. *Journal of Nuclear Materials 188*, pages 194–197, 1992.

[3] Masato Kato, Koji Maeda, Takayuki Ozawa, Motoaki Kashimura, and Yoshiyuki Kihara. Physical Properties and Irradiation Behavior Analysis of Np- and Am-Bearing MOX Fuels. *Journal of Nuclear Science and Technology*, 48(4):646–653, April 2011.

[4] Christian Duriez, Jean-Pierre Alessandri, Thierry Gervais, and Yannick Philipponneau. Thermal conductivity of hypostoichiometric low Pu content $(U, Pu)O_{2-x}$ mixed oxide. *Journal of Nuclear Materials*, page 16, 2000.

[5] Jean-Marc Bonnerot. Propriétés thermiques dex oxydes mixtes d'Uranium et de Plutonium. page 202.

[6] J.C. Van Craeynest and J.C. Weilbacher. Etude de la conductibilite thermique des oxydes mixtes d'uranium et de plutonium. *Journal of Nuclear Materials*, 26(1):132–136, April 1968.

[7] Marc Lainet, Bruno Michel, Jean-Christophe Dumas, Michel Pelletier, and Isabelle Ramière. GERMINAL, a fuel performance code of the PLEIADES platform to simulate the in-pile behaviour of mixed oxide fuel pins for sodium-cooled fast reactors. *Journal of Nuclear Materials*, 516:30–53, April 2019.

[8] B. Michel, I. Ramière, I. Viallard, C. Introini, M. Lainet, N. Chauvin, V. Marelle, A. Boulore, T. Helfer, R. Masson, J. Sercombe, J.C. Dumas, L. Noirot, and S. Bernaud. Two fuel performance codes of the PLEIADES platform: ALCYONE and GERMINAL. In *Nuclear Power Plant Design and Analysis Codes*, pages 207–233. Elsevier, 2021.

[9] https://www.gen-4.org/gif/jcms/c9260/public.

[10] Fast reactors, https://www.iaea.org/topics/fast-reactors, April 2016. Publisher: IAEA.

[11] Donald R Olander. Fundamental aspects of nuclear reactor fuel elements; published by technical information center. *Energy Research and Development Administration*, page 287, 1976.

[12] Réacteurs de 4e génération ,https://www.connaissancedesenergies.org/fiche-pedagogique/reacteurs-de-4e-generation. August 2014.

[13] Jeffrey Donovan. IAEA Bulletin: Nuclear power and the clean energy transition. Shrinking nuclear waste and increasing efficiency for a sustainable energy future. September 2020.

[14] Plutonium Management – PuMMA, https://pumma-h2020.eu/plutonium-management/.

[15] Jean-Louis Nigon and Gérard Le Bastard. Fabrication des combustibles au plutonium. *Génie nucléaire*, October 2002.

[16] R.D. Leggett. Oxide nuclear fuels. In RJ BROOK, editor, *Concise Encyclopedia of Advanced Ceramic Materials*, pages 337–340. Pergamon, Oxford, 1991.

[17] Stephen Novascone, Pavel Medvedev, John W. Peterson, Yongfeng Zhang, and Jason Hales. Modeling porosity migration in LWR and fast reactor MOX fuel using the finite element method. *Journal of Nuclear Materials*, 508:226–236, September 2018.

[18] Masaki Inoue, Koji Maeda, Kozo Katsuyama, Kosuke Tanaka, Kenji Mondo, and Masaki Hisada. Fuel-to-cladding gap evolution and its impact on thermal performance of high burnup fast reactor type uranium–plutonium oxide fuel pins. *Journal of Nuclear Materials*, 326(1):59–73, March 2004.

[19] Kozo Katsuyama, Tsuyoshi Nagamine, Shin-ichiro Matsumoto, and Masahiko Ito. Measurement of Central Void Diameter in FBR MOX Fuel by X-Ray Computer Tomography. *Journal of Nuclear Science and Technology*, 39(7):804–806, July 2002.

[20] M. Temmar, B. Michel, I. Ramiere, and N. Favrie. Multi-physics modelling of the pellet-to-cladding gap closure phenomenon for SFR fuel performance codes. *Journal of Nuclear Materials*, 529:151909, February 2020.

[21] Kosuke Tanaka, Shuhei Miwa, Shin-ichi Sekine, Hiroshi Yoshimochi, Hiroshi Obayashi, and Shin-ichi Koyama. Restructuring and redistribution of actinides in Am-MOX fuel during the first 24h of irradiation. *Journal of Nuclear Materials*, 440(1-3):480–488, September 2013.

[22] Jérôme Lamontagne, Philippe Martin, and Dragos Staicu. Preparing ESNII for Horizon 2020. Deliverable D732: NESTOR-3 experiment: Destructive Post-Irradiation Examinations on Pin 110. Technical Report Grant agreement no: 605172.

[23] C.N. Venkiteswaran, V.V. Jayaraj, B.K. Ojha, V. Anandaraj, M. Padalakshmi, S. Vinodkumar, V. Karthik, Ran Vijaykumar, A. Vijayaraghavan, R. Divakar, T. Johny, Jojo Joseph, S. Thirunavakkarasu, T. Saravanan, John Philip, B.P.C. Rao, K.V. Kasiviswanathan, and T. Jayakumar. Irradiation performance of PFBR MOX fuel after 112GWd/t burn-up. *Journal of Nuclear Materials*, 449(1-3):31–38, June 2014.

[24] P. Bonev, N. Chauvin, D. Staicu, E. Dahms, G. Montagnier, D. Papaioannou, J-C. Dumas, I. Boukhris, I. Viallard, M. Lainet, J. Lamontagne, and K. Hanifi. New recommendation for the thermal conductivity of irradiated (U, Pu)O2 fuels under fast reactor conditions. Comparison with recent experimental data. *Journal of Nuclear Materials*, 577:154326, April 2023.

[25] Dragos Staicu. ESNII+ : Preparing ESNII for Horizon 2020 : Deliverable D742 : Properties measurements on irradiated fuels (NESTOR 3). Technical report, September 2017.

[26] F. Cappia, K. Tanaka, M. Kato, K. McClellan, and J. Harp. Post-irradiation examinations of annular mixed oxide fuels with average burnup 4 and 5% FIMA. *Journal of Nuclear Materials*, 533:152076, May 2020.

[27] Riley J. Parrish, Fabiola Cappia, and Assel Aitkaliyeva. Comparison of the radial effects of burnup on fast reactor MOX fuel microstructure and solid fission products. *Journal of Nuclear Materials*, 531:152003, April 2020.

[28] Valentino Di Marcello, Vincenzo Rondinella, Arndt Schubert, Jacques Van De Laar, and Paul Van Uffelen. Modelling actinide redistribution in mixed oxide fuel for sodium fast reactors. *Progress in Nuclear Energy*, 72:83–90, April 2014.

[29] M. Bober, G. Schumacher, and D. Geithoff. Plutonium redistribution in fast reactor mixed oxide fuel pins. *Journal of Nuclear Materials*, 47(2):187–197, June 1973.

[30] Dragos Staicu. MOX fuel safety and performances, March 2021.

[31] V. Marelle, P. Goldbronn, S. Bernaud, E. Castelier, J. Julien, K. Nkonga, L. Noirot, and I. Ramiere. New developments in alcyone 2.0 fuel performance code.

[32] P.G Lucuta, Hj Matzke, and I.J Hastings. A pragmatic approach to modelling thermal conductivity of irradiated UO2 fuel : review and recommendations. *Journal of Nuclear Materials 232 (1996)*, pages 166–180.

[33] A Magni. Modelling and assessment of thermal conductivity and melting behaviour of MOX fuel for fast reactor applications. *Journal of Nuclear Materials*, page 13, 2020.

[34] Riley Parrish and Assel Aitkaliyeva. A review of microstructural features in fast reactor mixed oxide fuels. *Journal of Nuclear Materials*, 510:644–660, November 2018.

[35] Donald R. Olander. *Fundamental aspects of nuclear reactor fuel elements: prepared for the Division of Reactor Development and Demonstration, Energy Research and Development Administration*. Technical Information Center, Office of Public Affairs, Energy Research and Development Administration ; available [from] National Technical Information Service, U.S. Dept. of Commerce, Oak Ridge, Tenn. : Springfield, Va, 1976.

[36] P.G Lucuta, Hj Matzke, and R.A Verall. Modelling of UO2-based SIMFUEL thermal conductivity. The effect of burn-up. *Journal of Nuclear Materials 217 (1994)*, pages 279–286.

[37] P.G Lucuta, Hj Matzke, R.A Verall, and H.A Tasman. Thermal conductivity of SIMFUEL. *Journal of Nuclear Materials 188 (1992)*, pages 198–204.

[38] Rafael Caprani, Philippe Martin, Damien Prieur, Julien Martinez, Myrtille O.J.Y. Hunault, Florent Lebreton, Marie-Margaux Desagulier, Camille Aloin, Loic Picard, Méghan Alibert, Guillaume Gabriel, Patrice Signoret, and Nicolas Clavier. Fission products speciation in nuclear fuel: Synthesis and characterisation of mixed oxide (U,Pu)O2 SIMfuel. *Journal of Nuclear Materials*, 585:154607, November 2023.

[39] S.M Hartlib. Simulated Burnt Mixed Oxide Fuel: Preparation Creep and Thermal Diffusivity. *Harwell Report AERE-R.7325*, April 1973.

[40] Leslie Burris and Ira G. Dillon. Estimation of fission product spectra in discharged fuel from fast reactors. Technical Report ANL-5742, Argonne National Laboratory, July 1957.

[41] P.W Winter and D.A MacInnes. Meeting on Water Reactor Fuel Element Computer Modelling in Steady-State, Transient and Accident Conditions. IAEA Tech. Comm, Preston, UK, 1988.

[42] K. Yamamoto, T. Hirosawa, K. Yoshikawa, K. Morozumi, and S. Nomura. Melting temperature and thermal conductivity of irradiated mixed oxide fuel. *Journal of Nuclear Materials*, 204:85–92, September 1993.

[43] Koji Maeda and Takeo Asaga. Change of fuel-to-cladding gap width with the burn-up in FBR MOX fuel irradiated to high burn-up. *Journal of Nuclear Materials*, 2004.

[44] Karl Samuelsson, Jean-Christophe Dumas, Bo Sundman, Jérôme Lamontagne, and Christine Guéneau. Simulation of the chemical state of high burnup (U , Pu) O 2 fuel in fast reactors based on thermodynamic calculations. *Journal of Nuclear Materials*, 532:151969, April 2020.

[45] Y. Guerin. Fuel Performance of Fast Spectrum Oxide Fuel. In *Comprehensive Nuclear Materials 2.21*.

[46] Karl Samuelsson, Jean-Christophe Dumas, Bo Sundman, and Marc Lainet. An improved method to evaluate the "Joint Oxyde-Gaine" formation in (U,Pu)O $_2$ irradiated fuels using the GERMINAL V2 code coupled to Calphad thermodynamic computations. *EPJ Nuclear Sciences & Technologies*, 6:47, 2020.

[47] David H. Hurley, Anter El-Azab, Matthew S. Bryan, Michael W. D. Cooper, Cody A. Dennett, Krzysztof Gofryk, Lingfeng He, Marat Khafizov, Gerard H. Lander, Michael E. Manley, J. Matthew Mann, Chris A. Marianetti, Karl Rickert, Farida A. Selim, Michael R. Tonks, and Janelle P. Wharry. Thermal energy transport in oxide nuclear fuel. *Chemical Reviews*, 122(3):3711–3762, 2022. PMID: 34919381.

[48] X.-Y. Liu, M. W. D. Cooper, K. J. McClellan, J. C. Lashley, D. D. Byler, B. D. C. Bell, R. W. Grimes, C. R. Stanek, and D. A. Andersson. Molecular dynamics simulation of thermal transport in uo_2 containing uranium, oxygen, and fission-product defects. *Phys. Rev. Appl.*, 6:044015, Oct 2016.

[49] Miaomiao Jin, Cody A. Dennett, David H. Hurley, and Marat Khafizov. Impact of small defects and dislocation loops on phonon scattering and thermal transport in ThO_2. *Journal of Nuclear Materials*, 566:153758, August 2022.

[50] Katherine Mitchell, Jungkyu Park, Alex Resnick, Hunter Horner, and Eduardo B. Farfan. Phonon scattering and thermal conductivity of actinide oxides with defects. *Applied Sciences*, 10(5), 2020.

[51] B. Deng, A. Chernatynskiy, P. Shukla, S.B. Sinnott, and S.R. Phillpot. Effects of edge dislocations on thermal transport in uo2. *Journal of Nuclear Materials*, 434(1):203–209, 2013. Special Section on Spent Nuclear Fuel.

[52] Arthur L. Loeb. Thermal Conductivity: VIII, A Theory of Thermal Conductivity of Porous Materials. *Journal of the American Ceramic Society*, 37(2):96–99, February 1954.

[53] Brigitte Schulz. Thermal conductivity of porous and highly porous materials. page 12.

[54] G. Ondracek and B. Schulz. The porosity dependence of the thermal conductivity for nuclear fuels. *Journal of Nuclear Materials*, 46(3):253–258, April 1973.

[55] G. Ondracek and B. Schulz. Technical Report Berichte DKG, 48, 1971.

[56] G. Ondracek and B. Schulz. Technical Report KFK 1272/3, Ber. des Kernforschungszentrums Karlsruhe, 1972.

[57] H. Kämpf and G. Karsten. Effects of different types of void volumes on the radial temperature distribution of fuel pins. *Nuclear Applications and Technology*, 9(3):288–300, 1970.

[58] Jean Claude Van Craeynest and Jean Pierre Stora. Effet de la porosite sur la variation de conductibilite thermique du bioxyde d'uranium en fonction de la temperature. *Journal of Nuclear Materials*, 37(2):153–158, November 1970.

[59] R. Brandt and G. Neuer. Thermal Conductivity and Thermal Radiation Properties of UO 2. *Journal of Non-Equilibrium Thermodynamics*, 1(1), 1976.

[60] G.P. Marino. The porosity correction factor for the thermal conductivity of ceramic fuels. *Journal of Nuclear Materials*, 38(2):178–190, February 1971.

[61] G.P.Marino. Radiation transfer across a spherical pore in a linear temperature gradient. *Transactions of the metallurgical society of AIME, Vol. 245, April 1969-821*, pages 821–823, April 1969.

[62] J. Belle, R.M Berman, W.F Bourgeois, I Cohen, and R.C Daniel. Thermal conductivity of bulk oxide fuels, United States: N. p., 1967 WAPD-TM-586(Rev.), April 1967.

[63] D.R. Flynn. Thermal conductivity of Ceramics. In *Mechanical and Thermal Properties of Ceramics. Proceedings of a Symposium.*, pages 63–123. Gaithersburg, Maryland, j.b. wachtman, jr. edition, April 1968.

[64] A.E. Powers. Technical Report KAPL-2145/TUD (16th edition), 1970.

[65] Y Takahashi, M Murabayashi, Y Akimoto, and T Mukaibo. Uranium mononitride: heat capacity and thermal conductivity from 298 to 1000 k. *J. Nucl. Mater. 38: 303-8(Mar 1971).*

[66] Walter Niesel. Die dielektrizitätskonstanten heterogener mischkörper aus isotropen und anisotropen substanzen. *Annalen der Physik*, 445(6-7):336–348, 1952.

[67] Hugo Fricke. A Mathematical Treatment of the Electric Conductivity and Capacity of Disperse Systems I. The Electric Conductivity of a Suspension of Homogeneous Spheroids. *Physical Review*, 24(5):575–587, November 1924.

[68] Léo Moutin, Joane Meynard, Marc Josien, Michel Bornert, Christelle Duguay, Frédéric Adenot, Vincent Bouineau, Laurent Fayette, and Renaud Masson. Realistic morphological models of weakly to strongly branched pore networks for the computation of effective properties. *International Journal of Solids and Structures*, 275:112249, July 2023.

[69] Joane Meynard, Marcelle Ibrahim, Arnaud Monnier, Michel Bornert, Etienne Castelier, Christelle Duguay, Mihail Gărăjeu, and Renaud Masson. Effective properties of an isotropic solid weakened by micro-cracks located at inter-granular boundaries. *Journal of the Mechanics and Physics of Solids*, 158:104647, January 2022.

[70] Tristan Calvet, Jean-Mathieu Vanson, and Renaud Masson. A DEM/FFT approach to simulate the effective thermal conductivity of granular media. *International Journal of Thermal Sciences*, 172:107339, February 2022.

[71] Tommaso Barani, Isabelle Ramière, and Bruno Michel. Analysis of fabrication and crack-induced porosity migration in mixed oxide fuels for sodium fast reactors by the finite element method. *Journal of Nuclear Materials*, 558:153341, January 2022.

[72] Fabiola Cappia and Jason Harp. Microstructural and chemical characterization of medium burnup fast reactor MOX using electron microscopy. Technical Report INL/EXT–21-61757, 1784764, February 2021.

[73] C.-W. Lee, A. Chernatynskiy, P. Shukla, R.E. Stoller, S.B. Sinnott, and S.R. Phillpot. Effect of pores and he bubbles on the thermal transport properties of uo2 by molecular dynamics simulation. *Journal of Nuclear Materials*, 456:253–259, 2015.

[74] Weiming Chen, Michael Cooper, Ziqi Xiao, David Andersson, and Xian-Ming Bai. Effect of xe bubble size and pressure on the thermal conductivity of uo2—a molecular dynamics study. *Journal of Materials Research*, 34:1–11, 04 2019.

[75] Paul C. Millett, Dieter Wolf, Tapan Desai, Srujan Rokkam, and Anter El-Azab. Phase-field simulation of thermal conductivity in porous polycrystalline microstructures. *Journal of Applied Physics*, 104(3):033512, August 2008.

[76] Paul C. Millett and Michael Tonks. Meso-scale modeling of the influence of intergranular gas bubbles on effective thermal conductivity. *Journal of Nuclear Materials*, 412(3):281–286, May 2011.

[77] Paul C. Millett, Michael R. Tonks, K. Chockalingam, Yongfeng Zhang, and S.B. Biner. Three dimensional calculations of the effective Kapitza resistance of UO_2 grain boundaries containing intergranular bubbles. *Journal of Nuclear Materials*, 439(1-3):117–122, August 2013.

[78] M. Serizawa, H. Kaneko, Y. Yokouchi, and M. Koizumi. Thermal diffusivity and thermal conductivity of uranium-plutonium dioxide. *Journal of Nuclear Materials*, 34(2):224–226, February 1970.

[79] Juan J Carbajo, Gradyon L Yoder, Sergey G Popov, and Victor K Ivanov. A review of the thermophysical properties of MOX and UO2 fuels. *Journal of Nuclear Materials*, page 18, 2001.

[80] Kyoichi Morimoto, Masato Kato, Masahiro Ogasawara, and Motoaki Kashimura. Thermal conductivity of (U,Pu,Np)O2 solid solutions. *Journal of Nuclear Materials*, 389(1):179–185, May 2009.

[81] Kyoichi Morimoto, Masato Kato, Masahiro Ogasawara, Motoaki Kashimura, and Tomoyuki Abe. Thermal conductivities of (U, Pu, Am)O2 solid solutions. *Journal of Alloys and Compounds*, 452(1):54–60, March 2008.

[82] Kyoichi Morimoto, Masato Kato, Masahiro Ogasawara, and Motoaki Kashimura. Thermal conductivities of hypostoichiometric $(U, Pu, Am)O_{2-x}$ oxide. *Journal of Nuclear Materials*, 374(3):378–385, March 2008.

[83] F A Nichols. Review transport phenomena in nuclear fuels under severe temperature gradients. *Journal Of Nuclear Materials 84*, pages 1–25, 1979.

[84] J. Noirot, L. Desgranges, and J. Lamontagne. Detailed characterisations of high burn-up structures in oxide fuels. *Journal of Nuclear Materials*, 372(2-3):318–339, January 2008.

[85] J.C.Maxwell. *A treatise on Electricity and Magnetism*, volume Vol. I.

[86] J.C.Maxwell. *A treatise on Electricity and Magnetism*, volume Vol.2.

[87] J K Fink. Thermophysical properties of uranium dioxide. *Journal of Nuclear Materials*, page 18, 2000.

[88] W.G. Luscher and Kenneth J. Geelhood. Material Property Correlations: Comparisons between FRAPCON-3.5, FRAPTRAN-1.5, and MATPRO. Technical Report NUREG/CR-7024 Rev.1, PNNL-19417, Rev. 1, U.S.NRC.

[89] Alexander L Lindsay and LeRoy A Bromley. Thermal Conductivity of Gas Mixtures. 42(8):4, 1950.

[90] Richard S. Brokaw. Approximate Formulas for the Viscosity and Thermal Conductivity of Gas Mixtures. *The Journal of Chemical Physics*, 29(2):391–397, August 1958.

[91] A.M. Arnaud and L.Roche. Echanges thermiques dans une lame gazeuse coefficient d'échange thermique entre combustible et gaine, 1977.

[92] C. M. Allison, G. A. Berna, R. Chambers, E. W. Coryell, K. L. Davis, D. L. Hagrman, D. T. Hagrman, N. L. Hampton, J. K. Hohorst, R. E. Mason, M. L. McComas, K. A. McNeil, R. L. Miller, C. S. Olsen, G. A. Reymann, and L. J. Siefken. SCDAP/RELAP5/MOD3.1 code manual, volume IV: MATPRO-A library of materials properties for light-water-reactor accident analysis. Technical Report NUREG/CR-6150, EGG-2720, Idaho National Engineering Laboratory, 1993.

[93] K. Lassmann and F. Hohlefeld. The revised URGAP model to describe the gap conductance between fuel and cladding. *Nuclear Engineering and Design*, 103(2):215–221, August 1987.

[94] WG Luscher, KJ Geelhood, and IE Porter. Comparisons between FRAPCON-4.0, FRAPTRAN-2.0, and MATPRO. *Division of System Analysis Office of Nuclear Regulatory Research U.S. Nuclear Regulatory Commission.*

[95] A. Eucken. Thermal conductivity of ceramics refractory materials. *Forsch. Gebiete Ingenieur, Vol. B-3, Forschung Sheft N 353*, pages 6–21, 1932.

[96] Shinsuke Yamanaka, Tsuyoshi Hamaguchi, Taku Oyama, Tetsushi Matsuda, Shin-ichi Kobayashi, and Ken Kurosaki. Heat capacities and thermal conductivities of perovskite type BaZrO3 and BaCeO3. *Journal of Alloys and Compounds*, page 4, 2003.

[97] Shinsuke Yamanaka and Ken Kurosaki. Thermophysical properties of Mo–Ru–Rh–Pd alloys. *Journal of Alloys and Compounds*, 353(1-2):269–273, April 2003.

[98] Susumu Fukushima, Toshihiko Ohmichi, Atsushi Maeda, and Muneo Handa. Thermal conductivity of $(Pu, Nd)O_2$ and $(Pu, Y)O_2$ solid solutions. page 10.

[99] Fukushima, Toshihiko Ohmichi, Atsushi Maeda, and Muneo Handa. Thermal conductivity of near-stoichiometric (U, Pu, Nd)O2 and (U, Pu, Eu)O2 solid solutions. *Journal of Nuclear Materials 116 (1983)*, pages 287–296, 1983.

[100] S. Fukushima, Toshihiko Ohmichi, and Muneo Handa. The effect of rare earths on thermal conductivity of uranium, plutonium and their mixed oxide fuels. *Journal of the Less-Common Metals 121*, pages 631–636, 1986.

[101] Susumu Fukushima, Toshihiko Ohmichi, Atsushi Maeda, and Hitoshi Watanabe. The effect of gadolinium content on the thermal conductivity of near-stoichiometric (U,Gd)O2 solid solutions. *Journal of Nuclear Materials*, 105(2-3):201–210, February 1982.

[102] S. Fukushima, Toshihiko Ohmichi, Atsushi Maeda, and Hitoshi Watanabe. The effect of Yttrium content on the thermal conductivity of near-stoichiometric (U,Y)O2 solid solutions. *Journal of Nuclear Materials 102*, pages 30–39, 1981.

[103] Ken Kurosaki, Ryo Ohshima, Masayoshi Uno, Shinsuke Yamanaka, Kazuya Yamamoto, and Takashi Namekawa. Thermal conductivity of (U,Ce)O2 with and without Nd or Zr. *Journal of Nuclear Materials*, 294(1-2):193–197, April 2001.

[104] R. Ducroux and Ph. Jean Baptiste. Mesure du potentiel d'oxygène dans le système $(U_{0.7}, Ce_{0.3})O_2$ à l'aide d'une minisonde à l'électrolyte solide. *Journal of Nuclear Materials 97*, pages 333–336, 1981.

[105] R.L. Gibby. The effect of plutonium on the thermal conductivity of $(U, Pu)O_2$ solid solutions. *Journal of Nuclear Materials 38*, pages 163–177, 1971.

[106] Jean-Claude Van Craeynest and Jean-Claude Weilbacher. Etude de la conductibilité thermique des oxydes mixtes d'uranium et de plutonium. Technical Report CEA-R-3488, CEA Fontenay-aux-Roses.

[107] Masaki Inoue. Thermal conductivity of uranium–plutonium oxide fuel for fast reactors. *Journal of Nuclear Materials*, 282(2-3):186–195, December 2000.

[108] Joel Guidez, Janos Bodi, Konstantin Mikityuk, and Enrico Girardi. Chapter 11 - ESFR SMART: A european sodium fast reactor concept including the european feedback experience and the new safety commitments following fukushima accident. In Igor L. Pioro, editor, *Handbook of Generation IV Nuclear Reactors (Second Edition)*, Woodhead Publishing Series in Energy, pages 355–393. Woodhead Publishing, second edition edition, 2023.

[109] Plutonium Management for More Agility: https://cordis.europa.eu/project/id/945022.

[110] B. Rabu. Post-Irradiation Examinations on PHENIX axially heterogeneous pins relevant to ASTRID fuel design: ZEBRE and PAVIX irradiations. *Proc. of ACTINIDES 2013 Conference*, 2013.

[111] J. Guidez, P. Chaucheprat, B. Fontaine, E. Brunon, L. Martin, D. Warin, A. Zaetta, and Sudreau. Phenix: the irradiation program for transmutaton experiments.

[112] J. Somers, J.P Glatz, D. Haas, D.H. Wegen, S. Fourcaudot, C. Fuchs, A. Stalios, D. Plancq, and G. Muehling. Status of the TRABANT Irradiation Experiments. *American Nuclear Society*, 1999.

[113] I. Cheik Njifon and E. Torres. Phonons and thermophysical properties of $(U, Pu)O_2$ mixed oxide (MOX) fuels. *Journal of Nuclear Materials*, 537:152158, August 2020.

[114] Marat Khafizov, Janne Pakarinen, Lingfeng He, and David H. Hurley. Impact of irradiation induced dislocation loops on thermal conductivity in ceramics. *Journal of the American Ceramic Society*, 102(12):7533–7542, December 2019.

[115] Philip D. Thacher. Effect of Boundaries and Isotopes on the Thermal Conductivity of LiF. *Physical Review*, 156(3):975–988, April 1967.

[116] Paul G. Klemens. Thermal conductivity and lattice vibrational modes. *Solid State Physics*, pages 1–98, 1958.

[117] R.L Gibby. The thermal diffusivity and thermal conductivity of stoichiometric $(U_{0.8}, Pu_{0.2})O_2$. Technical Report BNWL-704, UC-25, Metals, Ceramics and Materials, Pacific Northwest Laboratory, May 1968.

[118] A.B.G. Washington. Technical Report UKAEA Report TRG Report 2236(D), 1973.

[119] R. Berman. *Thermal Conduction in Solids*. Oxford Science Publications. Clarendon Press, 1979.

[120] Donald T. Morelli and Glen A. Slack. High Lattice Thermal Conductivity Solids. In Subhash L. Shindé and Jitendra S. Goela, editors, *High Thermal Conductivity Materials*, pages 37–68. Springer New York, New York, NY, 2006.

[121] Joseph Callaway. Model for Lattice Thermal Conductivity at Low Temperatures. *Physical Review*, 113(4):1046–1051, February 1959.

[122] R.L Gibby. The effect of oxygen stoichiometry on the thermal diffusivity and conductivity of U0.75Pu0.25O2-x. Technical Report BNWL-927, UC-25, Metals, Ceramics and Materials, Batelle Memorial Institute, January 1969.

[123] P G Klemens. The Scattering of Low-Frequency Lattice Waves by Static Imperfections. *Proceedings of the Physical Society. Section A*, 68(12):1113–1128, December 1955.

[124] V. Ambegaokar. Thermal Resistance due to Isotopes at High Temperatures. *Physical Review*, 114(2):488–489, April 1959.

[125] Carl L. Julian. Theory of Heat Conduction in Rare-Gas Crystals. *Physical Review*, 137(1A):A128–A137, January 1965.

[126] Shun Hirooka and Masato Kato. Sound speeds in and mechanical properties of $(U, Pu)O_2$. *Journal of Nuclear Science and Technology*, 55(3):356–362, March 2018.

[127] Masato Kato, Yoshihisa Ikusawa, Takeo Sunaoshi, Andrew T. Nelson, and Kenneth J. McClellan. Thermal expansion measurement of $(U, Pu)O_{2-x}$ in oxygen partial pressure-controlled atmosphere. *Journal of Nuclear Materials*, 469:223–227, February 2016.

[128] Hiroyuki Serizawa, Kousaku Fukuda, Tetuo Shiratori, Takeo Fujino, Nobuaki Sato, and Kohta Yamada. Unusual variation of temperature factor of uranium dioxide at high temperature. *Journal of Alloys and Compounds*, 271-273:386–390, June 1998.

[129] Hiroyuki Serizawa, Yasuo Arai, and Yasufumi Suzuki. Simultaneous determination of X-ray Debye temperature and Grüneisen constant for actinide dioxides: PuO_2 and ThO_2. *Journal of Nuclear Materials*, 280(1):99–105, June 2000.

[130] R.B.Roof Jr. An experimental determination of the characteristic temperature for PuO_2. *Journal of Nuclear Materials 2, No.1 (1960) 39-42*, October 1959.

[131] Neutron diffraction studies of the actinide oxides I. Uranium dioxide and thorium dioxide at room temperature. *Proceedings of the Royal Society of London. Series A. Mathematical and Physical Sciences*, 274(1356):122–133, June 1963.

[132] J.B Ainscough and M/J Wheeler. *Brit.J.Appl.Physc.Ser., 2(1) (1968)*, page 853.

[133] C. Guéneau, M. Baichi, D. Labroche, C. Chatillon, and B. Sundman. Thermodynamic assessment of the uranium–oxygen system. *Journal of Nuclear Materials*, 304(2-3):161–175, August 2002.

[134] Christine Guéneau, Nathalie Dupin, Bo Sundman, Chantal Martial, Jean-Christophe Dumas, Stéphane Gossé, Sylvie Chatain, Franck De Bruycker, Dario Manara, and Rudy J.M. Konings. Thermodynamic modelling of advanced oxide and carbide nuclear fuels: Description of the U–Pu–O–C systems. *Journal of Nuclear Materials*, 419(1-3):145–167, December 2011.

[135] M Yann LE Romain Vauchy. Etude du rapport O/M dans des nouveaux combustibles oxydes à base d'U et Pu : élaboration et caractérisation de matériaux modèles $(U, Pu)O_{2-x}$. page 186.

[136] Thibaut Truphémus, Renaud C. Belin, Jean-Christophe Richaud, Muriel Reynaud, Marie-Annick Martinez, Isabelle Félines, Antoine Arredondo, Audrey Miard, Thierry Dubois, Frédéric Adenot, and Jacques Rogez. Structural studies of the phase separation in the UO_2˘PuO_2˘Pu_2O_3 ternary system. *Journal of Nuclear Materials*, 432(1-3):378–387, January 2013.

[137] Gunther Leibfried and Ernst Schlomann. Warmeleitung in elektrisch isolierenden Kristallen, May 1954.

[138] G.A. Slack. Nonmetallic crystals with high thermal conductivity. *Journal of Physics and Chemistry of Solids*, pages 321–335, 1973.

[139] O.L. Anderson. The debye temperature of vitreous silica. *Journal of Physics and Chemistry of Solids*, 12(1):41–52, December 1959.

[140] Andrea Saltelli, Ksenia Aleksankina, William Becker, Pamela Fennell, Federico Ferretti, Niels Holst, Sushan Li, and Qiongli Wu. Why so many published sensitivity analyses are false: A systematic review of sensitivity analysis practices. *Environmental Modelling & Software*, 114:29–39, April 2019.

[141] Sassi Ben Nasrallah, Fethi Albouchi, and Foued Mzali. Measurement of the Effective Thermal Conductivity of Powders Using a Three-Layer Structure. *Journal of Porous Media*, 10(6):537–550, 2007.

[142] Frédéric Chevy. Bose Polarons that Strongly Interact. *Physics*, 9:86, July 2016.

[143] C R A Catlow and N.C Pyper. A theoretical study of the electronic and valence properties of (U,Pu)O2. *Journal of Nuclear Materials 80 (1979)*, pages 110–114.

[144] Gregory Geneste, Francois Bottin, and Marc Torrent. Oxygen vacancies and self-trapped electronic polarons in PuO_2. page 15.

[145] P.J.Price. Cxxxv. ambipolar thermodiffusion of electrons and holes in semiconductors. *The London, Edinburgh, and Dublin Philosophical Magazine and Journal of Science*, 46(382):1252–1260, 1955.

[146] T.C. Harman and J.M Honig. *Thermoelectric and thermomagnetic effects and applications.* McGraw-Hill Book Company, Lincoln Laboratory (Massachusetts Institute of Technology).

[147] G.J. Hyland. Thermal conductivity of solid UO_2: Critique and recommendation. *Journal of Nuclear Materials*, 113(2-3):125–132, January 1983.

[148] R. Franz and G. Wiedemann. Ueber die wärme-leitungsfähigkeit der metalle. *Annalen der Physik*, 165(8):497–531, 1853.

[149] A R Massih. Electronic transport in pure and doped UO_2. *Journal of Nuclear Materials*, page 17, 2017.

[150] P.W. Winter. The electronic transport properties of UO_2. *Journal of Nuclear Materials 161 (1989) 38-43 North-Holland, Amsterdam.*

[151] T.R. Pavlov, M.R. Wenman, L. Vlahovic, D. Robba, R.J.M. Konings, P. Van Uffelen, and R.W. Grimes. Measurement and interpretation of the thermo-physical properties of UO_2 at high temperatures: The viral effect of oxygen defects. *Acta Materialia*, 139:138–154, October 2017.

[152] G. Delette and M. Charles. Fuel thermal performance. In *IAEA-TECDOC-957 : Water reactor fuel element modelling at high burnup and its experimental support*, Proceedings of a Technical Commitee meeting held in Windermere, United Kingdrom. 1994.

[153] Robert R. Heikes and Roland W. Ure. *Thermoelectricity: science and engineering.* Number 576 p. Interscience Publishers, New York, 1961.

[154] N.J. Dudney, R.L. Coble, and H.L. Tuller. Electrical Conductivity of Pure and Yttria-Doped Uranium Dioxide. *Journal of the American Ceramic Society*, 64(11):627–631, November 1981.

[155] I.G Lang and Y.A Firsov. Kinetic theory of semiconductors with low mobility. *Sov. Phys. JETP 16 (1963)*, pages 1301 – 1312.

[156] Anuj Bhargava, Cindy Y. Chen, Kapil Dhaka, Yuan Yao, Andrew Nelson, Kenneth D. Finkelstein, Christopher J. Pollock, Maytal Caspary Toroker, and Richard D. Robinson. Mn Cations Control Electronic Transport in Spinel $Co_xMn_{3-x}O_4$ Nanoparticles. *Chemistry of Materials*, 31(11):4228–4233, June 2019.

[157] Anuj Bhargava, Roni Eppstein, Jiaxin Sun, Michelle A. Smeaton, Hanjong Paik, Lena F. Kourkoutis, Darrell G. Schlom, Maytal Caspary Toroker, and Richard D. Robinson. Breakdown of the Small-Polaron Hopping Model in Higher-Order Spinels. *Advanced Materials*, 32(49):2004490, December 2020.

[158] Richard A. Swalin. *Thermodynamics of solids*. University of Minnesota, second edition.

[159] Takeo Fujino, Toshiyuki Yamashita, Kinji Ohuchi, Keiji Naito, and Toshihide Tsuji. High temperature electrical conductivity and conduction mechanism of $(U, Pu)O_2$ at low oxygen partial pressures. *Journal of Nuclear Materials*, 202(1-2):154–162, June 1993.

[160] T.L Markin and E.J. Mclever. *Plutonium 1965 : Proceedings of the Third International Conference on Plutonium*, pages 845–857, 1965.

[161] Masahiko Osaka, Ken Kurosaki, and Shinsuke Yamanaka. Chemical thermodynamic analysis of americium-containing UO_2 and $(U, Pu)O_2$. *Journal of Alloys and Compounds*, 428(1-2):355–361, January 2007.

[162] F. Schmitz, Y. Couty, and R. Lindner. Electrical conductivity of $(U, Pu)O_2$ in the pure state and with addition of molybdenum., 1976.

[163] M. Kurihara, J. Abe, S Fukushima, and J. Shimokawa. Some electrical properties of the uranium-plutonium mixed oxides.

[164] T. Yamashita, Kinji Ohuchi, Takeo Fujino, Keiji Naito, Toshihide Tsuji, M. Abe, T. Yamamoto, M. Sato, and K. Ando. High temperature electrical conductivities of UO_2-PuO_2 solid solutions.

[165] Daniel Petit and Denis Maillet. Techniques inverses et estimation de paramètres. Partie 1. *Techniques de l'Ingénieur, Sciences fondamentales, Physique-Chimie*, 2008.

[166] Daniel Petit and Denis Maillet. Techniques inverses et estimation de paramètres. Partie 2. *Techniques de l'Ingénieur, Sciences fondamentales, Physique-Chimie*, 2019.

[167] Adrien François. *Estimation of the thermal performance of building walls and thermal bridges using active infrared thermography and inverse techniques*. PhD thesis, Paris Est, December 2020.

[168] Kenneth Levenberg. A method for the solution of certain non-linear problems in least squares. *Quart. Appl. Math. 2*, pages 164–168, 1944.

[169] Donald W. Marquardt. An algorithm for least-squares estimation of nonlinear parameters. *Journal of the Society for Industrial and Applied Mathematics*, 11(2):431–441, 1963.

[170] Frank Vanden Berghen. Levenberg-Marquardt algorithms vs Trust Region algorithms.

[171] P. Ruello, K.D. Becker, K. Ullrich, L. Desgranges, C. Petot, and G. Petot-Ervas. Thermal variation of the optical absorption of UO_2: determination of the small polaron self-energy. *Journal of Nuclear Materials*, 328(1):46–54, June 2004.

[172] H L Tuller and A S Nowick. Small polaron electron transport in reduced CeO, single crystals. page 9.

[173] A. Al-Shahrani, A. Al-Hajry, and M. M. El-Desoky. Non-adiabatic small polaron hopping conduction in sodium borate tungstate glasses. *physica status solidi (a)*, 200(2):378–387, December 2003.

[174] J Lago, P D Battle, M J Rosseinsky, A I Coldea, and J Singleton. Non-adiabatic small polaron hopping in the $n = 3$ Ruddlesden–Popper compound $Ca_4Mn_3O_{10}$. *Journal of Physics: Condensed Matter*, 15(40):6817–6833, October 2003.

[175] Azeem Banday and Sevi Murugavel. Small polaron hopping conduction mechanism in $LiFePO_4$ glass and crystal. *J. Appl. Phys.*, page 10, 2017.

[176] D G Martin. A re-appraisal of the thermal conductivity of UO_2 and mixed (U, Pu) oxide fuels. page 22.

[177] J. L. Bates. Thermal conductivity of UO_2 improves at high temperature. *Nucleonics 19 (6)*, pages 83–87, 1961.

[178] P. Browning. On the relative importance of the electronic and radiative contributions to the thermal conductivity of uranium dioxide. *Journal of Nuclear Materials 92 (1980) 33-38*, pages 33–38, April 1980.

[179] H.P Myers and J.-A Gyllander. The transmission of infra-red radiation trhough sintered uranium dioxide.

[180] P.J Reid, M.J Richards, F.C Iglesias, and A.C Brito. Source 2.0 Model Development : UO_2 Thermal properties.

[181] J.L Bates. Visible and Infrared Absorption Spectra of Uranium Dioxide. *Nuclear Science and Enginerring : 21, 26-29 (1965)*, June 1964.

[182] R. Viskanta. Influence of Internal Thermal Radiation on Heat Transfer in UO_2 Fuel Elements. *Nuclear Science and Enginerring : 21, 13-19 (1965).*

[183] J.A Stoddard and N.J McCormick. Radiation Heat Transfer in Ceramic Oxide Fuel Elements. *Departament of Nuclear Engineering University of Washington Seattle, Washinton 98105*, pages 126–129, 1970.

[184] M. Bober, J. Singer, and K. Wagner. Spectral Reflectivity and Emissivity Measurements of Solid and Liquid UO_2 at 458, 514.5 and 647 nm as a Function of Polarization and Angle of Incidence.

[185] M.J Davies. A spectrophotometric study of the dioxides of cerium, thorium and uranium, Ph.D Thesis, University of Leeds, 1970.

[186] P. Chereau and J.-F. Wadier. Mesures de resistivite et de cinetique d'oxydation dans PuO_2. *Journal of Nuclear Materials*, 46(1):1–8, 1973.

[187] Masato Kato and Kenji Konashi. Lattice parameters of $(U, Pu, Am, Np)O_{2-x}$. *Journal of Nuclear Materials*, 385(1):117–121, March 2009.

[188] IAEA Thermo-Physical Materials Properties Database - Home.

[189] ESNII+ project, FP7-Fission-2013, Grant agreement no: 605172.

[190] Dragos Staicu. ESNII+ : Preparing ESNII for Horizon 2020 : Deliverable D742 : Properties measurements on irradiated fuels (NESTOR 3). Technical report, September 2017.

[191] K Morimoto, M Kato, M Ogasawara, and Motoaki Kashimura. The influence of Pu-content on thermal conductivities of (U, Pu)O2 solid solution. In *International Conference on Fast Reactors and Related Fuel Cycles : Challenges and Opportunities FR09*.

[192] Kyoichi Morimoto, Masato Kato, and Masahiro Ogasawara. Thermal diffusivity measurement of (U, Pu)O2-x at high temperatures up to 2190K. *Journal of Nuclear Materials*, 443(1-3):286–290, November 2013.

[193] A.K Sengupta, K.S Arora, A. Kumar, and C. Ganguly. Thermal conductivity of titania-doped UO2-4% PuO2. *High Temperatures - High Pressures, Volume 19*, pages 509–512, 1987.

[194] P.R. Vasudeva Rao, S. Anthonysamy, M.V. Krishnaiah, and V. Chandramouli. Oxygen potential and thermal conductivity of (U,Pu) mixed oxides. *Journal of Nuclear Materials*, 348(3):329–334, February 2006.

[195] Rudy J. M. Konings, Ondrej Beneš, Attila Kovács, Dario Manara, David Sedmidubský, Lev Gorokhov, Vladimir S. Iorish, Vladimir Yungman, E. Shenyavskaya, and E. Osina. The Thermodynamic Properties of the f -Elements and their Compounds. Part 2. The Lanthanide and Actinide Oxides. *Journal of Physical and Chemical Reference Data*, 43(1):013101, March 2014.

[196] Properties for LMFBR safety analysis. Technical Report ANL-CEN-RSD-76-1, 1976.

[197] H. Elbel and H.E. Schmidt. Characterisation of mixed oxide fuel pellets with respect to their thermal conductivity. *Nuclear fuel performance. BNES, London*, 1985.

[198] S.K. Evans and P.E Bohaboy. Thermal conductivity of physically mixed (U0.8.Pu0.2)O2-x. *Trans.Am.Nucl.Soc 13*, pages 571–572, 1970.

[199] R.L Gibby. Thermal conductivity of (Pu, U)O2. Technical Report BNWL -1349-1, UC-25, 1970.

[200] R.L Gibby. Thermal diffusivity of (U, Pu)O2. Technical Report BNWL-1058, UC-25, 1969.

[201] F.J Hetzler, T.E. Lannin, Perry K.J, and E.L Zebroski. The thermal conductivity of uranium and uranium-plutonium oxides. Technical Report GEAP-4879, General Electric.

[202] R.A Laskiewicz, G.F. Melde, S.K. Evans, and P.E. Bohaboy. Thermal conductivity of Uranium-Plutonium oxide. Technical Report GEAP-13733 AEC Research and Development report, September 1971.

[203] Kyoichi Morimoto, Masato Kato, Masahiro Ogasawara, Motoaki Kashimura, and Tomoyuki Abe. Thermal conductivities of $(U, Pu, Am)O_2$ solid solutions. *Journal of Alloys and Compounds*, 452(1):54–60, March 2008.

[204] Kyoichi Morimoto, Masato Kato, Masahiro Ogasawara, and Motoaki Kashimura. Thermal conductivities of hypostoichiometric $(U, Pu, Am)O_{2-x}$ oxide. *Journal of Nuclear Materials*, 374(3):378–385, March 2008.

[205] Toshihiro Yamaguchi, Hiromitsu Kaneko, and Yutaka Honda. Measurements of thermal conductivity for (U0.7Pu0.3)O2-x fuels. Technical Report PNCT831-80-01.

[206] P.R. Vasudeva Rao, S. Anthonysamy, M.V. Krishnaiah, and V. Chandramouli. Oxygen potential and thermal conductivity of (U,Pu) mixed oxides. *Journal of Nuclear Materials*, 348(3):329–334, February 2006.

[207] S Hirooka and M Kato. Mechanical and Thermal Properties of $(U, Pu)O_{2-x}$. page 6.

[208] Markus J. Rieder and Gottfried Kirchengast. An inversion algorithm for nonlinear retrieval problems extending Bayesian optimal estimation. *Radio Science*, 35(1):45–56, January 2000.

[209] Bobak Shahriari, Kevin Swersky, Ziyu Wang, Ryan P. Adams, and Nando De Freitas. Taking the Human Out of the Loop: A Review of Bayesian Optimization. *Proceedings of the IEEE*, 104(1):148–175, January 2016.

[210] Jasper Snoek, Hugo Larochelle, and Ryan P. Adams. Practical Bayesian Optimization of Machine Learning Algorithms, August 2012. arXiv:1206.2944 [cs, stat].

[211] Peter I. Frazier. A Tutorial on Bayesian Optimization, July 2018. arXiv:1807.02811 [cs, math, stat].

[212] Keiji Naito, Toshihide Tsuji, Takeo Fujino, and Toshiyuki Yamashita. Electrical conductivity and defect structure of $(U, Pu)O_{2+x}$. *Journal of Nuclear Materials*, 169:329–335, December 1989.

[213] Jon Mackey, Frederick Dynys, and Alp Sehirlioglu. Uncertainty analysis for common Seebeck and electrical resistivity measurement systems. *Review of Scientific Instruments*, 85(8):085119, August 2014.

[214] Fermin Uriz, Benjamin Remy, and Alain Degiovanni. Prise en compte du biais de modèle dans le calcul des écarts-types des paramètres identifiés par méthode inverse.

[215] A Young. Model for electronic contribution to thermal and transport properties of ThO_2, UO_2 and PuO_2 in the solid and liquid phases. page 14.

[216] J.C Kileen. The measurement of the electron to hole mobility ratio in UO_2 and its effect on thermal conductivity. *J. Nucl. Mat. 92 (1980) 13.*

[217] R.N. Hampton, G.A. Saunders, A.M. Stoneham, and J.H. Harding. The electrical impedance of single-crystal urania at elevated temperatures. *Journal of Nuclear Materials*, 154(2-3):245–252, July 1988.

[218] Masato Kato, Hiroki Nakamura, Masashi Watanabe, Taku Matsumoto, and Masahiko Machida. Defect Chemistry and Basic Properties of Non-Stoichiometric PuO_2. *Defect and Diffusion Forum*, 375:57–70, May 2017.

[219] Masato Kato, Masashi Watanabe, Shun Hirooka, and Romain Vauchy. Oxygen diffusion in the fluorite-type oxides CeO2, ThO2, UO2, PuO2, and (U, Pu)O2. *Frontiers in Nuclear Engineering*, 1:1081473, January 2023.

[220] Masato Kato and Masahiko Machida. *Materials Science and Fuel Technologies of Uranium and Plutonium Mixed Oxide*. CRC Press, Boca Raton, 1 edition, October 2022.

[221] Nicholas C. Pyper and Ian P. Grant. Studies in multiconfiguration Dirac–Fock theory. Part 3.—Interpretation of the electronic structure of neutral and ionized states of uranium. *J. Chem. Soc., Faraday Trans. 2*, 74(0):1885–1900, 1978. Publisher: The Royal Society of Chemistry.

[222] L. Leibowitz, D.F. Fischer, and M.G Chasanov. Enthalpy of Uranium-Plutonium oxides : $(U, Pu)O_{1.97}$ from 2350 to 3000 K. *Journal of Nuclear Materials 42*, pages 113–116, 1972.

[223] J. K. Fink. Enthalpy and heat capacity of the actinide oxides. *International Journal of Thermophysics*, 3(2):165–200, June 1982.

[224] Preparing ESNII for HORIZON 2020: https://cordis.europa.eu/project/id/605172/fr.

[225] Yoshihisa Ikusawa, Kyoichi Morimoto, Masato Kato, Kosuke Saito, and Masayoshi Uno. The Effects of Plutonium Content and Self-Irradiation on Thermal Conductivity of Mixed Oxide Fuel. *Nuclear Technology*, 205(3):474–485, March 2019.

[226] L.A. Goldsmidth and J.A.M. Douglas. The thermal conductivity of plutonium-uranium dioxide at temperatures up to 1273 K. *Journal of Nuclear Materials 43*, pages 225–233, 1972.

[227] Franklin L. Oetting. The chemical thermodynamics of nuclear materials. VII. The high-temperature enthalpy of plutonium dioxide. *Journal of Nuclear Materials 105*, pages 257–261, 1982.

[228] Allen E Ogard. High-temperature heat content of plutonium dioxide. *Proc. 4th International Conference on Plutonium and Other Actinides*, pages 78–83.

[229] Owen L. Kruger and Howard Savage. Heat capacity and Thermodynamic Properties of Plutonium Dioxide. *The Journal of Chemical Physics, Vol. 49, Number 10*, 1968.

[230] Takayuki Ozawa. JAEA Irradiation: B5D-2 & INTA-2 (IDF4.1.1 for F4)". Technical Report JAEA AST 2 AST NT JAE F4-IDF4.1.1-R0, October 2015.

[231] Takayuki Ozawa. Fuel R&D -F4 VVQ of Fuel Element Code - Deliverable DF 4.2.1 - JAEA Contribution to the Benchmark. Technical Report JAEA AST 2 AST NT JAE F4-DF4.2.1.

[232] Yukimoto Maeda, Takafumi Aoyama, Toshihiro Odo, Satoru Nakai, and Soju Suzuki. Distinguished Achievements of a Quarter-Century Operation and a Promising Project Named MK-III in JOYO. *Nuclear Technology*, 150(1):16–36, April 2005.

[233] T. Ozawa and T. Abe. Development and Verifications of Fast Reactor Fuel Design Code CEPTAR. *Nuclear Technology*, 156(1):39–55, October 2006.

[234] Takayuki Ozawa. Analysis of Fast Reactor Fuel Irradiation Behavior in the MA Recycle System. In *Volume 3: Nuclear Fuel and Material, Reactor Physics and Transport Theory; Innovative Nuclear Power Plant Design and New Technology Application*, page V003T02A006, Shanghai, China, July 2017. American Society of Mechanical Engineers.

[235] A YOSHIDAandS Yogo. Upgrading Program of the Experimental Fast Reactor Joyo.

[236] M. Morishita, H. Ohshima, and Y. Koizumi. *Sodium-cooled Fast Reactors*. JSME Series in Thermal and Nuclear Power Generation. Elsevier Science, 2022.

[237] http://www-cast3m.cea.fr/.

[238] N Chauvin, L Capriotti, S Gianfelici, J Harp, T Ogata, H Ohta, T Ozawa, A Schubert, P Van Uffelen, and S Cornet. Benchmark Study on Fuel Performance Codes for Fast Reactors.

[239] Rudy J. M. Konings, Ondrej Beneš, Attila Kovács, Dario Manara, David Sedmidubský, Lev Gorokhov, Vladimir S. Iorish, Vladimir Yungman, E. Shenyavskaya, and E. Osina. The Thermodynamic Properties of the f -Elements and their Compounds. Part 2. The Lanthanide and Actinide Oxides. *Journal of Physical and Chemical Reference Data*, 43(1):013101, March 2014.

[240] Ervin E. Underwood. *Quantitative Stereology*. Addison-Wesley, New York, Reading, Mass.„ 1970.

[241] C. L. Wan, W. Pan, Q. Xu, Y. X. Qin, J. D. Wang, Z. X. Qu, and M. H. Fang. Effect of point defects on the thermal transport properties of $(La, Gd_{1-x})_2Zr_2O_7$: Experiment and theoretical model. *Physical Review B*, 74(14):144109, October 2006.

[242] F. Seitz and A. Turnbull. *Solid State Physics*, volume 3. New York, 1956.

[243] J.H.Harding and D.G.Martin. A recommendation for the thermal conductivity of UO_2. *Journal of Nuclear Materials 166 (1989)*, pages 223–226, March 1989.

[244] Dongliang Zhao, Xin Qian, Xiaokun Gu, Saad Ayub Jajja, and Ronggui Yang. Measurement Techniques for Thermal Conductivity and Interfacial Thermal Conductance of Bulk and Thin Film Materials. *Journal of Electronic Packaging*, 138(4):040802, December 2016.

[245] Yuan Zhu. Heat-loss modified Angstrom method for simultaneous measurements of thermal diffusivity and conductivity of graphite sheets: The origins of heat loss in Angstrom method. *International Journal of Heat and Mass Transfer*, 92:784–791, January 2016.

[246] Wei Guo, Anqi Chen, Yanyan Wu, Yuan Zhu, and Shaobo Zeng. Algorithms for thermal diffusivity measurement of heterogeneous 1D materials based on Infrared Microscopy Enhanced Angstrom Method. *Journal of Physics: Conference Series*, 2116(1):012039, November 2021.

[247] Robert D. Cowan. Proposed method of measuring thermal diffusivity at high temperatures. *Journal of Applied Physics, Vol. 32, Nb. 7*, July 1961.

[248] M. Sheindlin, D. Halton, M. Musella, and C. Ronchi. Advances in the use of laser-flash techniques for thermal diffusivity measurement. *Review of Scientific Instruments*, 69(3):1426–1436, March 1998.

[249] Manuela Musella. *Development and test of a method for the simultaneous measurement of heat capacity and thermal diffusivity by laser-flash technique at very high temperatures. Application to uranium dioxide.* PhD thesis, University of Warwick.

[250] W J Parker and R J Jenkins. Thermal conductivity measurements on Bismuth Telluride in the presence of a 2MeV electron beam. *Advanced Energy Conversion*, 2:87–103, 1962.

[251] L.M Clark and R.E Taylor. Radiation loss in the flash method for thermal diffusivity. *Journal of Applied Physics*, 46:714, 1975.

[252] J.A. Cape and G.W. Lehman. Temperature and Finite Pulse-Time Effects in the Flash Method for Measuring Thermal Diffusivity. *Journal of Applied Physics 34*, pages 1909–1913, 1963.

[253] A. Degiovanni. *High Temp. - High. Press. 12, 683*, 1985.

[254] Fanny Cabezas. Projet de fin d'Etude en Entreprise: Mesure de propriétés sur des combustibles nucléaires MOX. Technical report.

[255] W. J. Parker, R. J. Jenkins, C. P. Butler, and G. L. Abbott. Flash Method of Determining Thermal Diffusivity, Heat Capacity, and Thermal Conductivity. *Journal of Applied Physics*, 32(9):1679–1684, September 1961.

[256] C. Ronchi, M. Sheindlin, M. Musella, and G. J. Hyland. Thermal conductivity of uranium dioxide up to 2900 K from simultaneous measurement of the heat capacity and thermal diffusivity. *Journal of Applied Physics*, 85(2):776–789, January 1999.

[257] Fredrik Grbnvold, Nils Jorgen Kveseth, and Arvid Sveen. Thermodynamics of the UO_{2+x} phase I. Heat capacities of $UO_{2.017}$ and $UO_{2.254}$ from 300 to 1000 K and electronic contributions. *J. Chem. Thermodynamics*, pages 665–679, 1970.

[258] Hideaki Inaba, Keiji Naito, and Masaomi Oguma. Heat capacity measurement of $(U_{1-y}, Gd_y)O_2$ ($0.00 < y < 0.142$) from 310 to 1500 K. *Journal of Nuclear Materials 149*, pages 341–348, 1987.

[259] James J Huntzicker and Edgar F Westrum. The magnetic transition, heat capacity, and thermodynamic properties of uranium dioxide from 5 to 350 K.

[260] Masaki Amaya, Katsumi Une, and Kazuo Minato. Heat capacity measurements on unirradiated and irradiated fuel pellets. *Journal of Nuclear Materials*, 294(1-2):1–7, April 2001.

[261] L. Leibowitz, L.W. Mishler, and M.G Chasanov. *Journal of Nuclear Materials 29:356*, 1969.

[262] R.A. Hein and P.N. Flagella. Enthalpy measurements on UO2 and Tungsten to 3260 K. Technical Report GE Report GEMP-578, 1968.

[263] D.R. Frederickson and M.G Chasanov. *J. Chem. Thermodynamics 2:263*, 1970.

[264] D.G Clifton. High-temperature calorimetry. Technical Report Quarterly Status Report on the Advanced Plutonium Fuels Program April to June 30, 1971 and Fifth Annual Report, FY 1971, R. D. Baker, ed., LA-4749-MS (Los Alamos Scientific Laboratory, 1971), p. 28.

[265] Christian Affortit. Contribution à l'études des chaleurs spécifiques des composés d'actinides. *CEA-R-4266*, page 90, 1972.

[266] L. Vlahovic, D. Staicu, A. Küst, and R.J.M. Konings. Thermal diffusivity of UO_2 up to the melting point. *Journal of Nuclear Materials*, 499:504–511, February 2018.

[267] M. Akoshima, B. Hay, M. Neda, and M. Grelard. Experimental Verification to Obtain Intrinsic Thermal Diffusivity by Laser-Flash Method. *International Journal of Thermophysics*, 34(5):778–791, May 2013.

[268] G. V. Kuznetsov and M. D. Kats. A theoretical analysis of the systematic errors in determining the thermal characteristics of structural materials by a pulse method in a sample of finite dimensions. *Measurement Techniques*, 52(4):384–387, April 2009.

[269] B. Hay, J. R. Filtz, J. Hameury, and L. Rongione. Uncertainty of Thermal Diffusivity Measurements by Laser Flash Method. *International Journal of Thermophysics*, 26(6):1883–1898, November 2005.

[270] J. Xue and R. Taylor. An evaluation of specific heat measurement methods using the laser flash technique. *International Journal of Thermophysics*, 14(2):313–320, March 1993.

[271] Michal Kövér, Mária Behúlová, Marián Drienovský, and Petr Motyčka. Determination of the specific heat using laser flash apparatus. *Journal of Thermal Analysis and Calorimetry*, 122(1):151–156, October 2015.

[272] Tsuyoshi Nishi, Masahide Takano, Mitsuo Akabori, and Yasuo Arai. Self-irradiation effect on thermal conductivity of (Pu0.91.Cm0.09)O2. *Journal of Nuclear Materials*, 433(1-3):531–533, February 2013.

[273] D. Staicu, T. Wiss, V.V. Rondinella, J.P. Hiernaut, R.J.M. Konings, and C. Ronchi. Impact of auto-irradiation on the thermophysical properties of oxide nuclear reactor fuels. *Journal of Nuclear Materials*, 397(1-3):8–18, February 2010.

[274] C. Ronchi, M. Sheindlin, D. Staicu, and M. Kinoshita. Effect of burn-up on the thermal conductivity of uranium dioxide up to 100.000 MWdt^{-1}. *Journal of Nuclear Materials*, 327(1):58–76, April 2004.